Development of a Multimodal MRI Study to Characterize Morpho-Functional Features in Rodent Models of Alzheimer's Disease

Thesis

Development of a multimodal MRI study to characterize morpho-functional features in rodent models of Alzheimer's Disease

Daniele TOLOMEO

Personal identifier: D1775168

Thesis submitted for the degree of ***Doctor of Philosophy***

School of Life, Health and Chemical Sciences

Open University of Milton Keynes, United Kingdom

Affiliated Research Centre:

Istituto di Ricerche Farmacologiche Mario Negri IRCCS – Milan, Italy

Director of Studies: Dr. Gianluigi Forloni

External Supervisor: Prof. Michael Chappell

September, 2018

Abstract

Alzheimer's Disease (AD) is the most common form of dementia, recognized by the World Health Organization as a global public health priority. It is a complex pathology characterized by the accumulation of the Amyloid-β (Aβ) peptide as extracellular plaques and of the intracellullar neuro fibrillary tangles (NFT) alongside with different events, such as chronic neuroinflammation and astrogliosis. None of the existing biomarkers is simultaneously specific for the pathology and sensitive to its progression. Metabolic and functional alterations are the earliest events described in the AD pathological cascade but shared with other form of dementia, while specific structural alterations occurs in a later stage of the disease. The use of transgenic models could simplify the development of new imaging biomarkers that would enable early diagnosis and making new treatments more effective. The objective of this work was to develop a multi-modal panel of magnetic resonance imaging (MRI) techniques and automated analysis pipelines, characterized by a high translational impact, in order to investigate the metabolic, functional and structural alterations in the brains of AD transgenic models. Results obtained in the APP23 transgenic mouse show that chemical exchange saturation transfer (CEST) imaging can be used to detect alterations in the brain uptake of the glucose analogue 2-deoxy-d-glucose (2DG) with a better resolution than PET and without the need of radioactive tracers. Moreover, a longitudinal study highlighted that significant structural and metabolic alterations can be found only in a late stage of the pathology. Furthermore, an advanced pipeline for the analysis of the rodent brain functional connectivity has been developed. This thesis demonstrates that the advantage to the experimental design adopted is simplifying longitudinal studies of the same animal cohort. The translation of the analysis pipelines adopted in human studies enables more powerful results and reduces the number of animals involved in research.

Acknowledgments

I must thank Gianluigi Forloni and the Mario Negri Institute for giving me the opportunity to work in a stimulating environment, learning advanced techniques and collaborating with great researchers of several fields.

A massive “thank you” goes to Edoardo Micotti; a great friend and mentor, who shared with me the joy and pain of the laboratory life. Without him this work wouldn’t be possible.

I owe a lot of gratitude to Michael Chappel, my external supervisor. Despite the distance, he has always supported me with many useful suggestions, hints and correcting my work.

I should also thank my colleagues, too many to be mentioned. You have always been there to fill the gap of knowledge of a physicist in a world of biologists... without you, I would have been a fish out water. I hope that the work I have made will be useful for you.

I must thank the International Brain Research Organization that allowed me to spend the month of July 2016 in Zurich at the ETH in the Neural Control Movement Lab headed by Nicole Wenderoth. I am particularly grateful to Valerio Zerbi, who kindly allowed me to assist at some laboratory sessions and introduced me to the universe of the functional MRI in the mouse models.

Table of Contents

List of abbreviations

2DG	2-deoxy-d-glucose
2DG6P	2DG-6-phosphate
3OMG	3-O-methy-D-glucose
[^{11}C]PIB	[^{11}C]Pittsburgh compund B
[^{18}F]FDG	2-deoxy-2-[^{18}F]fluoro-D-glucose
AC	Anterior commissure
AD	Alzheimer's Disease
AD	Axial Diffusivity
ADC	Aparent diffusion coefficient
ApoE	Apolipoprotein E
APP	Amyloid precursor protein
APT	Amide proton transfer
ASL	Arterial spin labeling
Aβ	Amyloid-beta
BCC	Body of the corpus callosum
BOLD	Blood oxygenation level dependent
CEST	Chemical Exchange Saturation Transfer
Cho	Choline
Cr	Creatine
CSF	Cerebrospinal fluid
DMN	Default mode network
DTI	Diffusion Tensor Imaging
DWS	direct water saturation
EC	External capsule
FA	Fractional Anisotropy
FID	Free induction decay
fMRI	Functional magnetic resonance imaging
rsfMRI	Resting state fMRI
FTD	Fronto temporal dementia
FI	Fimbria
GCE	glucose CEST enhancement
GCC	Genu of the corpus callosum

GlcN	2-amino-2-deoxy-D-glucose
Gln	Glutamine
GM	Gray matter
GSKβ	Glycogen synthase kinase 3β
IC	Internal capsule
LBD	Lewy body dementia
MCI	Mild cognitive impairment
MD	Mean Diffusivity
mI	Myo-inositol
MRI	Magnetic Resonance Imaging
MTR	Magnetization transfer ratio
NAA	N-acetyl-aspartate
NFT	Neurofibrillary tangles
OT	Optic tract
PBS	phosphate-buffered saline
PET	Positron emission tomography
PRESS	Point resolved spectroscopy
RA	Relative Anisotropy
RARE	Rapid acquisition with relaxation enhancement
RD	Radial Diffusivity
SCC	Splenium of the corpus callosum
rNOE	relayed nuclear Overhauser effect
T1	Longitudinal magnetisation relaxation time constant
T2	Transverse magnetisation relaxation time constant
TBSS	Tract Based Spatial Statistics
TE	Echo time
TE_{eff}	Effective echo time
TR	Repetition time
T-tau	Total tau
VBM	Voxel Based Mophometry
WASSR	water saturation shift referencing
WM	White matter
WT	wild type

Chapter 1: Introduction

1.1 – Alzheimer's Disease

Dementia is a clinical syndrome caused by progressive neurodegeneration, it is characterized by the deterioration in cognitive abilities and capacity of independent living. Recent estimates described that in 2010 over 35 million people lived with dementia world-wide. As the population continues to age, this number is expected to double every 20 years reaching 115 million in 2050 (Prince et al., 2013).

First described in 1906 by the German psychiatrist and neuropathologist Alois Alzheimer and named after him, Alzheimer's Disease (AD) is the most common form of dementia. Recognized by the World Health Organization as a global public health priority, it affects approximately 26 million people world-wide (Lane et al., 2018). Although the disease progression rate varies between patients, a person affected by AD lives four to eight years after diagnosis but, depending on other factors, can live as long as 20 years (Alzheimer's Assotiations 2018). AD symptoms worsen over time and can be described by a slow decline in memory, thinking and reasoning skills. Three categories have been defined to describe AD stages: Firstly a long and asymptomatic phase called preclinical stage, when pathological processes begins but there are not clincal signs of the disease. Subsequently, a prodromal stage called mild cognitive impairment (MCI) when mild symptoms appear with minimal impairment in instrumental activities of daily living. Finally the AD dementia phase when symptoms are severe and patients lose the ability to respond to their environment, to carry on a conversation and, eventually, to control movement (Alzheimer's Assotiations 2018).

Pathologically, AD can be considered as a complex interplay of different processes characterized by three main type of lesions (Figure 1): those related to accumulation of proteins, those that are due to the reactive processes such as inflammation and finally those that are due to plasticity losses of neurons and synapses that result in macroscopic brain atrophy in an advanced state of the disease (Duyckaerts et al., 2009).

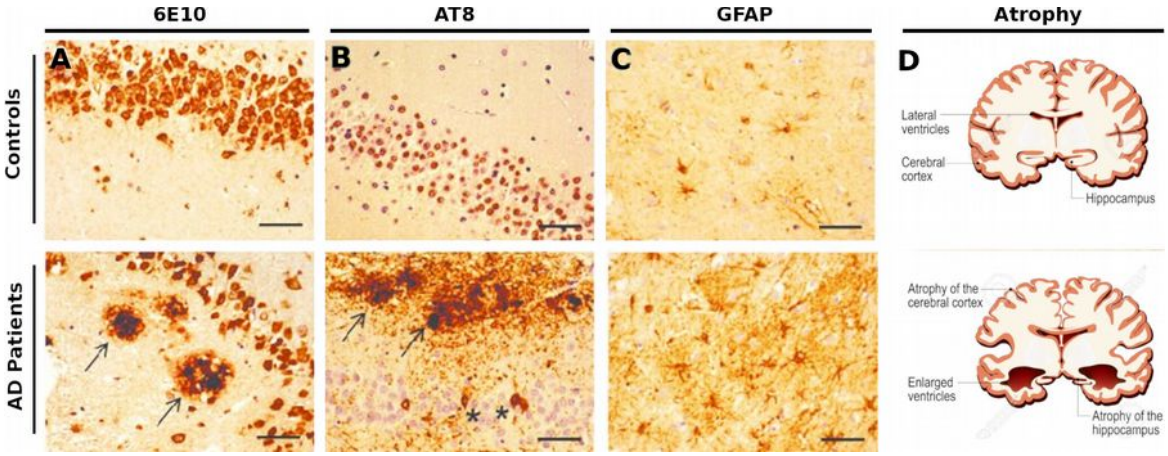

Figure 1: Neuropathology in the hippocampus of healthy controls subject and AD patients. (A) Diaminobenzidine (DAB) staining using the 6E10 antibody in hippocampal slices shows the presence of dense-core amyloid-positive plaques (arrows), which are absent in controls. (B) Immunohistochemistry with the AT8 antibody also shows AT8-positive senile plaques (arrows) and neurofibrillary tangles (asterisk), also revealing fiber-like structures resembling distorted neurites. (C) GFAP immunostaining reveals the presence of astrocytes with normal fine radial processes in the control brain; in the contrary, in the hippocampus of AD patients, several clusters of astrocytes with thick radial processes are observed. (Scale bars = 20µm). (D) In an advanced state of the disease, macroscopic brain atrophy and enlargement of ventricles can be identified as a result of the ongoing neural loss. Adapted from (Alves et al., 2016)

The underlying cause of the AD is not known in most of the cases. However, as shown in Figure 2, a small proportion of early-onset AD cases are due to familiar genetic mutations in one of three genes: those encoding amyloid precursor protein (APP), presenilin 1 (PSEN1) and presenilin 2 (PSEN2) which are components of secretases that are involved into the processing of amyloid-beta (Aβ) peptide. The majority of AD cases are called sporadic forms of AD which occur generally in people over 65 years of age, without obvious familial aggregation. A number of genes have been identified which are associated with a greatly increased risk of developing late onset. Among all of these, the

apolipoprotein E (ApoE) is the one which is associated with the most elevated risk for developing AD. It is a cholesterol carrier that supports lipid transport and injury repair in the brain (Mahley and Rall, 2000). Individuals carrying the ε4 allele have more than seven times increased risk of developing AD compared with those carrying the more common ε3 allele, whereas the ε2 allele was associated with a decreased risk. However, it remains unclear how Apoε4 is able to influences AD onset and progression (J. Kim et al., 2009; C.-C. Liu et al., 2013).

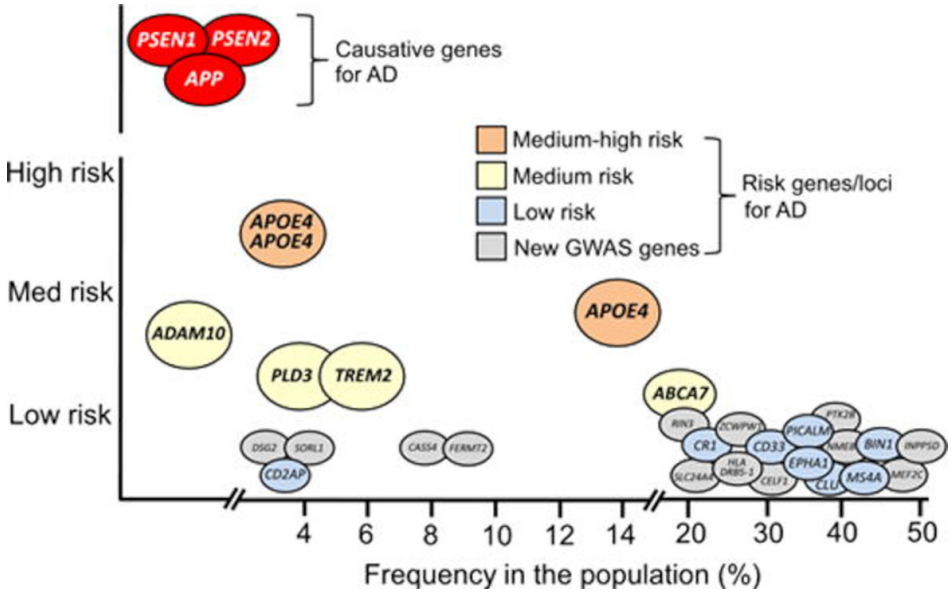

Figure 2: Risk-increasing effects (vertical axis) plotted against prevalence in general population (horizontal axis) between either causative or susceptible genes/loci. (Yamazaki et al., 2016)

A huge number of studies have focused on AD pathogeneses proposing different hypothesis. Nonetheless, the precise etiologies and pathogeneses of AD still remain to be clarified, especially the molecular pathways at the bottom of the various pathological alterations that impair the cognitive functions related to learning and memory.

The **"amyloid hypothesis"** is the most widely accepted. It posits that the amyloid plaques, formed by aggregates of amyloid-β are central to AD pathogenesis. Studying the familiar mutations of APP, PSEN1 and PSEN2 genes it has been found that the altered

production (Figure 3) and clearance of the Aβ peptide cause its deposition in the form of plaques in the brain parenchyma (Hardy and Allsop, 1991). In particular, these familiar genetic mutations results in a preferred amyloidogenic pathway producing the $A\beta_{1-42}$ form, with 42 amino acid length, which have higher self aggregation than the $A\beta_{1-40}$ peptide (Scheltens et al., 2016).

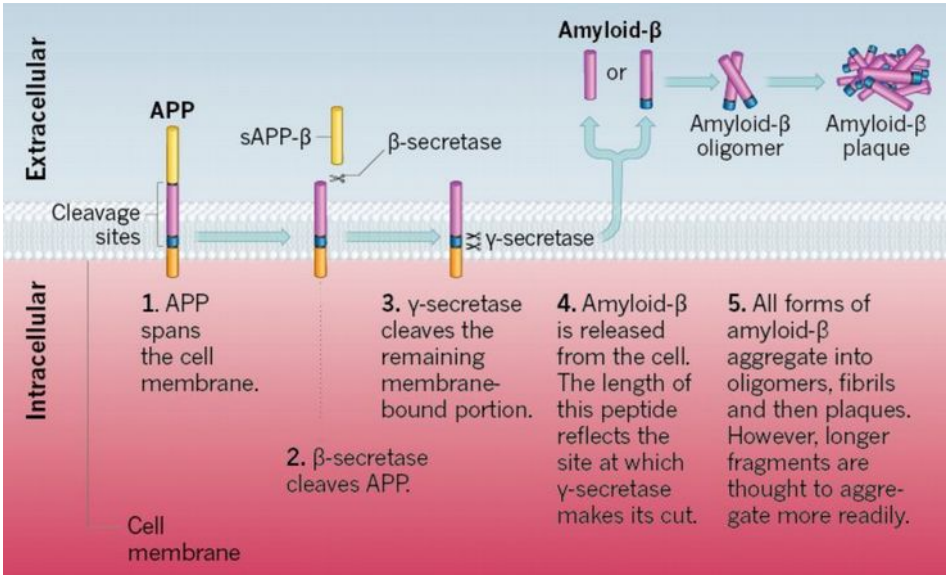

Figure 3: For the peptide amyloid-β to be released into the space between cells, the external portion of the membrane protein APP must be first cleaved off by the enzyme β-secretase. The enzime γ-secretase then cuts the remaining membrane-bound portion of the protein, freeing amyloid-β. Because γ-secretase can cut APP at a number of sites, the length of amyloid-β can vary. (Mucke, 2009)

Extracellular Aβ accumulation may also involve vessel walls of arteries, veins and capillaries (Figure 4). Small Aβ aggregates, called oligomers, have been described to be more toxic than mature fibrils and associated with a cognitive decline (Ferreira and Klein, 2011).

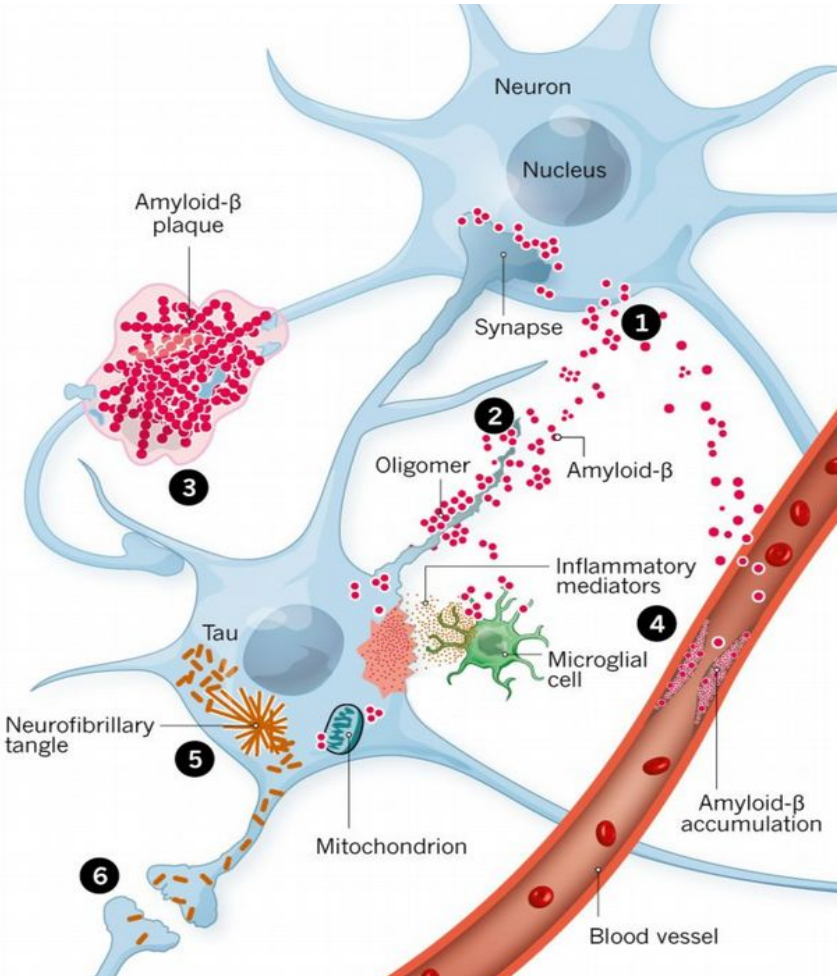

Figure 4: AD pathological cascade. (1) Processing of the APP at cell membrane level. (2) In the space between neurons, amiloyd-β forms oligomers that are thought to disrupt the function of synapses. (3) Fibrils of amyloid- β oligomers aggregate into plaques, which interfere with function of neurons. (4) Amyloid-β deposits outside cells and in blood vessels of the brain activate immune cells called microglial cells. This triggers the release of inflammatory mediators and might contribute to synaptic loss. (5) Misfolded tau aggregates into NFT inside neurons displacing intracellular organelles. (6) Misfolded tau pass through synapses to other neurons, where it catalyses further misfolding tau. Adapted from ("The amyloid hypothesis on trial. - PubMed - NCBI," n.d.).

Tau proteins are members of the microtubule-associated protein family, and are normally expressed in neurons, where they have a fundamental role in maintaining the neuronal microtubule network. Microtubules are involved in maintaining the cell shape and serve as tracks for axonal transport. Tau proteins also establish some links between microtubules and other cytoskeletal elements or proteins (Buée et al., 2000). In AD, the

APP cleavage products can activate the glycogen synthase kinase 3β (GSKβ) protein causing and abnormal tau hyperphosphorylation that lead to the formation of neurofibrillary tangles (NFT) (Grundke-Iqbal et al., 1986; Hooper et al., 2008). These NFT may accumulates in the cell body of the neuron but also in the dendrites as neuropil threads and in the axons forming the senile plaque neuritic corona, Figure 4. Other mutations such as DYRK1A (Janel et al., 2014) or Tau are involved in the NFT formation.

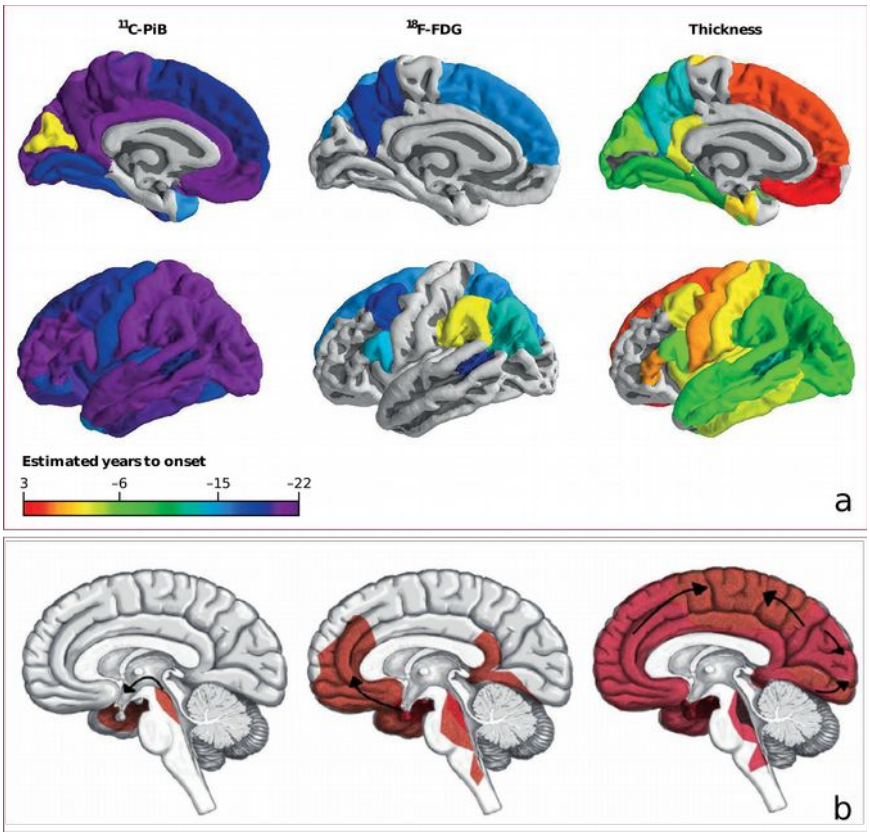

Figure 5: AD evolution a) The color scale represents the first point in the disease relative to estimated years to onset at which rates of biomarker. Increased Aβ deposition precedes hypometabolism that is followed by cortical thinning. (Gordon et al., 2018). b) Spreading of tau pathology in Alzheimer Disease. (Candela et al., 2013)

The progression of Aβ deposition, Figure 5a, begins in the neocortex, and evolves to the allocortex, to the subcortical structures and finally to the cerebellum. However, high inter-individual variability of the Aβ deposition was observed in early stages, making difficult the evaluation of the disease (Mann et al., 2001). The impairment in cerebral glucose

metabolism is an invariant pathophysiological feature in AD and its occurrence may precedes cognitive dysfunction for decades (Cunnane et al., 2011; Jack et al., 2010). Increased Aβ deposition precedes hypometabolism that is followed by cortical thinning (Gordon et al., 2018). In contrast to Aβ deposition, the spread of NFT in the bran has been described with little variations between subjects, and its progression was classified into six different stages (Braak and Braak, 1991). It begins from the entorhinal cortex, spreading to the hippocampus, and finally to the other parts of the isocortex (Figure 5b). Both depositions increase with age, but stages 1 of the NFT deposition can develop before the Aβ pathology (Braak and Del Tredici, 2014; Johnson et al., 2016).

1.1.1 – Diagnosis of AD

There are no validated models able to recapitulate the full pathological spectrum of the disease and the definitive diagnosis is still based on histological confirmation at postmortem examination. The AD diagnosis process is complicated by the presence of early symptoms that are shared with other neurological disorders.

An ideal biomarker would allow the clinician to distinguish AD form other form of dementia, such as vascular dementia, fronto temporal dementia (FTD) or Lewy body dementia (LBD). As shown in Figure 6, there is not a single imaging biomarker that is specific for the pathology but also to the disease progression. The metabolic impairment occurs in an early stage of the disease but it is shared with other forms of dementia, on the other side, the amyloid deposition is specific for AD but reaches a plateau by the mild cognitive impairment stage (MCI). Since, none of the existing biomarkers can fulfill all the conditions needed, a combination of the existing biomarkers is needed.

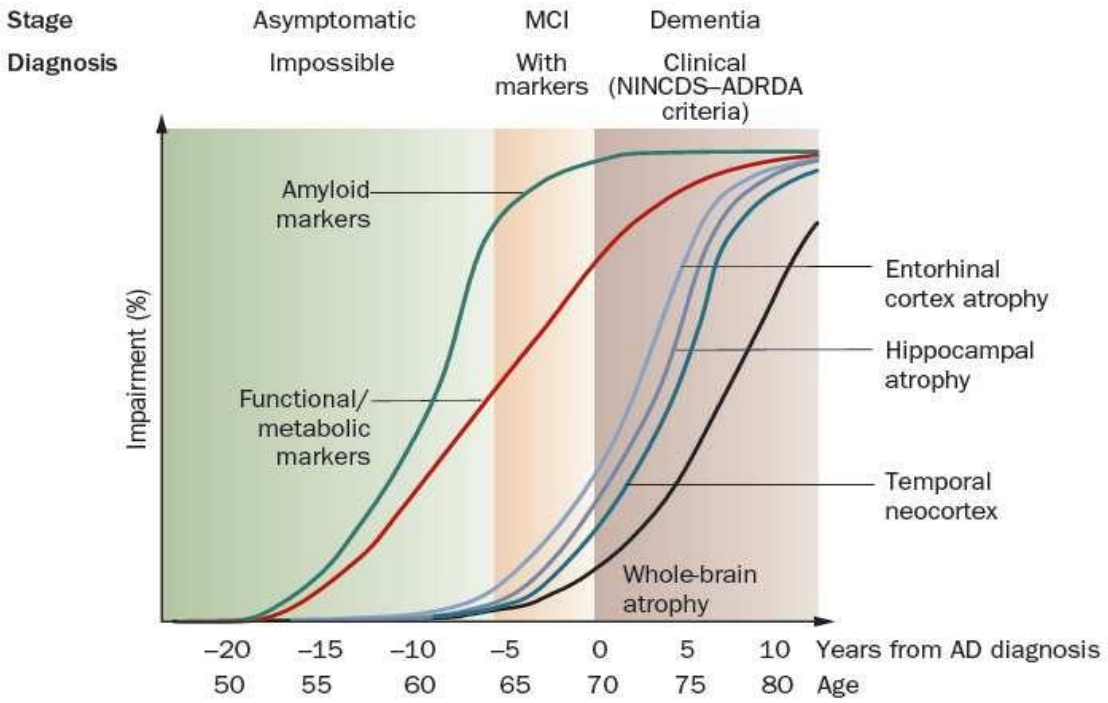

Figure 6: Theoretical model describing the natural progression of cognitive and biological markers of AD(Frisoni et al., 2010)

The diagnostic criteria have been recently updated, allowing the identification of the stage pathology, by the integration of the clinical evaluation of cognitive dysfunction by neuropsychological tests (Scheltens et al., 2016) with the so-called A/T/N classification (Figure 7), where "A" refers to the value of amyloid biomarkers; "T" to the value of a tau biomarkers; and "N," to biomarkers of neurodegeneration or neuronal injury (Jack et al., 2018, 2016). Even if cognitive impairment evaluations provides valuable information about the societal burden of cognitive disability, amnestic multidomain dementia and other variants are not synonymous with the presence of Aβ deposition and neurofibrillary degeneration. On the other hand, the absence of amnestic dementia is not synonymous with the absence of these hallmark lesions of AD and preclinical stage cannot be ascertained without the use of biomarkers. Up to 60% of cognitively unimpaired individuals over age 80 years have AD neuropathologic changes at autopsy or by biomarkers (Nelson et al., 2011, 2007; Serrano-Pozo et al., 2014). Thus, the use of just

cognitive evaluation in the clinical diagnosis of “AD” to ascertain absence of disease is associated with an error rate exceeding 50% (Jack et al., 2018).

		Syndromal Cognitive Stage		
		Cognitively unimpaired	**MCI**	**dementia**
Biomarker Profile	$A^- T^- (N)^-$	normal AD biomarkers, cognitively unimpaired	normal AD biomarkers with MCI	normal AD biomarkers with dementia
	$A^+ T^- (N)^-$	Preclinical Alzheimer's pathologic change	Alzheimer's pathologic change with MCI	Alzheimer's pathologic change with dementia
	$A^+ T^- (N)^+$	Alzheimer's and concomitant suspected non Alzheimer's pathologic change, cognitively unimpaired	Alzheimer's and concomitant suspected non Alzheimer's pathologic change with MCI	Alzheimer's and concomitant suspected non Alzheimer's pathologic change with dementia
	$A^+ T^+ (N)^-$	Preclinical Alzheimer's disease	Alzheimer's disease with MCI (Prodromal AD)	Alzheimer's disease with dementia
	$A^+ T^+ (N)^+$			

Figure 7: Risk of short-term cognitive decline based on the biomarker profile and cognitive stage. The sign beside the biomarker letter indicate whether it's positive or negative. When the rate of short term clinical progression is expected to be low the background color is white and gets darker when the expected progression rate is higher (Jack et al., 2018)

1.1.2 – Amyloid and Tau markers

Amyloid and tau deposition are the first events that occur in a preclinical stage of the pathology. But, since this deposition already reaches a plateau by the MCI stage, they cannot be considered good markers for the progression of the pathology in the clinical stage of the disease. Two main biomarkers are used to detect this deposition.

Firstly, biochemical measurements show a decrease of the $A\beta_{1-42}$ content in the cerebrospinal fluid (CSF) when the amyloid plaque load is increasing (Palmqvist et al., 2016). On the other side, increased levels of CSF total (T-tau) and tau phosphorylated at threonine 181 ($P\text{-}tau_{181}$) are related to the progression of the pathology and correlated with NFT burden at autopsy (Buerger et al., 2006; Tapiola et al., 2009). High diagnostic

accuracy was shown by the ratio $A\beta_{1-42}$/P-tau_{181} demonstrating an added discriminatory value for AD versus other forms of dementia (Engelborghs et al., 2008). However, CSF samples must be collected by lumbar puncture which represent an invasive exam.

Secondly, positron emission tomography (PET) is an imaging technique that is able to detect the gamma-rays pairs emitted by an injected radionuclide synthesized to bind selective molecular targets. Different amyloid tracers (e.g. Pittsburgh compound B [^{11}C]-PIB (Mathis et al., 2002), [^{18}F]-florbetapir (Wong et al., 2010; Yang et al., 2012) or [^{18}F]-florbetaben) have shown exceptional value in the identification of the Aβ deposition (Nordberg et al., 2010). High correlation of PIB binding and CSF $A\beta_{1-42}$ level was found when collected in the same individuals (Fagan et al., 2006). The progresses in radiotracer development has recently allowed the synthesis of tau PET ligands such as THK5317, THK5351, AV-1451, and PBB3 (Shah and Catafau, 2014; Saint-Aubert et al., 2017). More recently P-tau_{181} CSF content was associated with both Aβ and tau ligand measurements but also to cortical thickness (Mielke et al., 2018).

1.1.3 – Functional and metabolic markers

Although the amyloid hypothesis is evidenced by numerous experimental and clinical studies, none of the developed treatments were capable of reducing Aβ plaques or prevent the disease progression and almost all of the clinical trials proposed have shown small improvement of the cognitive function (Franco and Cedazo-Minguez, 2014; Holmes et al., 2008; Mangialasche et al., 2010). This situation has pushed researchers to develop diagnostic biomarkers that would enable to investigate the initial events of the disease. Thus, clarification of the etiological factor(s) and consequences associated with abnormal cerebral glucose metabolism could provide valuable clues for treatment strategies as well

as ideal diagnostic approaches in AD. Metabolic dysfunctions are correlated with the severity of dementia (Mosconi, 2005). The glucose radioactive analogue called [^{18}F]-FDG is a PET tracer able to detect synaptic activity (Sokoloff, 1981). Since glucose represent the brain principal source of energy, its detection allows an evaluation of the brain metabolism that has been shown to decrease with the progression of the pathology. A reduction in the parietotemporal, frontal and posterior cingulate cortex has been found in patients with AD compared with healthy subjects. [^{18}F]-FDG uptake correlates with post-mortem histological measurements of the synaptic vesicle protein called synaptophysin (Rocher et al., 2003).

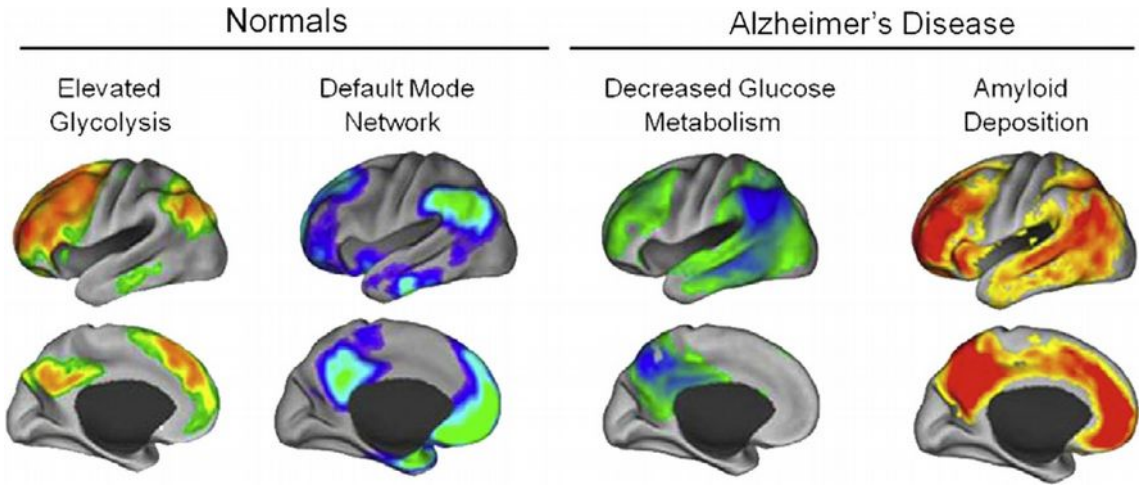

Figure 8: From left to right: DMN regions have increased aerobic glycolysis DMN regions in the normal brain; DMN regions have decreased glucose metabolism in AD; DMN regions are the first to develop amyloid deposition in AD. (Sheline and Raichle, 2013)

Moreover, regional analysis, represented in Figure 8, have shown that in cortical areas [^{11}C]PIB retention inversely correlates with glucose metabolism, measured with [^{18}F]-FDG (Y. Li et al., 2008; Mosconi et al., 2010; Oh et al., 2016, p.) possibly indicating an amyloid toxicity. [^{18}F]-FDG-PET is considered a robust biomarker of neurodegeneration, observed to be decreased before the onset of cognitive decline in patients who are later identified to be AD (Jagust, 2006; S. Zhang et al., 2012). However, neurodegeneration is not specific for AD, and must be integrated with other biomarkers. Moreover, PET is an

expensive technique limited by the need of specific infrastructures and that require the exposition to radioactivity.

Specific MRI techniques have also been developed to detect brain functional and metabolic alterations. With the application of magnetic resonance spectroscopy (MRS) localized alterations of brain metabolites can be measured. The ratio between N-acetyl-aspartate and Creatine (NAA/Cr) was found to be significantly reduced in the posterior cingulate and in the hippocampus of AD patients simultaneously with an increased myo-inositol (mI)/Cr ratio in posterior cingulate. These indexes were presented as possible AD biomarkers (Wang et al., 2015). Arterial spin labeling (ASL) is a technique able to measure the tissue perfusion trhough the assessment of the cerebral blood flow (CBF) (Petcharunpaisan et al., 2010). CBF is positively correlated with brain activity (Iadecola, 2004); lower perfusion in patients with MCI and AD was found in the parietal lobe, but also in angular and middle temporal areas as well as in the left middle occipital lobe and precuneus (Alexopoulos et al., 2012). Functional MRI (fMRI) is used to detect the neuronal activity by changes of the blood oxygenation level dependent signal (BOLD) (Ogawa et al., 1990). Correlating the time courses of the BOLD signal oscillation it is possible to link brain regions belonging to the same functional network. These networks can be evaluated in resting conditions or during cognitive tasks to assess the functional integrity of networks involved in memory and cognitive domain. The Default Mode Network (DMN) comprises different regions that are active in rest condition (Buckner et al., 2008) including the precuneus/posterior cingulate cortex, medial prefrontal cortex and the hippocampus (Figure 8). The decreased connectivity found within the DMN of MCI and AD patients could explain the hypometabolism measured by FDG-PET (Buckner et al., 2008; Dennis and Thompson, 2014; Sheline and Raichle, 2013). Recently it has been shown how the anatomical propagation of tau in the AD brain spreads along functional

networks. Tau pathology accumulation seems to correlate with functionally connected brain regions (Hoenig et al., 2018).

1.1.4 – Structural markers

MRI volumetric measurements can be used to visualize the progressive cerebral atrophy caused by the overall neurodegeneration due to dendritic and neuronal loss. The enthorinal cortex (Khan et al., 2014) was found to be one of the earliest region of atrophy followed by the shrinkage of hippocampus, amygdala and in the end of the temporal neocortex. This sequence of atrophy progression measured by MRI fits histopathological studies describing the same regional progression in the spread of NFT (Braak and Braak, 1991; Smith, 2002). Figure 9 shows the evolution of the cortical thickness within a period of 12 months.

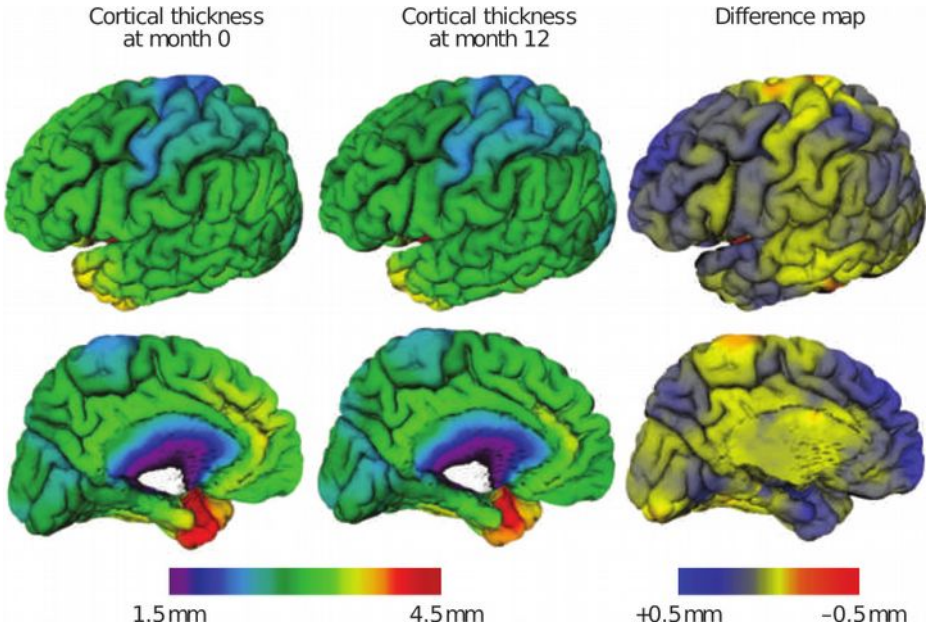

Figure 9: Cortical thinning in patients. Measurements were performed between baseline and 12months. The difference map shows thinning in the range of 0.5mm in the medial temporal cortex and frontal, parietal and temporal neocortices, with relative sparing of the sensorimotor strip and visual cortex. The thinning maps closely with the known progression of neurofibrillary tangles and neurodegeneration at autopsy. (Frisoni et al., 2010)

The distribution and the rate of regional atrophy were correlated also with cognitive impairment (Cardenas et al., 2011; Ridha et al., 2008). However, cerebral atrophy is nonspecific for AD and it might be produced by factors different from the progression of neural loss which should be ideally confirmed by a direct histopathological analysis.

Although major lesions characterizing AD were identified in the gray matter (GM), it has been shown that the cognitive impairment can be related to the cortical disconnection caused by the white matter (WM) degeneration (Gunning-Dixon and Raz, 2000). Increased levels of $A\beta_{40}$ and $A\beta_{42}$ were associated with a decrease in the myelin basic protein in human WM (Roher et al., 2002). Factors causing WM degeneration are still unclear and two competing models have been proposed (Alves et al., 2015): 1) The retrogenesis model suggest that WM disintegration occurring in AD is at the core of the earliest changes involved. Myelin breakdown disrupts brain functions with subsequent loss of neurons and progression to permanent deficits (Bartzokis, 2004). 2) The alternative hypothesis which considers the WM degeneration as a consequence of the Wallerian degeneration which postulates a posterior-anterior gradient of fibre degeneration where the cortical pathology is at the origin of the damage (Coleman, 2005). Diffusion Tensor Imaging (DTI) is a technique that makes MRI sensitive to the water diffusion in microstuctures. It is therefore used to investigate WM integrity showing abnormalities in corpus callosum, frontal, parietal, temporal cortices of AD patients. The most consistent impairment was found in the temporal white matter which is highly connected with entorhinal cortex and hippocampus suggesting a relation with the gray matter neurodegeneration (Acosta-Cabronero and Nestor, 2014; Amlien and Fjell, 2014; Chua et al., 2008; Stebbins and Murphy, 2009).

1.1.5 – AD Transgenic models

Advances in genetic engineering have allowed the creation of transgenic animal models harboring gene mutations known to cause familiar AD. Transgenic mice are the most commonly adopted (Balducci and Forloni, 2011; Hall and Roberson, 2012; Sasaguri et al., 2017; Esquerda-Canals et al., 2017) but the interest in the use of rat transgenic models is increasing (Benedikz et al., 2009; Do Carmo and Cuello, 2013). The use of these experimental models offers several advantages; their genome has been entirely mapped, they can be easily bred and manipulated in order to investigate their cognitive abilities (Ameen-Ali et al., 2017; Kobayashi and Chen, 2005; Webster et al., 2014). As shown in Table 1, available experimental models only partially reproduce the AD condition. They present some of the neuropathological features typical of the human pathology including cognitive impairment, neuroinflammation and plaque deposition in the brain parenchyma and in vessels. However, the onset of these features can vary greatly between models and only few of these present important features like neuronal loss and NFT deposition. A meta-analysis of 40 peer-reviewed studies that evaluated amyloid deposition in different transgenic models after assessing their cognitive performance found that only a weak association exists (Foley et al., 2015). Moreover it is difficult to model in mice the complexity of higher-order cognitive functions exclusive to humans. Instead, each mouse model allows the investigation of different cognitive dysfunction related to AD. The cognitive deficits progression in a specific behavioral task can be quite different among the mouse models and most of them display deficits in spatial working memory earlier than the deficits in other cognitive domains (Stewart et al., 2011; Webster et al., 2014).

Table 1: Most commonly used transgenic models; adapted from (Balducci and Forloni, 2011; Benedikz et al., 2009; Do Carmo and Cuello, 2013)

	Tg Line (Reference)	Mutation	Cognitive Impairments	Neuropathological Features
Mice	PDAPP (Games et al., 1995)	APP V717F (Indiana)	Reference working and spatial memory	Aβ plaques (6–9 months), dystrophic neurites, gliosis, loss of synaptic densities
	Tg2576 (Hsiao et al., 1996)	APP KM670/671NL (Swedish)	Reference, working and recognition memory, contextual memory; alternation in Y- and T-mazes	Aβ plaques (11–13 months), dystrophic neuritis, astrogliosis, microgliosis
	APP23 (Balducci et al., 2010; Sturchler-Pierrat et al., 1997)	APP KM670/671NL (Swedish)	Reference, working and spatial memory; passive avoidance; recognition memory	Aβ plaques (6–12* or 15–18** months), cerebrovascular Aβ, dystrophic neuritis, neuronal loss in CA1 region of hippocampus; astrogliosis and microgliosis
	PS/APP (Holcomb et al., 1998)	APP KM670/671NL (Swedish), PSEN1 M146L (A>C)	Reference, working and spatial memory; recognition memory	Aβ plaques (3–6 months), astrogliosis and microgliosis; dystrophic neuritis
	J20 (Mucke et al., 2000)	APP KM670/671NL (Swedish), APP V717F (Indiana)	Reference and working and spatial memory; recognition memory	Aβ plaques (8 months), gliosis
	TgCRND8 (Chishti et al., 2001)	APP KM670/671NL (Swedish), APP V717F (Indiana)	Reference, working and spatial memory; recognition memory	Aβ plaques (3 months), astrogliosis and microgliosis; dystrophic neuritis
	APP/PS1 (**or** APPPS1-21) (Radde et al., 2006)	APP KM670/671NL (Swedish), PSEN1 L166P	Impaired reversal learning in spatial maze task at eight months of age Earlier observations of cognitive impairment shown deficits in the Morris Water maze at seven months of age	Aβ deposition (6 weeks). Deposits appear in the hippocampus, striatum, thalamus, and brainstem (4-5 months). No fibrillar tau inclusions are seen. Global neuronal loss is not observed, but modest neuron loss was found in the granule cell layer of the dentate gyrus and other subregions with high neuron density at older ages (17 months)
	ArcAβ (Knobloch et al.,	APP KM670/671NL (Swedish),	Cognitive impairment at 6 months of age	Aβ plaques (6 months) affecting both the brain parenchyma and vasculature.

	2007)	APP E693G (Arctic)	measured by the Morris water maze and Y-maze	Plaques are abundant by 9 to 15 months. Develop early deficits in synaptic plasticity, LTP was impaired in slices from 3.5 and 7.5-month-old mice.
	P301L (Lewis et al., 2000)	MAPT P301L	Develop motor impairment, with 90 percent of animals exhibiting motor and behavioral problems by ten months.	Neurofibrillary tangles in an age and gene-dose dependent manner; as early as 4.5 months in homozygotes and 6.5 months in heterozygotes. Neuronal loss, especially in the spinal cord. Astrogliosis by 10 months.
	APP/PS1/Tau (Oddo et al., 2003)	hAPP 695, K670N/M671L (Swedish) PS1:M146L Tau: P301L	Progressive age-related memory impairment (4 months) correlated with intraneuronal Aβ	3–4 months: intracellular Aβ accumulation in the neocortex; 6 months: intracellular Aβ accumulation in the CA1 region of the hippocampus; 12 months: extracellular Aβ deposition in cortex and hippocampus; 12 months: NFTs appearance in the hippocampus
	TASTPM (Howlett et al., 2004)	APP KM670/671NL (Swedish), PSEN1 M146V	Age-dependent impairment in object recognition memory (6 months).	Aβ plaques (3–6 months), astrogliosis and microgliosis; localized neuronal cell loss
	5XFAD (Oakley et al., 2006)	APP KM670/671NL (Swedish), APP I716V (Florida), APP V717I (London), PSEN1 M146L (A>C), PSEN1 L286V	Impaired spatial memory (4-5 months) Impaired stress-related memory (6 months). Impaired remote memory stabilization (4 months).	Gliosis (2 months) in parallel with plaque deposition. Synapse degeneration (4 months) as well as neuronal loss.
	APP^{NL-G-F} (Saito et al., 2014)	APP KM670/671NL (Swedish), APP I716F (Iberian), APP E693G (Arctic)	Memory impairment in homozygous mice (6 months).	Aggressive amyloidosis (2 months) with near saturation by 7 months. Aβ deposition at 4 months in heterozygous mice. Microgliosis and astrogliosis (2months). Reduction of synaptophysin associated with Aβ plaques. Absent neural loss.

Rats	TgAPPswe (Ruiz-Opazo et al., 2004)	APPswe (Swedish)	Attenuated memory decline;	Increased APP mRNA (56%) and Aβ-40 and Aβ-42 peptides No plaques
	UKUR25 (Echeverria et al., 2004)	hAPP751 (Swedish)	Mild impairment (16 months)	No plaques
	Tg6590 (Folkesson et al., 2007)	APPswe (Swedish)	Impairment in morris water maze (9 months)	Rare diffuse Aβ plaques; Increased tau phosphorylation
	PSAPP Tg478/Tg1116/Tg 11587 (Flood et al., 2009)	APP695 Swe APPswe/ind hPS1 Finn	Starting from 7 months	Mostly diffuse plaques Few compact plaques in hippocampus. No vascular Aβ deposits; Astrogliosis and microgliosis. No neuronal loss
	McGill-R-Thy1-APP (Leon et al., 2010)	hAPP751 (Swedish)	Progressive learning deficits.	Aβ plaques (6-9 months.) Dystrophic neurites and astrogliosis around plaques
	TgF344-AD (Cohen et al., 2013; Pentkowski et al., 2018)	hAPP695 (Swedish) PS1ΔE9	Increased anxiety-like behavior without significant deficits in the spatial memory	Progressive Aβ deposition. Tau hyperphosphorylation and neurofibrillary tangles. Gliosis, apoptotic loss of neurons in the cerebral cortex and hippocampus.

Technological progress has allowed the translation of MRI and PET imaging investigations to experimental models. However, as shown in table Table 2, results obtained are still insufficient and unclear, showing a high dependence on the transgenic line studied as a consequence of the complex spectrum of neuropathological features presented by these models.

Brain structural modifications of these transgenic models have been investigated through high resolution structural MRI showing that atrophy is difficult to identify. Structural alterations are not always present or are not extensive enough to affect the whole structures. Moreover, atrophy involves brain regions that aren’t affected in AD patients, predicting the locations of amyloid formations at later stages. Similarities between the

outcomes of humans and rodents DTI studies were described. The use of transgenic models gave also the opportunity to demonstrate that fibrillar amyloid deposits and associated gliosis in brains of aged transgenic mice are accompanied by a reduction in the apparent diffusion coefficient (Mueggler et al., 2004).

Metabolic alterations similar to those described in humans were observed with MRS in transgenic models, although these were mostly found in aged mice (Mlynárik et al., 2012). Recent studies have also shown how such metabolic alterations can be detected also through the chemical exchange saturation transfer (CEST) MRI (van Zijl and Yadav, 2011). This technique exploits the natural exchange of hydrogen's atoms between water and its surrounding molecules. By the application of a saturation pulse before the acquisition, the intensity of CEST images can be modulated depending on the metabolite concentration in the tissue. With this approach it was possible to create maps of the glutamate (Crescenzi et al., 2016; Haris et al., 2013a) or the myo-inositol content (Haris et al., 2013b) in the brain of transgenic mice and therefore to detect alterations in their concentration, allowing researchers to overcome the resolution limit typical of the MRS technique.

As shown in Table 2, [^{18}F]-FDG PET studies have shown a huge variability of the glucose brain metabolism between transgenic models at different ages. These variations might be related not only to the intrinsic complexity of the transgenic models but also to differences in microPET acquisition parameters and environmental factors (e.g. temperature, fasting time, stress level) during the experiments. These factors could reduce sensitivity and affect mouse metabolism adding variability between different studies (Kuntner et al., 2009; Deleye et al., 2016). Different PET radioligands were also recently developed to detect activated microglia showing a correlation with Aβ formation or

showing that its deposition is preceded by astrogliosis (Matthias Brendel et al., 2016; Donat et al., 2018).

CBF and resting state fMRI studies with transgenic models confirmed results obtained in humans. Although in few cases no difference between transgenic models and wild type mice was detected. Hypoperfusion and deficits in functional connectivity of the hippocampus and/or cortex were described but an important considerations should be done: a great care must be taken in the choice of the anesthesia because it plays an important role in the modulation of brain networks. Moreover, many studies in patients are carried out with task-based fMRI which is not feasible in rodent making impossible the investigation of specific brain circuits.

Different class of MRI contrast agents were synthesized to bind Aβ plaques. Some of these have never been tested in patients but only in transgenic models. Aβ was labeled with chelated forms of gadolinium (GdDTPA) or iron-oxide nanoparticles trying to create respectively hyper or hypo-intense spots in correspondence of the plaques (Dudeffant et al., 2017; Poduslo et al., 2002; Sigurdsson et al., 2008; Wadghiri et al., 2003). Similarly, MRI contrast agents were also developed labeling with 19F existing molecules used for ex-vivo amyloid staining. By MRI sequences sensitive to T2* changes, it was also possible to visualize the plaque load without the need of esogenous agents but using the contrast arising from the iron content within the plaques. [^{11}C]-PIB has been widely used both in humans and experimental models showing that its binding to Aβ deposits is highly dependent on the transgenic model adopted and to the structure of the Aβ plaques. Different tau radioligands were also developed with the help of transgenic models and recently translated to patients (Shah and Catafau, 2014).

Table 2: MRI and PET methods applied to transgenic models.

	Method	*Tg Line*	*Outcomes (References)*
MRI	Structural MRI	PDAPP	Severe atrophy of the medial and temporal lobe with a focus in the hippocampus (8-12-24 months) (Gonzalez-Lima et al., 2001; Weiss et al., 2002; Redwine et al., 2003; Valla et al., 2006)
		APP/PS1	Atrophy identified in the midbrain area and not, as expected, at isocortical/hippocampal levels. The severity of brain atrophy in aged mice was not correlated with the extent of cerebral amyloidosis (Delatour et al., 2006; Lau et al., 2008)
		TASTPM APP/PS2/Tau	Hippocampal atrophy was found in TG mice. In APP/PS2/Tau the effect was age-dependent, whereas in TASTPM it was detectable from the first investigated time point. Both mice displayed an age-related entorhinal cortex thinning and robust striatal atrophy. (Micotti et al., 2015)
		J20	Increased regional cortical thickness in young TG mice relative to age-matched WT mice. However, the transgenic mice shown a greater rate of cortical thinning over 15 months. (Grand'maison et al., 2013; Hébert et al., 2013)
		PS2APP	Do not present volumetric difference in whole brain and ventricles (von Kienlin et al., 2005)
	DTI	APP23	Aβ deposits and associated gliosis of TG mice are accompanied by a reduction in the apparent diffusion coefficient at 24 months. (Mueggler et al., 2004)
		PDAPP	No differences in young mice. Significantly decreased FA and increased MD in PDAPP mice compared to WT mice at 15 months. (Song et al., 2004)
		APP/PS1	Changes in water diffusion parallel and perpendicular to axonal tracts in corpus callosum, fimbria of the hippocampus. A significant increase in diffusivity was found in specific hippocampal subregions correlate with neural loss. (Shu et al., 2013, p. 1; Zerbi et al., 2013)
		Tg2576	Reduction in MD and AD were observed in gray and white matter starting from 12 months age in transgenic mice. (Sun et al., 2005)
	MRS	Tg2576 5xFAD TASTPM	Altered metabolites content were detected mostly in aged mice, in frontal cortex, hippocampus and striatum (Mlynárik et al., 2012; Nilsen et al., 2012; Forster et al., 2013;

		APP/PS1 McGill-R-Thy1-APP	Micotti et al., 2015): - Decreased levels of N-acetyl-aspartate, glutamate and GABA - Increased levels of Myo-inositol
	CEST	APP/PS1 PS19	Metabolite high resolution imaging highlighted differences between WT and TG mice: - Decreased of glutamate levels. (Haris et al., 2013a; Crescenzi et al., 2014, 2016) - Increased Myo-inositol (Haris et al., 2013b)
	rsfMRI	APP/PS1 ArcAβ PS/APP McGill-R-Thy1-APP	Reduced functional connectivity both in mice and rats models. (Shah et al., 2013; Grandjean et al., 2016; Parent et al., 2017; Wiesmann et al., 2017)
		E22ΔAβ	No differences. (Grandjean et al., 2016)
		Tg2576	Increased connectivity in hippocampal and cortical networks prior to amyloid plaque formation. Decreased connectivity in those areas after plaque formation.(Shah et al., 2016)
		APP^{NL}	Decreased connectivity between the prefrontal cortex and hippocampus, relative to APP^{NL-G-F} mice, at 3 months, but not at 7 or 11 months. (Latif-Hernandez et al., 2017)
		$APP^{NL-GL-F}$	Increased connectivity between the prefrontal cortex and hippocampus, relative to APP^{NL} mice, at 3 months, but not at 7 or 11 months. (Latif-Hernandez et al., 2017)
	rCBF	APP23 ArcAβ J20	Hypoperfusion in old mice (Hébert et al., 2013; Maier et al., 2014, 2015, p. 23; Wiesmann et al., 2015; Sierra-Marcos, 2017; Ni et al., 2018)
	Gd-enhanced plaque imaging	APP/PS1 APP23 APPSwDI 3xTg Tg2576	Paramagnetic labeling with a chelated form of gadolinium (GdDTPA) (Poduslo et al., 2002; Wadghiri et al., 2003; Sigurdsson et al., 2008; Dudeffant et al., 2017)
	Susceptibility-enhanced plaque imaging	APP/PS1 Tg2576 APP[V717I] APP23; APP23xPS45	- Iron-oxide nanoparticles were used for magnetic labeling of Aβ deposits.(Beckmann et al., 2011; Yang et al., 2011; Wadghiri et al., 2013) - T2* sensitive sequences without contrast agents using the contrast arising from the iron content within the plaques (Jack et al., 2004, 2005; G et al., n.d.; Braakman et al., 2006; Maier et al., 2015)

	Measure of T1 and T2 relaxation times	APP/PS1	Compared to WT mice, the T2 values in younger AD mice were significantly greater, while the T2 values in older AD mice were significantly less. (Li et al., 2016)
		TASTPM	T1 /T2 values were shorter overall in TG mice, indicating possible differences in water content. (Forster et al., 2013)
		PS/APP	The T2 was significantly reduced in the hippocampus, cingulate, and retrosplenial cortex, but not the corpus callosum, of TG mice. No differences in T1 values or proton density were detected (16-23 months).(Helpern et al., 2004)
		Tg2576	Decrease in T2 in the cortex, hippocampus at 16 and 18 months of age. (Braakman et al., 2006)
	Fluorine-19 amyloid detection	Tg2576 APP/PS1 APP23	Amyloid deposition detected in elderly mice with curcumin and styrylbenzoxazole derivated.(Higuchi et al., 2005; Okamura et al., 2004, 2004; Yanagisawa et al., 2014; Tooyama et al., 2016)
PET	Glucose metabolism [18F]-FDG	APP23	No differences detected at 13 months age (Heneka et al., 2006)
		APP/PS1	Hypermetabolism starting from 12 months (Poisnel et al., 2012, p. 1)
		Tg2576	Hypermetabolism at 7 months but it normalizes with age. (Luo et al., 2012)
		TASTPM	Hypometabolism starting from 9 months (Deleye et al., 2016; Waldron et al., 2017, p. 45, 2015c)
		APPPS1-21	Hypometabolism (12-13 months)(Waldron et al., 2015b; Takkinen et al., 2016)
		5xFAD	Hypometabolism (13 months) (Macdonald et al., 2014)
		McGill-R-Thy1-APP	Hypometabolism (16-19 months)(Parent et al., 2017)
	Amyloid plaques	APP23 Tg2576 APP/PS1 APPPS1-21	- [11C]PIB binding to Aβ deposits is highly dependent on the Tg model and the structure of its Aβ plaques. (Snellman et al., 2013). An inverse relationship between [11C]PIB and rCBF MR imaging was observed in APP23 mice. (Maier et al., 2015, 2014) - [18F]flutemetamol and [18F]florbetaben retention were also detected to be increased in aged mice. (Snellman et al., 2014, 2012; Waldron et al., 2015a)
	Tau pathology	P301S	[18F]THK5117 accumulation correlated with

		GSK-3b·Tau-P301L	immunhistochemical tau loads in aged mice (M. Brendel et al., 2016)
		PS19	In vivo optical and PET imaging demonstrated sensitive detection of tau inclusions by [11C]PBB3. (Maruyama et al., 2013)
		TauP301L	[18F]THK523 shown high affinity and selectivity for tau pathology both in vitro and in vivo. (Fodero-Tavoletti et al., 2011, p. 523)
	Microglial activation	5xFAD	The mitochondrial translocator protein TSPO tracer [11C]PBR28 provides an accurate visualization and quantification of changes in microglial density. (Donat et al., 2018)
		PS2/APP	Positive correlation between the TSPO tracer [18F]GE180 of microglial activation and amyloid load measured with [18F]florbetaben and likewise with metabolism measured with [18F]-FDG. (Matthias Brendel et al., 2016)
	Astroglial activation	APPswe	Cortical and hippocampal [11C]DED PET binding was significantly higher at 6 months than at 8-15 months or 18-24 months preceding amyloid plaque deposition. (Olsen et al., 2018; Rodriguez-Vieitez et al., 2015)

Despite this complex scenario, studying transgenic models has still a great value. Such models allow the isolation of the contribution of a single pathological change to the disease progression. Their translational power is boosted by the opportunity for the application of imaging techniques used to diagnose AD in humans, owing to similarities in acquisition parameters and outcomes. The use of such imaging techniques permits longitudinal and non-invasive investigations reducing the number of animals needed in research studies. Potential imaging biomarkers identified in animal models can suggest targets for the intervention in humans. Equally, findings in human studies can suggest targets for multi-modal studies in transgenic models. These data can be integrated with invasive techniques not feasible in humans, such as high resolution multi-photon microscopy or electrophysiology, creating a virtual link between micro and macro-structures and providing new insight into the observed alterations.

1.2 – Magnetic Resonance Imaging

Within this section I will give a brief overview of the MRI technique. Rather than describing in detail the spatial encoding process behind the formation of an MRI image, the attention will be focused on the introduction of the MRI signal. By explaining how each MRI technique manipulates the signal it will be possible to describe the principal acquisition parameters that will be found in the chapters describing methods and results. For a complete quantum mechanical description please refer to chapters 3-6 of the book entitled "Magnetic Resonance Imaging – Physical principles and Sequence Design" (Brown et al., 2014).

1.2.1 – MRI signal

MRI imaging takes advantage of the atom's magnetic properties. The nucleus of an atom is formed by protons and neutrons and it is characterized by the so called total angular momentum otherwise known as nuclear spin. Atoms with even atomic number are unaffected by external magnetic fields, on the contrary nuclei with half-integer spin (such as ^{1}H, ^{17}O, ^{19}F, ^{23}Na or ^{31}P) have a characteristic magnetic behavior. Due to its natural abundance in biological tissues, the hydrogen atom can be detected by magnetic resonance techniques. It is formed by a single proton and a single electron orbiting the nucleus. Hydrogen nuclei behavior in a magnetic field is very similar to the needle of a compass in presence of the external earth's magnetic field. Similarly, hydrogen nuclei are oriented in a random manner and the sum of all their magnetic moments has a zero value, but when immersed in the static magnetic field of the MRI scanner they point along it's principal direction. Experiencing both the effect of the MRI and the earth magnetic fields, all protons starts precessing (Figure 10c) around the direction of the main MRI magnetic

field, yielding to a non zero net magnetization. The angular frequency of the precession, called Larmor frequency ω_0, depends on the strength of the applied magnetic field B_0, according to the equation:

$$\omega_0 = \gamma B_0 \quad [1]$$

where γ is a constant called the gyromagnetic ratio, whose value is characteristic for the nucleus of interest.

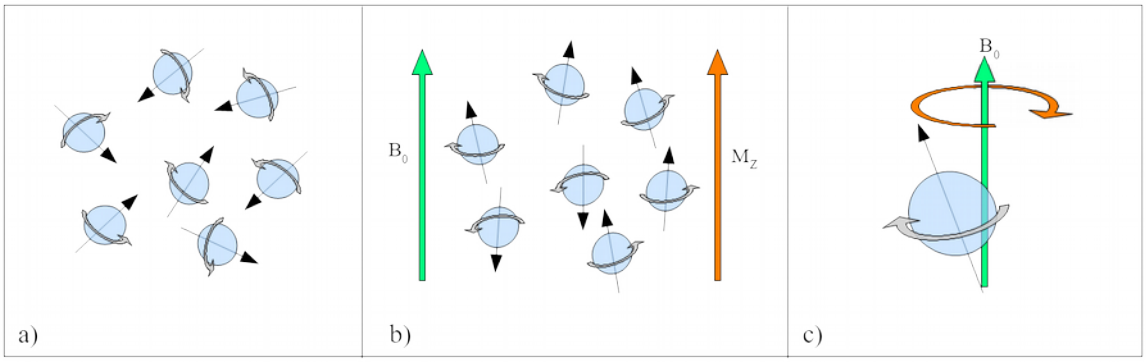

Figure 10: Spin orientation in absence (a) and in presence (b) of an external magnetic field. M_z is the net magnetization representing the contribution of all spins. c) Precessional motion of a spin.

As shown in Figure 11, some energy can be introduced when an external electromagnetic wave (B_1) with an orientation of 90° respect to the direction of the main magnetic field and characterized by a frequency equal to the Larmor frequency is applied.

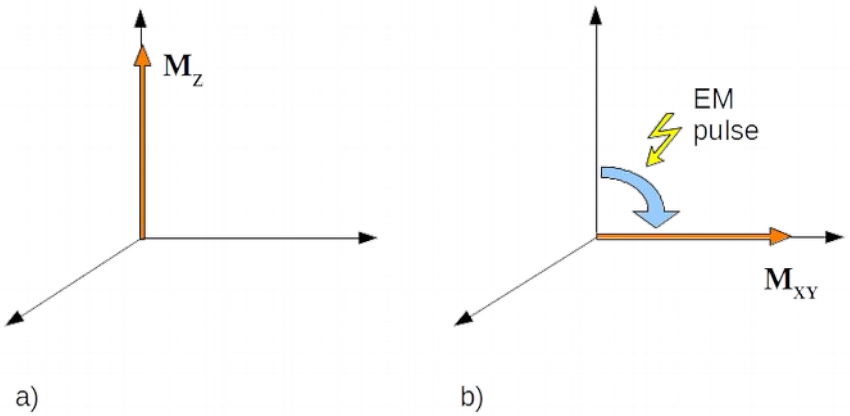

Figure 11: Net magnetization a) under normal conditions and b) after the effect of the external electromagnetic wave.

All the longitudinal magnetized spins are reversed in the transverse xy-plane, resulting in a net magnetization that is now denoted as M_{xy} rather than M_z. This magnetization rapidly fades out due to two independent processes. Once that the magnetization has been reversed, the spins start preceeding with different phases due to the spin-spin interaction (Figure 12) causing the so called T2 relaxation of the signal. The T2* decay is also described in medical imaging and it's due to additional field inhomogeneities contributing to the dephasing process. T2 decay is more or less independent of the strength of the external magnetic field (B_0) and it is in the range of 40-300ms.

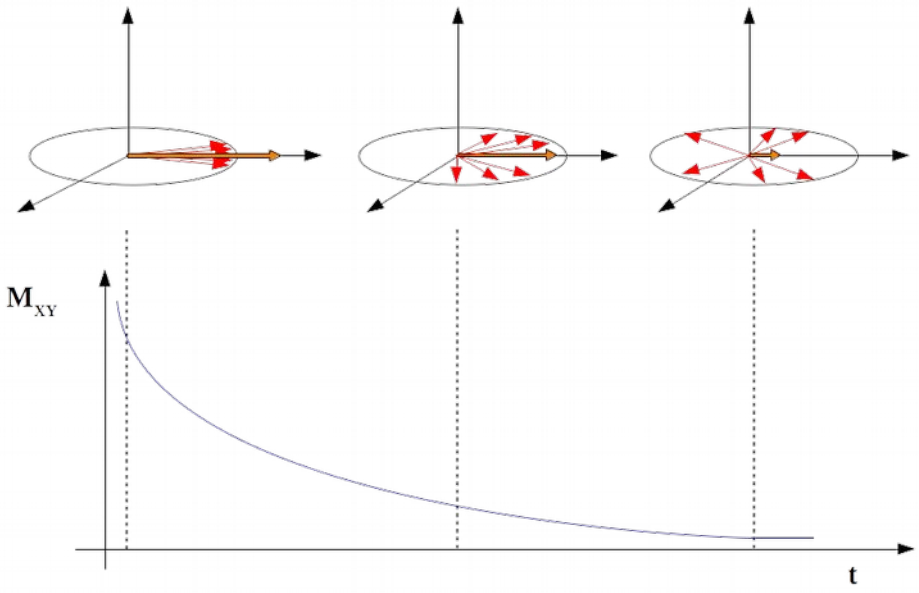

Figure 12: Relaxation process. Spins reversed in the transverse plane start preceding around the main direction of the magnetic field causing. The sum of these spins (M_{XY}) decrease with a time called T2 relaxation time.

While the transverse magnetization (M_{XY}) decays the magnetic moments gradually realign with the z-axis of the main magnetic field (B_0) following the so called spin-lattice interaction process that reflects the interaction of nuclei with their molecular surroundings, and how quickly the energy can be transferred from the nuclei to the environment. This process is regulated by the T1 relaxation recovery time which is in the range of 0.5-3sec (Figure 13).

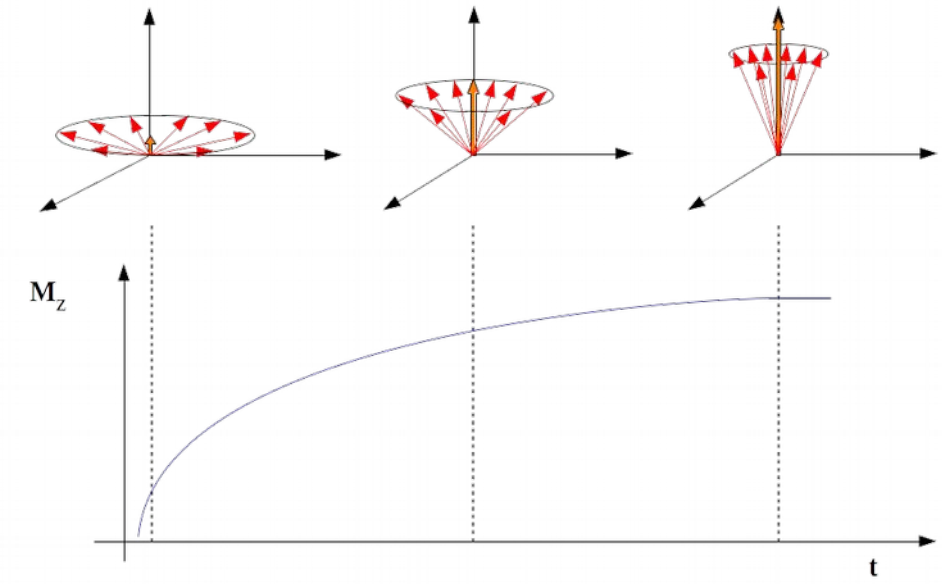

Figure 13: Relaxation recovery process. Relaxation process. Once the effect of external 90° RF pulse end, spins reversed in the transverse plane start recovering their original magnetization (M_Z) with a recovery time called T1.

Since the oscillating spins are charged particles moving in a magnetic field, currents can be induced in conductor coils making the detection feasible. The detected signal is known as free induction decay (FID) and it is proportional to the number of excited nuclei in the tissue and it lasts as long as there is a transverse component (M_{XY}) of the net magnetization vector.

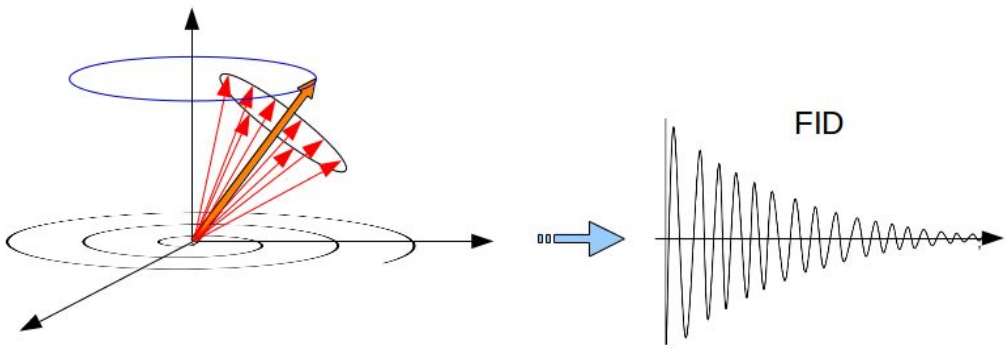

Figure 14: Left: Temporal evolution of the net Magnetization. Right: Free Induction Decay obtained by reading the transverse magnetization.

While the T1 is few order of magnitude longer than the T2 relaxation time, the transverse magnetization can be recovered by applying a further 180° electromagnetic pulse (Figure

15). The spins' rotation is reverted obtaining their refocusing in the transverse plane and the recovering of the transverse magnetization.

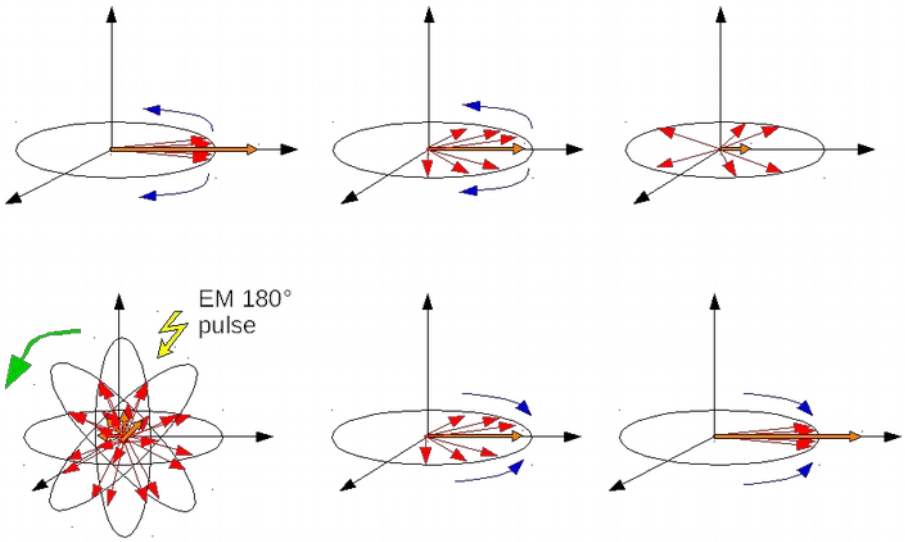

Figure 15: Spin refocusing with a 180° EM pulse.

A second class of detectable signal called "*echo*" is then produced (Error: Reference source not found).

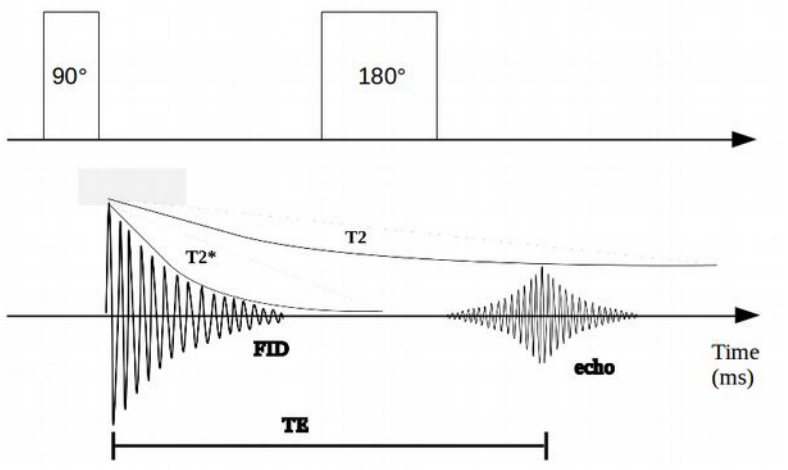

Figure 16: Spin-echo sequence.

A series of echoes caused by a train of consecutive 180° RF pulses can be obtained and detected. The amplitudes of the echoes diminishes with the T2 (Figure 17).

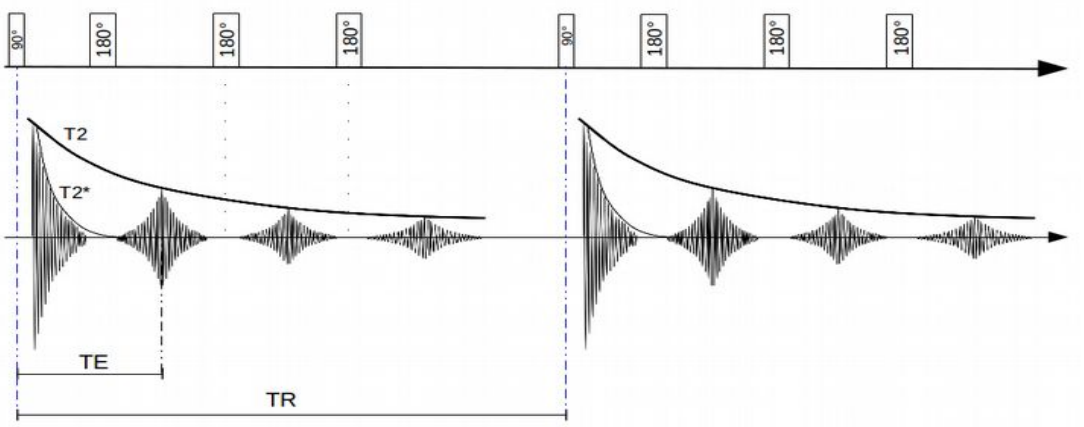

Figure 17: Generation of a series of echoes using a train of consecutive 180° pulses, following. TR is the time between 90° pulses.

1.2.2 – T1 and T2 mapping

When an MRI image is generated, the acquisition parameters TR and TE can be chosen in order to emphasize it's contrast properties. The signal, S, in a spin-echo sequence could be described by:

$$S \propto \rho \cdot \left[1 - \exp\left(-\frac{TR}{T1}\right)\right] \cdot \exp\left(-\frac{TE}{T2}\right) \quad [2]$$

Where ρ is the spin density, and represents the number of protons per unit volume. Indicating that altering the TR and TE acquisition parameters an effect on the image contrast will be dependent by the T1 or T2 of the tissues (Figure 18). Increasing the TR period the T1 information of the image increases resulting in a modulation of the gray/white matter contrast but CSF remains dark. On the other hand, by shortening the TE the CSF is characterized by a small signal. For intermediate TE the overall contrast is poor but at long TE a large signal, resulting in a bright area, for the CSF can be obtained.

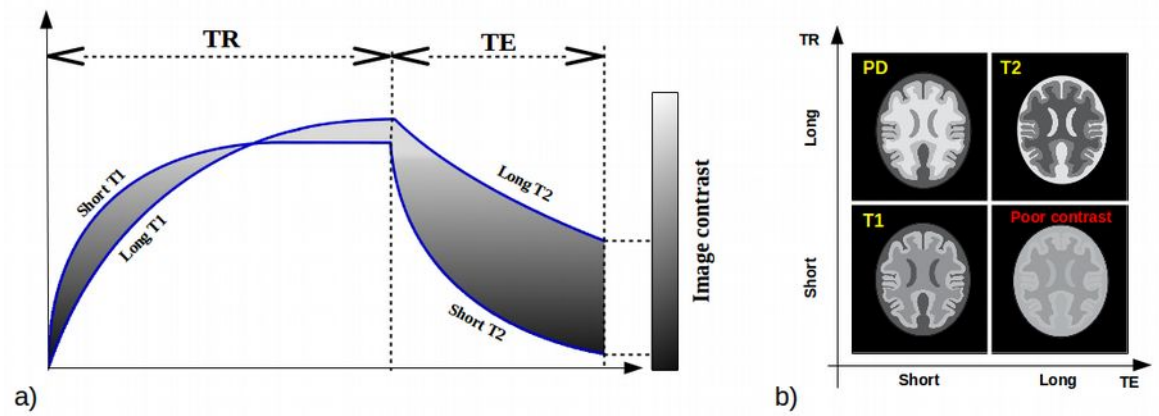

Figure 18: Simulation that shows how tissues intensities can be modulated varying TR and TE (panel b adapted from (Dowsett, 2006)).

The so called T1-weighted or T2-weighted images can be used to evaluate the volume alterations of different brain regions that are typical of the AD pathology. Moreover, the T1 and T2 tissues times can be measured by acquiring a series of images with respectively fixed TR and varying TE or varying TR and fixed TE. The equations describing the signal evolution can be derived from the equation 2:

$$S \propto [\exp(-\frac{TE}{T2})] \quad [3]$$

$$S \propto [1-\exp(-\frac{TR}{T1})] \quad [4]$$

Pathological alteration of the tissue composition can alter T1 and T2 measurements. An accumulation of lipids or iron leads to a reduction of the measured T1 when compared to healthy tissue. An increase of the water (e.g. edema) has the consequence of altering both relaxation times but is more pronounced in T2 sensitive measurements (Puntmann et al., 2016). Similarly the formation of NFT and amyloid plaques, resulting in cell loss are expected to alter relaxation times by altering the biochemical environment of the tissue. The in-vivo evaluation of the T2 time have shown differences between transgenic and age-matched wild type mice (see table Table 2).

1.2.3 – Magnetic Resonance Spectroscopy

The magnetic resonance spectroscopy technique is able to investigate the concentration of different chemical species in a selected volume. To explain its operating principle, the concept explained with equation 1 must be further elaborated. When an atom is placed in a magnetic field its orbiting electrons causes a small magnetic field which opposes the externally applied field. The effective magnetic field at the nucleus is generally less than the applied field by a fraction σ and described by:

$$B = B_0(1-\sigma) \quad [5]$$

The electron density around each nucleus in a molecule varies according to the types of nuclei and bonds in the molecule leading to different emission frequency associated with it. This is called the 'chemical shift' phenomenon that provides a mechanism for separating the signal contribution of chemically different nuclei. However, because of the high water concentration in biological tissues, the MR signal is dominated by its protons making the contribution of other chemical species negligible. To overcome this issue a saturation pulse is added to the sequence in order to suppress the water contribution of water to the signal (Griffey and P. Flamig, 1990). The Point RESolved Spectroscopy (PRESS) sequence is the most commonly used spectroscopy method. It consists of three slice-selective RF-pulses (90º−180º−180º) applied with three orthogonal gradients (x, y and z). The signal at time TE is derived only from protons located in a voxel where the three imaging planes overlap (Figure 19).

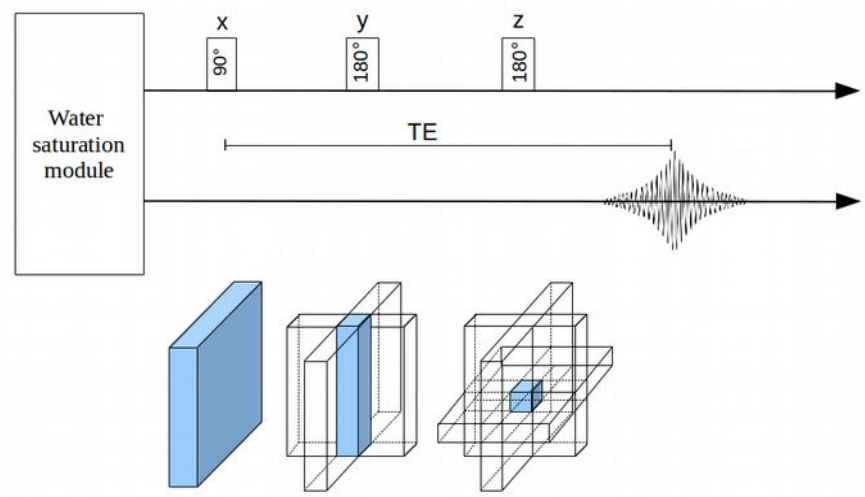

Figure 19: PRESS MRS sequence.

The acquired signal is called ‘spectrum’ and it can be considered as the summation of each metabolite contribution (Figure 20). The principal metabolites detectable in the brain are:

- *N-acetyl-Aspartate* (NAA). The largest peak in the spectrum, located around 2 p.p.m. It is an amino-acid derivative synthesized in neurons and transported along axons. It is therefore considered an index of neural and axonal integrity. NAA plays a diagnostic role in brain tumors, head injury and dementias.
- *Creatine* (Cr) is a peak, located at 3.03 p.p.m. It is composed by the contribution of both creatine and phospocreatine that are involved in the energy metabolism.
- *Choline* (Cho) is located at 3.22 p.p.m. It represents the sum of choline and phosphocholine contributions. Since these are involoved into phospolipids syntesis and degradation process, Cho is considered as a marker of cellular membrane turnover.
- *Myo-inositol* (mI) is assigned at 3.56 p.p.m. Increased mI contents has been associated with astroglial activation. It’s increase has been observed in AD patients.

- *Glutamate* (Glu) and *Glutamine* (Glm). Since these are difficult to be differentiated are often considered as a unique peak called Glx and located at 2.05 p.p.m. Glutamate is a excitatory neurotrasmitter involved in the redox cycle.

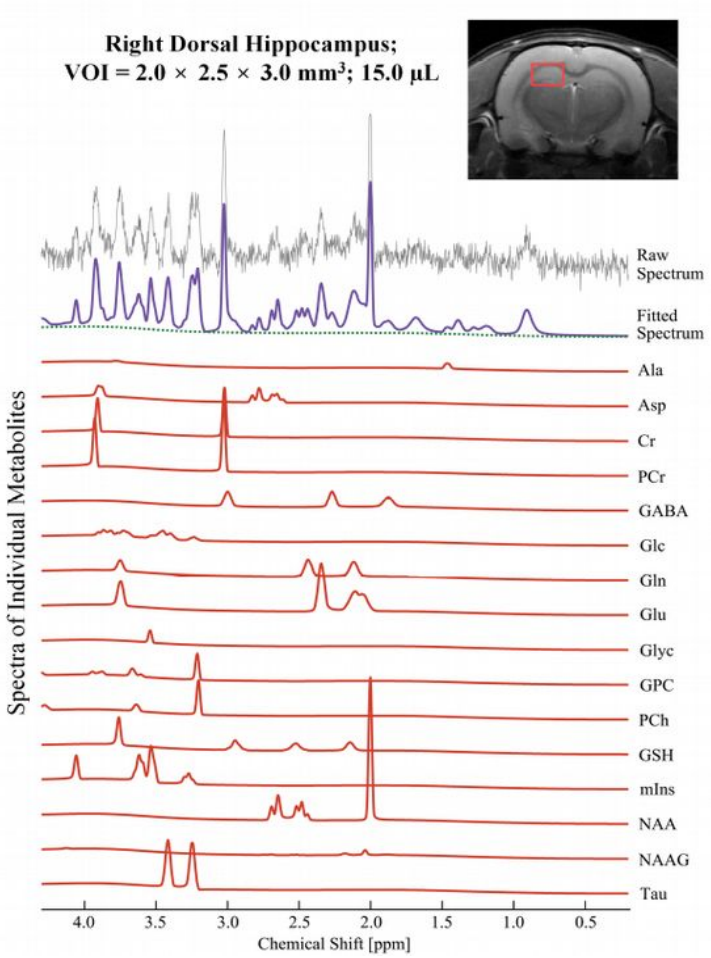

Figure 20: Quantification of 16 neuro-metabolite signals from in vivo 1H-MRS in the right dorsal hippocampal region of a rat. Adapted from (Lee et al., 2016)

1.2.4 – Chemical Exchange Saturation Transfer

MR spectroscopy is a technique that suffers with certain limitations. Physiological and non-physiological motion may causes an increased of the acquired line widths, shifts of the overall frequency, reduced peak areas, and decreased quality of water suppression. Al of these may lead to signal degradation resulting noisy spectra that may be not acquired in small portion of the brain. To overcome these limitation the chemical exchange saturation transfer (CEST) technique may be helpful allowing the indirect detection of different chemical species. CEST technique takes advantage of the natural exchange of protons between water and its surrounding molecules. Since the MRI image is obtained by acquiring the water's protons signal, its intensity can be modulated with the application of a selective saturation pulse just before its acquisition.

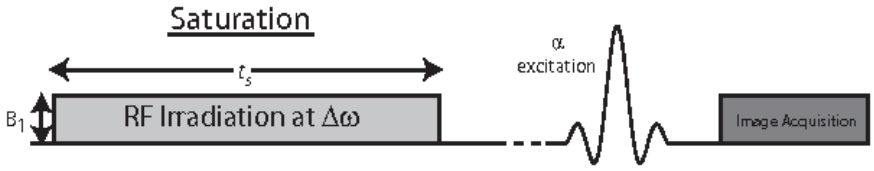

Figure 21: Pulse sequence diagram. (Dula et al., n.d.)

The solute protons belonging to CEST agents have frequency of resonance different than the water. Consequently, if the RF pulse is able to selectively saturate these protons, when they exchange with water they won't contribute anymore to the overall signal resulting in decreased intensity of the image. The so-called Z-spectrum is generated by measuring the normalized water saturation (S_{sat}/S_0) as a function of irradiation frequency. The minimum intensity of the Z-spectrum, represented as 0 p.p.m, is obtained by saturating at the water's frequency of resonance. With the analysis of the Z-spectrum asymmetry, called Magnetization Transfer Ratio (MTR = 1 – S_{sat}/S_0), information about the CEST agents content can be obtained. However, the magnitude of the MTR asymmetry depends on

different factors affected by the physiological conditions (concentration, temperature, pH, spectral position of the protons and relaxation times of protons involved) but also by experimental parameters (intensity and duration and homogeneity of the RF pulse but also the homogeneity of the static magnetic field B_0).

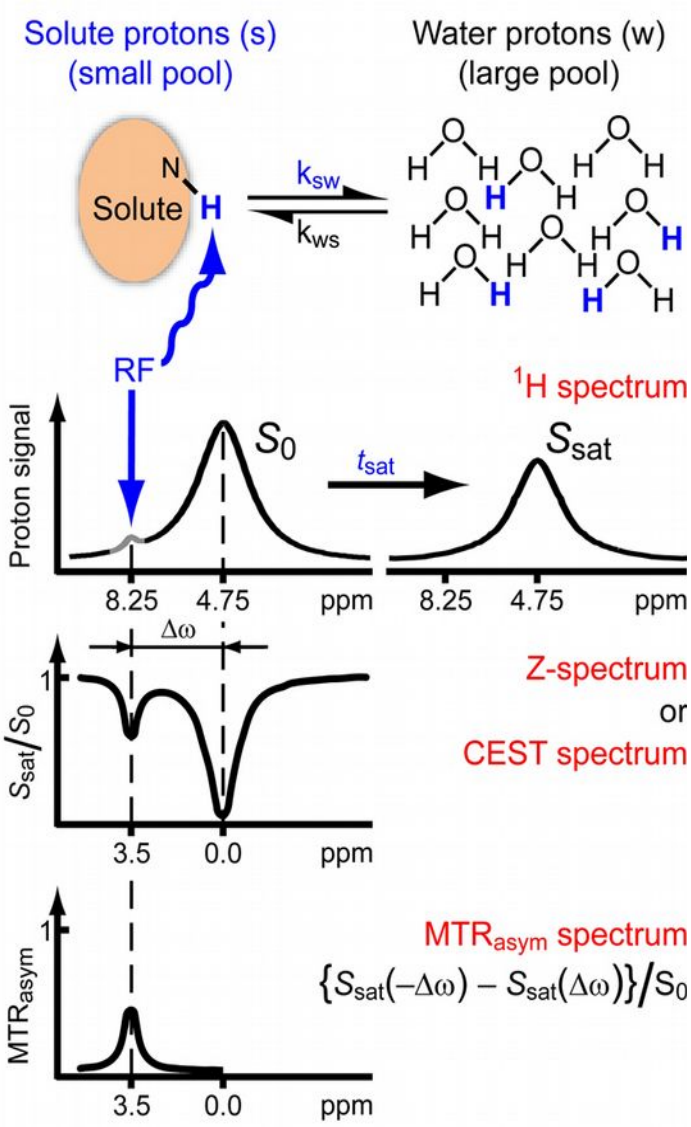

Figure 22: Chemical Exchange Saturation Transfer (CEST): principles and measurement approach.(van Zijl and Yadav, 2011)

As long as the RF pulse is active the effect can become visible thanks to the continuous transfer of the saturation. To successfully generate a CEST contrast the frequency of resonance gap between the CEST agent and the water (expressed in rads/sec) must be

bigger than their exchange rate (Soesbe et al., 2013; Ward et al., 2000). Therefore with high magnetic field strengths an increased frequency of separation allows the imaging of CEST agents with faster exchange rate. The effect of the magnetic field is amplified also by the slower recovery of the magnetization that produce longer T1 relaxation times resulting in larger CEST contrast.

Table 3: MR properties for CEST imaging of the mouse cortex at different B0 field strengths.(G. Liu et al., 2013)

B_0 (Tesla)	Frequency separation (Hz) per 1 ppm	T_1 (ms)	T_2 (ms)
2.35	100	1010	68.5
4	170	1286	65.2
4.7	200	1315	54.6
9.4	400	1948	42.1
11.7	500	2073	36.2
17.6	750	2030	30

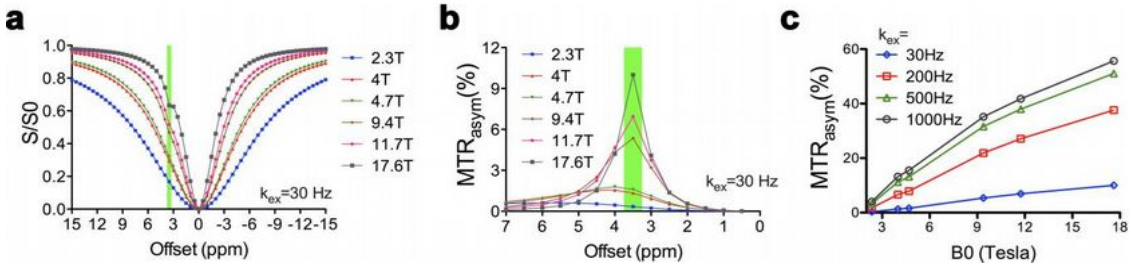

Figure 23: Numerical simulation of B_0 field dispersion influences on CEST contrast in the mouse cortex using the Bloch equations: a) z spectra, b) MTRasym plots, and c) peak CEST values plotted against the B_0 field with the proton exchange rate ranging from 30 Hz to 1000 Hz. (G. Liu et al., 2013)

Different class of CEST agents have been investigated and separated in two main categories. The paramagnetic CEST (paraCEST) agents are molecules containing metallic ions which can be visualized far away from water resonance if compared to the second class called diamagnetic CEST (diaCEST) agents that usually have Z-spectrum comprised within 6p.p.m from water. ParaCEST are usually exogenous molecules that need to be injected and their use could be associated with toxicity due to their metal content. As

shown in table Table 4, diaCEST agents could be endogenous molecules containing three class of exchangeable groups.

Table 4: CEST Exchange properties for endogenous molecules (Kogan et al., 2013)

	Amide protons (-NH)	**Amine protons ($-NH_2$)**	**Hydroxyl protons (-OH)**
Chemical Shift	3.5 p.p.m.	1.8-3.0 p.p.m.	0.5 – 1.5 p.p.m.
Exchange Rate (k_{sw}) Range	10-100 s^{-1}	> 500 s^{-1}	500-1500 s^{-1}
Endogenous Metabolite	Multiple Unknown	Glutamate (Glu), Creatine (Cr)	Glycosaminoglycans (GAG), Glycogen, Myo-Inositol (MI), Glucose
$CEST_{asym}$	1-4 %	7-10%	2-8%
Sensitivity to pH	Yes	Yes	Yes
CEST Applications	Cancer/Stroke	Skeletal Muscle and Myocardial Muscle Energetics, Cancer Metabolism (Cr), Neuropsychiatric Disorders (Glu)	Osteoarthritis (GAG), Neurological Disorders (MI), Cancer Metabolism (Glucose)

AmideCEST, often reported as amide proton transfer (APT), was firstly described in rodents showing that it can be used to produce a pH weighted images in stroke (Zhou et al., 2003b) and tumor models (Zhou et al., 2003a). Thanks to the amides slow exchange rate, APT is not limited by the strength of the magnetic field and it has been consequently translated to the clinical context (Zhou, 2011).

AmineCEST has been used to create spatial maps of the glutamate and creatine content in the brain and thus referred respectively as GluCEST (Cai et al., 2012) or CrCEST (Kogan et al., 2014a, 2014b; Cai et al., 2017). GluCEST measurements shown significantly decreased levels of glutamate in mouse models of middle cerebral artery

occlusion (MCAO) (Cai et al., 2012) and stroke (Zaiss et al., n.d.) but also to neurodegenerative disorders mouse models of AD (Bagga et al., 2016; Crescenzi et al., 2016, 2014; Haris et al., 2013a) and Huntington disease (Pépin et al., 2016) GluCEST spatial distribution was verified using PET maps of the glutamate receptor subtype 5 (Ametamey et al., 2007) and its reproducibility demonstrated in humans (Nanga et al., n.d.). When applied to individuals with a psychosis spectrum it was also able to show abnormal levels of glutamate when compared with healthy subjects (Roalf et al., 2017)

The chemical exchange of **hydroxyl** groups is characterized by a high exchange rate corresponding to a region of interest in the Z-spectrum which is the closer one to the water frequency of resonance among all the diaCEST agents. This makes the CEST imaging of hydroxyl protons feasible only with high fields MRI scanner (> 7T). Different metabolites have been mapped with this technique such as glycosaminoglycan (GAG) or myo-inositol or glucose and in the same fashion of other CEST agents it may be respectively called as GagCEST, MICEST or GlucoCEST. Since a non-uniform distribution of mI was shown in early stages of AD and related to dysfunctional glial cells (von Bernhardi, 2007), MICEST was presented as a potential biomarker showing showing that elevated levels of mI can be measured in AD transgenic models (Haris et al., 2013b). Due to its limited concentration, a direct mapping of endogenous glucose is difficult. However, as shown in Figure 24, the injection of D-glucose has been proposed as MRI contrast agent alternative to [^{18}F]FDG-PET in the identification of tumor regions that are characterized by an altered metabolic consumption (Rivlin et al., 2014, 2013; Walker-Samuel et al., 2013). Results in cancer research with animal models and [^{18}F]FDG-PET have been duplicated with different molecules homologue to D-glucose as the 2-deoxy-D-glucose (2DG) (Rivlin et al., 2013), 3-O-methy-D-glucose (3OMG) (Rivlin et al., 2014) and 2-amino-2-deoxy-D-glucose (GlcN) (Rivlin and Navon, 2016). The feasibility of this

approach has been recently shown also in human studies (Paech et al., 2017; Schuenke et al., 2017). Similar studies have demonstrated that the uptake of D-glucose can be detected in the brain of healthy rats (Nasrallah et al., 2013). However, due to its fast metabolism in the brain the D-glucose CEST signal rapidly fade out. 2DG was proposed as an alternative to D-glucose to detect brain metabolism since it enters cells by the same transporters but it does not go into glycolysis. 2DG is only phosphorylated by hexokinase into 2DG-6-phosphate (2DG6P) and trapped in cells for many hours because it's minimally metabolized (Jin et al., 2016).

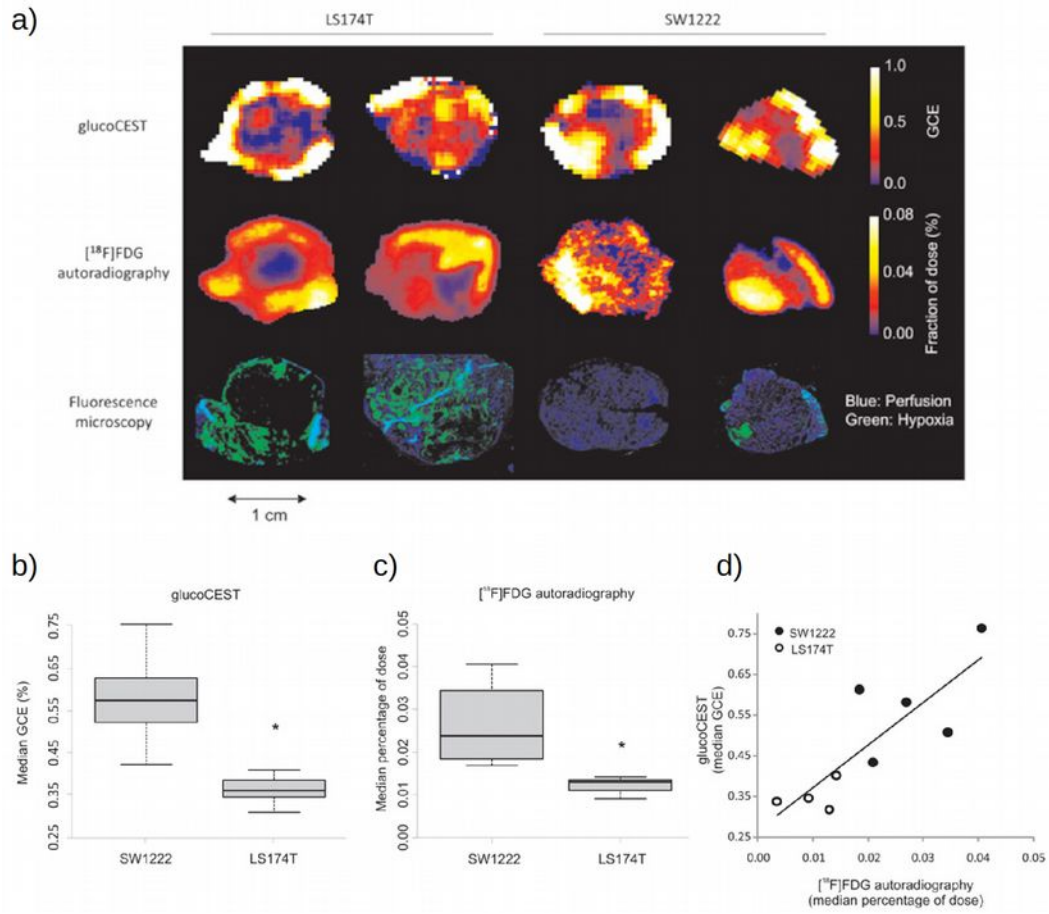

Figure 24: (a) Comparison of tumor glucose uptake measured with glucoCEST and [^{18}F]FDG autoradiography in two human colorectal tumor xenograft models (SW1222 and LS174T). The fluorescence microscopy images show perfused (blue) and hypoxic regions (green) corresponding to Hoechst 33342 and pimonidazole staining, respectively. (b) and (c) Show that the uptake of both glucose and FDG was significantly different between tumor types (*, $P < 0.01$, Mann-Whitney). (d) Scatter plot of median tumor [^{18}F]FDG and glucoCEST enhancement, which shows a significant correlation ($P < 0.01$, Spearman's rho). Adapted from (Walker-Samuel et al., 2013)

1.2.5 – Diffusion Tensor Imaging

As previously mentioned, the principle underlying DTI imaging is the water molecules diffusion. In 1905 Albert Einstein was the first to describe that the particles random movement in a liquid is governed by their thermal energy and thus it can be described with a diffusion coefficient (D) (Einstein, 1905).

As shown in Figure 25, water molecules motility can influence the process regulating the magnetization recovery and thus the MRI signal. This influence can be measured by slightly modifying the spin-echo pulse sequencing by adding a field gradient module (characterized by the diffusion weighting a factor) just before the 180° degree pulse. A magnetic field gradient can be described as variation of the magnetic field along one spatial direction. Once that the 90° pulse has been applied protons start dephasing around the main direction of the magnetic field. The amount of this dephasing is proportional to the diffusion distance covered by water molecules during the gradient pulse. The effect of this "dephasing" is a reduction of the MRI signal amplitudes. The equation 2 describing the MRI signal could be than extended as:

$$S = \rho \cdot \left[1 - \exp\left(-\frac{TR}{T1}\right)\right] \cdot \exp\left(-\frac{TE}{T2}\right) \cdot \exp\left(-b \cdot D\right) \quad [6]$$

Where b is the diffusion weighting factor and D is the diffusion coefficient. In regions with fast water diffusion (e.g. CSF), the signal is reduced more when compared to the signal reduction of areas with slow water diffusion (e.g. white matter). The so-called apparent diffusion coefficient (ADC) map is can be created by acquiring a series of images with fixed TR and TE and b variable.

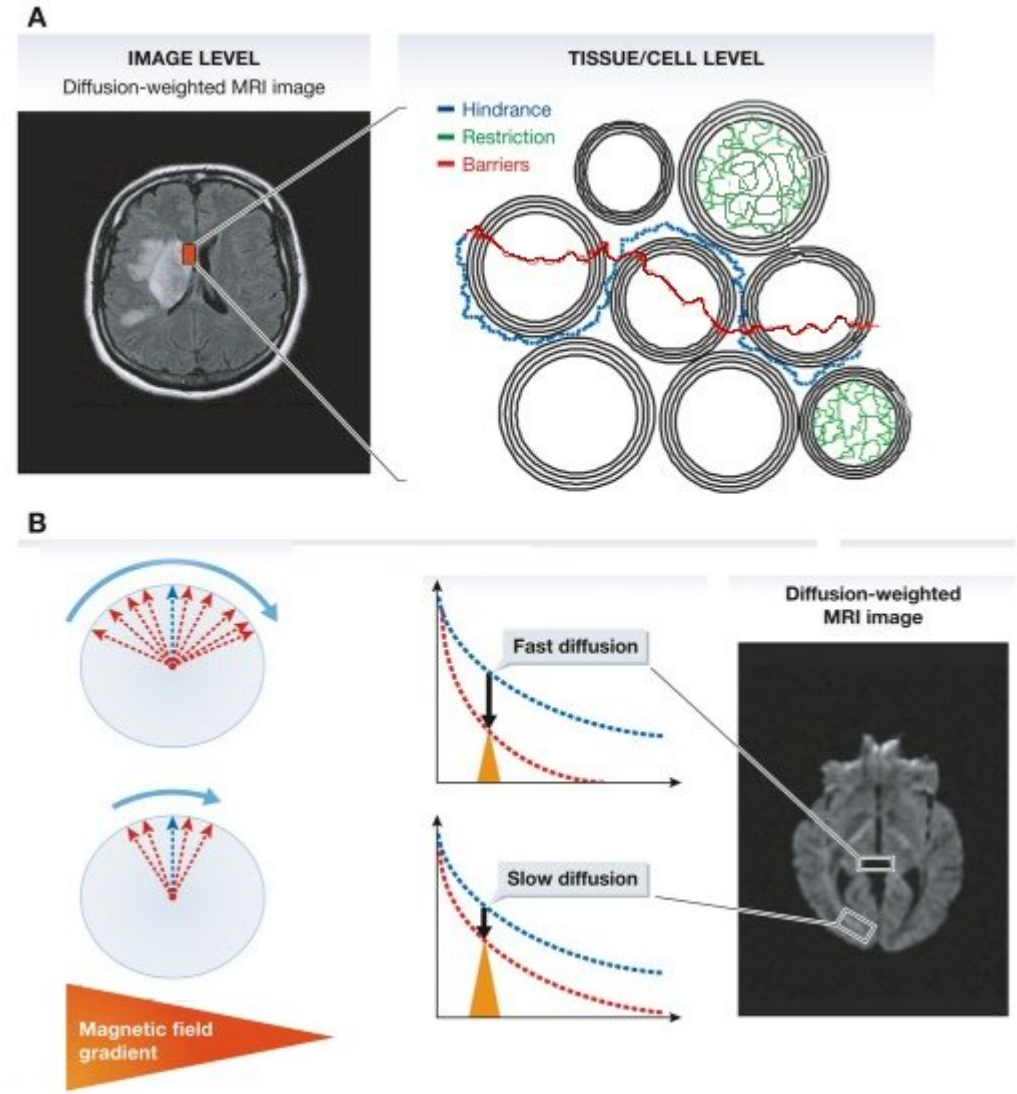

Figure 25: The origin of DTI contrast. (A) Contrast and signal levels in the diffusion-weighted image of a human brain (left) reflect water diffusion behavior (random walk) (right). Diffusion behavior is modulated by tissue structure at the cellular level: For instance, diffusion can be restricted within cells, water may escape when cell membranes are permeable and might then experience a tortuous pathway in the extracellular space (hindrance). (B) In the presence of a magnetic field gradient, magnetized water molecule hydrogen atoms are dephased. The amount of dephasing is directly related to the diffusion distance covered by water molecules during measurement. The overall effect of this dephasing is an interference, which reduces MRI signal amplitudes. In areas with fast water diffusion (e.g. within ventricules), the signal is deeply reduced, while in areas of slow water diffusion (e.g. white matter bundles), the signal is only slightly reduced. This differential effect results in a contrast in the diffusion-weighted MRI images, which is not visible in standard MRI images. Adapted from (Le Bihan, 2014)

The measured ADC value can vary because the diffusion may not be uniform in all orientations. To overcome this issue different images with fixed b but different gradient orientations can be acquired. In Figure 26a is illustrated an ideal phantom that consists of two parts. An upper part that contain ordered structures, shown as arrows, that represent a

bundle of axons or well-organized neurons with coherent tissue orientations. A lower part that contains random structures without coherent orientations. In the right panel of Figure 26a is shown what happen when ADC is measured along three different orientations, these measurements in the upper part of the phantom show orientation dependence (i.e. anisotropic diffusion). Thus the image intensity, representing ADC values measured in the orange box, change from high to low when the measuring orientation changes from horizontal to vertical. When ADC is measured in the lower part the image intensity does not change due to the random orientation of structures.

A mathematical model (Basser et al., 1994a, 1994b) can be applied to estimate the components of the effective diffusion tensor that can be visualized as an ellipsoid. The length of this ellipsoid, Figure 26b, is proportional to the eigenvalues of the diffusion tensor (λ_1, λ_2, λ_3). The size, shape, and orientation of each ellipsoid can be described by combinations of these components corresponding to the diffusion tensor.

Where:

- Mean Diffusivity: $MD = \frac{(\lambda_1 + \lambda_2 + \lambda_3)}{3}$ [7]
- Axial Diffusivity (often indicated as $\lambda_{\parallel}$): $AD = \lambda_1$ [8]
- Radial Diffusivity (often indicated as $\lambda_{\perp}$): $RD = \frac{(\lambda_1 + \lambda_2)}{2}$ [9]
- Fractional Anisotropy: $FA = \sqrt{\frac{(\lambda_1 - \lambda_2)^2 + (\lambda_1 - \lambda_3)^2 + (\lambda_2 - \lambda_3)^2}{2(\lambda_1^2 + \lambda_2^2 + \lambda_3^2)}}$ [10]
- Relative Anisotropy: $RA = \sqrt{\frac{(\lambda_1 - \lambda_2)^2 + (\lambda_1 - \lambda_3)^2 + (\lambda_2 - \lambda_3)^2}{(\lambda_1 + \lambda_2 + \lambda_3)^2}}$ [11]

In the anisotropy map, (Figure 26b), the upper part of the phantom has higher diffusion anisotropy than the lower part. Consequently, when the diffusion anisotropy is high, the long axes of the diffusion tensor often coincide with the underlying structural orientation and can be visualized using a direction-encoded color map (DEC) where regions with structural orientation running horizontally are red and those running vertically are green. Transition areas become yellow, a mixture of red and green.

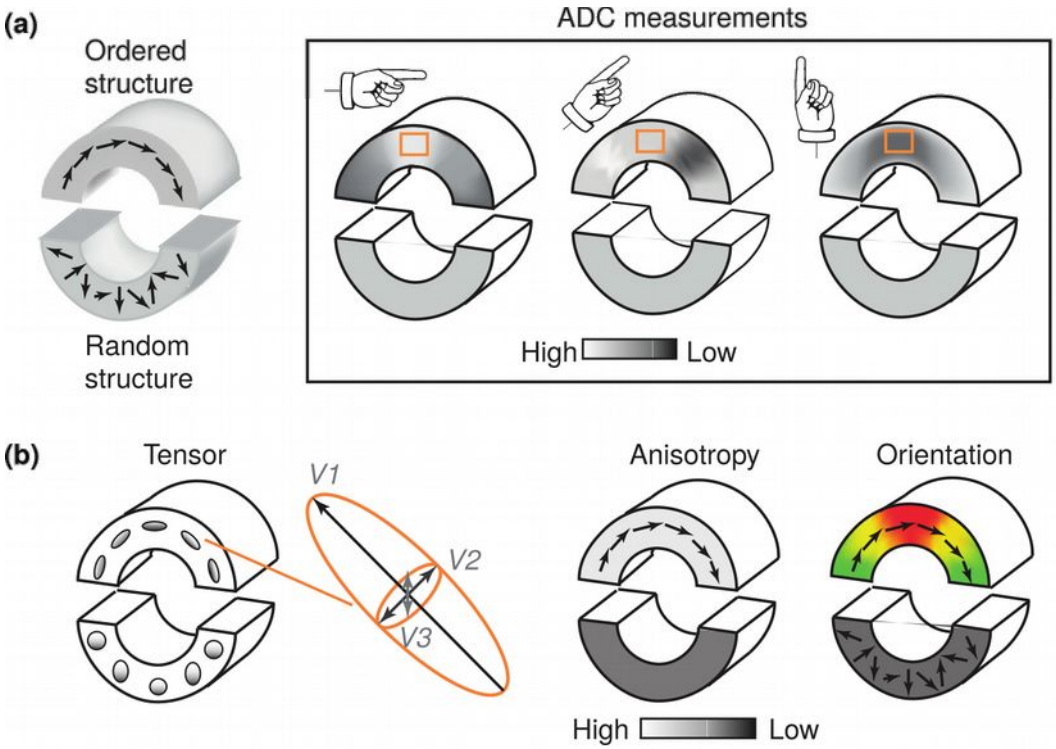

Figure 26: From diffusion anisotropy to diffusion tensor. (a) An ideal phantom composed by ordered (upper part) and random (lower part) structures. The image intensity is high when the structures have the same orientation as the diffusion gradient applied (represented by the hand). (b) Diffusion tensors visualized as ellipsoids and rendered as anisotropy and orientation-encoded color maps. (J. Zhang et al., 2012)

The tensor-derived scalar indices are used to generate grayscale images for visualization and quantification. In Figure 27 are represented the DTI contrasts of a mouse brain. In the mean diffusivity image the CSF appears bright while the mouse brain parenchyma appears rather homogeneous. The axial diffusivity and radial diffusivity images show more contrasts between GM and WM structures than the mean diffusivity image. The corpus callosum (CC) has higher axial diffusivity values and lower radial diffusivity

values than the neighboring cortical regions. In the FA and RA images, major white-matter structures, such as the CC, can be distinguished from GM structures by their high anisotropy values. In the DEC image, the CC appears red because most fibers are arranged along the left–right orientation.

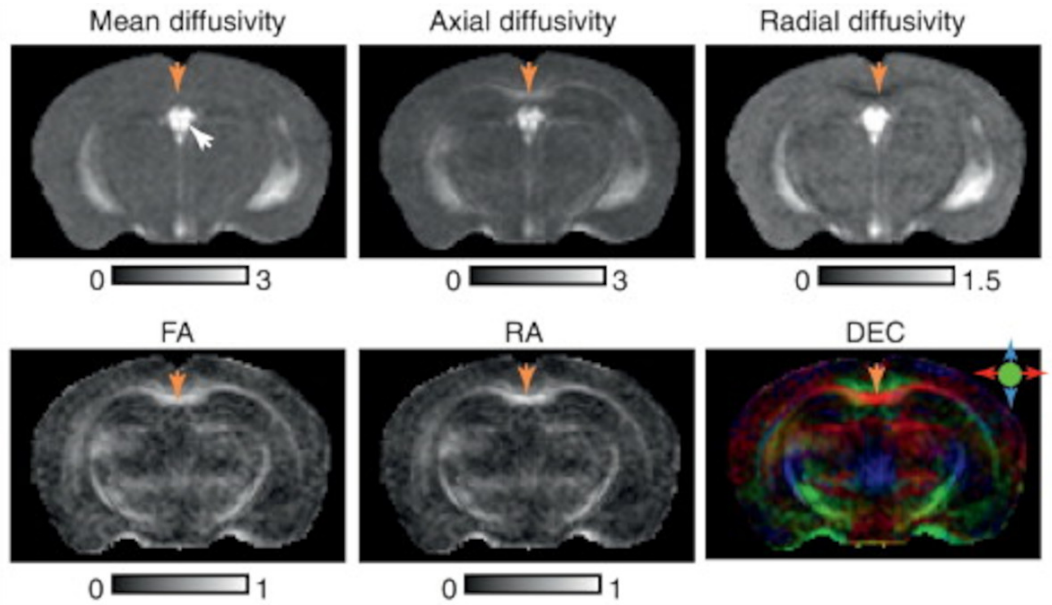

Figure 27: DTI contrasts in the mouse brain. The CSF in the ventricle is indicated by the white arrow. The CC is indicated by yellow arrows. The unit for mean, axial, and radial diffusivity is $\mu m^2/ms$. FA and RA are unitless. In the DEC image, major white-matter tracts characterized by high anisotropy are shown with color-coded orientations. The color scheme is: red, left–right; green, rostral–caudal; and blue, superior–inferior. (J. Zhang et al., 2012)

Different models have been proposed to explain how cell infiltration in white-matter regions might influence the diffusion anisotropy and diffusivity measurements (Figure 28). The presence of axon and myelin injury during early stages will lead to decreases in axial diffusivity and increases in radial diffusivity (Sun et al., 2008). When axon and myelin debrils are removed both axial and radial diffusivity increase (Mac Donald et al., 2007). The presence of inflammation infiltrating cells will contribute to decrease of axial diffusivity but an increase of radial diffusivity.

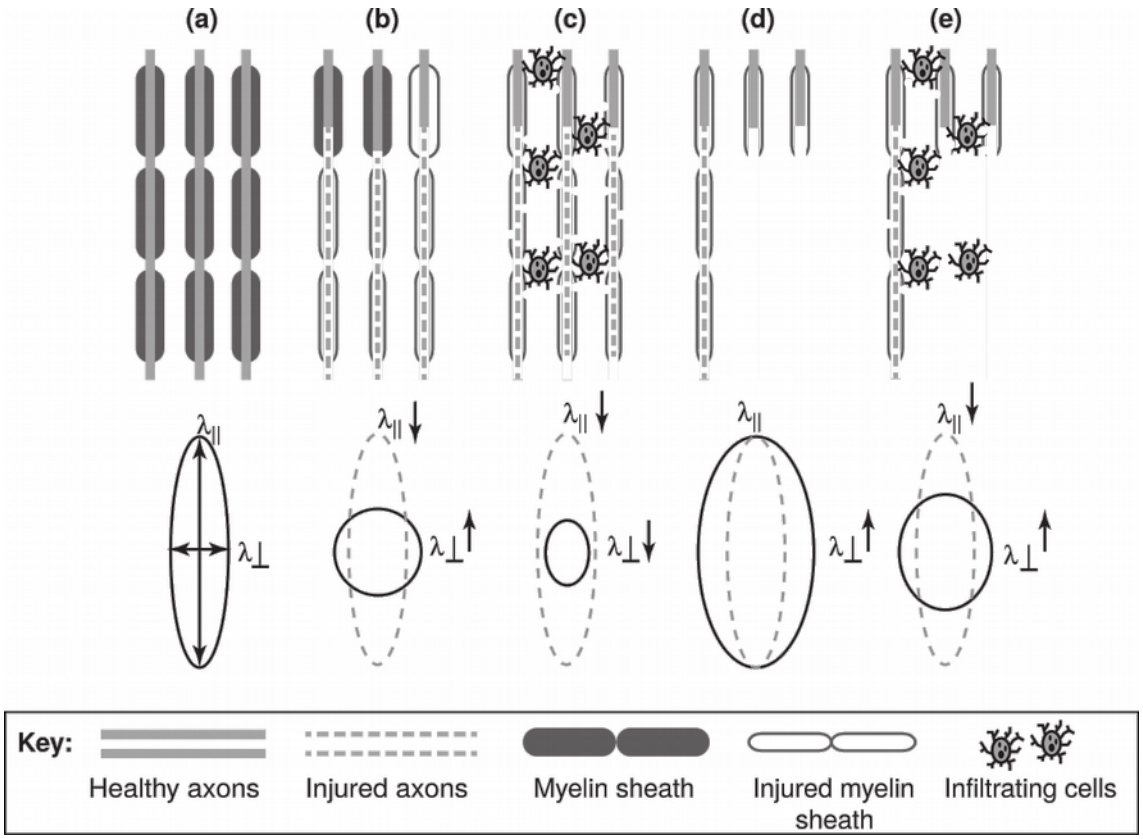

Figure 28: Schematic diagrams illustrating how complex neuropathology can affect DTI results. (a) Normal myelinated axons and the corresponding diffusion tensor and axial and radial diffusivity ($\lambda_{\parallel}$ and $\lambda_{\perp}$, respectively). The diffusion tensor is represented by the ellipsoid here, and is shown in subsequent plots as a grey ellipsoid with dashed lines. (b,c) Axon and myelin injury with and without cell infiltration. (d,e) Axon and myelin injury with axonal loss, with and without cell infiltration. (J. Zhang et al., 2012)

1.2.6 – Functional Magnetic Resonance Imaging

The fMRI technique takes advantage of the blood oxygen level–dependent (BOLD) signal change that occurs when a brain region is more active (Ogawa et al., 1990; Ogawa and Lee, 1990) Deoxyhemoglobin is, in fact, paramagnetic but when it's bound to oxygen, oxyhemoglobin, becomes diamagnetic (Pauling and Coryell, 1936). When red blood cells, containing lower levels of deoxyhemoglobin, are recruited by neural activation, differences in magnetic susceptibility between the blood and the surrounding tissue can induce small magnetic field distortions that may influence the relaxation process of water protons and thus a local signal change (Figure 29).

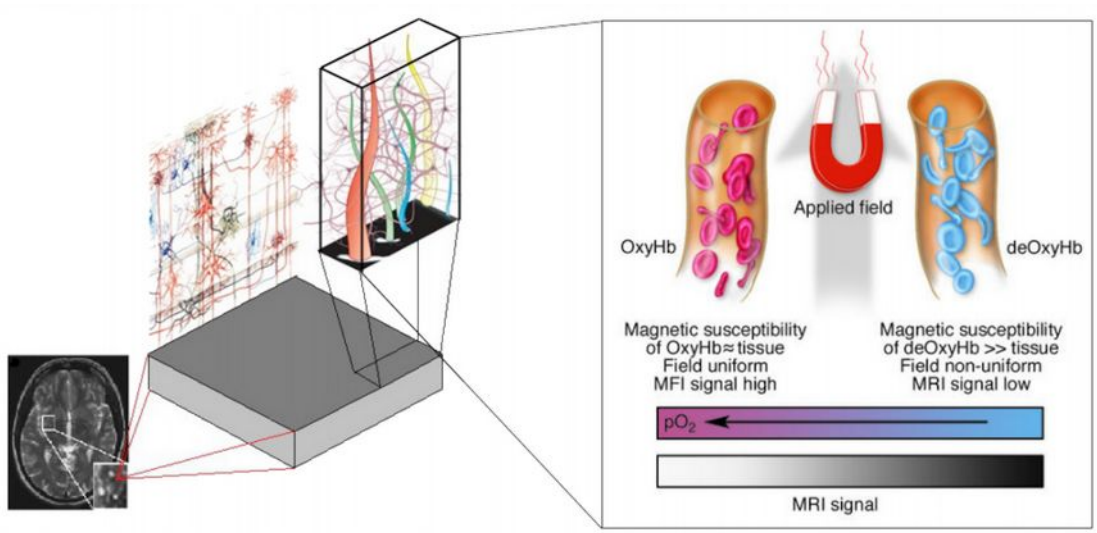

Figure 29: Origin of the fMRI contrast. On the left a hypothetical distribution of vascular and neural elements in a voxel of the MRI image (indicated by red lines). The drawing shows vessels surrounded by some of the typical neuronal types. On the right, a schematic illustration of the origins of the BOLD effect in fMRI. While arterial blood is similar in its magnetic properties to tissue, deoxygenated blood is paramagnetic and so induces inhomogeneities within the magnetic field in tissue. These cause the MRI signal to decay faster. Signals from activated regions of cortex increase as the tissue becomes more magnetically uniform. Adapted from (Gore, 2003; Logothetis, 2008)

To detect spontaneous activity fluctuation in different brain regions, long time series of MRI images are acquired. The functional networks can be identified by correlating the BOLD time course from a local region of interest with the time course of all voxels within the entire brain region (Figure 30).

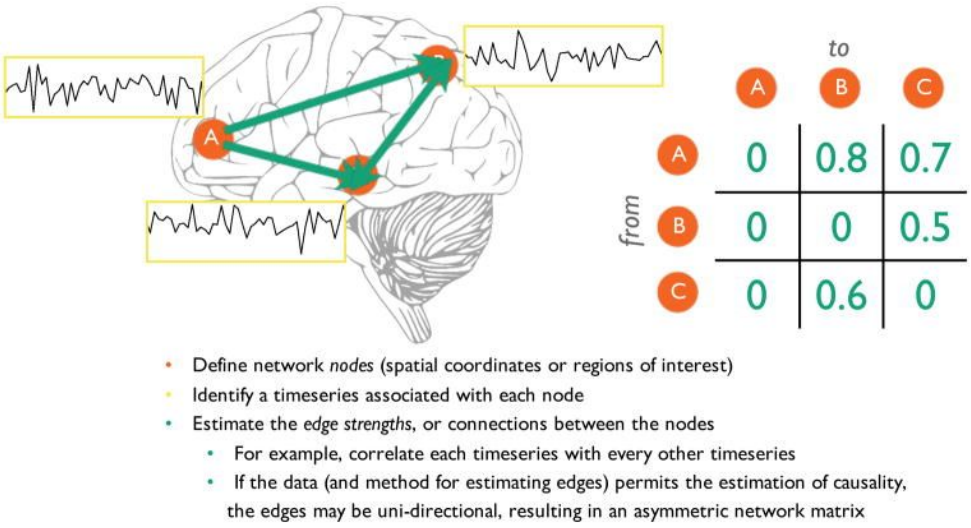

Figure 30: Main steps involved into fMRI data analysis. First identifying a number of network nodes (or functionally distinct brain regions) and then estimating the functional connections (network edges) between these nodes. (Smith et al., 2013)

Thus, a functional network may be broadly defined as a set of brain regions that are consistently synchronous. These networks are usually represented as color coded activation maps describing the correlation strength between regions (Figure 31).

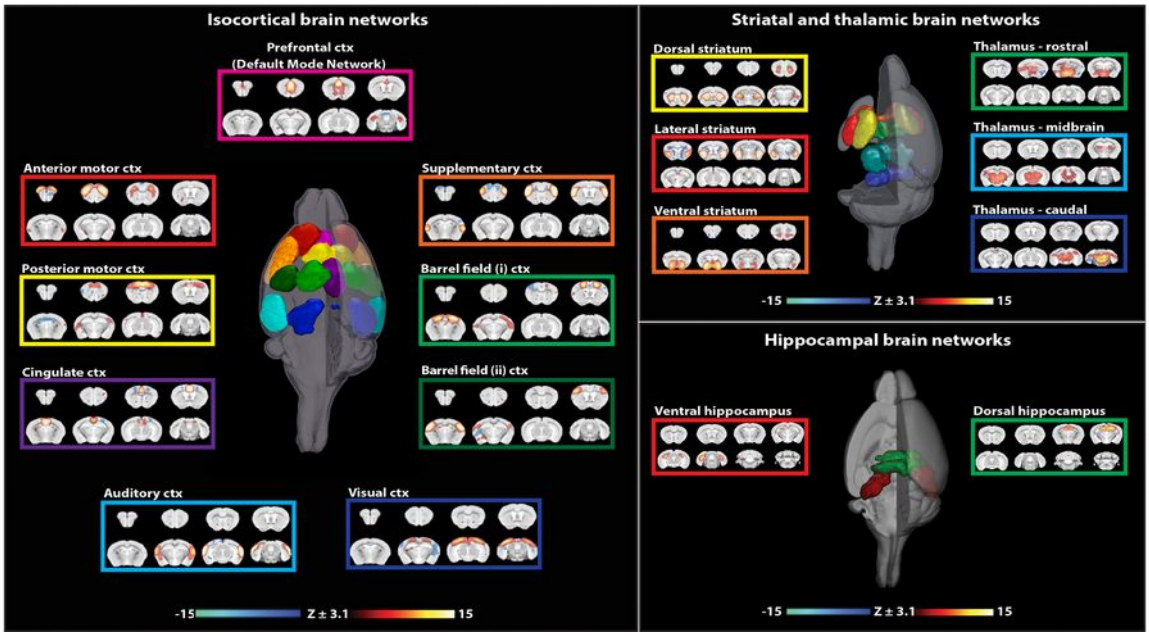

Figure 31: Resting-state networks in the mouse brain. Subdivided into isocortical, striatal, thalamic, and hippocampal networks. Each network is represented in the three-dimensional view and can be identified by the color of the square box. The strength of the correlation is represented by the Z score. (Grandjean et al., 2017)

Among all of the networks that can be identified, the Default Mode Network (DMN) is a group of brain regions that are active in the absence of a task in rodents, primates and humans (Figure 32). It includes the posterior cingulate cortex/precuneus, medial prefrontal cortex, inferior parietal lobules, lateral temporal cortices, and hippocampus (Buckner et al., 2008; Raichle et al., 2001). It has been advanced the hypothesis that the DMN activity is involved in the memory consolidation process (Fox and Raichle, 2007).

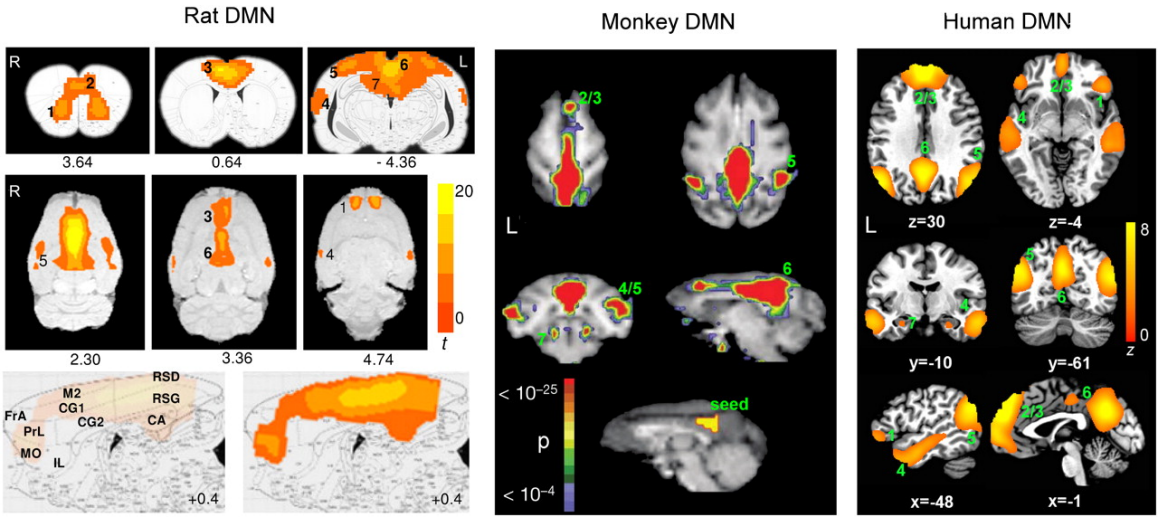

Figure 32: Comparison of the DMN in rat, monkey, and human. For **rat** DMN (*Left*), significant clusters include: 1, orbital cortex; 2, prelimbic cortex (PrL); 3, cingulate cortex (CG1, CG2); 4, auditory/temporal association cortex (Au1, AuD, AuV, TeA); 5, posterior parietal cortex; 6, retrosplenial cortex, which corresponds to posterior cingulate cortex in humans; 7, hippocampus (CA1). (*Center*) Connectivity maps in the axial plane. Note the strong connectivity between prefrontal and posterior cingulate cortices, which can best be visualized in the sagittal plane (*Bottom*, medial-lateral: +0.4 mm). FrA, frontal association cortex; MO, medial orbital cortex; R, right; RSG/RSD, granular/dysgranular retrosplenial cortex. Color bar indicates *t* scores (n = 16, thresholded at $t > 5.6$, corrected $P < 0.05$). Numbers below images are approximate coordinates relative to bregma. For **human** DMN (*Right*), significant clusters include: 1, orbital frontal cortex; 2/3, medial prefrontal cortex/anterior cingulate cortex; 4, lateral temporal cortex; 5, inferior parietal lobe; 6, posterior cingulate/retrosplenial cortex; 7, hippocampus/parahippocampal cortex (n = 39, thresholded at z > 2.1, corrected $P < 0.05$). For **monkey** DMN (*Center*): 2/3, dorsal medial prefrontal cortex; 4/5, lateral temporoparietal cortex (including area 7a and superior temporal gyrus); 6, posterior cingulate/precuneus cortex; 7, posterior parahippocampal cortex. (Lu et al., 2012)

1.3 – Aim of the Thesis

Thank to its versatility, MRI has become a fundamental tool, providing a variety of techniques used to study the morphological and physiological changes associated with the progression of AD. The development of small-bore MRI scanners allowed the translation of the same procedures to the study of AD transgenic models enabling the creation of a link between macroscopic imaging alterations and molecular/cellular aspect of the pathology. Therefore, the principal aim of the present work is to provide a multi-modal panel of MRI techniques, in order to characterize the metabolic, structural and functional phenotype of AD mouse models.

Since glucose is the central nervous system's only energy source, imaging techniques capable of detecting pathological alterations of brain metabolism are useful for assessing the evaluation efficacy of therapies in pre-clinical and clinical stages of neurodegenerative diseases. The development of an MRI method which can detect pathological alterations in the brain metabolism of AD transgenic models will be presented. In particular, since the injection of D-glucose has been proposed as an MRI contrast agent to ease the identification of tumors, the measure of the 2DG brain uptake by CEST MRI will be tested as a possible alternative to PET imaging in preclinical studies of neurodegenerative diseases. Although [18F]FDG-PET is a technique widely adopted in the clinical studies, it suffers certain drawbacks such as the low spatial resolution. Moreover, the need of special infrastructure to synthesize, distribute and dispose of radioactive tracers makes it expensive and limits repeated longitudinal measurements.

With the objective to carry out preclinical MRI studies characterized by a high translational impact, the analysis pipelines developed for investigating alterations in brain

morphology and in the brain structural connectivity, were adapted to resemble the procedures used in clinical studies. The quantity of information that can be obtained with these approaches is higher compared to the manual analysis procedures. Moreover, these approaches are independent of the operator resulting in more powerful and reproducible results, reducing the time needed for the manual delineation of ROIs and leading to the reduction of the number of animals necessary for the research.

Since the functional alterations are one of the earliest event occurring several years before the onset of the AD (Clark et al., 2012), the rsfMRI analysis pipeline, that was recently introduced within the frame of the Human Connectome Project, will be adapted to rodent studies. The efficacy of this approach has been recently demonstrated in the analysis of mouse rsfMRI data (Zerbi et al., 2015). However, since various experimental factors make the application of the rsfMRI technique easier in rats than in mice, a preliminary rsfMRI experiment will be carried out in rats. The final objective will be to optimize the analysis pipeline and translate it to the study of brain functional alterations of AD transgenic models.

Chapter 2: Material and Methods.

All the procedures involving animals and their care were conducted according to European Union (EEC Council Directive 86/609, OJ L 358,1; December 12, 1987) and Italian (D.L. n.116, G.U., Suppl. 40, February 18, 1992) laws and policies, and in accordance with the United States Department of Agriculture Animal Welfare Act and the National Institutes of Health (Bethesda, MA, USA) policy on Humane Care and Use of Laboratory Animals. They were reviewed and approved by the Mario Negri Institute Animal Care and Use Committee that includes ad hoc members for ethical issues, and the Italian Ministry of Health (project number 926/2016-PR).

2.1 – Experimental plan

Experiments were carried out with the following timeline:

1) Preliminary CEST studies were carried out in-vitro and in-vivo to optimize the experimental procedures that would have been adopted in the following experiments.
2) A study to test the tolerance of two different 2DG doses (0.5g/kg and 1g/kg) in wild-type (WT) C57BL/6N mice.
3) A study was carried out on APP23 mice over-expressing the human full-length AβPP (AβPP751) harboring the “Swedish” double mutation (K670N/M671L) breed on C57BL/6N genetic background (Balducci et al., 2010; Balducci and Forloni, 2011; Sturchler-Pierrat et al., 1997). The aim of this experiment was to assess

whether differences in the brain uptake of 2DG between 20 months aged APP23 transgenic (N =7) and age-matched WT mice (N=7) are present.

4) A multi-parametric and longitudinal study (at 6, 12 and 20 months of age) on a group of APP23 mice (N=9) and WT littermates (N=9) was assessed. Each time-point was divided into two MRI sessions. A first one with anatomical, DTI and T2 maps and after one week the 2DG-CEST. A further time-point at 24 months of age was done without the acquisition of the 2DG-CEST since elderly mice could have not tolerated well the injection of 2DG. Aim of this experiment was to assess the reproducibility of results previously obtained at 20 months of age with 2DG-CEST but also to investigate if a metabolic impairment can be observed in earlier stage of the pathology and whether concomitant structural alterations are present.

5) A rsfMRI study was carried out on thirty five male winstar rats (weight ~ 300g) to optimize the post-processing analysis protocol. A baseline acquisition was firstly reordered, rats were than separated into four groups receiving different pharmacological challenges: Saline (N=8, iv); Nicotine (0.05 mg/kg, iv, N=10); Nicotine (0.1 mg/kg, iv, N=8); Mecamylamine (subcutaneous 3 mg/kg, N=9) followed by Nicotine (0.1 mg/kg, iv) 30 minute later.

Animals were housed in standard conditions on a 12-hour dark/light cycle, with free access to food and water before imaging. Respiration was monitored during the experiment and body temperature maintained at approximately 37°C by a warm water circulating heating cradle. Mice were anesthetized with isoflurane (4%) in oxygen and anesthesia maintained with isofluorane (2%). Anesthesia protocol was slightly changed for CEST experiments to detect alterations in the uptake of 2DG. Mice were fasted overnight, with free access to water before imaging and anesthesia was maintained with isoflurane (1.5%) in oxygen. After the induction of the anesthesia, the tail vein of these

mice was cannulated with a catheter connected to a solution of 2DG. Rats used in rsfMRI experiments anesthetized with isoflurane (4%) in a mixture of O_2 (30%) and N_2O (70%) that was slowly discontinued and maintained with an intravenous [iv] infusion in the tail of a medetomidine solution (0.14 mg/kg/h at 1 ml/h).

2.2 – Acquisition parameters

Experiments were done on a 7T Bruker Biospin 70/30 Avance III system, equipped with a 12 cm diameter gradient coil (400 mT/m) and running ParaVision 5.1.

Mice experiments were carried out with a set of two actively decoupled radio frequency coils: A 7.2 cm diameter volume coil as the transmitter and a quadrature single channel surface coil as the receiver. While rsfMRI experiments were done using a 7.2 cm diameter volume resonator coil as transmitter in combination with a four-channel receive-only coil array for the rat brain as a receiver.

2.2.1 – In-vitro CEST

Experimental parameters, such as the saturation power and time, were chosen on the base of a previously published paper (Nasrallah et al., 2013). CEST Z-spectra were measured using a rapid acquisition with relaxation enhancement (RARE) sequence (TR/TE 5000/4.3 ms, RARE factor 24, single slice thickness 2 mm, matrix size 45×45, field of view 16×16 mm^2, resulting in an in-plane resolution of 0.35×0.35 mm^2) preceded by a continuous wave saturation pulse (B_1 =1.5 μT, t_{sat}=4 s) over 58 frequency steps (300 ±20 ±5 ±4.66 ±4.33 ±4 ±3.83 ±3.67 ±3.5 ±3.33 ±3.17 ±3 ±2.83 ±2.67 ±2.5 ±2.33 ±2.17 ±2 ±1.83 ±1.67 ±1.5 ±1.33 ±1.167 ±1 ±0.83 ±0.67 ±0.5 ±0.33 ±0.167 0 ppm) resulting in a total scan time per Z-spectrum of around 8 min.

To assess the goodness of the chosen parameters, preliminary in-vitro experiment were carried out on a phantom that consisted in six glass micro-tubes (ϕ = 2mm) filled with a solution of 2DG (Santa Cruz Biotecnology) at different concentrations (0, 7, 15, 30, 60, 120 mM and pH 7) and positioned in a 15ml falcon that was filled with 1 × phosphate-buffered saline (PBS).

A Matlab script was used to fit the in-vitro Z-spectra with a spline curve and B_0 shift automatically compensated evaluating the minimum of the acquired spectra. Results obtained, Figure 33, show that we were able to detect efficiently the asymmetry at all the 2DG concentrations tested, included the lower ones (7 and 15 mM) selected in the range of the glucose brain concentrations (2-20mM) (Silver and Erecińska, 1994).

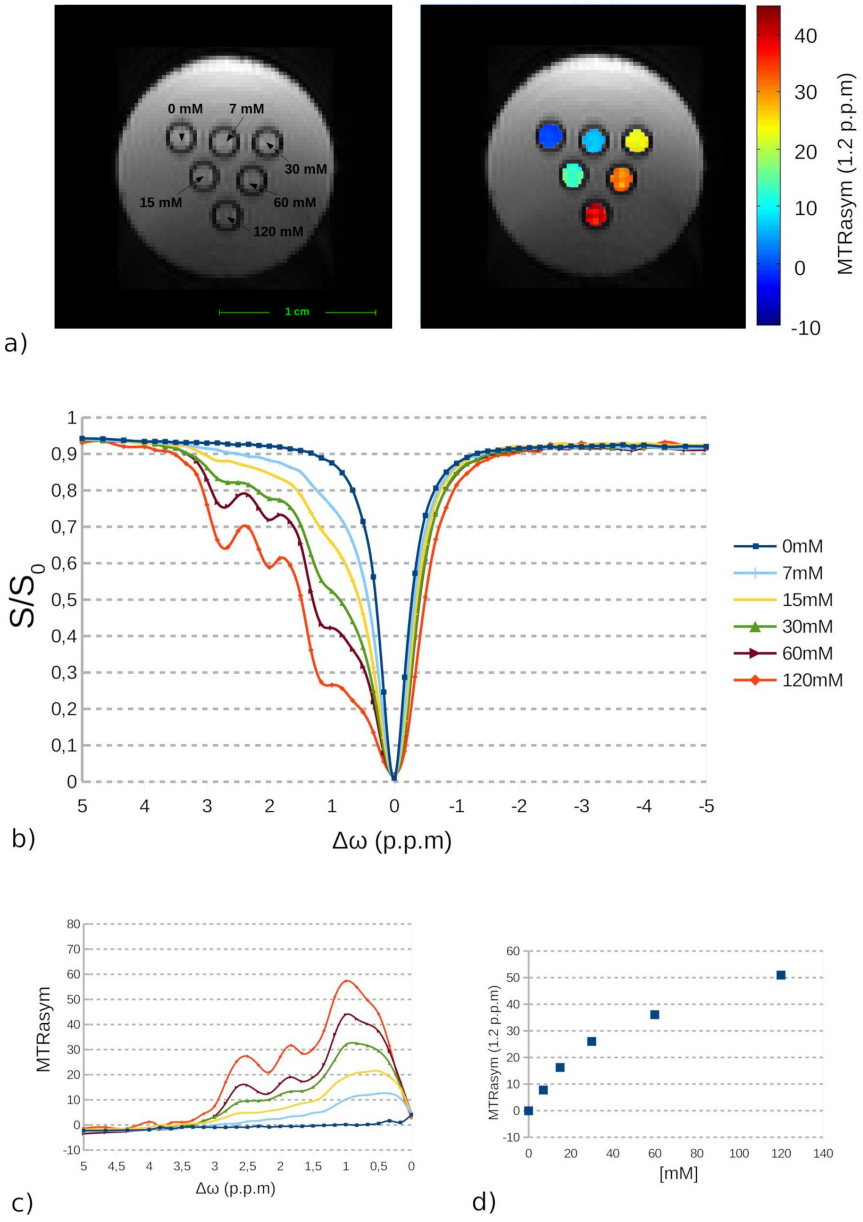

Figure 33: In-vitro results. a) Unsaturated slice and color coded map representing the asymmetry at 1.2 p.p.m. c) Z-Spectra and d) Asymmetry curves at different 2DG concentrations. e) plot of the asymmetry at 1.2 p.p.m as a function of the concentrations.

2.2.2 – In-vivo CEST

Before CEST measurements, a B_0 field map was acquired and 1st and 2nd order shims adjusted using the MAPSHIM routine, over a voxel (5×7×7.5 mm^3) set to cover the brain, excluding the olfactory bulb and cerebellum. CEST Z-spectra were measured using the same pulse sequence used in in vitro tests and positioned in the dorsal hippocampus region (as shown in Figure 34).

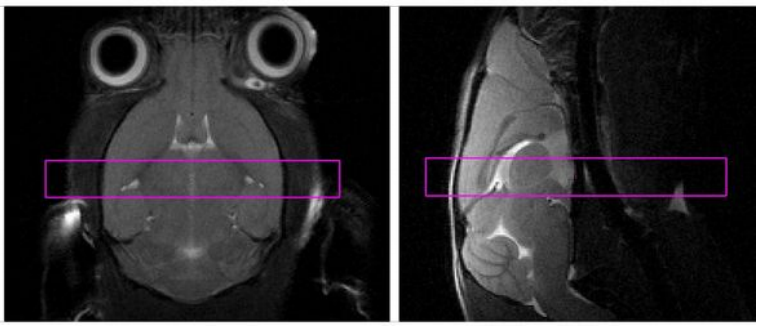

Figure 34: CEST slice positioning

Since B_0 inhomogeneities could lead to errors in the evaluation of the CEST effect, the simultaneous mapping of the B_0 and B_1 inhomogeneities was assessed using the WASABI (Schuenke et al., 2016) obtained with a continuous wave saturation pulse (B_1=3,7μT, t_{sat}=5ms, 43 frequency offsets between ±1.5 ppm).

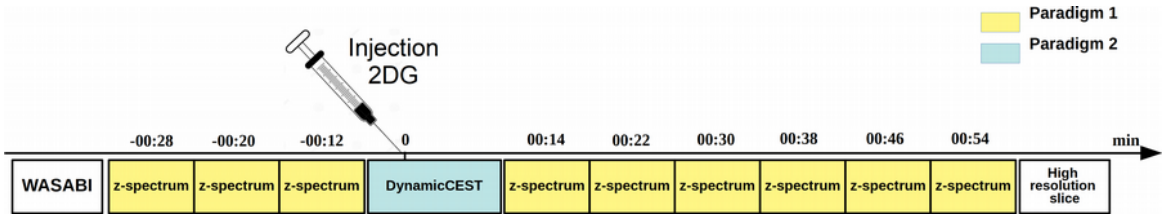

Figure 35: Timing of the experiment

As shown in Figure 35, each experiment comprised the simultaneous B_0 and B_1 inhomogeneities mapping and two different paradigms followed by one last "high-resolution" unsaturated reference image that was acquired with a RARE sequence (TR/TE=5000/4.3 ms, RARE factor 16, slice thickness 2 mm, matrix size 90×90, field of view 16×16 mm^2 resulting in an in-plane resolution of 0.18×0.18 mm^2).

2.2.3 – Anatomical images

An in-house high resolution reference template was created by acquiring ten anatomical T2-weighted images on wild-type mice. A 3D rapid acquisition with relaxation enhancement (RARE) was used with a voxel size of 83 × 83 × 83 μm^3 (matrix size 360 × 164 × 128 and FOV of 3 × 1,36 × 1,06 cm); TR= 2500 ms, effective echo time TE_{eff} = 50 ms, and RARE factor of 16, for 1 average and acquisition time of 54 min.

During the longitudinal study, anatomical images of APP23 and littermates WT mice were acquired with different acquisition parameters: voxel size of 100 × 100 × 100 μm^3 (matrix size 300 × 100 × 120 and FOV = 3 × 1 × 1.2 cm), TR = 2500 ms, TE_{eff} = 50 ms, and RARE factor of 16, for 1 average and acquisition time of 30 min. Reducing the scanning time it is possible to acquire other image modalities without protracting anesthesia for a long time.

2.2.4 – DTI images

Coronal DTI echo-planar imaging (EPI) sequences acquired with an in-plane image resolution of 117 × 156 μm^2 (FOV 1.5 × 1.5 cm^2, acquisition matrix 128 × 96, 18 slices with thickness of 0.5 mm); TR/TE=4500/32 ms. Four averages were used to boost the signal-to-noise ratio. Diffusion, encoding b factors of 800 mm^2/s was applied along 19 isotropic directions, acquistion time 24 min. 1st and 2nd order shims were adjusted using the MAPSHIM routine, over a voxel (5 × 7 × 8 mm^3) set to cover the brain before DTI measurements. A 2D coronal anatomical reference image was acquired with a RARE sequence with an in-plane resolution of 76 × 76 μm^2 (TR/TE_{eff} = 4000/52, RF = 8, FOV = 1.5 × 1.5 cm^2, acquisition matrix 196 × 196, 18 slices with thickness of 0.5 mm, for a total scan time of 6 min).

2.2.5 – Multi slice multi echo images (MSME)

The T2 values of the tissues was estimated acquiring a multi slice multi echo (MSME) sequence with TR=3500ms and ten different TE (11, 22, 33, 44, 55, 66, 77, 88, 99, 110 ms) with an in-plane image resolution of 76 × 76 μm^2 (FOV 1. 5 × 1.5 cm, acquisition matrix 196 × 196, slice thickness 1 mm), acquisition time 8 min.

2.2.6 – rsfMRI images

After the acquisition of a tripilot scan, to correctly position the brain in center of the scanner, an anatomical reference scan was acquired using a T2-weighted Rapid Acquisition with Relaxation Enhancement (RARE) sequence with the following parameters: field of view (FOV) = 36 × 25 × 24 mm^3, matrix dimension (MD) = 240 × 124 × 64, repetition time (TR) = 2500 ms, effective echo time (TE_{eff}) = 60 ms, RARE factor = 20, number of averages (NA) = 1.

B_0 field homogeneity correction were made with the Bruker Mapshim routine over a region of interest that covers the entire brain volume. A fieldmap acqusition was acquired twice, before and after the B_0 correction.

The fMRI time series were acquired using a single-segment gradient-echo planar imaging (EPI) sequence with: TR/TE=2000/20ms; MD= 92 × 92; FOV=35 × 35mm^2; 27 slices with thickness of 0.5 mm and slice gap of 0.2 mm; 300 volumes.

Chapter 3 – Results

This chapter include three main sections that illustrate the results obtained respectively in the study of brain metabolism and structural alterations of the transgenic mouse brain and the development of the rsfMRI method. The description of the analysis procedures is included in this chapter because their development is itself a result obtained in the frame of this project.

3.1 – Study of the mouse brain metabolism with 2DG-CEST

Aim of the experiments described within this section was to develop a novel MRI technique, alternative to the [^{18}F]FDG-PET, able to detect pathological alterations in the brain glucose metabolism of Alzheimer's disease transgenic mice.

3.1.1 – CEST analysis workflow

All the analysis have been done with custom MATLAB scripts. All the steps needed by the developed analysis pipeline are shown in Figure 36 and consist of three different steps:

- **B_1 and B_0 mapping. N**eeded because CEST effect is susceptible to inhomogeneities of the static magnetic field and of the RF saturation pulse.
- **Paradigm 1**: To analyze the full Z-spectra acquired before and after the 2DG injection.
- **Paradigm 2**: To analyze the data acquired dynamically during the 2DG injection.

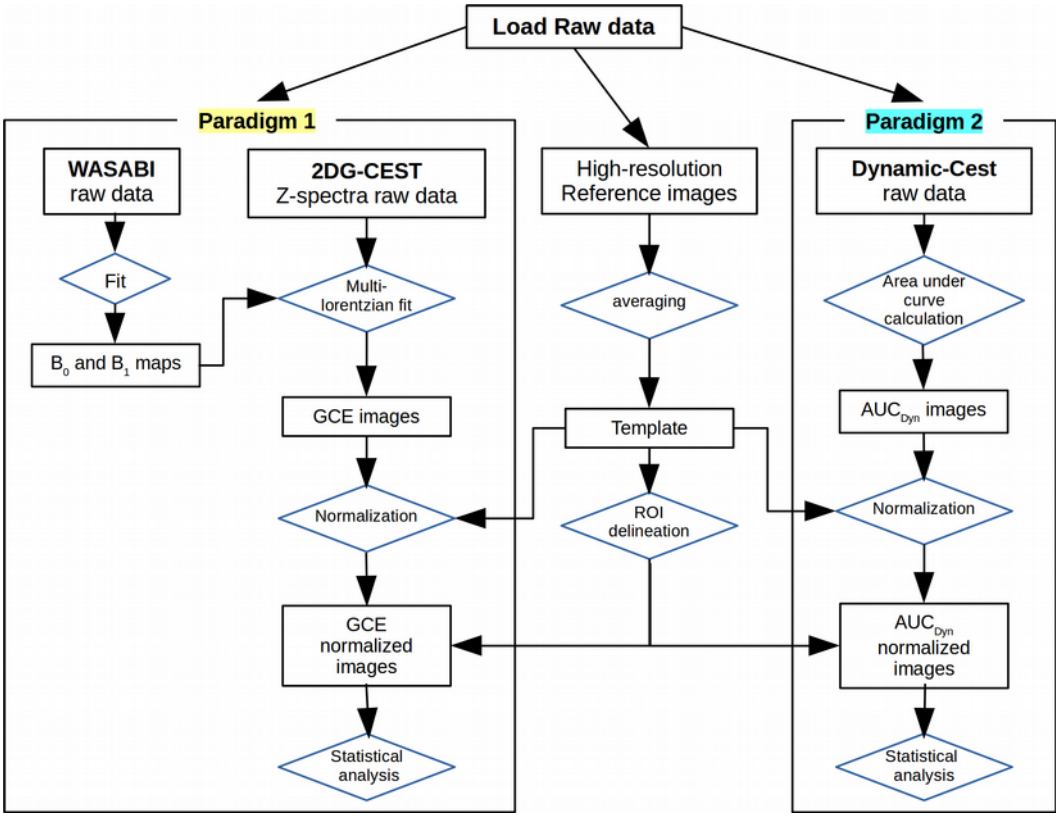

Figure 36: Flowchart describing the CEST data processing procedures. Diamonds shape indicate the processing steps done with the developed software while square boxes indicate processed images.

B_1 and B_0 mapping. CEST effect is susceptible to the B_0 inhomogeneity of the static magnetic field; because of the presence of the so called "spillover effect" the measured Z-specturm is no longer symmetric resulting into an erroneous evaluation of the asymmetry curve Figure 37. Furthermore, the B_1 inhomogeneity of the RF pulse may also cause spatial variation in the saturation efficiency affecting the CEST quantification (G. Liu et al., 2013).

The most commonly adopted method to correct the B_0 inhomogeneity is called "water saturation shift referencing (WASSR)" (M. Kim et al., 2009). Through a weak intensity preparation block (one rectangular pulse with pulse duration t_p = 500 ms and nominal RF amplitude B_1=0.1μT and 31 frequency offsets), followed by a spoiler gradient and a conventional MRI readout, it allows the direct measurement of the absolute water

frequency in each voxel and enables a proper centering of Z-spectra on a voxel-by-voxel basis (Figure 37). However, since WASSR method does enable to map the B_1 inhomogeneity mapping, a separate sequence should be adopted extending the acquisition time.

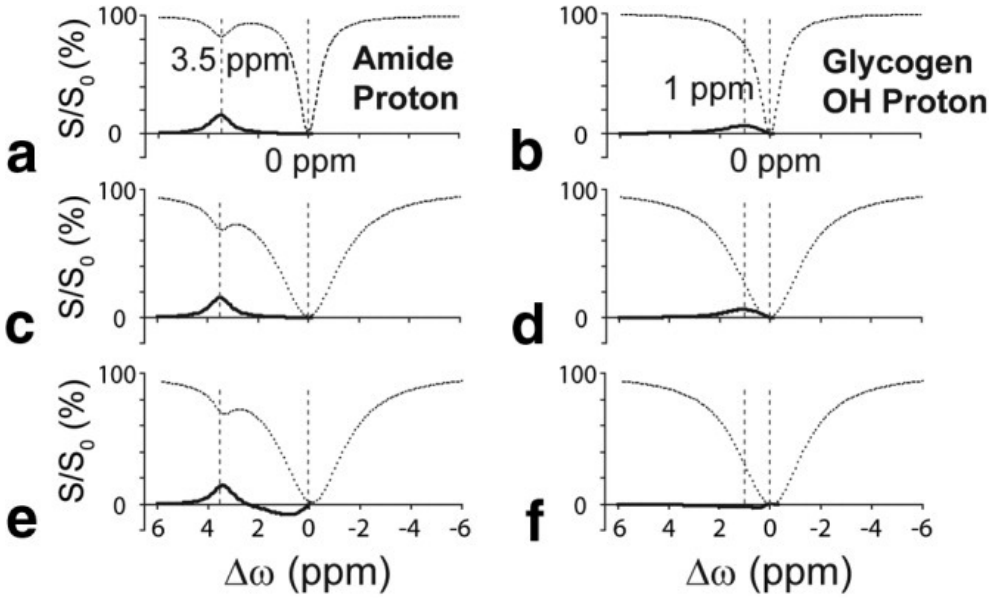

Figure 37: Simulated Z-spectra (dashed lines) and MTRasym plots (solid lines) for an amide proton (a,c,e) and a glycogen OH proton (b,d,f). The large intensity drop around 0 ppm is due to direct water saturation, with the water frequency assigned to 0 ppm. **a**: An amide proton at 3.5 ppm shows a clear CEST effect in both the Z-spectrum and MTRasym plot. **b**: A glycogen OH proton at 1 ppm shows a relatively clear but small CEST effect in the MTRasym plot, but the CEST effect is not clearly visible in the Z-spectrum because the OH protons resonate close to the water frequency. When the direct saturation lineshape broadens (c and d), the CEST effects of the amide and OH protons can be still observed in the MTRasym plot as long as the saturation curve is properly centered. However, a shift as small as 0.1 ppm in the Z-spectra can cause relatively large changes in MTRasym, affecting the CEST quantification of the amide proton (e) and obviating the CEST effect of the OH proton (f). (M. Kim et al., 2009)

The WASABI method adopted allows the simultaneous mapping of the B_0 and B_1 inhomogeneities. It consists of a short preparation block (one rectangular pulse with pulse duration $t_p = 5$ ms and nominal RF amplitude $B_1 = 3.7$ μT), followed by a spoiler gradient and a conventional MRI readout. Sampling of several frequency offsets around the water resonance reveals the sinc shaped saturation spectrum of the pulse (Figure 38), from

which the absolute water frequency δω and the B_1 amplitude can be derived. The shape of the saturation spectrum can be described mathematically by the following equation:

$$Z(\Delta\omega)=\left|c-d\cdot\sin^2\left(\tan^{-1}\left(\frac{\gamma\cdot B_1}{\Delta\omega-\delta\omega}\right)\right)\cdot\sin^2\left(\sqrt{(\gamma\cdot B_1)^2+(\Delta\omega-\delta\omega)^2}+\frac{t_p}{2}\right)\right| \quad [12]$$

Where the t_p is the pulse duration and the γ is giromagnetic ratio are constant and *c*, *d*, B_1, and δω the free parameters estimated.

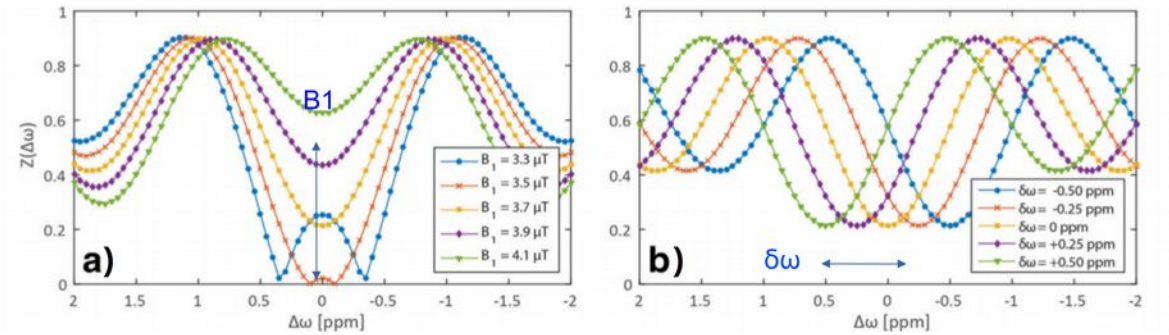

Figure 38: Simulated WASABI Z-spectra. **(a)** Shows the effect of the RF amplitude (B_1) on the shape of the signal. **(b)** The water frequency shifts δω. (Schuenke et al., 2017b)

A high correlation between the B_0 map obtained with the WASABI method with the ones obtained with the WASSR have been measured, as shown in Figure 39.

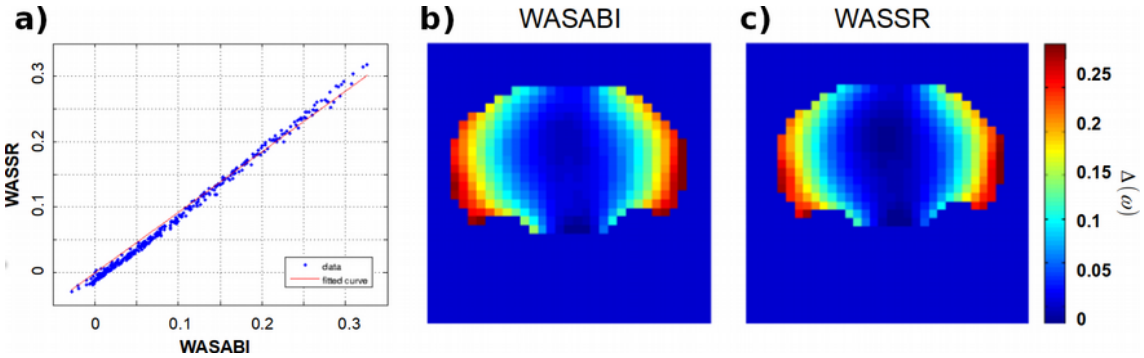

Figure 39: Comparison between B_0 map obtained with the WASABI and the WASSR approaches. **a)** linear correlation between values calculated with the two methods in each voxel. **b** and **c)** Color-coded maps representing the shift from the absolute water frequency (δω) calculated in the mouse brain region with the two methods.

An example of a measured wasabi-spectrum is shown in Figure 40. A relative B_1 map can be obtained by normalizing the measured B_1 map by the setting value (3.7μT) equal to the selected RF amplitude.

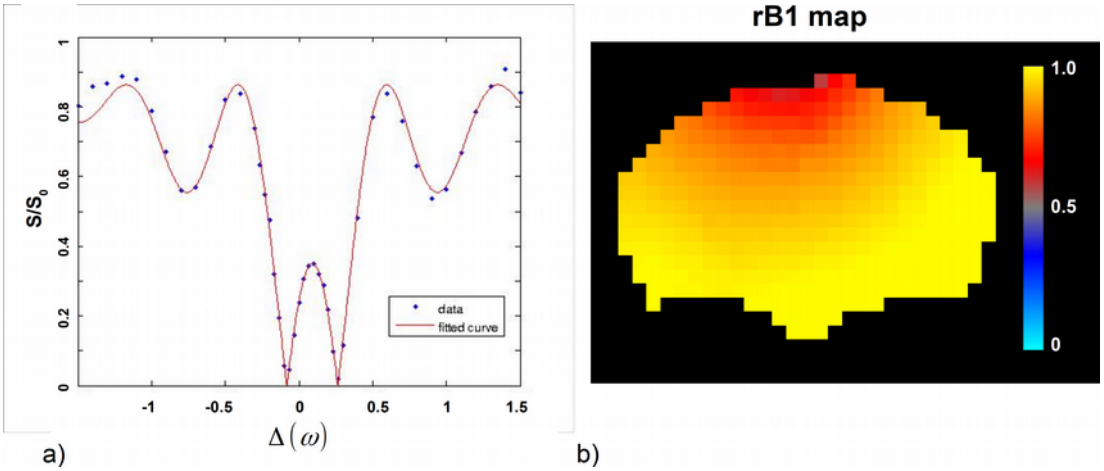

Figure 40: Fit results of the WASABI technique. In **(a)** is shown a example of an acquired spectra and the fit obtained. In **(b)** a relative B_1 map obtained within the mouse brain region. The color-coded map shows that regions with rB1 close to 1 are those where RF amplitude is closer to the setting value (3.7μT).

Paradigm 1: Z-spectrum asymmetry changes. As shown in Figure 35, three baseline Z-spectra were acquired before the injection of the bolus and six more Z-spectra acquired after. Each one was evaluated voxel-wise within a mask brain region that was manually drawn using ITK-SNAP software (Yushkevich et al., 2006) using a multi-lorentzian fitting approach (Jones et al., 2013; Wang et al., 2016). Each CEST Z-spectrum signal, expressed as a function of the frequency offset (Δω), was modeled as a sum of five inverted Lorentzian curves with amplitude (A_i) and full width half maximum (L_i).

$$Z(\Delta\omega) = 1 - \sum_{1}^{5} A_i \left(1 + \left(\frac{\Delta\omega - \delta\omega_i}{0.5 \cdot L_i} \right)^2 \right)^{-1} + MT \quad [13]$$

This represents the effect of the saturation on the signal intensity directly on the free water molecules and from the exchanging amine ($-NH_2$), amide (-NH), hydroxyl (-OH)

and the signal of aliphatic protons (relayed nuclear Overhauser effect rNOE). While the semi-solid magnetization transfer contribution was considered just as an additional parameter since the saturation power is weak and calculated as:

$$MT = \frac{\left[S_0 - S_{5\,ppm}\right]}{S_0} \quad [14]$$

where S_0 is the signal with saturation pulse at 300 ppm.

To ensure a reliable fit careful correction of the B_0 inhomogenities the fit function of the Z-spectrum signal was evaluated with a slightly different procedure from the previously published (Desmond et al., 2014; Wang et al., 2016; Windschuh et al., 2015; Zaiss et al., 2011; Zhou et al., 2017) by splitting it into two subsequent steps as shown in Figure 41.

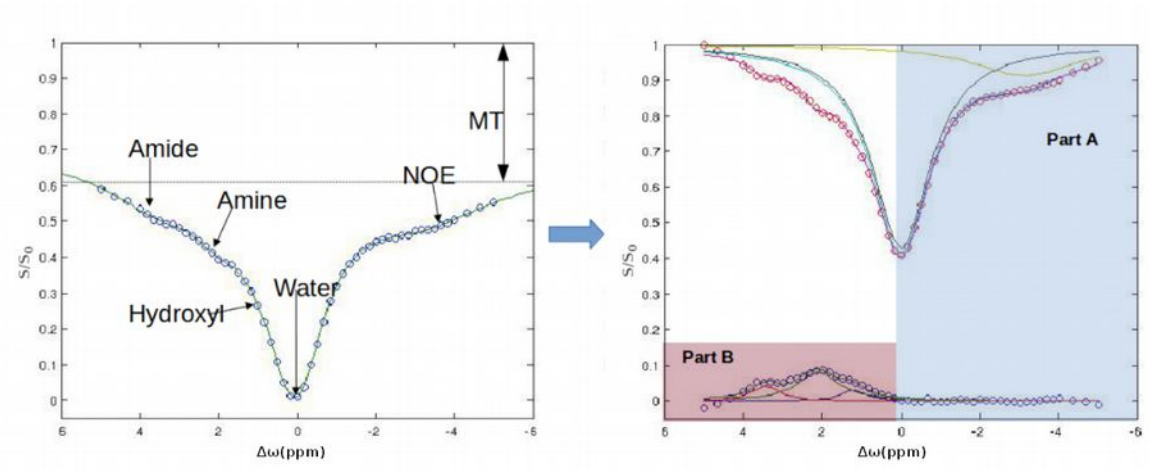

Figure 41: Fitting procedure. The left panel shows the location of the different compounds. Analysis firstly fitted the contribution of water and NOE (part A) and in a second step the other compounds contributions (part B).

To avoid over-fitting errors, direct water saturation (DWS) and the contribution of NOE protons were firstly evaluated as the sum of two Lorentzian curves over the non-hydroxyl containing region using a subset of frequency offsets (Miller et al., 2015) between -6 ppm and 0.5 ppm The water shift (δω) starting point was set using the previously calculated B_0 map and signal drifts were corrected using the minimum of the water Lorentzian curve. Then the residue signal was fitted by the sum of the three remaining proton groups. This

approach has the advantage of allowing a better correction of the 0 ppm offset of the Z-spectrum without any potential bias due to effects present elsewhere in the spectrum, this is then incorporated into the model as compensation in the second step. We have observed a signal drift that results in a shifting of the Z-spectrum during the experiment that can cover 90 minutes, hence the need for a direct correction as part of the fitting. Although the traditional evaluation of the six-pool approach in a single step is able to produce good looking fit and low residuals it could lead to errors in the evaluation of the hydroxyl protons when combined with unconstrained fitting of other parameters. In Figure 42 and 43 the fit obtained within the same voxel, 20 minutes before the 2DG injection and 60 minutes after and analyzed with the two approaches, are shown. In Figure 42 it can be seen that, with the single step six-pool approach, good results can be obtained just with the first Z-spectra when the B_0 map was calculated using the WASABI sequence right before the Z-spectra acquisition. Although the B_0 shift produced by the signal drift is not very large, we observe that it can influence the quality of the single-step six-pool approach that gives a wrong estimation, leading to a wrong asymmetry curve that presents negative values close to the zero point. This could be due to an over-fitting error; with a high number of unconstrained variables in the fitting procedure less robust results were obtained. Hence our approach was to initially shift the signal using the B_0 map obtained with the WASABI sequence, then we fit the right part of the Z-spectra as the sum of two lorentzian contribution (Water and NOE) between 0.5ppm and -6ppm. After fixing the parameters belonging to water and NOE we evaluate other pools. This approach avoids the hydroxyl contribution being erroneously assigned to the water pool. Moreover, considering the MT contribution constant we further reduce the number of variables involved into the fitting procedure obtaining more robust results Figure 43. Both

approaches published starting points and boundaries of fit parameters have been used (Windschuh et al., 2015).

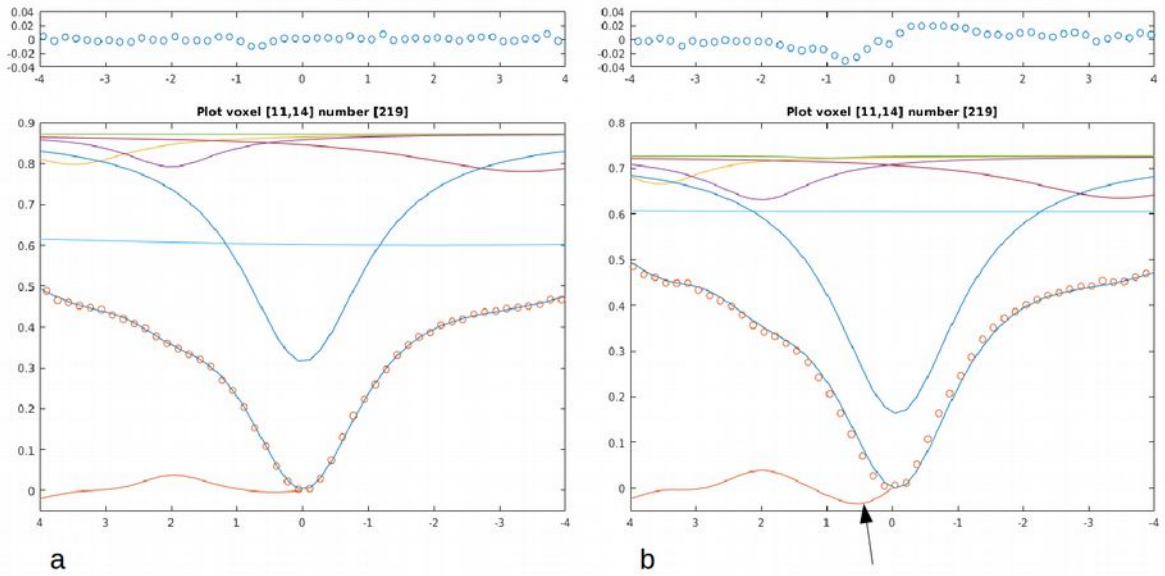

Figure 42: Six pool fitting procedure within the same voxel (a) 20 minutes before and (b) 54 minutes after the 2DG injection. With the black arrow is show that, although a good looking fit is obtained, an error in the asymmetry curve is obtained due to the erroneously compensated B0 signal drift.

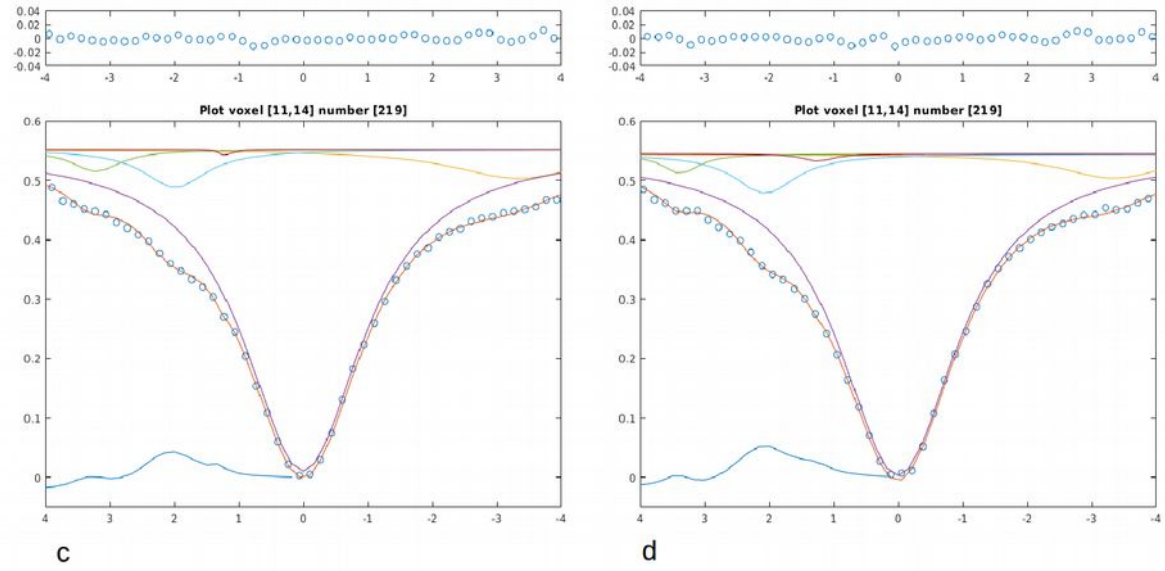

Figure 43: Five pool fitting procedure separated into two different steps. Within the same voxel (a) 20 minutes before and (b) 54 minutes after the 2DG injection.

To assess the accumulation in brain cells of 2DG, and therefore of 2DG6P, the differences between the three baseline and the post-injection Z-spectra were measured as the change of the asymmetry of the fitted signal in each voxel of the brain mask.

The asymmetry curve is normally obtained as:

$$MTR_{asym} = \frac{S_{ref} - S_{lab}}{S_0} \quad [15]$$

where S_{ref} and S_{lab} are the measured signal intensity and the label intensity of the acquired Z-spectrum and S_0 is the unsaturated signal intensity. However, since a fit curve has been computed, the asymmetry can be expressed as a Lorentzian Difference (LD) (Jones et al., 2013):

$$LD = Z_{ref} - Z_{lab} \quad [16]$$

Where Z_{ref} and Z_{lab} are the corresponding images with intensities given by the fit. In addition a linear correction for B_1 was applied by multiplying the asymmetry curve by the previously relative B_1 calculated. This simplified B_1 correction was applied because we found small B_1 differences.

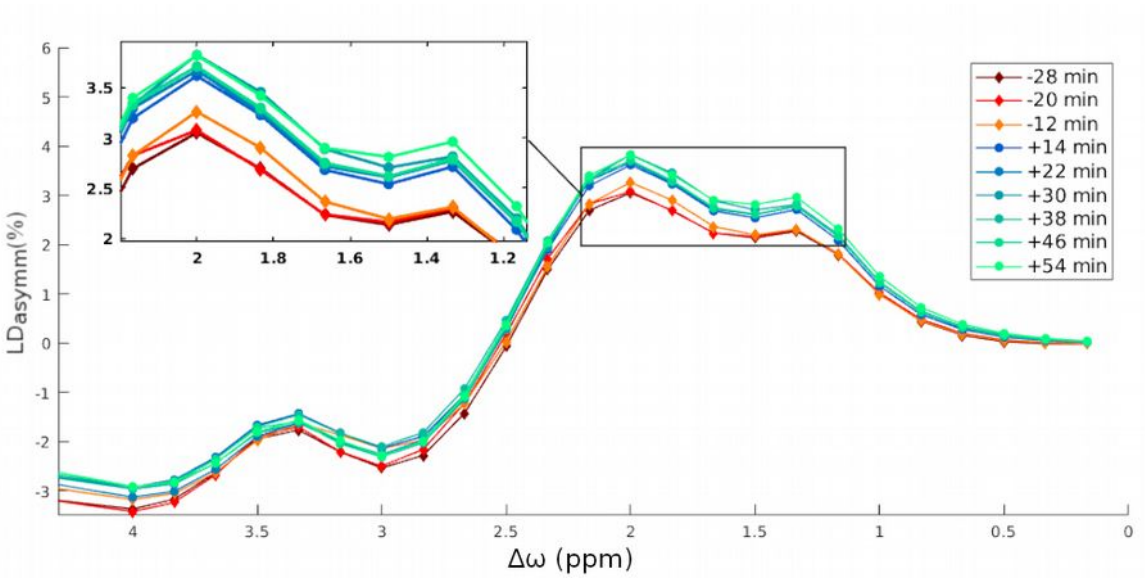

Figure 44: Asymmetry enhancement. Mean asymmetry fitted curves over the cortex region of a single WT mouse before and after 2DG injection. Highlighted by the square is the area where the cest enhancement has been evaluated.

The glucose CEST enhancement (GCE) was then expressed as the change of the area under the lotentzian difference curve (AUC_{LD}) between 2.3 and 1 ppm that corresponds to the hydroxyl group resonating region (Figure 44) and described by:

$$GCE(t)=\left[\frac{AUC_{LD}(t)-AUC_{LD}(Baseline)}{AUC_{LD}(Baseline)}\right] \quad [17]$$

To enable an automated regional of interest analysis, a custom template was created using the buildtemplateparallel.sh script, provided by ANTs (Avants et al., 2010, 2011), that perform the averaging of all the "high-resolution" reference slices acquired at the end of each experiment. The unsaturated images of each Z-spectra were then co-registered with an affine transformation and resampled to this high-resolution template The transformations obtained were then applied to the images describing the GCE and the mean was calculated over selected regions of interest (ROI) traced over the template in the cortex, hippocampus, thalamus and ventricles.

Paradigm 2: Continuous single offset acquisition. In order to reduce the sampling time and measure changes of the blood-brain volume dynamically, the direct measurement of the signal change during the 2DG injection (Dynamic-CEST) (Xu et al., 2015a, 2015b) was achieved by repeating the saturation (t_{sat}=4 s, B_1 =1.5 μT) in the region of interest of the hydroxyl protons, 1.2 ppm. The 2DG bolus was injected, without stopping the acquisition, after 15 baseline scans and over a period of 90 seconds. The dynamic acquisition covered a total of 90 repetitions and lasted 13.5 minutes. Since, one image was obtained every 9 seconds, which intensity depends on the amount of 2DG in the tissues, the signal change can be established as the difference in the signal intensity from the baseline calculated averaging the first 15 images. The area under the curve (AUC_{Dyn}) could be related to the amount of blood reaching the brain tissues. It was computed as the total sum of the differences of the signal from the baseline, starting from the end of the infusion (110 sec) following:

$$AUC_{Dyn} = \sum_{n=110}^{700} \left[\frac{S_{baseline} - S(t_n)}{S_{baseline}} \right] \quad [18]$$

Images representing the AUC_{Dyn} were again co-registered to the template space and wild-type and transgenic mice compared using student's t-test and the ROI approach.

3.1.2 – CEST preliminary in-vivo tests

Results shown within this section were carried out to verify that we were able to detect the 2DG uptake in the mouse brain with the selected acquisition parameters but also to find a suitable dose of 2DG to be injected. Obstructing the glucose utilization, high doses of 2DG could lead to intracellular glucopenia and eventually to death. However, it has been shown how fairly high doses of 2DG (from 0.25 g/kg up to 2 g/kg) must be injected to compensate the low sensitivity of the MRI technique (Rivlin et al., 2013, 2014; Rivlin and Navon, 2016; Jin et al., 2016).

Two groups of wild-type mice (each with N=8 and 20 months of age) received respectively two different dose of 2DG (0.5 g/kg and 1 g/kg). The GCE was measured averaging the signal changes of the Z-spectrum asymmetry (Paradigm 1) in the whole brain slice and in the cortex, hippocampus, thalamus and ventricles regions (Figure 45). The two-way analysis of variance (ANOVA) followed by the Hochberg correction (R software, https://cran.r-project.org/) was computed considering all time-points. It did not shown significant interaction between dose injected and time for all ROIs investigated. However, a significant effect of time was highlighted when the GCE was averaged all over the whole brain mask ($F=28.27$, $p<2\times10^{-16}$), in the cortex ($F=46.64$, $p<2\times10^{-16}$) and in the thalamus ($F=16.74$,$p=3\times10^{-16}$). In the hippocampus a significant effect of time ($F=22.03$,$p=2\times10^{-16}$) and a significant effect of the dose injected ($F=8.39$,$p=0.004$) was

shown. Similarly, in ventricles a significant effect of time ($F=18.33, p=2\times10^{-16}$) and a significant effect of the dose injected ($F=4.57, p=0.03$) was shown. The significant effect of time could indicate that the uptake of 2DG is faster after the injection of the higher dose but at the same time that the concentration of 2DG, and therefore of 2DG6P trapped in cells, is equal between the two groups at longer times.

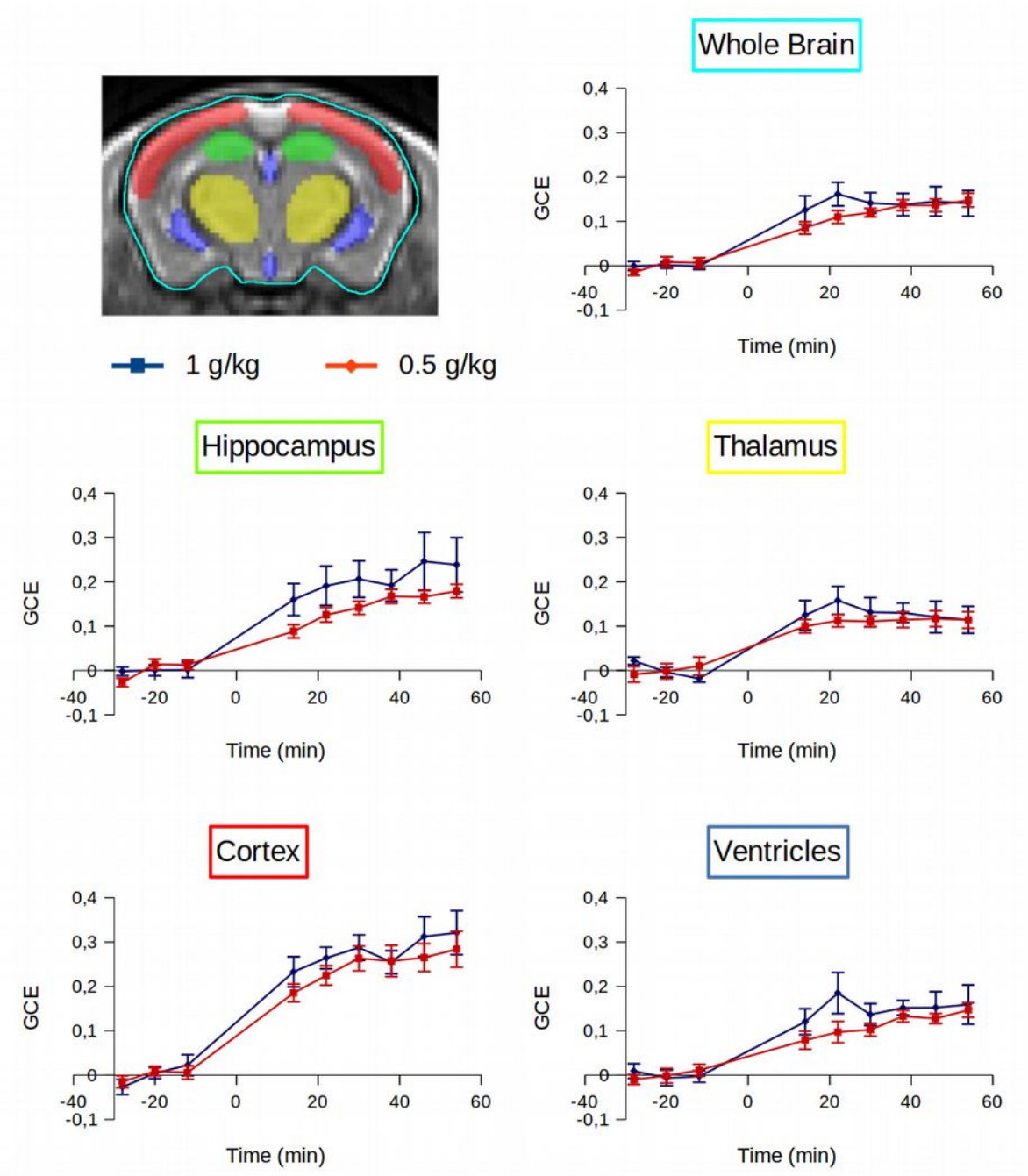

Figure 45: Temporal GCE. Group mean ± standard errors (s.e.m.) are visualized and injection time is indicated as zero. ***p <0.001,**p <0.01, *p <0.05.

No difference were detected with the paradigm 2; the signal change obtained acquiring continuously the 1.2 ppm offset present similar trend between the two groups (Figure 46).

The dosage of 1g/kg of 2DG was not well tolerated. Respiration rate struggled to get back to a normal condition and mice remained unresponsive for many hours after the 2DG injection. The respiration rate of one of these mice collapsed during the experiment causing its death and the same happened to other two mice that died in the following days; the data belonging to these mice were discarded. Mice that received the 0.5g/kg dose were, on the other hand, able to recover completely within an hour after the end of the experiment and they were responsive to external stimulation after few minutes. Since the statistical analysis did not show differences between the two dosage and since mice did not suffer a dose of 0.5 g/kg we decided to adopt it for the following experiments.

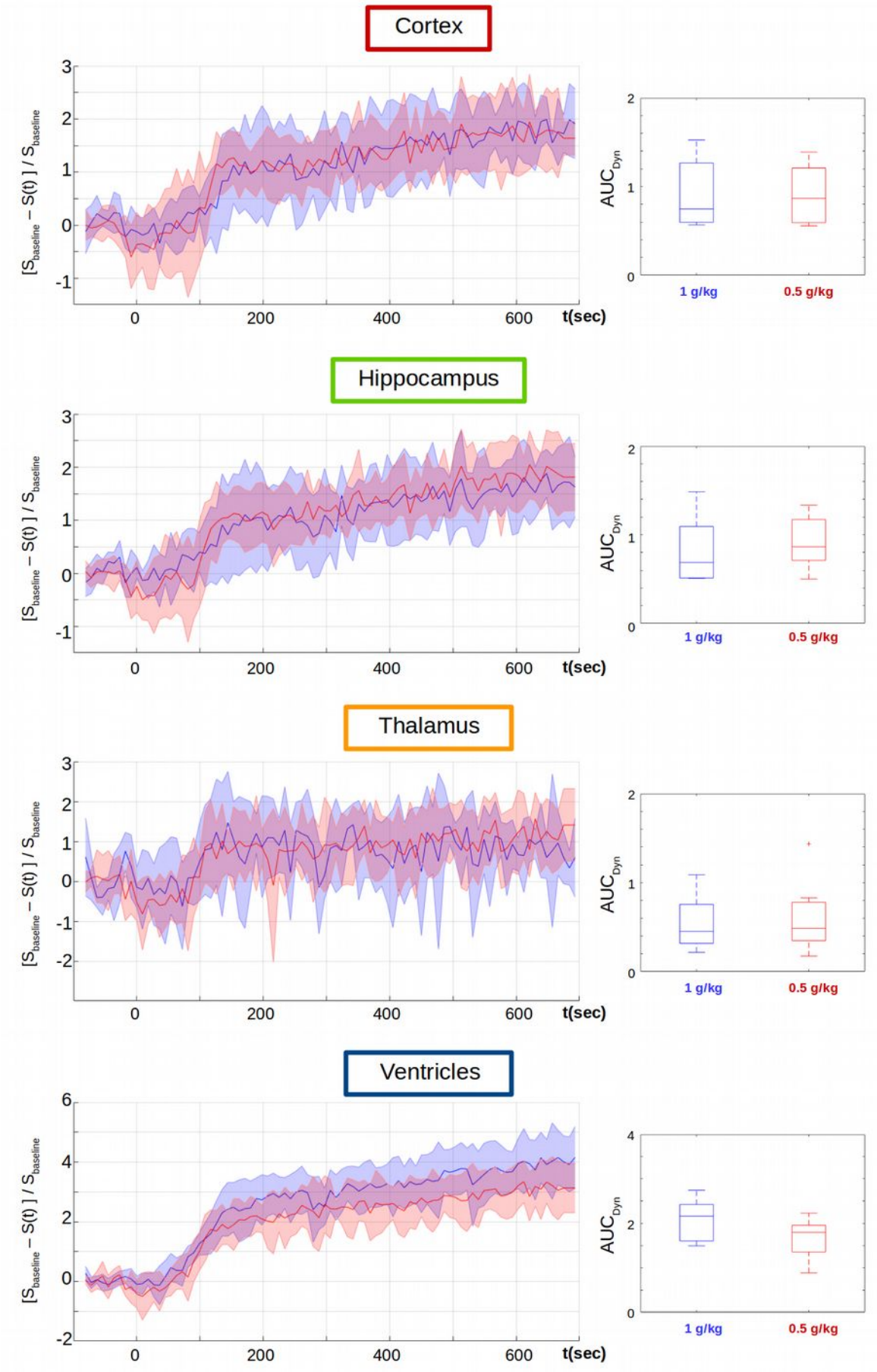

Figure 46: DynamicCEST measurements. Group mean dynamic curves and AUC_{Dyn} obtained by averaging the signal in the each hippocampus, thalamus and ventricles.

3.1.3 – Detection of the 2DG cerebral uptake in the APP23 mice

A 20-months age group of APP23 mice (N=7) and wild-type littermates were analyzed with an injected dose of 0.5 g/Kg of 2DG. The animals were randomized and scanned over a period of eight days. All mice fully recovered few minutes after the end of the anesthesia.

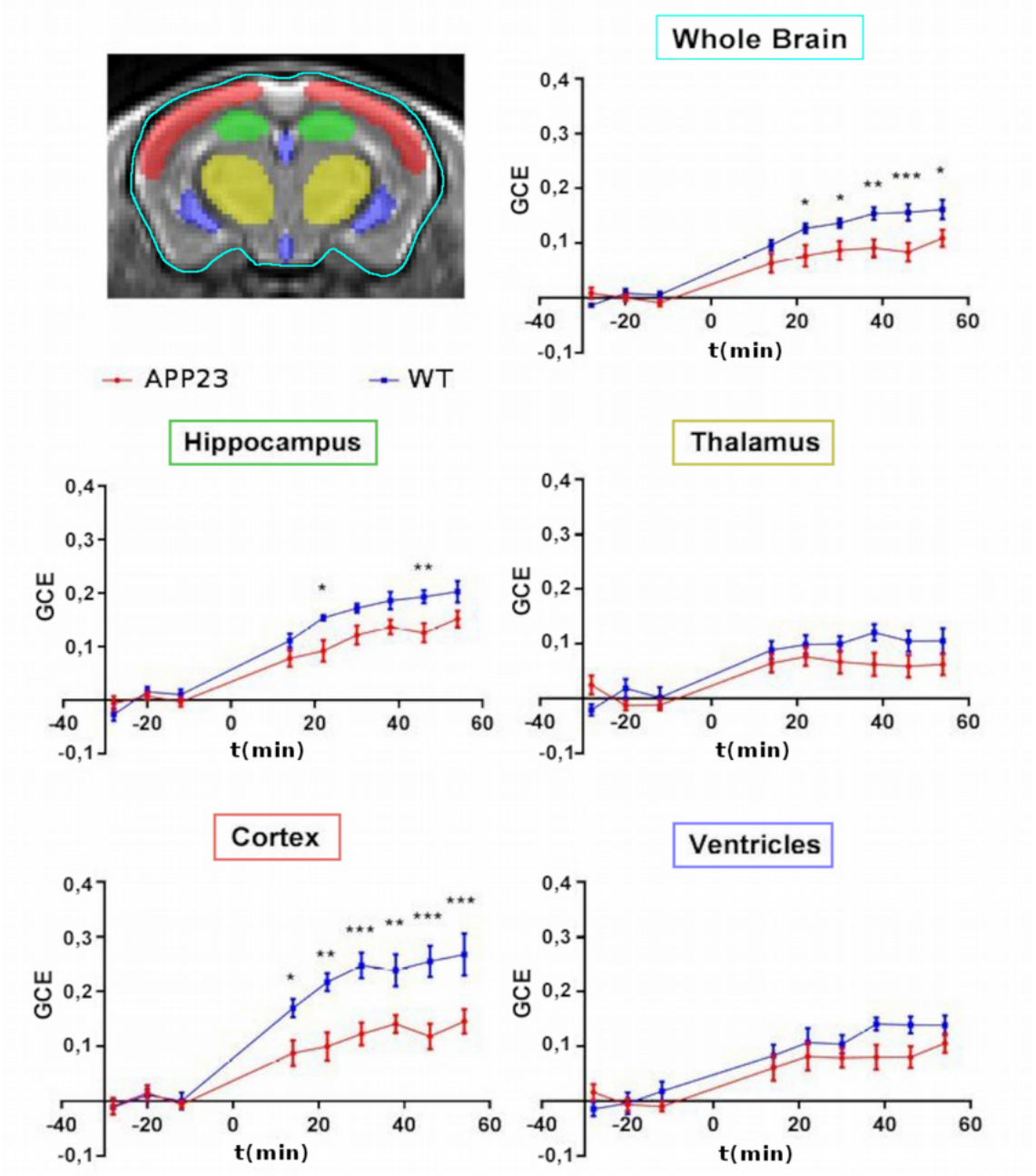

Figure 47: Temporal GCE. Group mean ± standard errors (s.e.m.) are visualized and injection time is indicated as zero. ***p <0.001,**p <0.01, *p <0.05.

The two-way ANOVA followed by the Hochberg correction was computed considering all time-points (Figure 47). A significant decrease of the brain 2DG uptake was detected in APP23 mice. When the GCE was averaged all over the whole brain mask, statistical analysis indicated a significant effect of genotype ($F=35$, $p= 3.9\times10^{-8}$), a significant effect of time ($F=41.44$, $p<2.2\times10^{-16}$) and a significant interaction genotype×time ($F=2.8$, $p=0.007$). Similarly, in the cortex, the analysis shows a significant effect of genotype ($F=56.46$, $p=1.77\times10^{-11}$), a significant effect of time ($F=36.1$, $p<2.2\times10^{-16}$) and a significant interaction genotype×time ($F=3.8$, $p=0.0006$). In the hippocampus time and genotype effects were also significantly different (respectively $F=61.5$, $p<2.2\times10^{-16}$ and $F=28.67$, $p=4.9\times10^{-7}$) as was the interaction genotype×time ($F=2.25$, $p=0.03$). In the thalamus and ventricles the single effects were significant but not the interaction genotype×time.

All the co-registered images representing the GCE were averaged at different time-points (Figure 58) enabling a visual comparison of the 2DG accumulation between wild-type and transgenic mice.

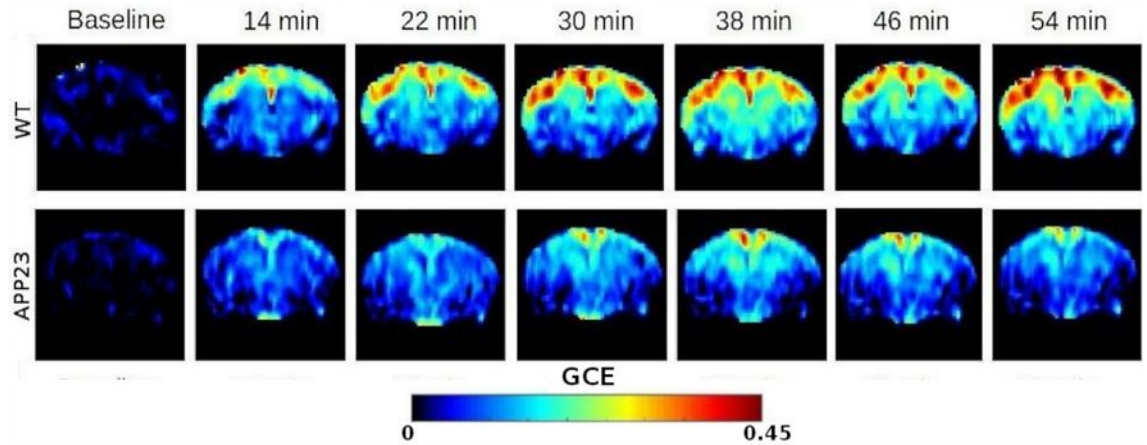

Figure 48: Graphic representation of the GCE time course. Each frame was obtained averaging all the images of each timepoint. Baseline shown is the mean of the first three time points.

Since the analysis shown in Figure 47 revealed a significant difference between the two groups, we ran a voxel-wise student's t test comparing the GCE images acquired 54

minutes after injection using randomise (Winkler et al., 2014) embedded in the FSL software library (Jenkinson et al., 2012). The cortex area of wild-type mice shows significantly greater CEST asymmetry than the APP23 transgenic mice (Figure 49). Similarly, a difference was seen in the thalamus area, but does not appear in the ROI analysis where all the time points were considered.

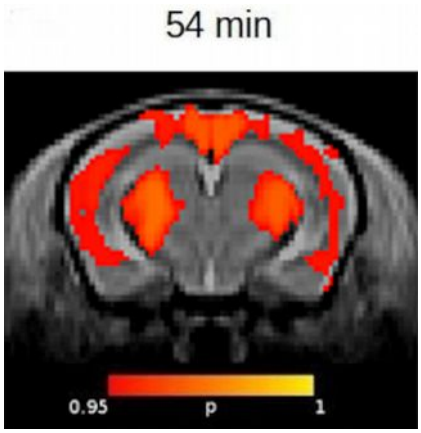

Figure 49: Voxel wise comparison. T-test on the normalized images representing the GCE 54 minutes after 2DG injection. In red the areas where WT >APP23 with $p < 0.05$.

The analysis of the continuous single offset acquisition by DynamicCEST, shown in Figure 50, revealed a non significant decrease of the AUC_{Dyn} in the cortex of APP23 mice.

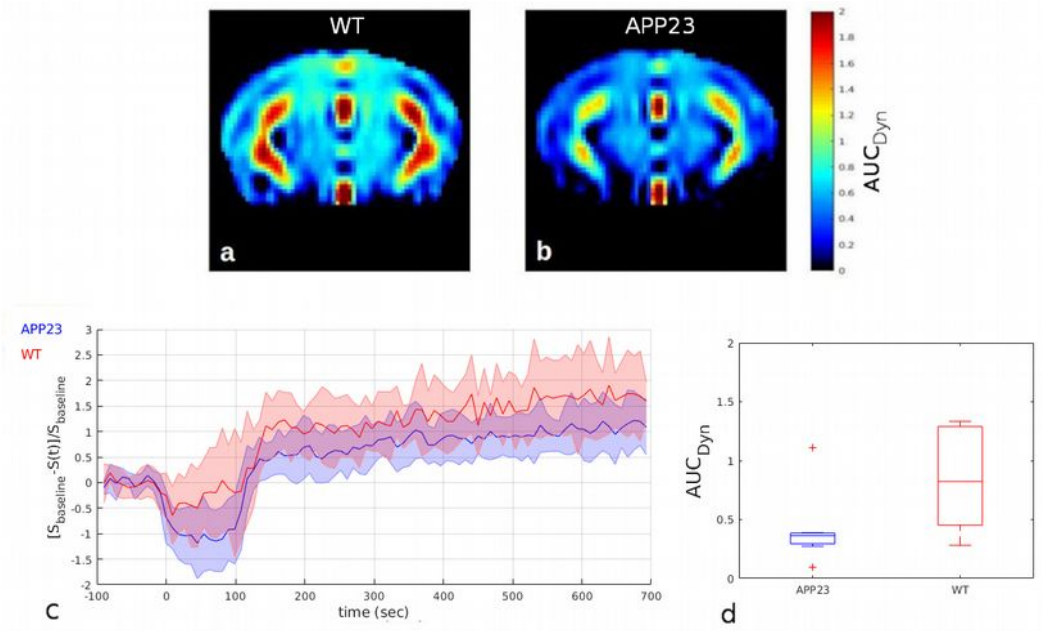

Figure 50: DynamicCEST measurements. (a,b) Group mean AUC_{Dyn} images normalized to the template. (c) group mean dynamic curves obtained by averaging the signal in the cortex. (d) AUC Dyn calculated in the cortex area.

3.1.4 – Longitudinal study of the 2DG cerebral uptake in the APP23 mice

A group of APP23 mice (N=9) and wild-type litter-mates were followed longitudinally at three different ages (6, 12 and 20 months). Three APP23 mice and one WT mouse died around 10 months of age and two more WT mice died before the last acquisition. However, although I cannot exclude that the injection resulted toxic with a longitudinal 2DG treatment, mice died a certain amount of time after the injection likely due to external causes probably related to the aging process.

In order to perform a statistical analysis that include the age as a factor, the area under the GCE curve was computed as the sum of all time points (for each mouse and each ROI):

$$AUC_{GCE} = \sum_{t=0}^{54\,min} GCE(t) \quad [18]$$

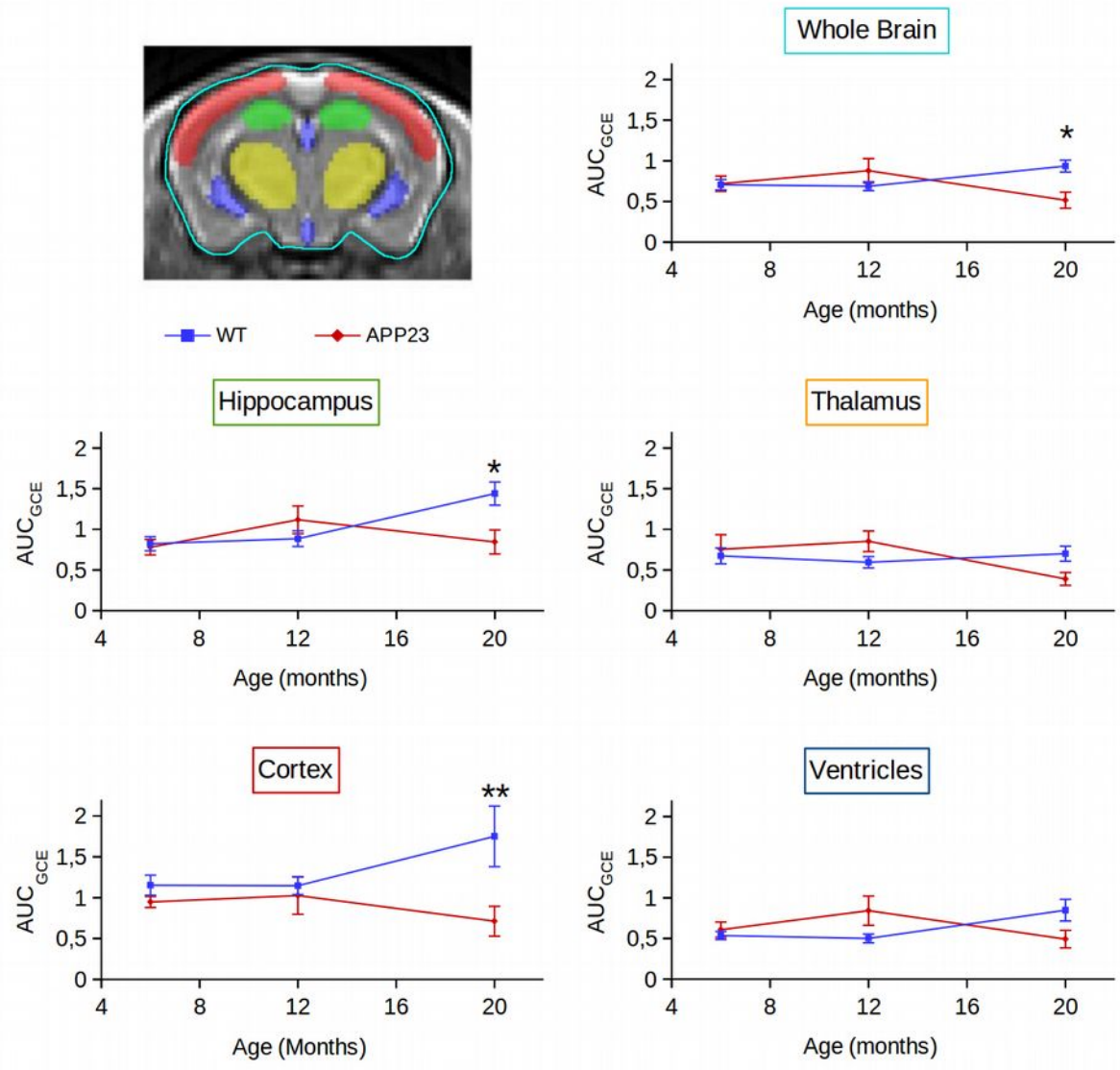

Figure 51: Temporal AUC_{GCE}. Group mean ± standard errors (s.e.m.) are visualized. ***p <0.001,**p <0.01, *p <0.05.

Shown in Figure 51, the two-way ANOVA, followed by a post-hoc Hocberg correction, shows that when the whole brain region is considered a significant interaction between the genotype and age is present ($F= 5.04$, $p < 0.05$) but no significant effect of age and genotype. As shown in Figure 51, in the cortex region a significant interaction between the genotype and age is present ($F= 3.87$, $p < 0.05$) and a significant effect of genotype ($F = 7.897$, $p = 0.008$) but not significant effect of age. In the hippocampal region a significant interaction between the genotype and age ($F= 5.39$, $p < 0.01$) and a significant

effect of age (F = 3.65, p = 0.03) but not significant effect of genotype. In the thalamus and ventricles no significant differences were detectable.

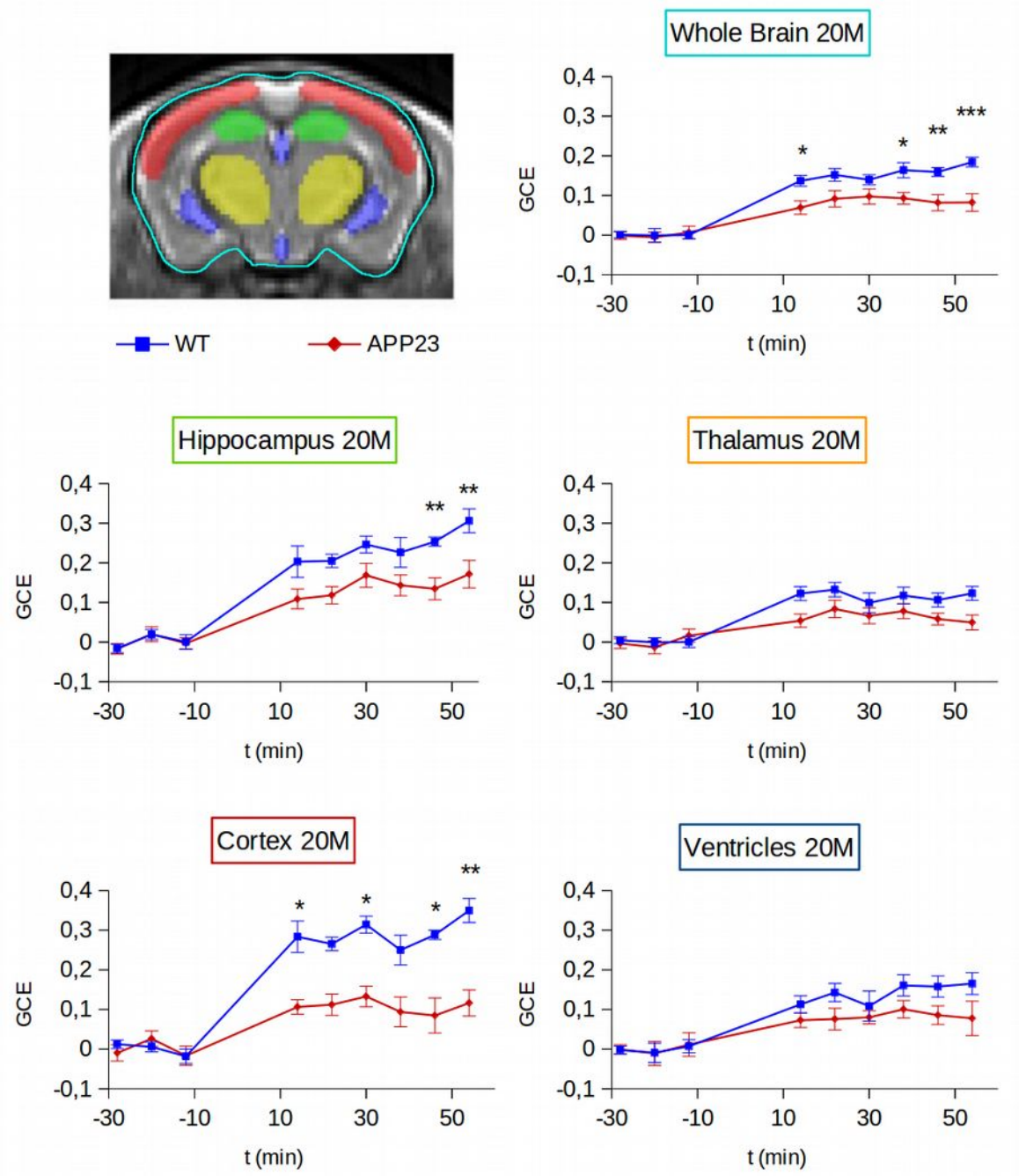

Figure 52: Temporal GCE. Group mean ± standard errors (s.e.m.) are visualized and injection time is indicated as zero. ***p <0.001,**p <0.01, *p <0.05.

Since no differences could be detected at 6 and 12 months of age, I present the GCE curves at 20 months of age (Figure 52) showing a similar trend to the one obtained in the previous experiment (Figure 47). The two-way ANOVA, followed by a post-hoc Hocberg

correction, shows a significant effect of genotype ($F=37.31$, $p=3.3\times10^{-8}$) and a significant effect of time ($F=27.10$, $p<2.2\times10^{-16}$) but also an interaction between the genotype and time was present ($F=2.81$, $p<0.008$) when the GCE is averaged in the whole brain region. In the cortex region a significant effect of genotype ($F=35.8$, $p=5.7\times10^{-8}$) and a significant effect of time ($F=10.17$, $p=1\times10^{-9}$) but also an interaction between the genotype and time was present ($F= 2.41$, $p=0.02$). In the hippocampal region a significant effect of genotype ($F=32.1$, $p=2.2\times10^{-7}$) and a significant effect of time ($F=30.58$, $p < 2.2\times10^{-16}$) but also an interaction between the genotype and time ($F=2.26$, $p=0.03$). In the thalamus and ventricles no significant interaction between the genotype and time was detectable

The two-way ANOVA analysis of the area under the curve of the continuous single offset acquisition (paradigm 2) by DynamicCEST, did not show significant differences in all the region of interests considered (Figure 53).

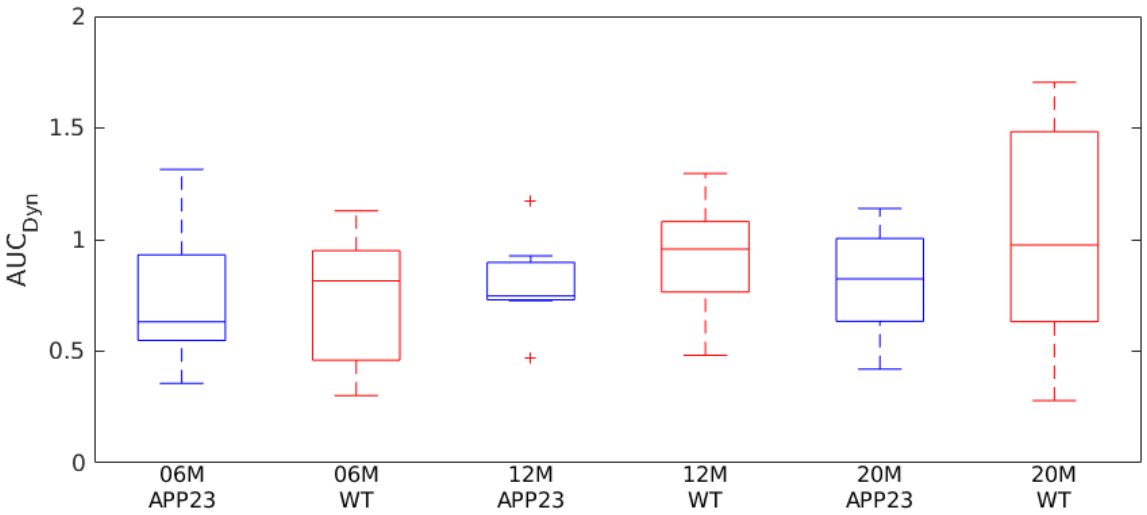

Figure 53: Longitidunal results of the dynamicCEST measurements in the cortex region.

3.1.5 – Summary (1)

In this section, an MRI method able to detect pathological alteration of the brain glucose uptake has been developed. The adopted workflow enabled the detection of an increase of CEST asymmetry after the injection of a 2DG bolus with two different doses (0.5g/kg and 1 g/kg). Since no significant difference in the 2DG-CEST asymmetry was detected, the lower doses was adopted in the following in vivo studies. Experiments in APP23 transgenic mice revealed a significantly decreased uptake of 2DG in the cortex of transgenic mice when compared to wild-type litter-mates. However, this difference was seen only in a late stage of the pathology (20 months of age). Similar results have been described in a longitudinal study showing impaired 2DG uptake in 20 months of age APP23 when compared to WT mice but no significant differences at 6 and 12 months of ages. Contrary to the observed metabolism in healthy aged human, that exhibited focal decreases in brain activity (particularly in the medial network) as a function of normal aging (Pardo et al., 2007), our longitudinal CEST study revealed an increase of the 2DG uptake in elderly WT mice. This age-dependent hyper-metabolism has been observed in different [^{18}F]FDG-PET studies (de Cristóbal et al., 2014; Waldron et al., 2015c; Takkinen et al., 2016; Matthias Brendel et al., 2016) and related to an age-dependent neuroinflammation (Brendel et al., 2017).

No significant differences between APP23 and WT mice were detectable with the Dymanic-CEST method. Only a slight decrease was seen in the cortex of APP23 mice that could be driven by a reduction of CBF. This impairment has already been described in APP23 mice in a late stage of the pathology (Maier et al., 2014). This may indicate that the dynamic acquisition of CEST images at the saturation frequency of hydroxyl protons is not the best method to measure CBF within the context of the neurodegenerative diseases. Previous studies describing dynamicCEST acquisitions were made in tumor

lesions where the massive blood volume and glucose consumption compared to healthy brain makes this technique feasible.

To understand the importance of the results obtained, a visual comparison between the [^{18}F]FDG-PET and the 2DG-CEST images, developed within this project, is shown in Figure 54. It's evident that image representing the enhancement of the CEST signal after the 2DG injection (Figure 54b) is acquired with a better in-plane resolution (equal to 0.35 × 0.35 mm^2) than the acquired PET image (Figure 54a). Although both techniques are characterized by an intrinsic variability, PET is characterized by a modest resolution of 0.8 × 0.8 mm^2 (Kuntner and Stout, 2014). This limit makes a reliable differentiation between small regions of the mouse brain challenging with images acquired with the PET technique.

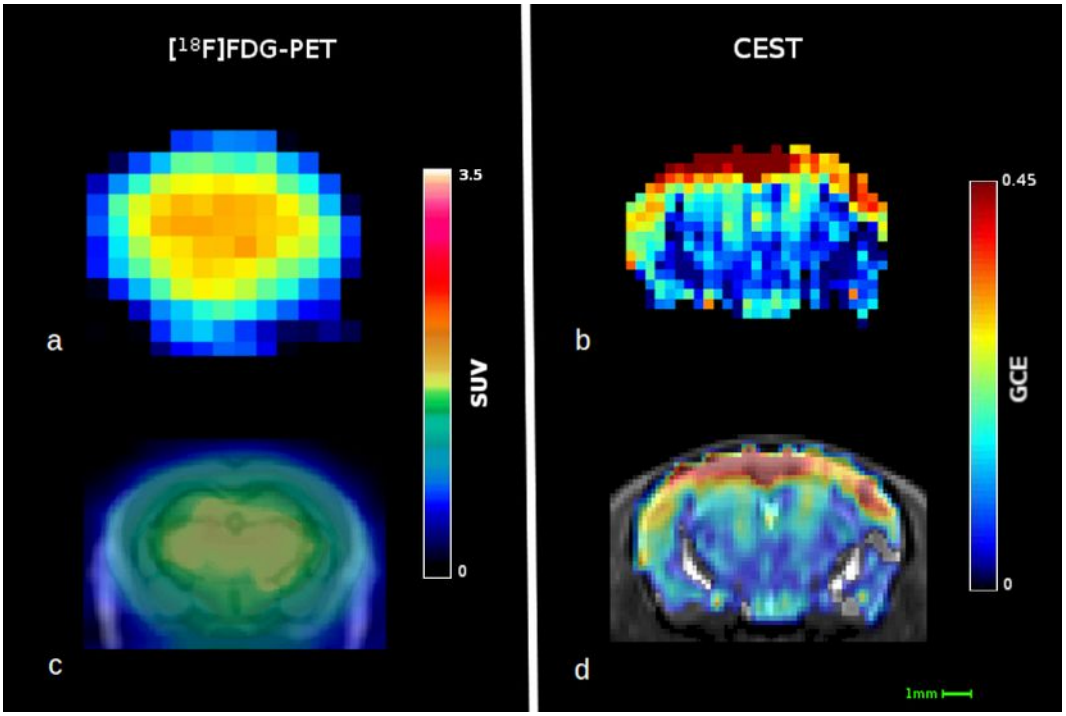

Figure 54: Visual comparison of the two techniques. a) Single WT mouse PET imagerepresenting ^{18}F-FDG uptake 50-60 minutes after injection with a voxel size of 0.78 × 0.78 × 0.8mm^3; b) image representing the GCE of a single mouse 1 hour after the 2DG injection, it has a voxel size of 0.35 × 0.35 × 2 mm^3; c) PET image coregistered with computed tomography image and superimposed on a general mouse brain MRI template; d) GCE image coregistered and superimposed on the in-house template. SUV = standard uptake value; GCE = glucose cest enhancement. (Tolomeo et al., 2018)

Even if, due to the methodological differences, it is difficult to directly compare the regional distribution observed with the two techniques it is evident that the 2DG-CEST technique have a great potential since it does not require the use of radioactive tracers and it could be further optimized by extending the acquisition time or using coils with higher signal to noise ratio.

We cannot exclude that the different detected glucose distribution between the two techniques could be due to the rather high doses of 2DG needed by CEST, whereas PET utilizes non-pharmacological tracer doses. However, the pattern of accumulation observed with CEST could be compared more in detail with those given by [^{14}C]-2DG or [^{18}F]FDG autoradiography (Lundgaard et al., 2015; Waldron et al., 2015b) or those obtained by [^{18}F]FDG-PET in rats, whose larger brains allows the easier differentiation of accumulation patterns in different brain regions (Zimmer et al., 2014).

3.2 – Brain structural alterations of Alzheimer's disease mouse models

This section focuses on the development and on the application of a panel of MRI techniques to characterize brain structural pathological changes in transgenic mouse models of neurodegeneration. To improve the translational impact of the reported studies, these techniques were directly adapted from human MRI analysis procedures and are aimed to:

- Investigate alterations in GM morphology. Two different approaches were adopted; 1) A multi-atlas parcellation procedure which is an automated workflow able to measure the volume different brain regions. 2) A voxel based morphology (VBM) approach that is able to measure differences in local concentrations of brain tissue, through a voxel-wise comparison of multiple brain images.
- To investigate WM integrity. By means of DTI measurements and an analysis workflow called "tract based spatial statistic" (TBSS) which is developed to compare automatically WM tracts of multiple images.
- To investigate alterations in the brain tissue composition. With the measurement of the T2 relaxation time.

3.2.1 – Brain structural parcellation method

Different studies have reported automatic brain segmentation methods able to warp a single reference brain atlas into the space of an acquired brain enabling the evaluation of brain regions volume without the need of manual tracing (Ma et al., 2008; Redwine et al., 2003). However, it has been shown that a multi-atlas approach, that take advantage of the use of different reference atlases, has a better segmentation accuracy compared to single-atlas based segmentation (Bai et al., 2012; Ma et al., 2014; Nie and Shen, 2013).

Methods described within this section can be separated into two subsequent steps:

- The creation of an in-house set of mouse brain atlases, to further improve the efficacy the segmentation method.
- The development of the multi-atlas segmentation procedure and a tested on a dataset of images that was manually analyzed in the frame of a previous project.

Brain atlases creation. A set of high-resolution (83 × 83 × 83 μm^3) T2-weighted brain images was acquired using ten wild-type mice to be used as the reference in the following studies. To obtain the brain anatomical segmentation of each one of these images was processed following different steps (Figure 56):

- Since the use of the surface coil leads to an artifact that present a signal intensity that decrease smoothly along the coronal direction across the image, an intensity non-uniformity algorithm, with the N4BiasFieldCorrection tool (Tustison et al., 2010), was firstly applied (Figure 55).

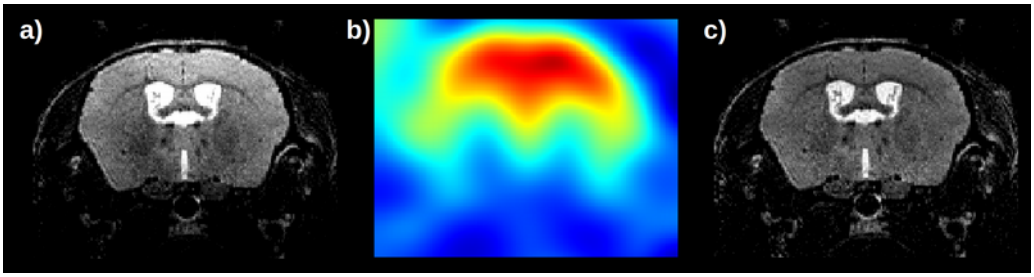

Figure 55: Illustrative image showing the result of the bias field correction. (a) The original subject image which is characterized by higher intensity on the upper part of the brain. (b) The estimated bias field and (c) resulted corrected image.

- Corrected images were subsequently averaged, with the buildtemplateparrallel.sh script (Avants et al., 2011a), to create a preliminary template including all the tissues.

- This template was normalized to an existing ex-vivo template (Dorr et al., 2008), with the antsIntroduction.sh script (Klein et al., 2009), obtaining a brain mask.
- This mask was back-projected to the original set of images allowed the brain extraction.
- The intensity non-uniformity correction was newly computed on the brain extracted images to improve it’s efficacy (Pagani et al., 2016).
- Extracted brains were newly averaged to obtain an in-vivo skull stripped brain template. To improve segmentation accuracy, this template was newly normalized to the ex-vivo template and the ex-vivo atlas back-projected to the in-vivo brains. These in-vivo atlases were manually slightly modified in order to correct mistakes that are due to the differences between the in-vivo average template and the ex-vivo reference template, which present a different intensity range and local deformations due to the perfusion of the brains used to create it.

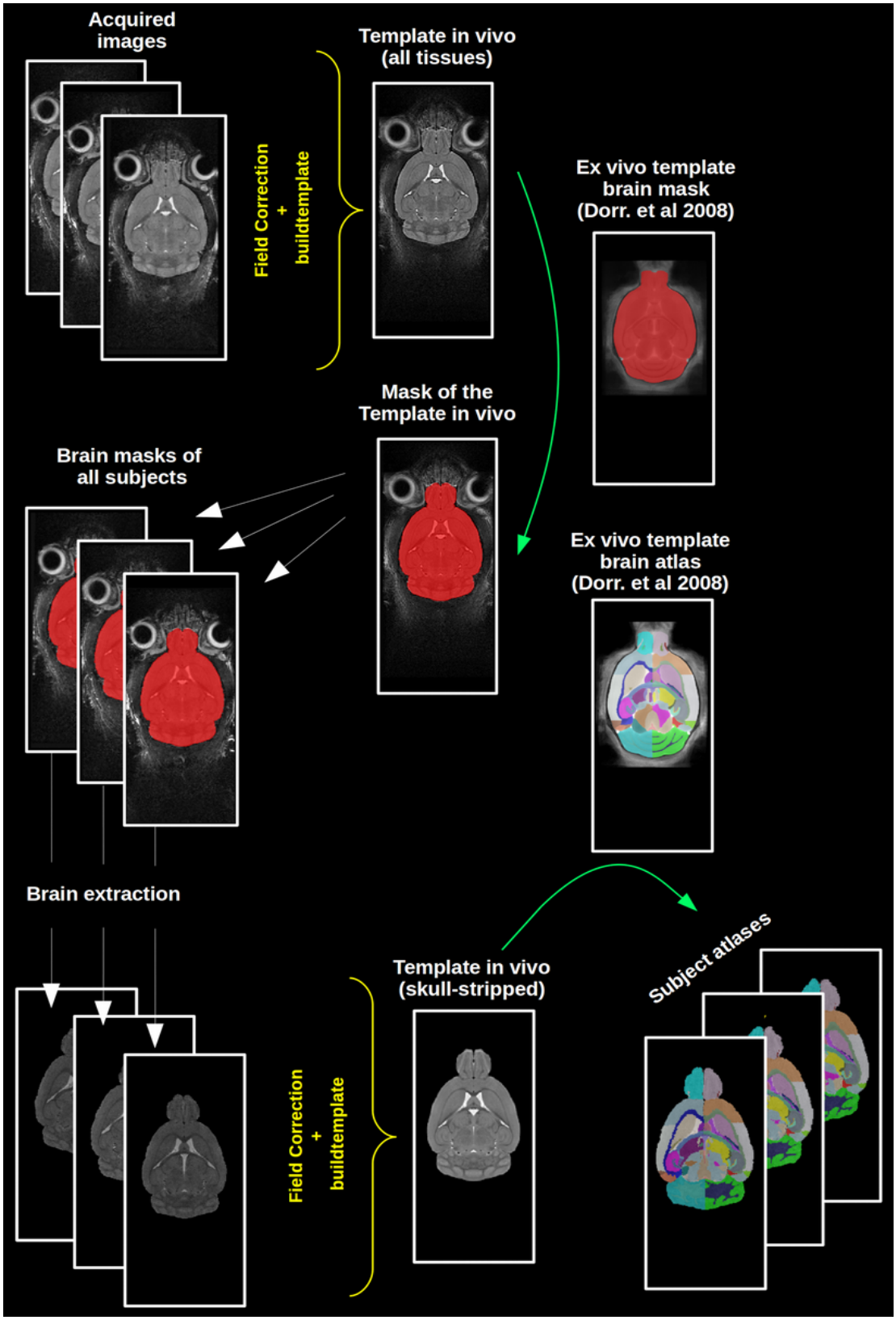

Figure 56: Workflow followed to create the in house atlases. Acquired images are corrected and averaged to create an in house Template. This is normalized over an ex vivo template and masked. The template mask is projected to the reference images that are subsequently masked and averaged to create an in-house skull stripped template. This brain template is again normalized over the ex-vivo template and reference atlases obtained back-projecting the ex-vivo atlas.

Multi-atlas segmentation. All the anatomical brain images acquired in the longitudinal study were preprocessed by correcting the non-uniform bias field and parcellated following the steps (Figure 57):

1. Each subject was warped to the full template and the template mask was back-projected to the subject space obtaining the subject mask and therefore the brain extraction.
2. A multi-atlas segmentation approach, using the antsJointLabelFusion.sh script (Wang et al., 2013) embedded in the ANTs software (Avants et al., 2014) have been used to warp the ten brains templates to the subject brain
3. The reference atlases were back-projected to the subject space and fused together to create the anatomical parcellation.

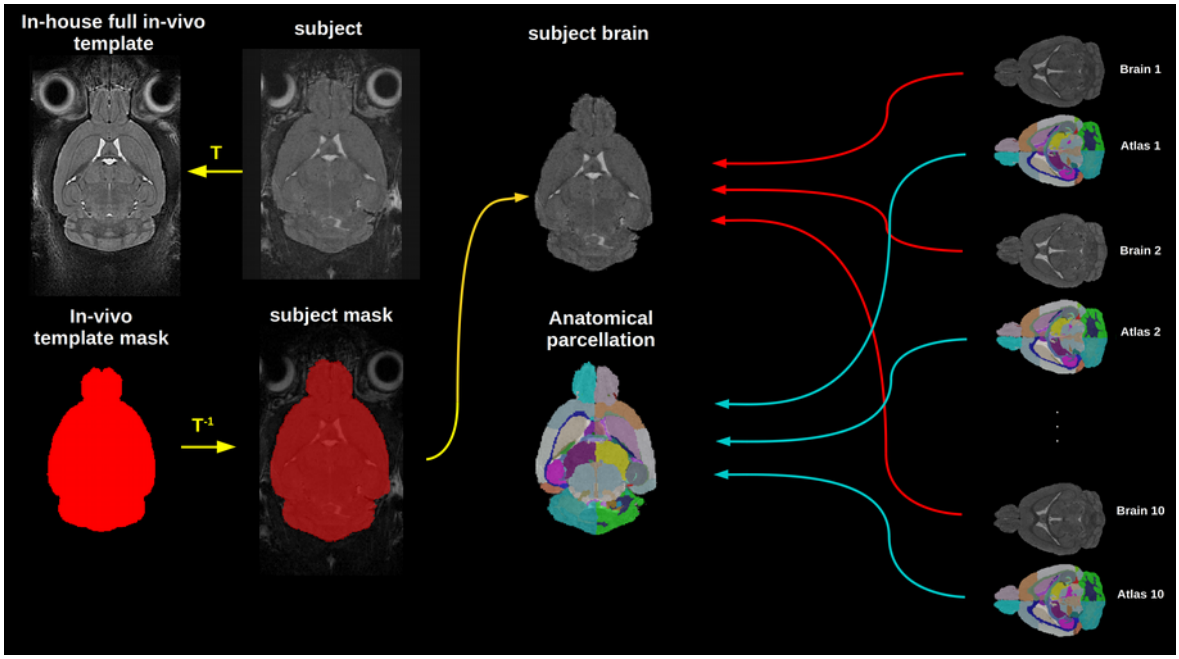

Figure 57: Automatic parcellation procedure. Firstly the brain extraction is performed (yellow arrows). Subsequently the normalization of the reference images to the subject brain (red arrows) allowed the projection and the fusion of all the reference atlases to the subject space (blue arrows).

Accuracy test. A preliminary test was carried out to segment a dataset of anatomical brain images that was manually segmented within the frame of a previous project. These brain images were acquired on a group of aged (24 months) APP/PS2/Tau mice which have a mutation on the tau gene (P301L) besides APP_{swe} and PS2(M141I) mutations (Rhein et al., 2009). Manual segmentation revealed an age-dependent hippocampal and entorhinal cortex atrophy in APP/PS2/Tau mice when compared with WT (Micotti et al., 2015).

A comparison between the volumes obtained manually with the ones obtained with the automated parcellation procedure showing a high correlation. Notably, both methods were able to distinguish between WT and APP/PS2/Tau mice (Figure 58) suggesting that the automated parcellation method here described is able to give reliable results.

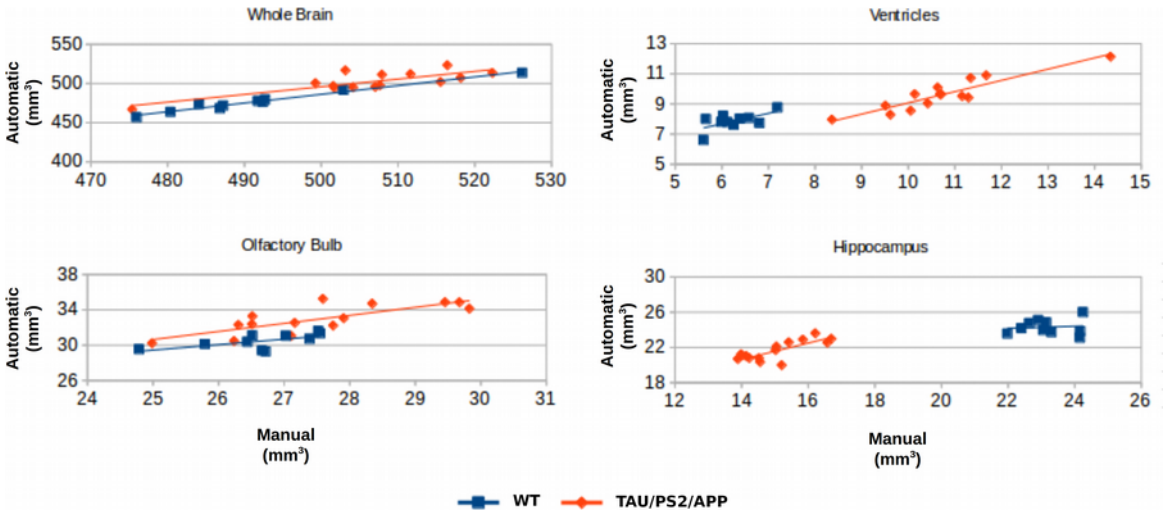

Figure 58: Volumes of different regions obtained with the automatic parcellation method and with the manual tracing shows high correlation.

3.2.2 – Longitudinal brain structural parcellation of the APP23 mice

Once established that the automated method is robust, it was applied to the analysis of the APP23 bran images that were acquired longitudinally within the frame of this project.

	WT								APP23							
	5M		12M		20M		24M		5M		12M		20M		24M	
	Mean ± s.e.m		Mean ± s.e.m		Mean ± s.e.m		Mean ± s.e.m		Mean ± s.e.m		Mean ± s.e.m		Mean ± s.e.m		Mean ± s.e.m	
amygdala	13,47	0,07	13,76	0,13	13,91	0,12	14,04	0,17	14,11	0,30	14,30	0,13	14,42	0,19	14,64	0,24
anterior commissure: pars anterior	1,50	0,03	1,48	0,03	1,54	0,02	1,76	0,05	1,48	0,01	1,53	0,02	1,66	0,02	1,64	0,04
anterior commissure: pars posterior	0,44	0,01	0,39	0,01	0,42	0,01	0,46	0,01	0,38	0,01	0,38	0,02	0,42	0,02	0,43	0,01
arbor vita of cerebellum	10,62	0,07	10,99	0,11	11,12	0,11	11,56	0,20	10,40	0,11	11,19	0,12	11,27	0,19	11,22	0,12
basal forebrain	4,26	0,05	4,68	0,04	4,86	0,04	4,80	0,09	4,41	0,08	4,80	0,07	4,93	0,08	4,75	0,06
bed nucleus of stria terminalis	1,33	0,03	1,38	0,01	1,40	0,01	1,44	0,03	1,35	0,03	1,45	0,03	1,45	0,03	1,42	0,04
cerebellar cortex	45,04	0,40	45,73	0,44	45,66	0,44	44,45	0,82	45,52	0,51	46,80	0,67	46,91	1,02	45,40	0,56
cerebellar peduncle: inferior	0,72	0,02	0,77	0,02	0,80	0,01	0,72	0,02	0,73	0,01	0,83	0,03	0,83	0,03	0,82	0,03
cerebellar peduncle: middle	1,13	0,02	1,18	0,04	1,27	0,03	1,28	0,04	1,11	0,02	1,20	0,02	1,26	0,04	1,25	0,03
cerebellar peduncle: superior	0,42	0,02	0,65	0,02	0,73	0,02	0,62	0,05	0,41	0,01	0,66	0,02	0,73	0,02	0,73	0,05
cerebral cortex: entorhinal cortex	10,82	0,09	10,81	0,11	10,85	0,12	10,83	0,19	11,39	0,26	11,43	0,14	11,45	0,23	10,95	0,17
cerebral cortex: frontal lobe	40,74	0,29	40,91	0,38	40,57	0,38	40,38	0,74	42,73	0,58	42,31	0,55	43,11	0,84	43,15	0,70
cerebral cortex: occipital lobe	6,39	0,07	6,27	0,13	6,01	0,11	6,21	0,10	6,66	0,13	6,34	0,11	6,18	0,15	6,39	0,11
cerebral cortex: parieto-temporal lobe	70,79	0,64	71,42	0,77	70,98	0,65	70,96	1,05	73,17	1,00	73,40	1,21	73,82	1,60	73,72	1,28
cerebral peduncle	2,18	0,04	2,32	0,04	2,52	0,06	2,67	0,06	2,18	0,03	2,32	0,06	2,54	0,07	2,49	0,03
colliculus: inferior	5,83	0,05	6,02	0,05	6,04	0,05	6,20	0,09	5,89	0,07	6,23	0,09	6,28	0,08	6,16	0,08
colliculus: superior	9,36	0,14	9,74	0,15	9,91	0,15	10,48	0,16	9,60	0,07	10,18	0,11	10,21	0,17	10,18	0,14
corpus callosum	19,63	0,17	18,59	0,23	19,10	0,17	22,32	0,37	19,09	0,24	18,74	0,39	19,42	0,43	20,53	0,51
corticospinal tract/pyramids	2,53	0,05	2,83	0,09	2,89	0,08	3,01	0,15	2,56	0,11	2,67	0,07	2,71	0,11	2,90	0,13
cuneate nucleus	0,12	0,01	0,13	0,01	0,14	0,01	0,15	0,01	0,13	0,01	0,12	0,01	0,13	0,01	0,15	0,01
dentate gyrus of hippocampus	2,61	0,05	2,67	0,07	2,90	0,02	2,80	0,07	2,68	0,07	2,78	0,06	2,87	0,11	2,83	0,10
facial nerve (cranial nerve 7)	0,04	0,00	0,04	0,01	0,04	0,00	0,05	0,01	0,04	0,00	0,05	0,00	0,07	0,01	0,06	0,01
fasciculus retroflexus	0,23	0,00	0,28	0,01	0,29	0,00	0,32	0,01	0,23	0,00	0,28	0,01	0,31	0,01	0,31	0,01
fimbria	3,64	0,04	3,76	0,05	3,90	0,06	4,13	0,11	3,42	0,04	3,76	0,06	3,88	0,07	3,85	0,12
fornix	0,57	0,01	0,62	0,01	0,68	0,01	0,68	0,02	0,55	0,01	0,65	0,01	0,67	0,01	0,65	0,02
fundus of striatum	0,07	0,00	0,06	0,00	0,07	0,01	0,09	0,00	0,07	0,01	0,07	0,00	0,08	0,01	0,09	0,00
globus pallidus	2,95	0,02	3,12	0,03	3,36	0,02	3,63	0,05	2,95	0,03	3,12	0,04	3,40	0,05	3,52	0,05
hippocampus	20,18	0,16	21,25	0,17	21,14	0,17	21,60	0,30	20,70	0,52	21,76	0,45	21,67	0,46	21,91	0,38
hypothalamus	11,07	0,06	11,76	0,05	12,12	0,13	12,15	0,23	11,23	0,09	12,17	0,06	12,43	0,09	11,85	0,18
inferior olivary complex	0,42	0,02	0,49	0,02	0,50	0,03	0,43	0,02	0,34	0,03	0,41	0,02	0,41	0,02	0,38	0,03
internal capsule	2,06	0,01	2,09	0,02	2,24	0,02	2,39	0,04	2,09	0,02	2,18	0,03	2,26	0,05	2,38	0,05
lateral olfactory tract	1,31	0,02	1,32	0,03	1,38	0,02	1,44	0,03	1,37	0,02	1,41	0,01	1,45	0,02	1,47	0,03
lateral septum	3,14	0,02	3,22	0,02	3,22	0,02	3,23	0,06	3,26	0,05	3,38	0,02	3,34	0,03	3,31	0,07
lateral ventricle	5,81	0,35	6,25	0,37	6,27	0,41	5,85	0,34	4,51	0,17	5,39	0,23	5,26	0,22	5,04	0,32
mammillary bodies	0,73	0,01	0,72	0,02	0,77	0,05	0,77	0,03	0,72	0,02	0,73	0,02	0,76	0,04	0,72	0,05
mammilothalamic tract	0,16	0,01	0,16	0,01	0,20	0,00	0,20	0,01	0,18	0,01	0,16	0,01	0,20	0,01	0,20	0,01
medial longitudinal fasciculus	1,82	0,06	1,73	0,07	1,81	0,06	2,04	0,09	1,90	0,08	1,68	0,06	1,71	0,10	2,04	0,07
medial septum	1,13	0,02	1,23	0,01	1,24	0,02	1,19	0,03	1,16	0,02	1,25	0,01	1,30	0,04	1,25	0,04
nucleus accumbens	3,49	0,04	3,49	0,04	3,54	0,04	3,52	0,06	3,54	0,06	3,56	0,05	3,66	0,08	3,51	0,07
olfactory bulbs	30,32	0,33	31,48	0,39	32,03	0,35	33,04	0,43	30,45	0,22	32,18	0,42	32,85	0,54	32,39	0,61
olfactory tubercle	4,23	0,03	4,09	0,04	4,04	0,04	4,30	0,08	4,21	0,05	4,04	0,07	4,13	0,09	4,22	0,06
optic tract	1,51	0,05	1,53	0,04	1,60	0,05	1,79	0,03	1,59	0,02	1,60	0,03	1,69	0,03	1,70	0,05
pontine nucleus	1,24	0,03	1,28	0,04	1,47	0,09	1,47	0,07	1,23	0,03	1,33	0,03	1,43	0,06	1,33	0,04
pre-para subiculum	1,67	0,04	1,66	0,03	1,72	0,03	1,96	0,08	1,86	0,03	1,78	0,04	1,79	0,07	1,86	0,04
stratum granulosum of hippocampus	0,15	0,01	0,21	0,02	0,26	0,01	0,19	0,02	0,14	0,01	0,19	0,01	0,24	0,02	0,23	0,03
stria medullaris	0,69	0,02	0,69	0,01	0,70	0,01	0,74	0,02	0,68	0,01	0,69	0,02	0,72	0,01	0,70	0,01
stria terminalis	0,66	0,01	0,70	0,01	0,77	0,01	0,82	0,01	0,68	0,01	0,76	0,02	0,79	0,02	0,83	0,02
striatum	20,91	0,22	21,21	0,22	21,40	0,26	20,55	0,39	21,01	0,21	21,66	0,31	22,01	0,43	20,62	0,38
subependymale zone / rhinocele	0,003	0,001	0,005	0,001	0,010	0,002	0,011	0,001	0,002	0,001	0,004	0,001	0,009	0,002	0,008	0,002
superior olivary complex	0,61	0,01	0,69	0,03	0,71	0,03	0,70	0,03	0,63	0,01	0,67	0,03	0,75	0,03	0,75	0,03
thalamus	17,93	0,15	18,51	0,23	19,05	0,23	19,70	0,35	18,27	0,10	19,41	0,22	20,01	0,37	20,22	0,30
periaqueductal grey	4,26	0,06	3,94	0,05	3,96	0,03	4,53	0,07	4,22	0,06	3,99	0,05	3,97	0,03	4,10	0,05
posterior commissure	0,13	0,00	0,12	0,00	0,12	0,00	0,15	0,01	0,12	0,00	0,12	0,01	0,12	0,01	0,12	0,01
fourth ventricle	0,47	0,01	0,46	0,01	0,45	0,02	0,49	0,02	0,44	0,01	0,42	0,01	0,42	0,01	0,41	0,01
cerebral aqueduct	0,35	0,01	0,32	0,02	0,32	0,01	0,44	0,04	0,31	0,01	0,33	0,01	0,32	0,01	0,32	0,02
third ventricle	1,32	0,03	1,34	0,03	1,36	0,03	1,46	0,05	1,25	0,04	1,30	0,03	1,30	0,03	1,28	0,03
ventral tegmental decussation	0,07	0,00	0,07	0,00	0,08	0,00	0,08	0,01	0,08	0,00	0,06	0,00	0,09	0,00	0,10	0,00
interpedunclar nucleus	0,22	0,01	0,25	0,01	0,25	0,01	0,28	0,01	0,20	0,01	0,24	0,01	0,26	0,02	0,27	0,01
medulla	32,95	0,25	34,80	0,42	36,25	0,61	36,98	0,51	31,71	0,39	33,33	0,32	34,67	0,62	35,92	0,45
pons	17,82	0,12	19,20	0,14	19,83	0,16	20,89	0,33	17,57	0,10	19,11	0,19	19,85	0,40	19,87	0,21
midbrain	14,80	0,13	15,55	0,11	15,76	0,13	16,50	0,29	14,39	0,08	15,74	0,18	15,96	0,25	15,71	0,21
Whole brain	461	2	472	3	479	4	488	7	465	4	481	5	489	8	487	6

Figure 59: Volumes of the brain regions.

The statistical analysis did not show a significant interaction between age and genetic background comparing the volumes of the brain region obtained with the automatic parcellation method in the longitudinal study in the APP23 and WT mice (Figure 59).

3.2.3 – Voxel Based Morphometry (VBM)

The small size of mice brain and the low image contrast between GM and WM make the exact estimation of the volume shrinkage difficult. Atrophy sometimes is not present or is not extensive enough to involve the whole structure volume. Thus, automated voxel based methods have been developed to identify small alterations in the volume of GM that may be lost with the volume estimation of the entire regions. The VBM (Ashburner and Friston, 2000) technique was developed to characterize alterations in the GM tissue concentration across human subjects. This approach was also described in the study transgenic mouse models (Pagani et al., 2016).

The analysis pipeline include the following steps:

- A study based template was created (with the buildtemplateparallel.sh script) considering all the extracted brains obtained within the automate parcellation procedure previously described.
- The tissues of the template were then classified, using the Atropos command of the ANTs toolkit (Avants et al., 2011b), into six independent classes that were subsequently merged into three classes defining the WM, the GM and the CSF (Figure 60).

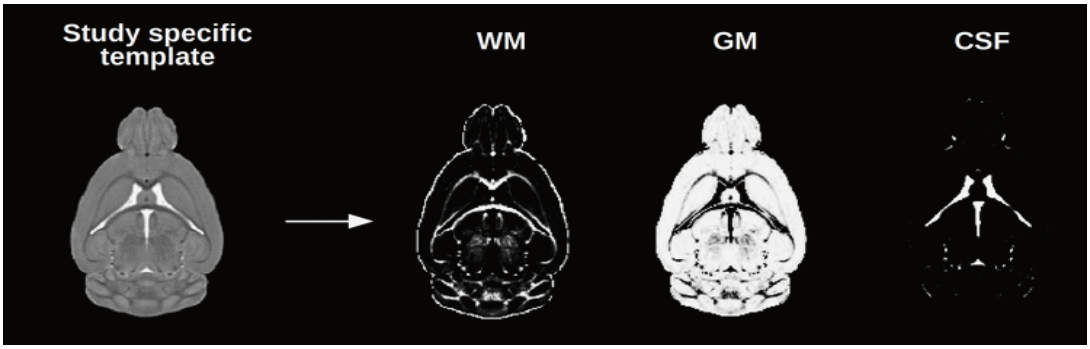

Figure 60: Tissues probability maps of the study specific template.

- Each brain was registered to the study specific template using a diffeomorphic transformation that resulted in a deformation field describing how local structures must be adjusted to match the template (Figure 61). The voxel-wise volume changes can be derived from this deformation field calculating its Jacobian determinant (with ANTSJacobian command) which encodes the local volume difference between the source and target image.

- Individual tissue probability maps were then obtained from the spatially normalized brains using Atropos command and adopting the template tissues classification as starting prior probability images.

- The Jacobian determinant was finally modulated using the subject GM probability map obtained, this step allows the analysis of GM probability maps in terms of local anatomical variation instead of tissue density. More specifically, when a structure of the brain with a certain amount of GM becomes bigger/smaller during normalization it will have larger/shorter local GM values than are truly present. The Jacobian determinants allow the quantification of the difference between true GM and apparent GM.

- The resulting modulated GM probability maps are smoothed using a Gaussian kernel with a sigma of three voxel width (FWHM = 0.64 mm) and employed for voxel-wise statistical comparison.

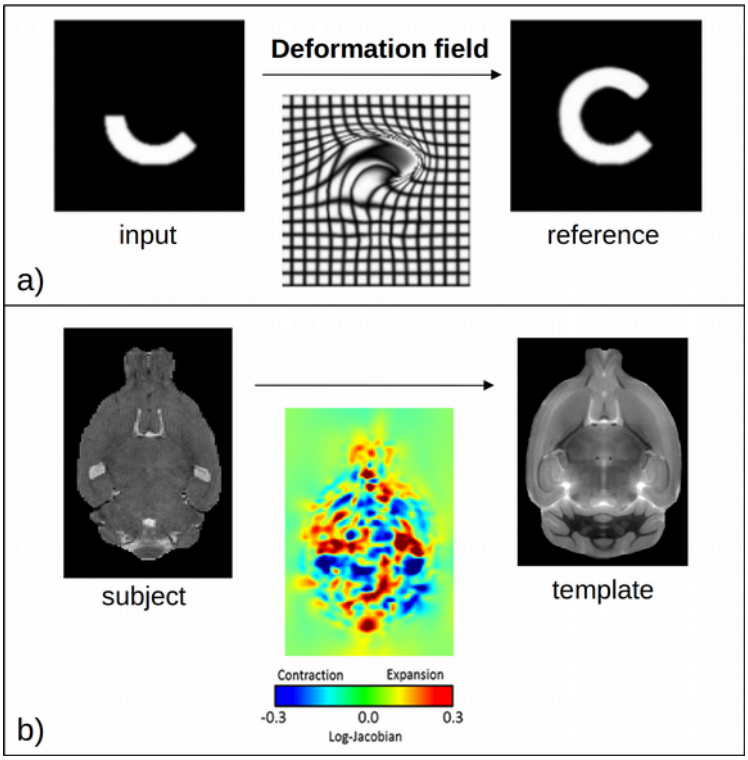

Figure 61: Image normalization. (a) Shows how an input image and the deformation field that must be applied to perfectly resemble a reference image. Similarly in (b) a brain image can be warped to a template image obtaining the Jacobian determinant. The color code indicate that blue regions were bigger in the subject image and that need to be contracted, on the other side region with smaller volume need to be expanded to resemble the template and are shown in red.

Results: The test dataset composed by WT mice and APP/PS2/Tau transgenic mice of 24 months of age was again used to test the method developed. The results are shown in Figure 62; the hippocampal and enthorinal cortex regions were significantly bigger (yellow enhanced regions) in WT mice when compared to transgenic mice. As expected also the ventricle region was significantly bigger (blue enhanced regions) in transgenic mice when compared to WT ones.

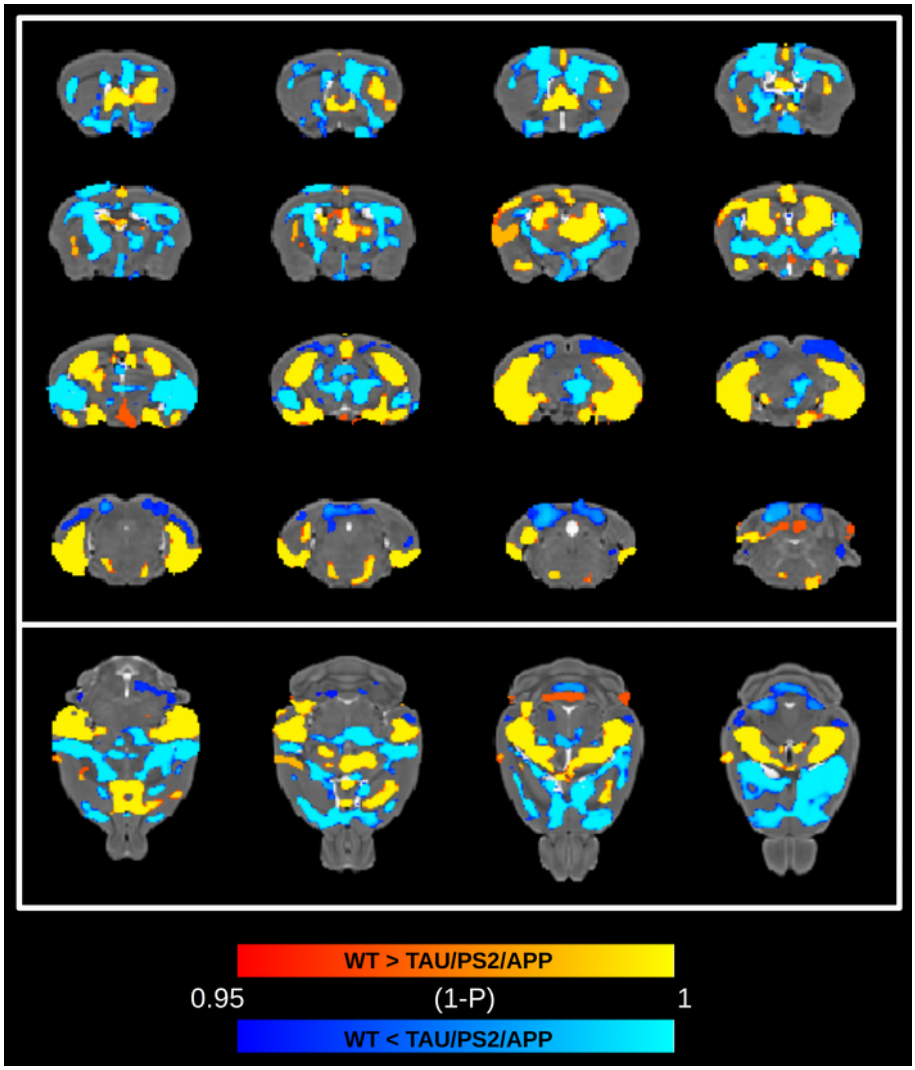

Figure 62: VBM results of a 24 month old group of triple transgenic mice. The upper box shows a series of the template coronal slices while in the bottom box four axial views. The colored superimposed statistical map indicate regions statistically bigger ($p < 0.05$) in the group of WT mice, while blue regions are those that resulted bigger in transgenic mice.

Again, VBM did not show significantly different regions between APP23 and WT mice at all time points considered confirming results obtained with the automatic parcellation procedure.

3.2.3 – DTI analysis.

Within this section the development of the DTI analysis protocol, to investigate WM pathology, is shown. The following pre-processing steps were adopted to prepare the DTI images for the voxel based analysis:

- The bias field intensity was firstly corrected in all the 2D anatomical reference images with the N4BiasFieldCorrection tool (Tustison et al., 2010). These images, composed of 18 slices with a thickness of 0.5 mm, were averaged to create a 2D anatomical reference template using the buildtemplateparallel.sh script (Avants et al., 2011a).
- This 2D anatomical template was co-registered with the in-house high resolution anatomical template (created during the parcellation of hig resolution anatomical images) in order to automatically a 2D reference brain mask.
- A correction of the distortion due to eddy currents was applied to all DTI volumes with the specific tool embedded in the FSL software (Andersson and Sotiropoulos, 2016).
- The B_0 image, representing the volume acquired without the application of the diffusion gradient, was extracted from each DTI volume, corrected for intensity non-uniformity and normalized antsIntroduction.sh script (Klein et al., 2009) with a non-linear greedy transformation to the 2D anatomical template. This step allowed the creation of a brain mask for each subject by back-projecting the 2D template brain mask.
- The diffusion tensor was finally modeled with the dtifit tool (Jenkinson et al., 2012) applied to the preprocessed images, obtaining the images representing the fractional

anysotropy (FA), the axial diffusivity (AD), the mean diffusivity and the radial diffusivity (RD).

Once that the diffusion tensor was calculated for each DTI image, a voxelwise analysis of whole brain white matter (WM) called “tract based spatial statistic” (TBSS) was applied (Smith et al., 2006). It included the following processing steps:

- A group mean full tensor template was firstly created using a population-based dti atlas construction algorithm that adopts a tensor based registration procedure embedded in the DTI-TK software library (Zhang et al., 2007). The template was constructed over three rigid registration iterations, followed by three affine iterations and, finally, six non-linear diffeomorphic iterations with a threshold on convergence of 0.002. The template was updated after each iteration by averaging the normalized images. The average template was resampled to an in plane resolution of 100 × 100 μm^2 and a slice thickness of 0.2 mm. The mean FA skeleton is shown in Figure 63, which represents all the tracts “common” to all subjects, was created from the mean FA image with the FSL tbss_skeleton command with a threshold of 0.2.

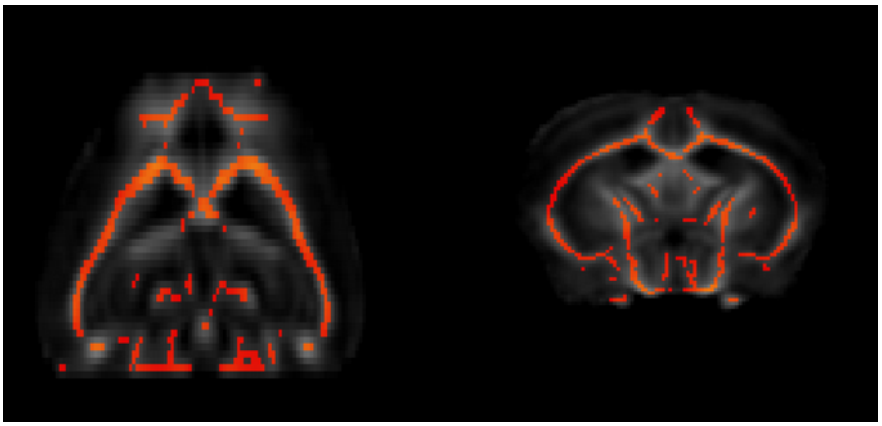

Figure 63: mean FA template in background and FA skeleton in orange.

- The skeleton obtained was binarized and manually subdivided into 8 white matter tract of interest (Figure 64 and 65).

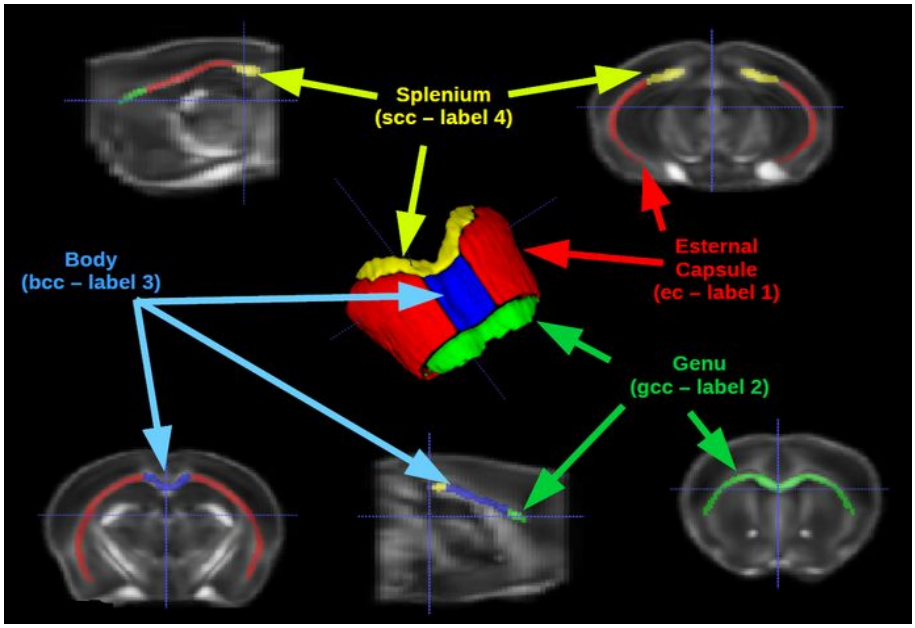

Figure 64: Subdivision of the corpus callosum white matter tracts and their 3D reconstruction.

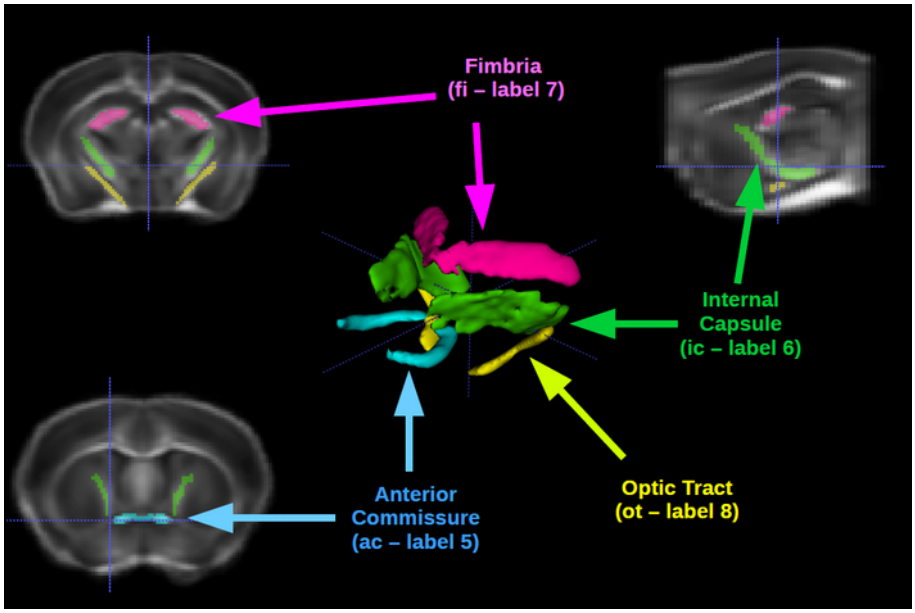

Figure 65: Subdivision of the internal white matter tracts and their 3D reconstruction.

- Individual FA images were finally normalized to the mean FA template with a diffeomorphic transformation that was subsequently applied also to AD, RD and MD images. Each normalized FA, AD, RD and MD image was projected onto the mean skeleton by filling the skeleton with values from the nearest relevant tract center.
- Mean FA, RD, AD, MD values extracted for each subject in each tract of interest enabling the statistical analysis (two-way ANOVA using R software).

3.2.4 – Longitudinal DTI study of the APP23 mice

Although in a late stage of the pathology, the statistical analysis revealed significant differences in most of the cortical tract selected.

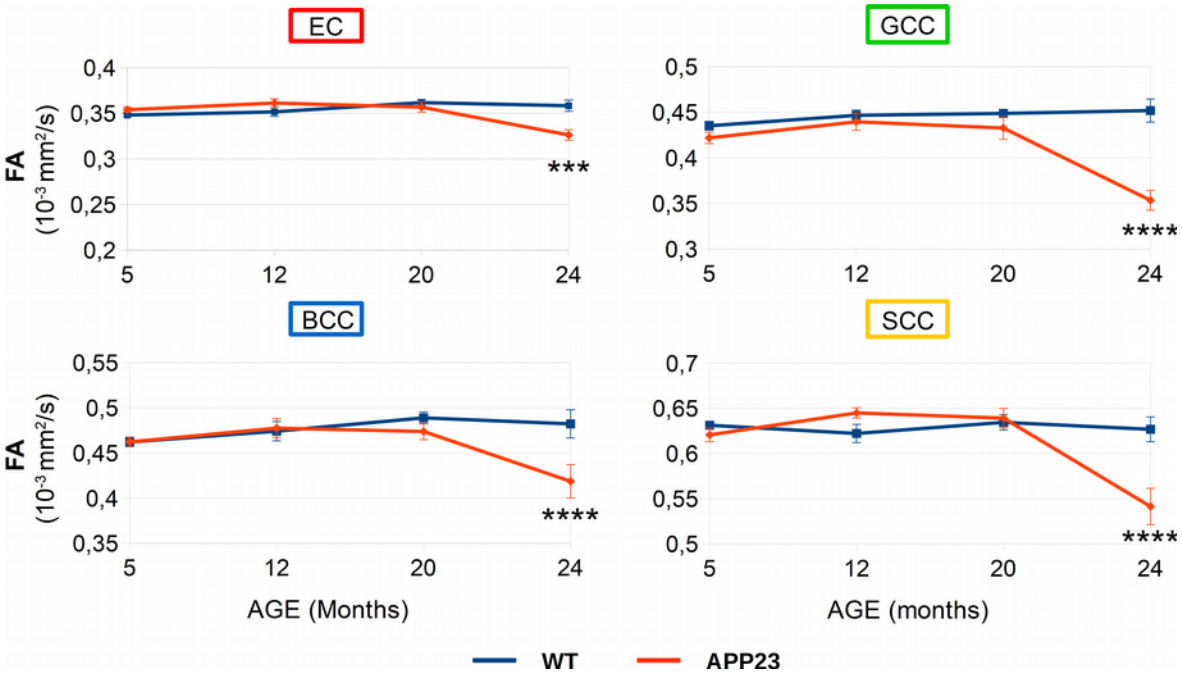

Figure 66: Panels representing FA values (expressed as Mean ± s.e.m.) of WM tracts presenting a significant interaction between age and genotype. Post-hoc test results shown as: ****p <0.0001, ***p <0.001,**p <0.01, *p <0.05.

FA values (Figure 66) show a significant interaction between age and genotype in the EC (P=0.0001, F=8.0314), in the GCC (P< $1*10^{-6}$, F = 12.43), in the BCC (P=0.01, F=4.24),

in the SCC ($P < 1*10^{-5}$, F=9.66). Although there wasn't a significant interaction between age and genotype, a significant effect of age and genotype was found in the IC ($P_{AGE} < 1*10^{-5}$; $P_{GENOTYPE} = 0.001$) and in the FI ($P_{AGE} = 0.003$; $P_{GENOTYPE} = 0.003$). In the AC just the effect of age was significant ($P_{AGE} < 1*10^{-5}$).

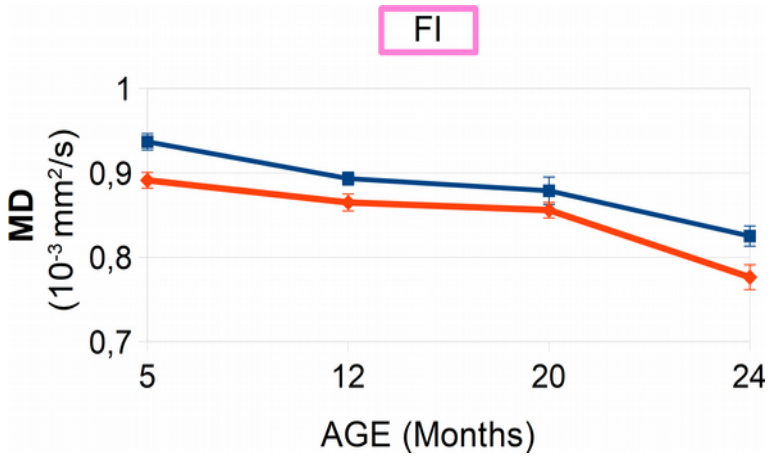

Figure 67: MD values in the FI (expressed as Mean ± s.e.m.)

No interaction between age and genotype was detected when the MD values were considered. However, an effect of age was seen in the GCC ($P_{AGE} = 0.004$), in the BCC ($P_{AGE} < 1*10^{-7}$) in the SCC ($P_{AGE} = 0.0002$), in the IC ($P_{AGE} = 0.0001$) and in the OT ($P_{AGE} = 0.01$) indicating that the two groups have a similar trend. Both the age effect ($P_{AGE} = 0.0002$) and genotpype effect ($P_{GENOTYPE} < 1*10^{-10}$) were significant in the FI indicating that MD was impaired already at the earliest time-point and that both groups decrease with the same trend along their lifespan (Figure 67)

The longitudinal analysis of RD values revealed a significant interaction between age and genotype (P= 0.006, F=4.55) only in the GCC Figure 68. A significant effect of age was seen in AC ($P_{AGE} < 1*10^{-4}$), in the IC ($P_{AGE} = 0.0002$) and in the OT ($P_{AGE} = 0.002$) while a significant difference between groups ($P_{GENOTYPE} < 1*10-4$) and a significant effect of age ($P_{AGE} < 1*10^{-4}$) but not significant interaction was seen in the FI.

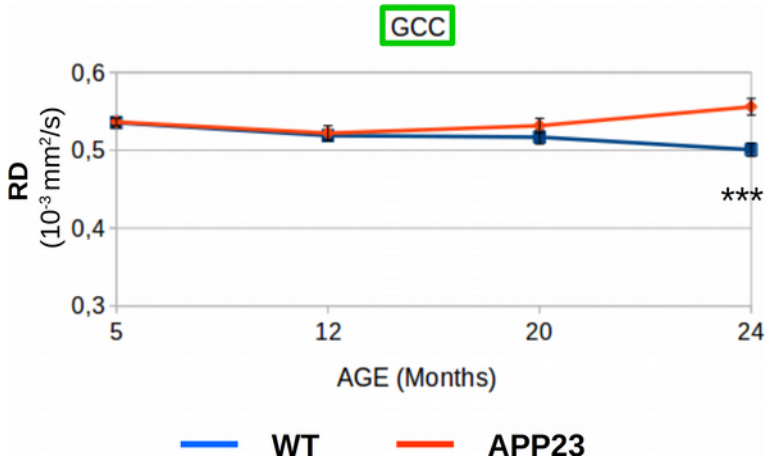

Figure 68: RD values in the GCC (expressed as Mean ± s.e.m.). Post-hoc test results shown as:****p <0.0001, ***p <0.001,**p <0.01, *p <0.05.

In Figure 69 are shown tracts where the analysis found statistically significant differences in the AD values. A significant interaction between age and genotype was found in the AC (P = 0.006, F=4.5), in the GCC (P = 0.02, F=3.6), in the BCC (P = 0.01, F = 3.96) and in the SCC (P = 0.0003, F=7,19).

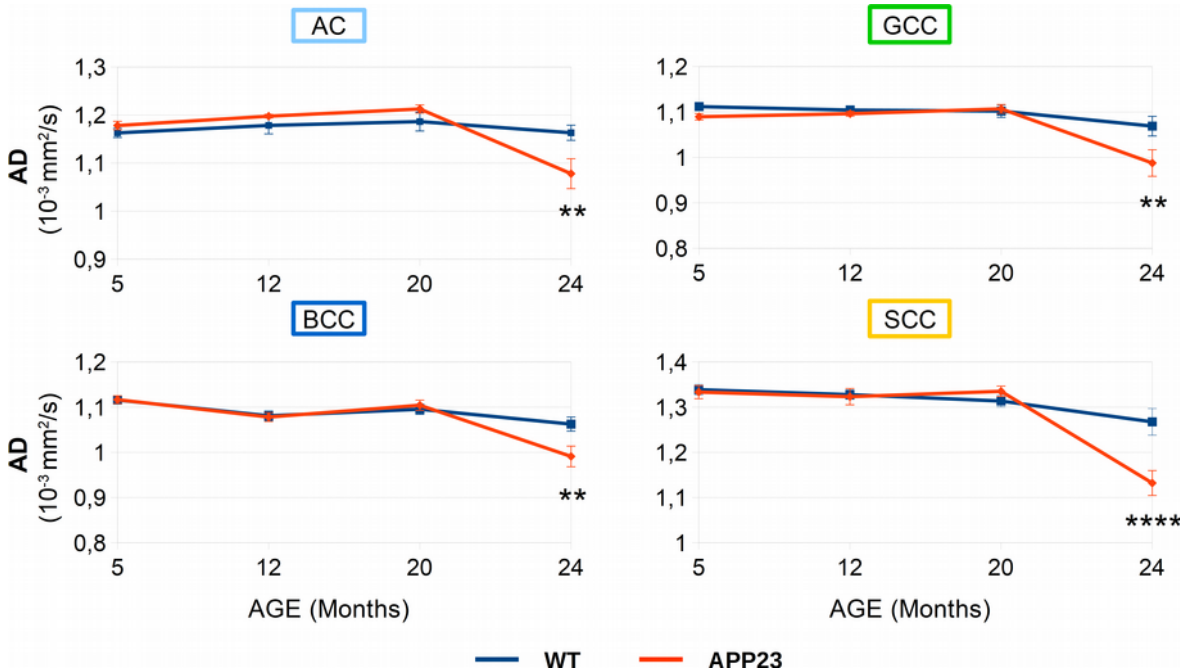

Figure 69: Panels representing AD values (expressed as Mean ± s.e.m.) of WM tracts presenting a significant interaction between age and genotype. Post-hoc test results shown as: ****p <0.0001, ***p <0.001,**p <0.01, *p <0.05.

		FA					AD				
	AGE (months)	WT Mean ± s.e.m		APP23 Mean ± s.e.m		P	WT Mean ± s.e.m		APP23 Mean ± s.e.m		P
EC	5	0,348	0,002	0,354	0,003	ns	1,03	0,01	1,02	0,01	ns
	12	0,352	0,005	0,361	0,005	ns	1,02	0,01	1,01	0,01	ns
	20	0,362	0,003	0,357	0,006	ns	1,02	0,01	1,03	0,01	ns
	24	0,36	0,01	0,33	0,01	0,0001	1,00	0,01	0,97	0,02	ns
GCC	5	0,435	0,005	0,42	0,01	ns	1,112	0,005	1,09	0,01	ns
	12	0,45	0,01	0,44	0,01	ns	1,10	0,01	1,10	0,01	ns
	20	0,449	0,004	0,43	0,01	ns	1,10	0,01	1,11	0,01	ns
	24	0,45	0,01	0,35	0,01	$< 1*10^{-8}$	1,07	0,02	0,99	0,03	0,001
BCC	5	0,462	0,003	0,46	0,01	ns	1,12	0,01	1,12	0,01	ns
	12	0,47	0,01	0,48	0,01	ns	1,08	0,01	1,08	0,01	ns
	20	0,49	0,01	0,47	0,01	ns	1,10	0,01	1,10	0,01	ns
	24	0,48	0,02	0,42	0,02	< 0,001	1,06	0,02	0,99	0,02	0,002
SCC	5	0,631	0,004	0,62	0,01	ns	1,34	0,01	1,33	0,01	ns
	12	0,62	0,01	0,64	0,01	ns	1,33	0,01	1,32	0,02	ns
	20	0,63	0,01	0,64	0,01	ns	1,31	0,01	1,33	0,01	ns
	24	0,63	0,01	0,54	0,02	$< 1*10^{-5}$	1,27	0,03	1,13	0,03	$< 1*10^{-5}$
AC	5	0,46	0,01	0,48	0,01	ns	1,16	0,01	1,18	0,01	ns
	12	0,50	0,01	0,51	0,01	ns	1,18	0,02	1,198	0,004	ns
	20	0,52	0,01	0,51	0,01	ns	1,19	0,02	1,21	0,01	ns
	24	0,47	0,01	0,44	0,02	ns	1,16	0,02	1,08	0,03	0,01
IC	5	0,504	0,004	0,491	0,004	ns	1,16	0,01	1,14	0,01	ns
	12	0,52	0,00	0,51	0,01	ns	1,14	0,01	1,13	0,01	ns
	20	0,52	0,01	0,50	0,01	ns	1,14	0,01	1,14	0,01	ns
	24	0,49	0,01	0,47	0,01	ns	1,09	0,02	1,06	0,02	ns
FI	5	0,563	0,004	0,60	0,01	ns	1,62	0,01	1,60	0,01	ns
	12	0,59	0,01	0,62	0,01	ns	1,59	0,01	1,58	0,02	ns
	20	0,60	0,01	0,62	0,01	ns	1,59	0,02	1,57	0,01	ns
	24	0,60	0,01	0,60	0,02	ns	1,48	0,03	1,40	0,04	ns
OT	5	0,53	0,01	0,56	0,01	ns	1,34	0,02	1,36	0,01	ns
	12	0,55	0,02	0,57	0,01	ns	1,27	0,02	1,31	0,02	ns
	20	0,58	0,02	0,60	0,01	ns	1,34	0,02	1,33	0,02	ns
	24	0,53	0,02	0,57	0,02	ns	1,33	0,03	1,32	0,03	ns

Figure 70: FA and AD values in the selected WM tract (units: 10^{-3} mm^2/s).

		RD					MD				
	AGE (months)	WT Mean ± s.e.m		APP23 Mean ± s.e.m		P	WT Mean ± s.e.m		APP23 Mean ± s.e.m		P
EC	5	0,62	0,01	0,601	0,004	ns	0,75	0,01	0,740	0,005	ns
	12	0,61	0,01	0,59	0,01	ns	0,745	0,004	0,733	0,005	ns
	20	0,60	0,01	0,61	0,00	ns	0,74	0,01	0,75	0,00	ns
	24	0,59	0,01	0,59	0,01	ns	0,73	0,01	0,72	0,01	ns
GCC	5	0,54	0,01	0,536	0,005	ns	0,728	0,005	0,721	0,003	ns
	12	0,52	0,01	0,52	0,01	ns	0,714	0,005	0,71	0,01	ns
	20	0,52	0,01	0,53	0,01	ns	0,71	0,01	0,723	0,004	ns
	24	0,50	0,01	0,56	0,01	0,0001	0,69	0,01	0,70	0,02	ns
BCC	5	0,55	0,01	0,55	0,01	ns	0,74	0,01	0,74	0,01	ns
	12	0,52	0,01	0,53	0,01	ns	0,71	0,01	0,71	0,01	ns
	20	0,52	0,01	0,53	0,01	ns	0,71	0,01	0,72	0,01	ns
	24	0,50	0,01	0,52	0,01	ns	0,69	0,01	0,67	0,01	ns
SCC	5	0,40	0,01	0,41	0,01	ns	0,71	0,01	0,72	0,01	ns
	12	0,41	0,01	0,38	0,01	ns	0,72	0,00	0,70	0,01	ns
	20	0,39	0,01	0,39	0,01	ns	0,70	0,01	0,70	0,00	ns
	24	0,38	0,01	0,43	0,02	ns	0,68	0,01	0,66	0,02	ns
AC	5	0,54	0,01	0,52	0,01	ns	0,75	0,01	0,742	0,005	ns
	12	0,50	0,01	0,50	0,01	ns	0,73	0,01	0,73	0,01	ns
	20	0,48	0,01	0,50	0,01	ns	0,72	0,01	0,74	0,01	ns
	24	0,53	0,01	0,52	0,01	ns	0,74	0,01	0,70	0,01	ns
IC	5	0,473	0,004	0,479	0,004	ns	0,702	0,004	0,699	0,004	ns
	12	0,454	0,002	0,452	0,005	ns	0,684	0,002	0,677	0,004	ns
	20	0,45	0,01	0,468	0,005	ns	0,68	0,01	0,693	0,004	ns
	24	0,46	0,01	0,47	0,01	ns	0,67	0,01	0,67	0,01	ns
FI	5	0,59	0,01	0,53	0,01	ns	0,94	0,01	0,89	0,01	ns
	12	0,55	0,01	0,51	0,01	ns	0,89	0,01	0,87	0,01	ns
	20	0,52	0,01	0,50	0,01	ns	0,88	0,02	0,86	0,01	ns
	24	0,50	0,01	0,47	0,02	ns	0,83	0,01	0,78	0,01	ns
OT	5	0,53	0,01	0,50	0,01	ns	0,80	0,01	0,79	0,01	ns
	12	0,49	0,02	0,49	0,01	ns	0,75	0,02	0,76	0,01	ns
	20	0,48	0,03	0,45	0,01	ns	0,76	0,02	0,74	0,01	ns
	24	0,53	0,02	0,49	0,02	ns	0,80	0,01	0,76	0,02	ns

Figure 71: RD and MD values in the selected WM tract (units: 10^{-3} mm^2/s).

3.2.5 – T2 relaxation time

T2 weighted imaging, can be used to measure signal reductions due to local field inhomogeneities resulting from a variety of factors. Among these, iron content has been particularly investigated (Haacke et al., 2005). The presence of iron potentiates reactive oxygen species, and thus contributes to an increase of the oxidative stress implicated in neuronal loss in many neurodegenerative disorders such as Alzheimer's disease (Bush, 2003; Jellinger et al., 1990).

To calculate the T2 relaxation time of the mouse brain the following steps have been performed:

- Images with the higher signal to noise ratio (corresponding to TE = 11ms) were extracted from each MSME acquisition and used to create a reference template (with the buildtemplateparallel.sh ANTs script) that was manually masked.
- The template brain mask was back-projectied to the subject space obtaining an automatic estimation of the brain region.
- T2 maps were computed with a custom MATLAB script programmed to fit voxel-wise the acquired signal within the subject brain mask as shown in Figure 72.

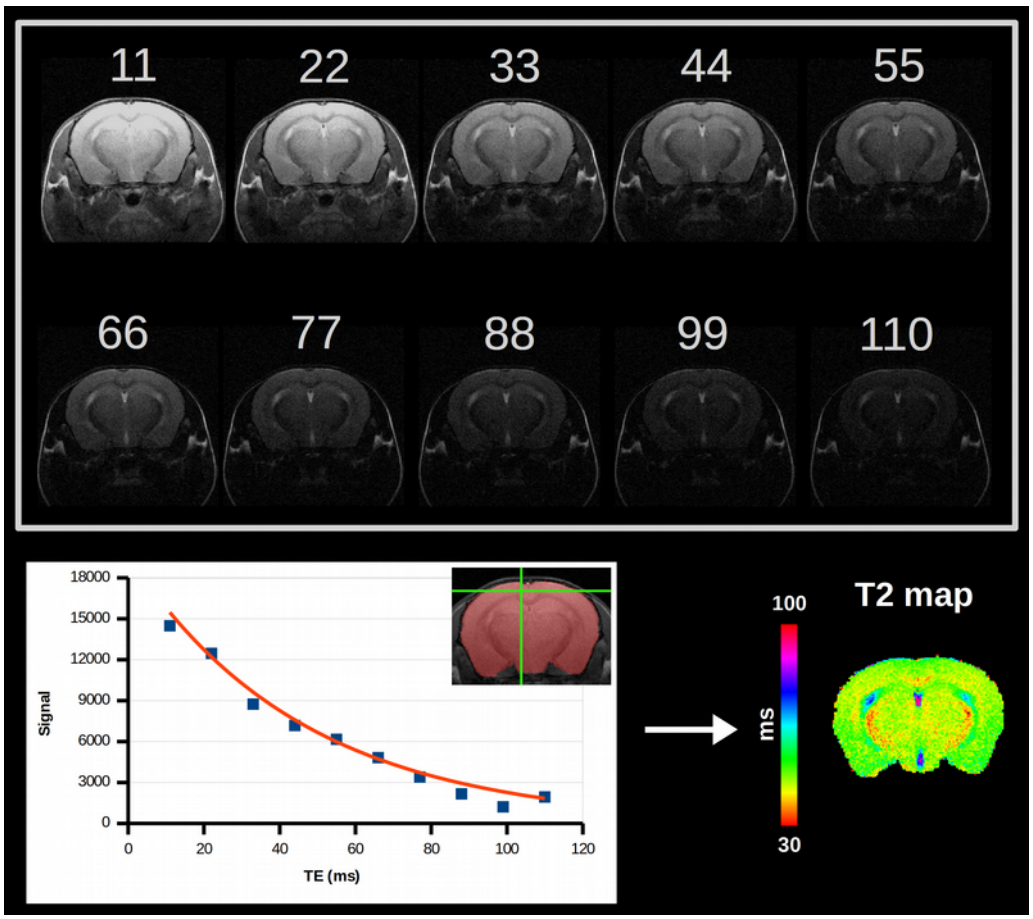

Figure 72: T2 mapping workflow. In the upper panel the images acquired at different TE (ms) indicated on top of the slice. In the lower panel an example of the fit obtained in the voxel indicated by the green cross and the T2 map obtained.

- Seven roi were defined manually over the brain template (Figure 73).

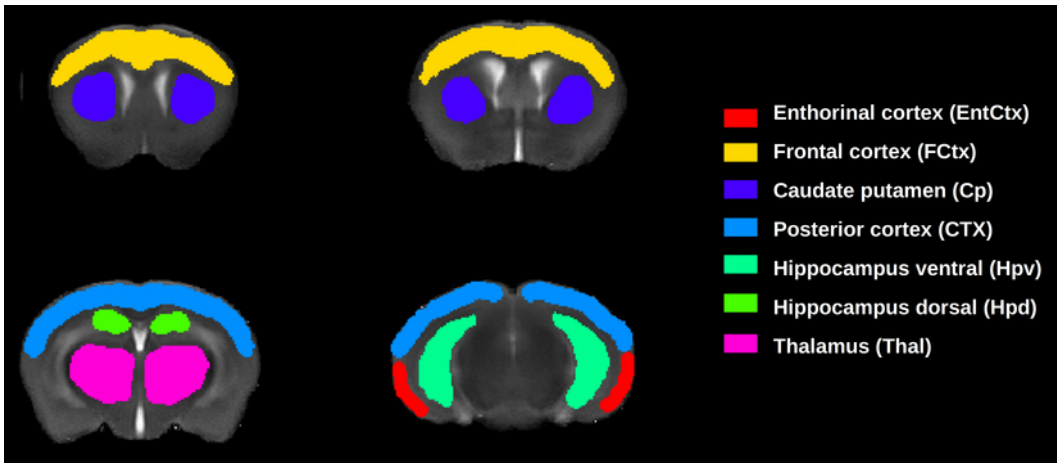

Figure 73: Region of interests defined over the brain template.

- The calculated T2 maps were normalized to the reference template by applying the non-linear diffeomorphic transformations previously computed.
- The T2 value was averaged in the selected ROIs and the statistical analysis (two-way anova) was computed with R software.

3.2.6 – Longitudinal T2 evaluation

The longitudinal two-way ANOVA analysis of the T2 values revealed a slight but significant interaction between age and genotype (P = 0.049; F = 2.75) only in the HPd region. Although there was not a significant interaction, a significant effect of age and genotype was seen in the CP ($P_{AGE} < 1*10^{-16}$; $P_{GENOTYPE} = 0.02$) and in the Thal ($P_{AGE} < 1*10^{-5}$; $P_{GENOTYPE} < 1*10^{-5}$) while only a significant effect of age was seen in the Ctx ($P_{AGE} < 1*10^{-5}$), in the Fctx ($P_{AGE} < 1*10^{-5}$) and in the EntCtx ($P_{AGE} < 1*10^{-7}$).

The cortical and the hippocampal regions appeared to be significantly lower in 24 months of age APP23 mice compared to WT littermates when a voxel-wise statististical t-test was computed (Figure 75).

	AGE	WT Mean ± s.e.m.		APP23 Mean ± s.e.m.		P
Fctx	5	46,3	0,2	46,8	0,2	ns
	12	46,3	0,2	46,9	0,1	ns
	20	46,3	0,2	46,4	0,3	ns
	24	45,6	0,2	45,4	0,3	ns
Hpd	5	47,3	0,2	47,3	0,2	ns
	12	46,9	0,2	46,9	0,1	ns
	20	47,3	0,3	47,1	0,2	ns
	24	48,1	0,3	46,7	0,4	0,004
Hpv	5	46,4	0,2	46,6	0,1	ns
	12	46,4	0,2	46,8	0,2	ns
	20	46,7	0,2	46,4	0,2	ns
	24	47,0	0,3	46,5	0,4	ns
Ctx	5	46,4	0,1	46,96	0,05	ns
	12	46,3	0,1	46,7	0,1	ns
	20	46,4	0,2	46,8	0,3	ns
	24	46,1	0,2	45,6	0,2	ns
CP	5	45,4	0,1	45,7	0,1	ns
	12	44,0	0,1	44,3	0,1	ns
	20	43,4	0,2	43,8	0,2	ns
	24	43,4	0,3	43,7	0,2	ns
Thal	5	43,0	0,1	43,4	0,2	ns
	12	42,4	0,1	42,9	0,1	ns
	20	42,0	0,2	42,4	0,2	ns
	24	42,1	0,2	42,9	0,2	ns
EntCtx	5	48,7	0,3	48,8	0,3	ns
	12	47,9	0,3	48,2	0,3	ns
	20	48,0	0,2	48,4	0,2	ns
	24	46,0	0,7	46,0	0,6	ns

Figure 74: T2 mean values within the ROI defined (units ms).

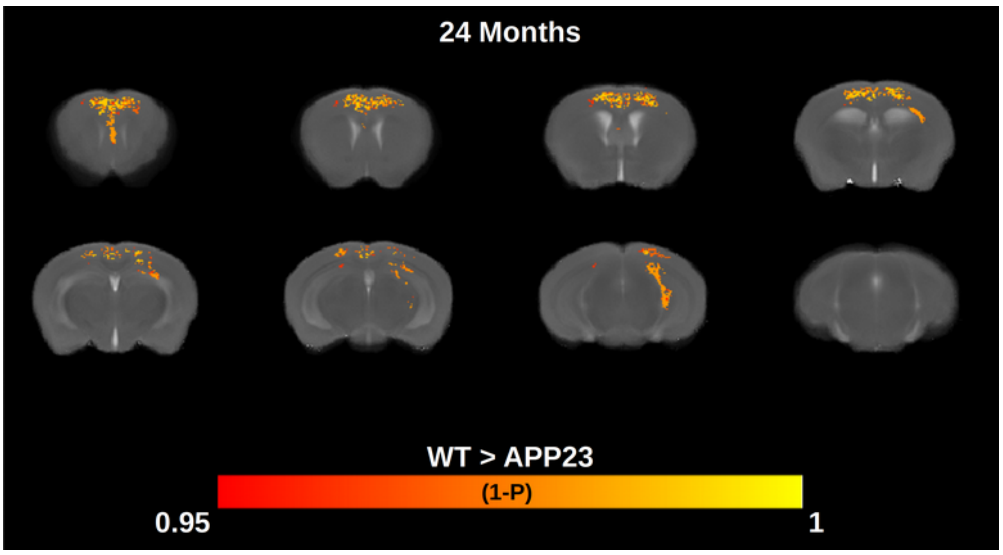

Figure 75: Significance map computed with FSL randomise to compare 24 months of age APP23 and WT mice.

3.2.6 – Summary (2)

A multi-parametric MRI study has been carried out to characterize the pathological alterations of gray and white matter in AD transgenic models. To increase the reliability of results and the translational impact of the study, aim of this section was to develop automated and operator independent analysis procedures that resemble the analysis pipelines adopted in human MRI studies.

A multi-atlas parcellation procedure, to measure volumes of brain regions, and an automated VBM analysis, to detect alterations in the GM density, were firstly developed. The reliability of these procedures were tested on a dataset of brain structural images, acquired and analyzed manually within the frame of a previous project. Results obtained with the automatic procedures shows good accordance with those obtained manually. In particular, 24 months of age APP/PS2/Tau transgenic mice compared with WT litter-mates showed a significant shrinkage of the hippocampus and of the enthorinal cortex and a significant enlargement of the ventricles. Nevertheless, when applied on the brain structural images acquired longitudinally on the APP23 transgenic mice, no significant alterations in the volumes of ROI evaluated and no alterations in GM density by means of VBM were detected. This is not an unexpected result because, even if the APP23 is a transgenic model that has been widely adopted in research studies, no alterations in its brain morphology were previously described in literature. As shown in Table 2, brain atrophy is often a minor component of the transgenic mice phenotype and sometimes it is not present when single transgenic models are studied (Borg and Chereul, 2008).

An automatic TBSS approach was developed to analyze DTI images revealing that the APP23 mice model show detectable WM alterations only in a late stage of the pathology. The corpus callosum of 24 months of age APP23 mice present a significant decrease of the FA and AD (Figure 67-68) and an increased RD (Figure 70). These alterations might

be associated both with a structural damage due to a demyelination process, resulting in an increased freedom for water molecules to move across white matter tracts, or with the infiltration of immune cells typical of a neuroinflammatory state (J. Zhang et al., 2012). Supporting our findings, It has been demonstrated that a cerebral amyloidosis in the neocortex of 27-months old APP23 mice causes a modest but significant neuron loss and marked gliogenesis (Bondolfi et al., 2002). Another study on aged APP23 mice (24 months of age) demonstrated that fibrillar amyloid deposits and associated gliosis are accompanied by a reduction in the apparent diffusion coefficient (Mueggler et al., 2004). This may suggest that the extracellular deposition of fibrillar amyloid and/or associated glial proliferation cause restrictions to interstitial fluid diffusion. Reduced diffusivity within the interstitial space may alter volume transmission and therefore contribute to the cognitive impairment.

The longitudinal analysis of the T2 relaxation times revealed a slight but significant decrease in the hippocampus of aged APP23 when compared to age-matched WT. Other region investigated showed a significant effect of age. When a voxel-wise approach was used to compare only the 24 months of age APP23 mice with the age-matched WT a region characterized by a decreased T2 values was found in the cortical region. Several factors have been described to influence the T2 relaxation time, including water content, myelin density and by the presence of paramagnetic molecules, such as iron (Jara et al., 2006; Paus et al., 2001). Therefore, the increased concentration of iron in the brain tissue of patients with AD (Connor et al., 1992) and the presence of iron in amyloid plaques (Collingwood et al., 2008) has suggested that the measurement of the T2 relaxation time can be considered as a possible marker of tissue characteristics easily measurable both with preclinical and clinical settings. However, described changes of T2 time in AD have not been consistent either in patients or in mouse models. As shown in table Table 2,

studies in transgenic models found significantly greater T2 in young transgenic mice when compared to WT, while in older transgenic mice T2 values were significantly reduced. Significantly lower T2 values were found in AD patients showing a positive correlation with cognitive scores but these results were not confirmed by other studies that described inversely that the increased T2 values found in the hippocampus are correlated with the severity of functional and cognitive impairments in AD patients (Tang et al., 2018).

3.3 – Optimization of the rsfMRI analysis workflow

As reported in Table 2 and described by a recent review (Asaad and Lee, 2018), the assessment of the brain functional connectivity by means of rsfMRI imaging is playing a fundamental role in the study of AD as functional alterations are the primary events occurring the pathological cascade. The interest in this technique have recently grown because different studies were able to observe deficits in the hippocampus and/or in the cortex of transgenic mice, sometimes at early ages.

This section includes the development of the processing pipeline to analyze the rodent rsfMRI data. Preliminary experiments were carried out on rats; this choice was made to overcome different issues:

- Firstly, the significant small size of mouse brain requires image acquisition at a high spatial resolution at the expense of the signal-to-noise ratio. This problem may be compensated by the use of last generation of radiofrequency cryogenic coils that can boost the signal-to-noise ratio minimizing the thermal noise influence. The only mouse coil configuration available at the beginning of this study was characterized by a lower signal-to-noise ratio when compared to the available quadrature receiver coil for the rat brain. We were able to install a cryogenic coil system for the mouse brain only at the beginning of 2018.
- Secondly, since the conditions affecting the cerebral blood flow could lead to an incorrect interpretation of the observed changes in brain activity a great care in the use of anesthesia is needed and the bigger size of rats makes the anesthesia protocol easier to perform in rats. Although it is necessary to minimize the animal movement and to enable the imaging acquisition, anesthesia can alter the physiology and the brain activity of animals leading to results that are not representative of the awake

state (Grandjean et al., 2014; Liang et al., 2012). To avoid the suppression of signal arising from the brain activation, animals must be kept sedated without the induction of a deep anesthesia state. Isofluorane at 1,5-2% is able to suppress brain activity (Liang et al., 2015) while a dose-dependent decrease of the functional connectivity was found with the use of medetomidine (Nasrallah et al., 2014). The combined use of low doses of medetomidine and isoflurane was suggested as it retained strong correlations both within cortical and subcortical structures, without the potential seizure-inducing effects of medetomidine (Grandjean et al., 2014). Some research groups have recently shown that a mechanical ventilation in combination with the administered anesthetic and an injection of pancuronium bromide, a muscle relaxant that allow the minimization of animal movements, are needed to obtain reliable results in mice studies (Bertero et al., 2018; Zerbi et al., 2015).

- In the end, since a great care in the optimization of the analysis protocol must be adopted we decided, in collaboration with Luigi Cervo research group, to induce functional connectivity alterations by means of a pharmacological challenge. Different published rsfMRI studies in rats were able to detect strong functional alterations after the injection of a pharmacological challenges such as ketamine (Gass et al., 2014; Grimm et al., 2015) or nicotine (Gozzi et al., 2006; Z. Li et al., 2008; Bruijnzeel et al., 2014). This experiment enabled the optimization of the analysis procedure since the expected functional alterations must have been detected after the injection of a pharmacological challenge.

The aim of the presented work is to develop a reliable analysis pipeline to be translated to future rsfMRI studies in AD transgenic mouse models.

3.3.1 – rsfMRI analysis pre-processing

The analysis pipeline adopted was recently introduced within the frame of the Human Connectome Project and its efficacy has been recently demonstrated in the analysis of mouse rsfMRI data (Zerbi et al., 2015). It is characterized by the removal of artifact components by automatic classification carried out by the FMRIB's ICA-based Xnoiseifier (FIX) (Salimi-Khorshidi et al., 2014) software which does not need the recording of external physiology (e.g. respiration or cardiac cycle) or the segmentation of CSF and WM.

To make possible the identification of different functional networks, different steps were implemented to pre-process the rsfMRI raw data:

- A slice timing correction was initially applied to the fMRI timeseries (SPM8) followed by a realignment with motion parameter estimation and a correction for B_0 inhomogeneities (FieldMap toolbox SPM8).

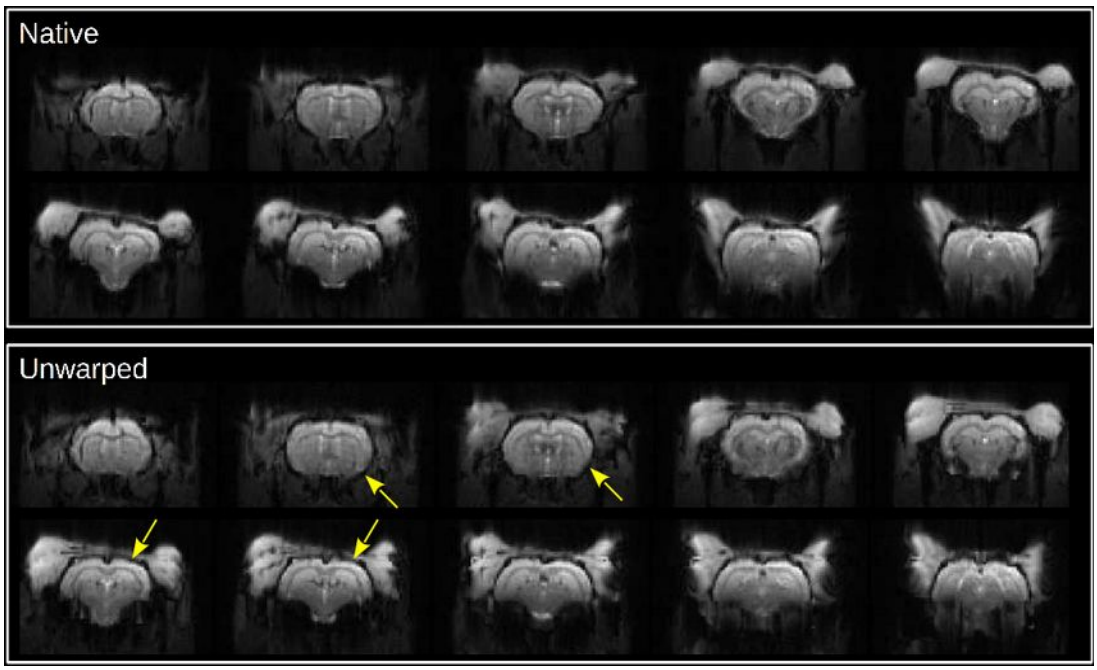

Figure 76: The effect of the B_0 inhomogeneity correction. Within the upper box the acquired image is shown. The effect of the unwarping correction is higlighted by yellow arrows in the bottom box.

Few coronal slices of the native image are shown in the upper frame of Figure 76 while in the lower frame it can be seen how the FieldMap toolbox is able to compensate the main deformations caused by the B_0 inhomogeneities.

- Each anatomical reference scan was spatially normalized, through linear affine and nonlinear diffeomorphic transformation metric mapping with the ANTs software (Avants et al., 2011a), to a rat brain template with co-registered anatomical atlas positioned in the Paxinos stereotactic coordinate system (Schwarz et al., 2006). In order to improve the spatial normalization quality, an in-house brain template was created by averaging the obtained normalized anatomical images. Each anatomical reference was then anew spatially normalized with a greedy non-linear transformation to the study specific template. The transformations obtained were used to back-project to each subject space the template brain mask label, performing an automatic brain extraction also of the fMRI data.
- 50 independent components were estimated for each brain extracted fMRI timeseries using FSL MELODIC (Multivariate Exploratory Linear Optimized Decomposition of Independent Components) (Beckmann and Smith, 2004; Jenkinson et al., 2012).
- On a random subset of 20 timeseries, a hand-classification of the ICA components into signal (Figure 77) and noise derived from respiratory motion (Figure 78) and cardiac motion (Figure 79) was made on the basis of different factors previously described (Pan et al., 2015; Zerbi et al., 2015). Firstly, the shape of the thresholded spatial maps that must resemble the shape of previously described activation components while in case of respiratory and cardiac noise can be identified respectively on the edge of the brain and in correspondence of the main vessels on the bottom of the brain. Secondly the temporal power spectrum of a signal

component have a low frequency fluctuation (Figure 77) while the noise components present spikes at higher frequency (Figure 78 and 79). The components that were not easily identified as one of the three described categories were assigned as unknown component.

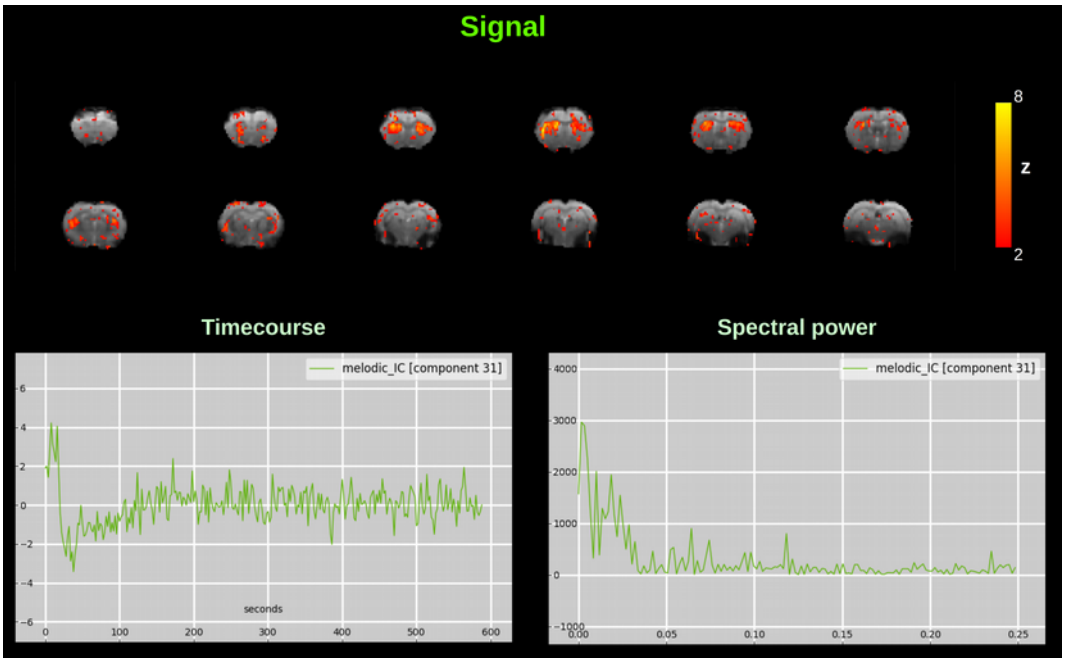

Figure 77: Example of a signal components which exhibit a low frequency fluctuations.

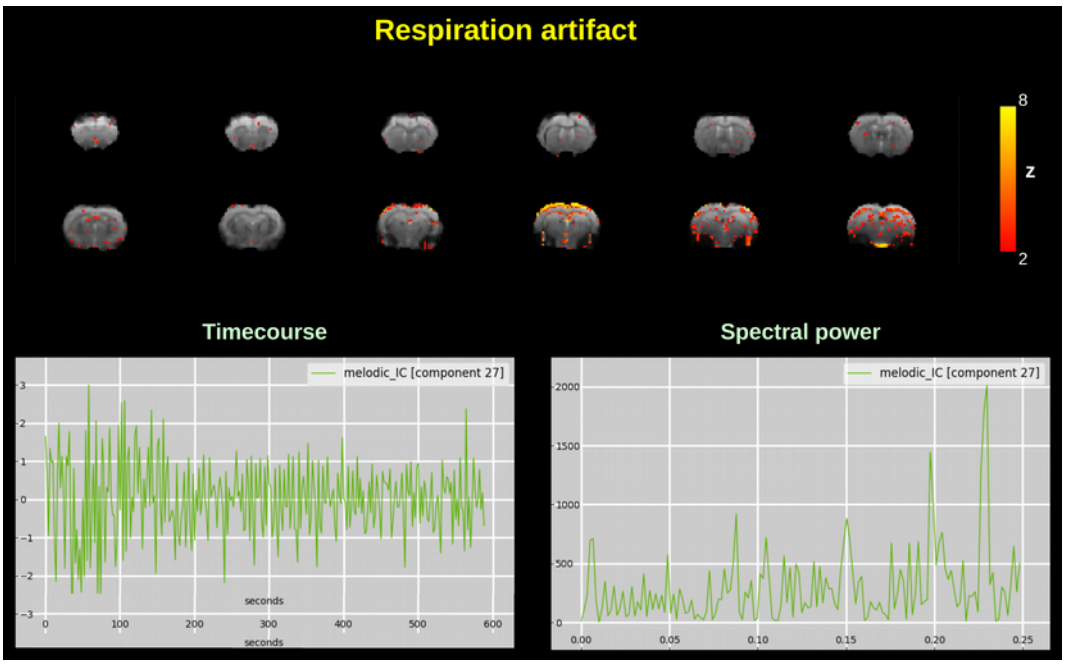

Figure 78: Respiratory effects can be localized near the midline, the ventricles, and the surface of the brain.

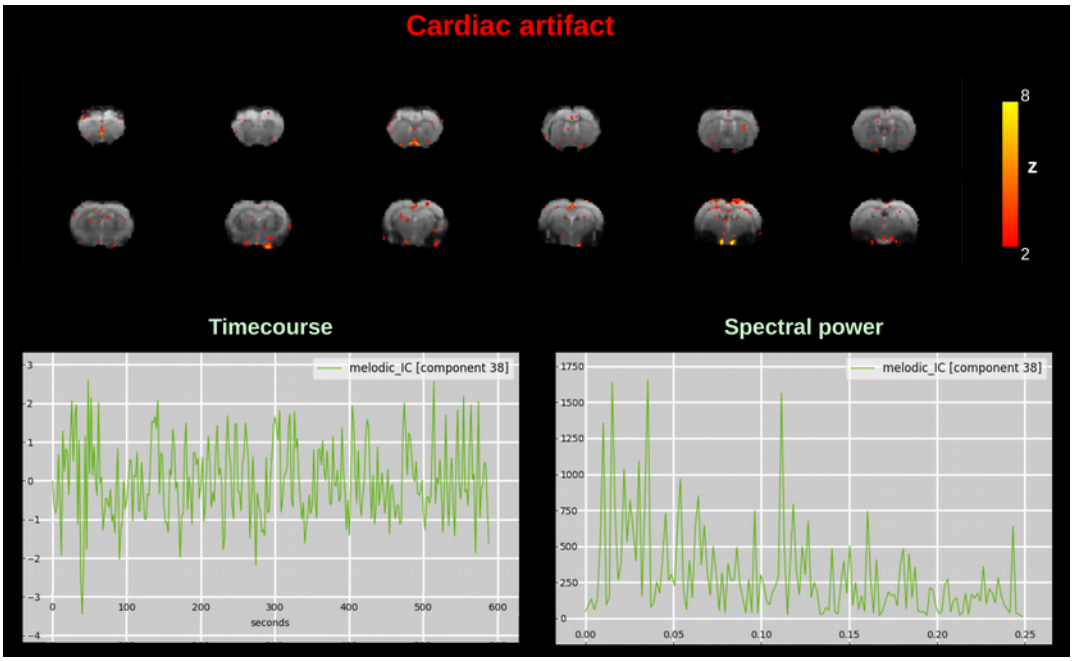

Figure 79: Cardiac artifact are associated with regions along the surface and at the base of the brain.

- These classified ICA components were used as a training set for FSL-FIX (Griffanti et al., 2014; Salimi-Khorshidi et al., 2014). After training, a “soft” artifact removal of motion parameters and noise components of all datasets was applied using FSL-FIX.
- Each denoised fMRI timeseries was finally spatially normalized to the in-house template by applying the transformations previously obtained. Normalized images have a final resolution of $2 \times 2 \times 2$ mm^3.

Two methodologies are widely used for evaluating the functional connectivity rsfMRI data: The spatial independent component analysis (ICA), which is a mathematical technique that identifies functional networks maximizing their statistical independence (Beckmann et al., 2005); And the seed based analysis (SBA) which allow the identification of functional networks through the temporal correlation of a specified seed voxel with the rest of the brain voxels (Biswal et al., 1995; Joel et al., 2011).

To establish the consistency of the observed variations, both analysis techniques were developed since ICA derived network maps have shown similar connectivity maps to those obtained with the SBA.

3.3.2 – Independent component analysis (ICA)

The assessment of the resting-state functional connectivity was carried out following these steps:

- The temporal concatenation, using the FSL MELODIC software, of all the pre-processed and normalized fMRI timeseries allowed the extraction of 50 ICA components (ICs). A subset of 18 ICs (Figure 80) was selected through a visual comparison with previously reported networks in rats and mice (Jonckers et al., 2011; Liang et al., 2011; Bukhari et al., 2017; Grandjean et al., 2017).

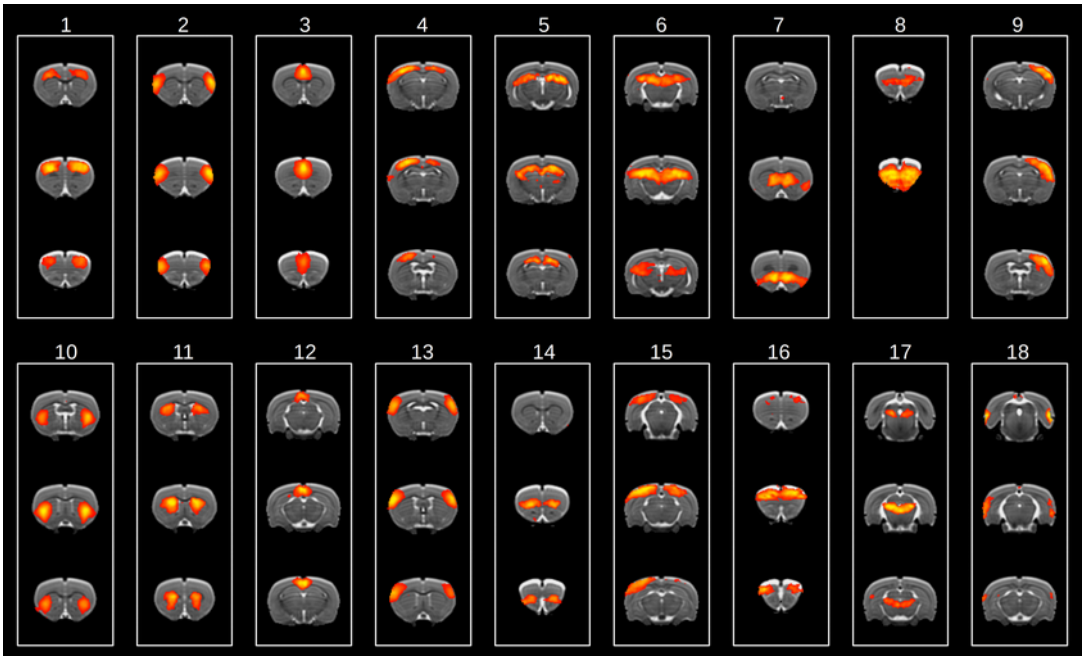

Figure 80: Selected ICs components representing the principal resting state networks identified. 1- Motor Cortex; 2 – Insular Cortex; 3 – Cingulate Cortex; 4 and 9 – Somaosesory Cortex; 5 – Hippocampus dorsal; 6 – Thalamus + Hippocampus ventral; 7 – Ventral Striatum; 8 and 14 – Orbitofrontal Cortex; 10 - Lateral Striatum; 11 – Dorsal Striatum; 12 – Retrosplenial Cortex; 13 – Barel field Cortex; 15 – Visual Cortex; 18 – Auditory Cortex.

This subset of 18 ICs represent the functional template of networks to be used in the following steps.

- A dual regression approach was applied to regress out the time courses and the spatial distribution of the initially identified 50 ICs for each fMRI acquisition (Beckmann et al., 2009; Cole et al., 2010; Filippini et al., 2009; Nickerson et al., 2017). As shown in Figure 81, in the first step of dual regression, the full set of 50 ICs (including identified networks and artifact components) were used in a multiple spatial regression against each dataset resulting in a set of matrices (time points x components) representing the average time course of voxels in each functional network for each subject. The normalized time courses were subsequently used in a second multiple regression step to identify unique spatial maps for each subject, representing the brain regions correlating with each time course.

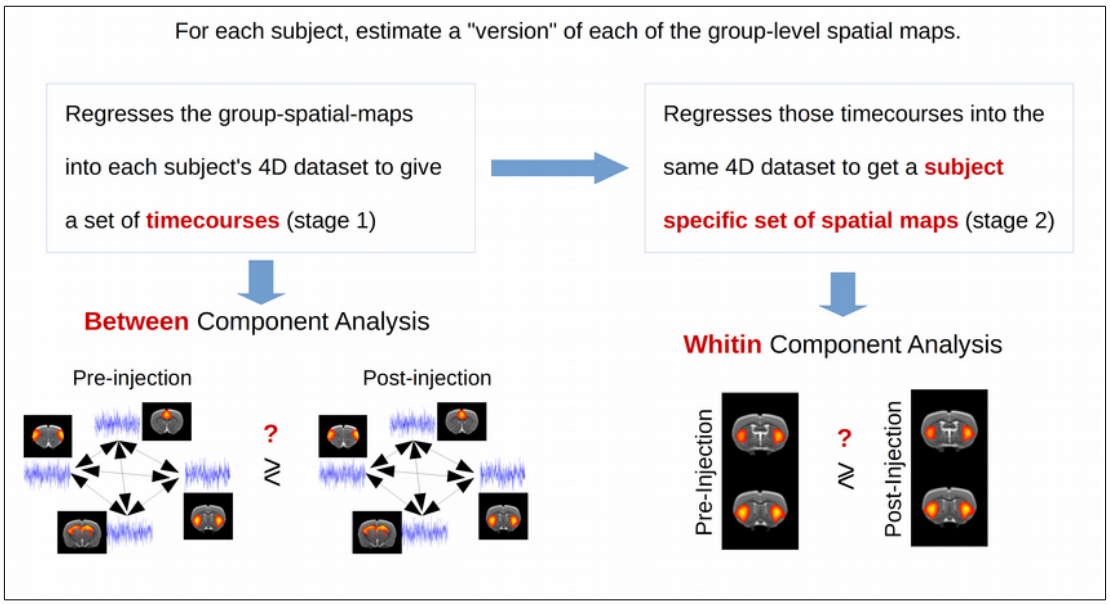

Figure 81: Flowchart showing the dual regression workflow. The regression of the template spatial maps into each subject space allow the estimation of subject specific spatial maps and relative timecourses. The extracted subject specific timecourses are used to make a comparison **between** components. While the subject specific spatial maps are used to evaluate differences **within** the component identified.

- Alterations of the connectivity **between** the identified RSNs were investigated using FSL-Nets (Jenkinson et al., 2012). Each matrix of time courses was processed firstly by removing the artifact components and cleaning up the residual time-courses representing the identified RSNs. A network matrix was then computed, using normalized covariance and transformed to Fisher-z scores, for each subject. In order to investigate the effect of nicotine on the correlation between RSNs, the difference between the network matrix post-injection and the network matrix pre-injection was computed for each subject.

- Alterations of the connectivity **within** the RSNs identified were assessed by evaluating the changes of the spatial correlation obtained in the second step of dual regression. For each subject, a subtraction of the spatial maps of the components obtained with the post-injection dataset to those obtained with the pre-injection dataset was computed. The average delta correlation was than computed over a region obtained by applying a threshold ($Z > 4$) and a binarization to the corresponding component of the template. A spatial-correlation matrix representing the correlation intensity alteration within each component was in the end created for each subject.

- A one-way anova was finally applied (Matlab) to the networks-matrices and to the spatial-correlation matrices. The evaluation of the nicotine effect was assessed respectively between and within each identified network and whether this effect is dependent on the dose injected. A post-hoc test was applied just to connections found to be significantly different between groups.

3.3.3 – Within component ICA analysis

Our analysis shows a significantly increased correlation after the injection of a nicotine bolus at a dose of 0.1 g/kg within some of the selected components. This increase was not seen after the injection of a saline solution or after the injection of a lower dose of 0.05 g/kg or when a bolus of mecamylamine was administered after the injection of nicotine at 0.1 g/kg. In Figure 82 to 96 the variation of the correlation, expressed as the difference between post and pre-injection correlation value (Δz), in the four experimental groups is shown. Only components that showed a statistical significant difference between groups are shown. The results of the statistical analysis is reported in each figure where outliers are shown as red crosses and post-hoc tests results are indicated with ***p <0.001,**p <0.01, *p <0.05.

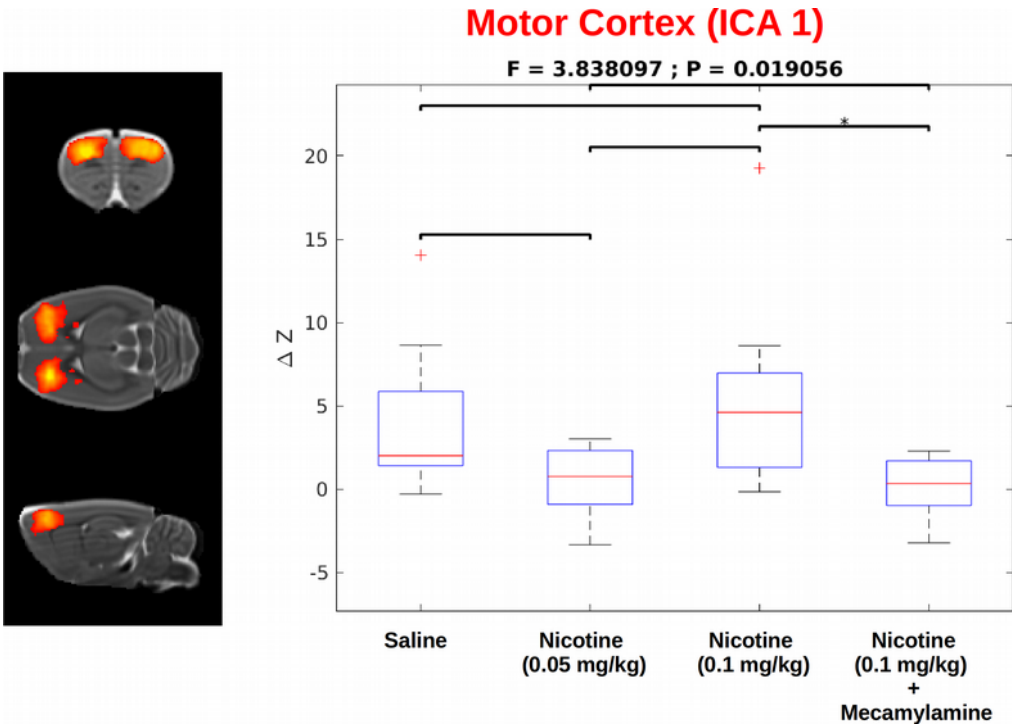

Figure 82: Nicotine effect on the ica component 1. Left panel shows its location and right chart show the difference of the correlation (ΔZ) due to the pharmacological challenge. F and P values are highlighted on top of the chart (***p <0.001,**p <0.01, *p <0.05) red crosses indicate the outliers excluded.

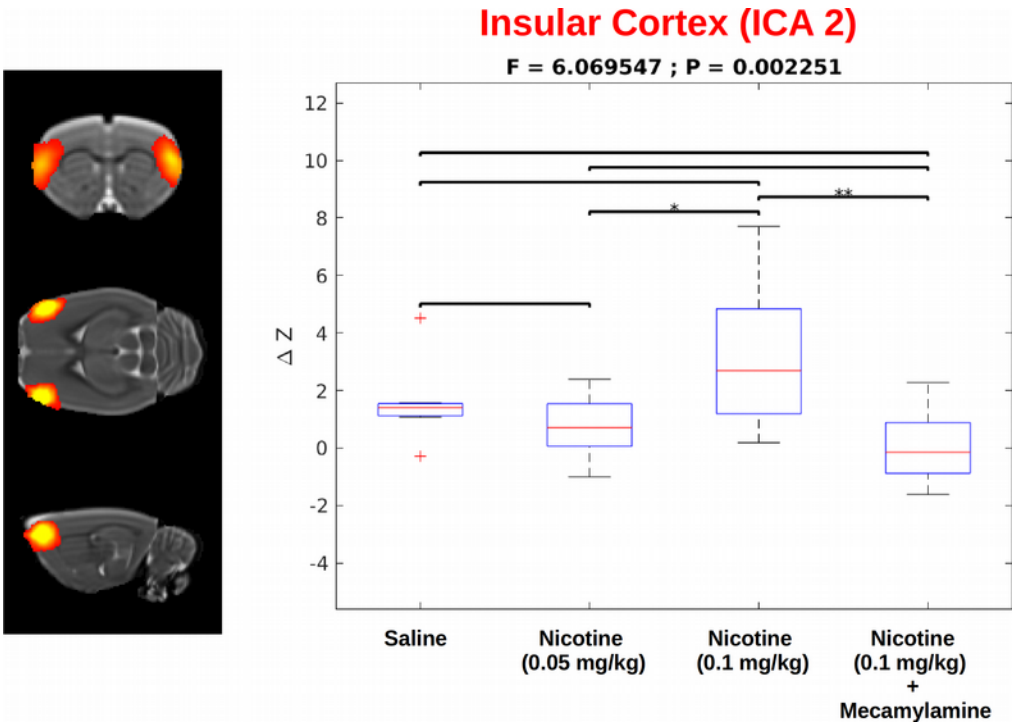

Figure 83: Nicotine effect on the ica component 2. Left panel shows its location and right chart show the difference of the correlation (ΔZ) due to the pharmacological challenge. F and P values are highlighted on top of the chart (***p <0.001,**p <0.01, *p <0.05) red crosses indicate the outliers excluded.

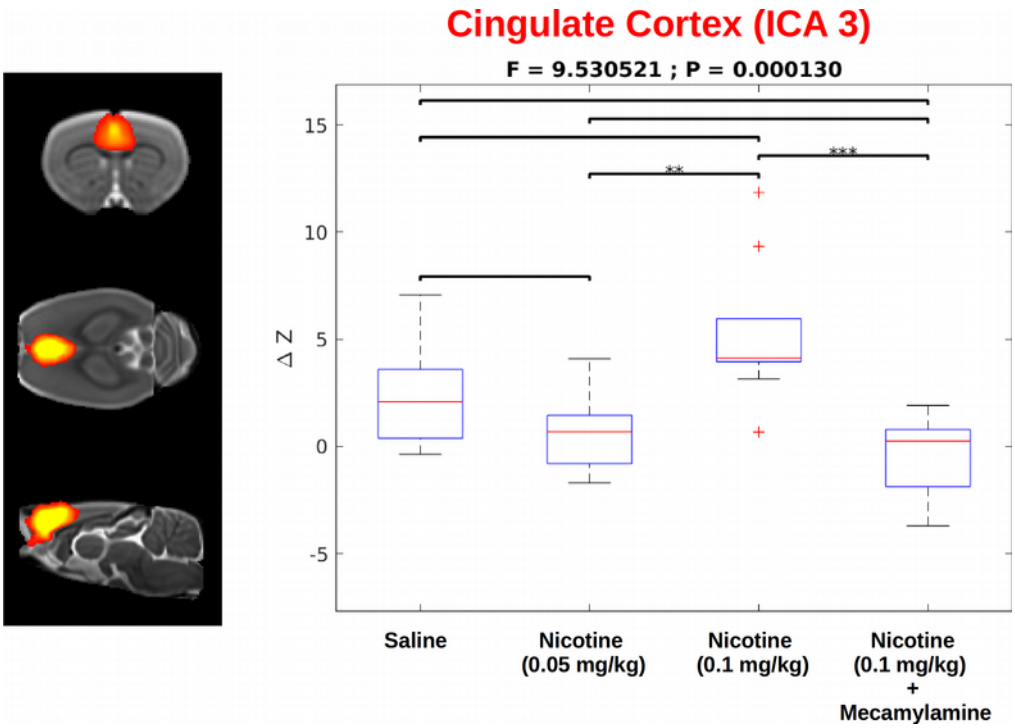

Figure 84: Nicotine effect on the ica component 3. Left panel shows its location and right chart show the difference of the correlation (ΔZ) due to the pharmacological challenge. F and P values are highlighted on top of the chart (***p <0.001,**p <0.01, *p <0.05) red crosses indicate the outliers excluded.

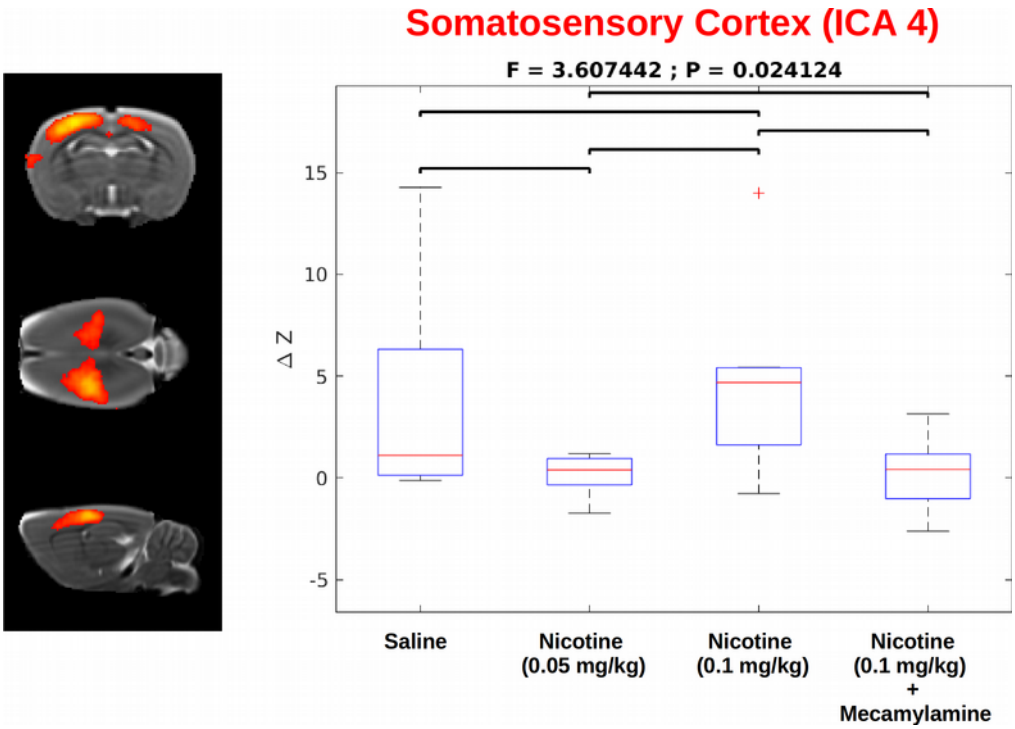

Figure 85Nicotine effect on the ica component 4 . Left panel shows its location and right chart show the difference of the correlation (ΔZ) due to the pharmacological challenge. F and P values are highlighted on top of the chart (***p <0.001,**p <0.01, *p <0.05) red crosses indicate the outliers excluded.

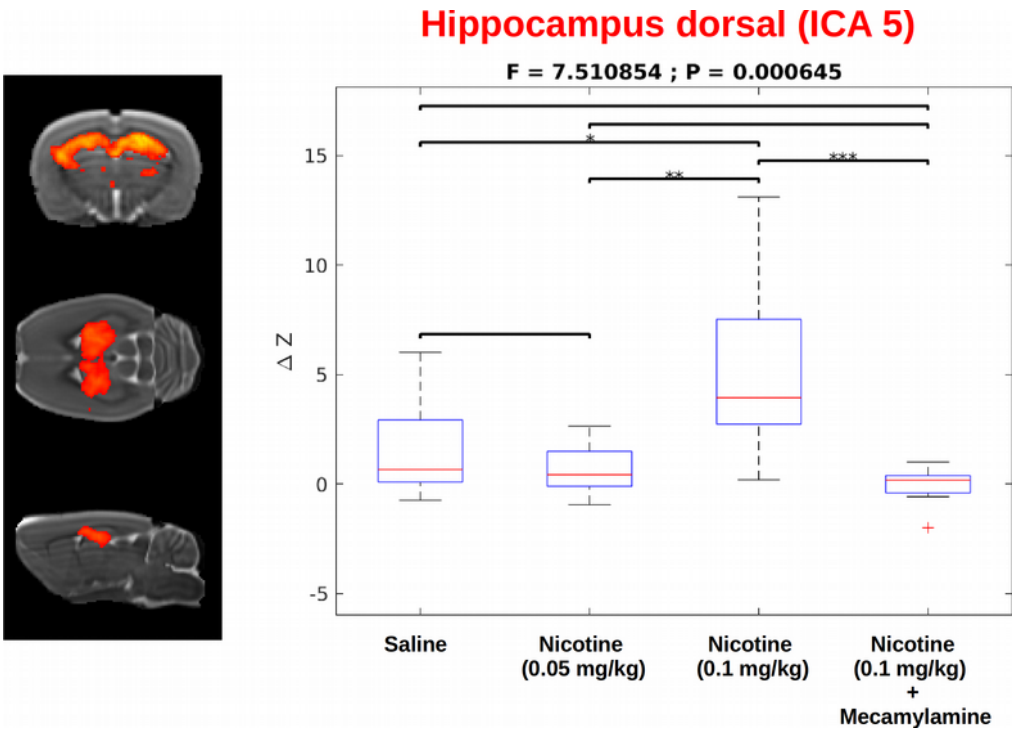

Figure 86: Nicotine effect on the ica component 5. Left panel shows its location and right chart show the difference of the correlation (ΔZ) due to the pharmacological challenge. F and P values are highlighted on top of the chart (***p <0.001,**p <0.01, *p <0.05) red crosses indicate the outliers excluded.

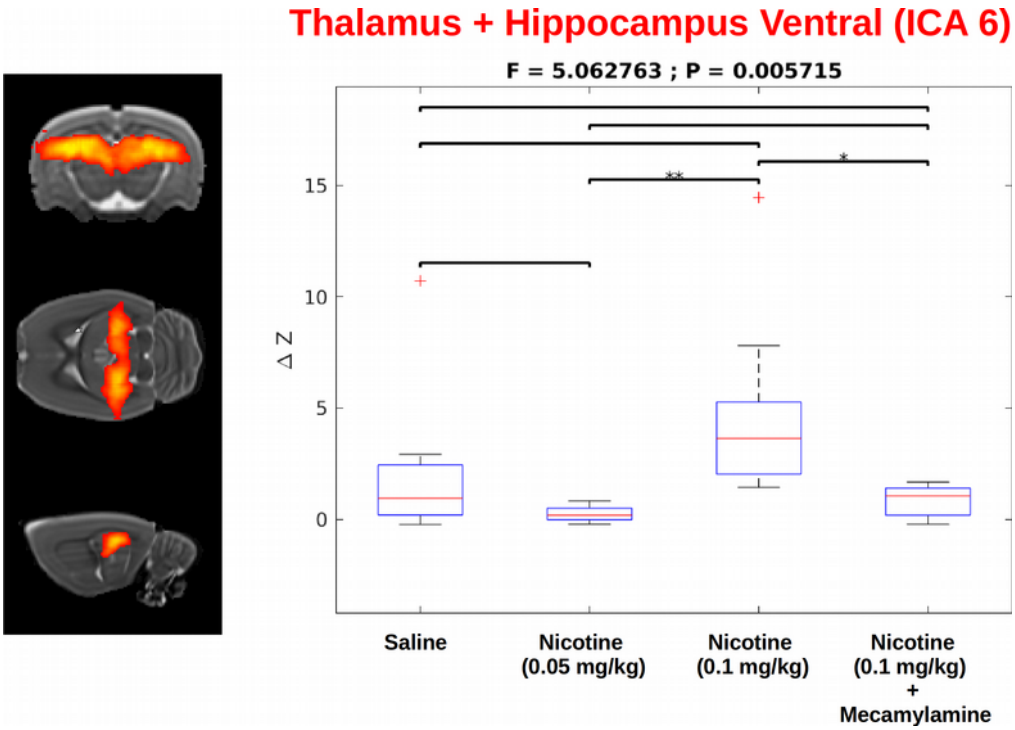

Figure 87: Nicotine effect on the ica component 6. Left panel shows its location and right chart show the difference of the correlation (ΔZ) due to the pharmacological challenge. F and P values are highlighted on top of the chart (***p <0.001,**p <0.01, *p <0.05) red crosses indicate the outliers excluded.

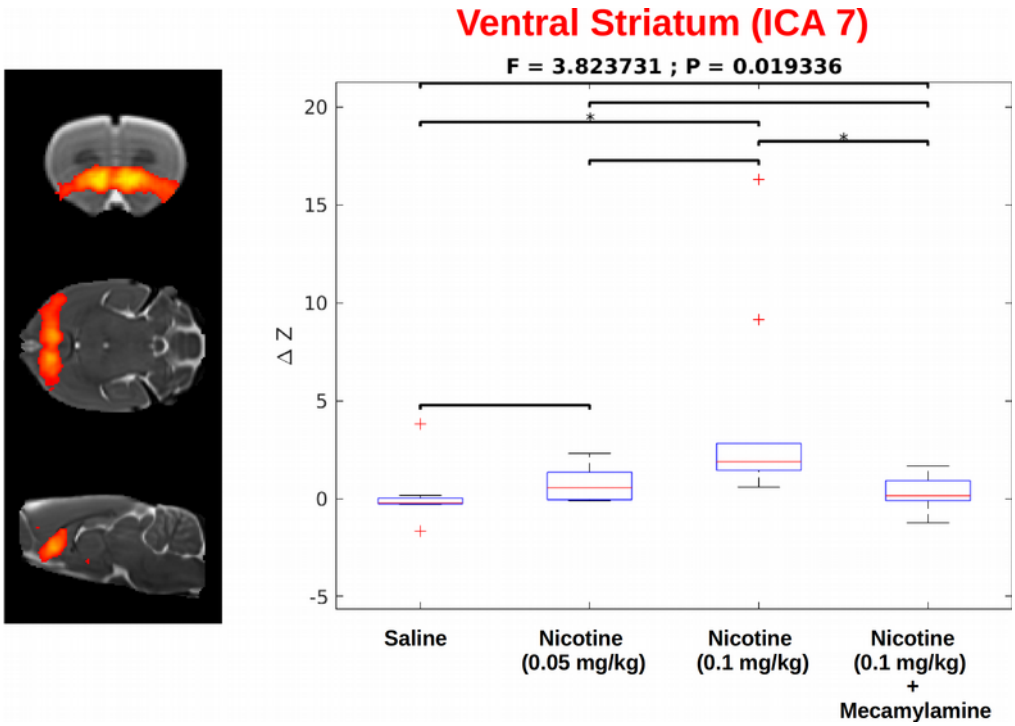

Figure 88: Nicotine effect on the ica component 7. Left panel shows its location and right chart show the difference of the correlation (ΔZ) due to the pharmacological challenge. F and P values are highlighted on top of the chart (***p <0.001,**p <0.01, *p <0.05) red crosses indicate the outliers excluded.

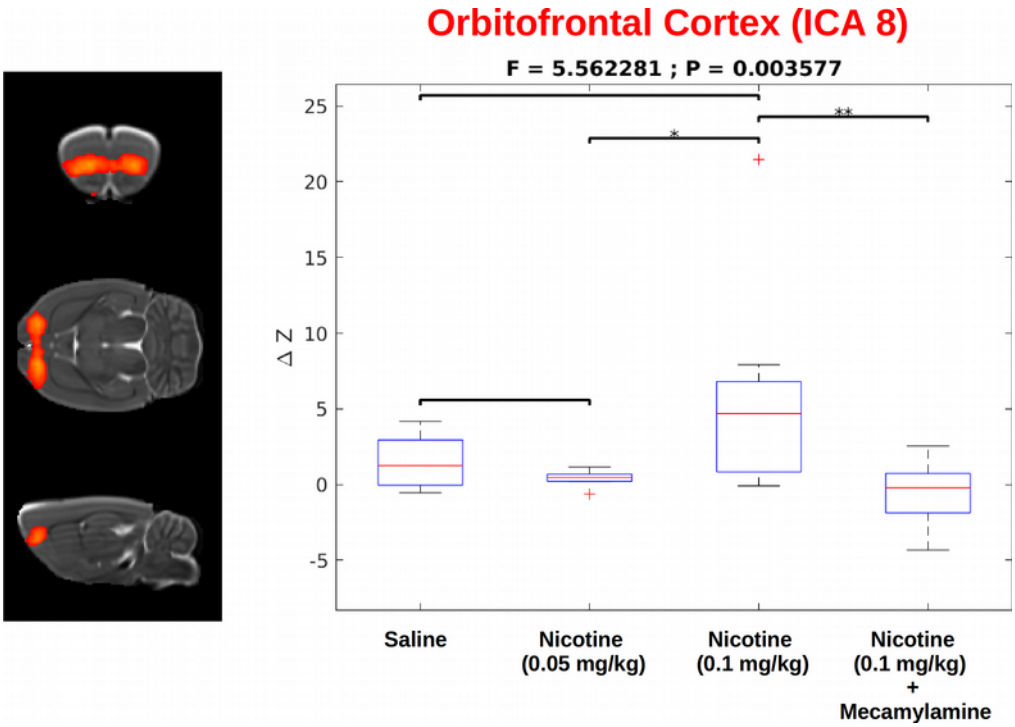

Figure 89: Nicotine effect on the ica component 8. Left panel shows its location and right chart show the difference of the correlation (ΔZ) due to the pharmacological challenge. F and P values are highlighted on top of the chart (***p <0.001,**p <0.01, *p <0.05) red crosses indicate the outliers excluded.

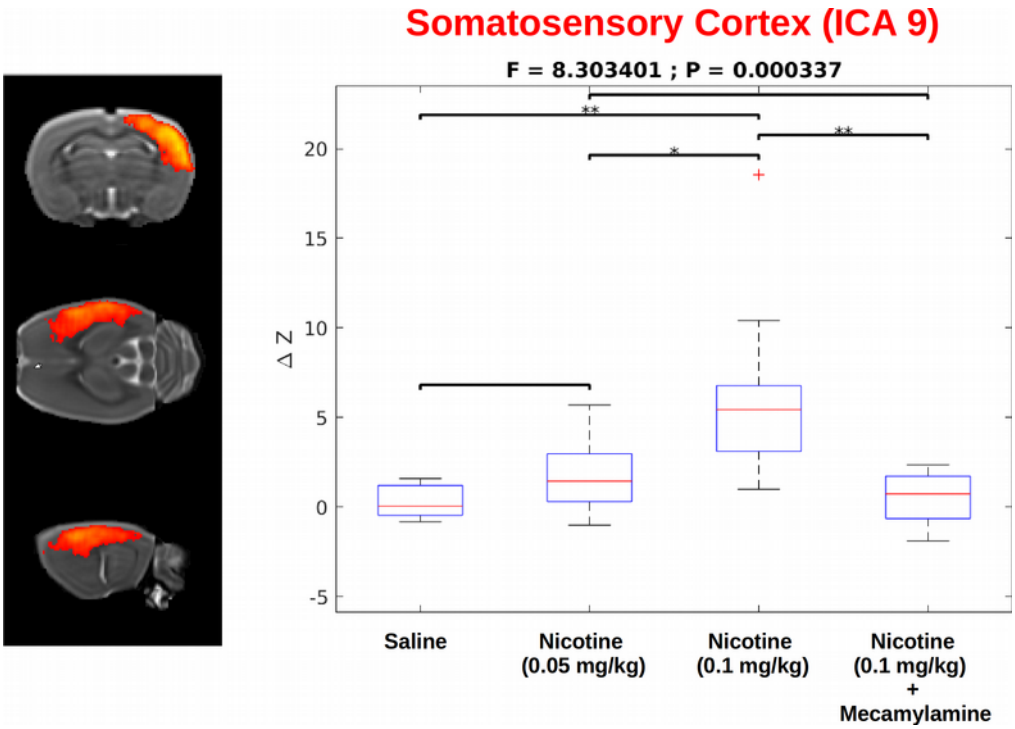

Figure 90: Nicotine effect on the ica component 9. Left panel shows its location and right chart show the difference of the correlation (ΔZ) due to the pharmacological challenge. F and P values are highlighted on top of the chart (***p <0.001,**p <0.01, *p <0.05) red crosses indicate the outliers excluded.

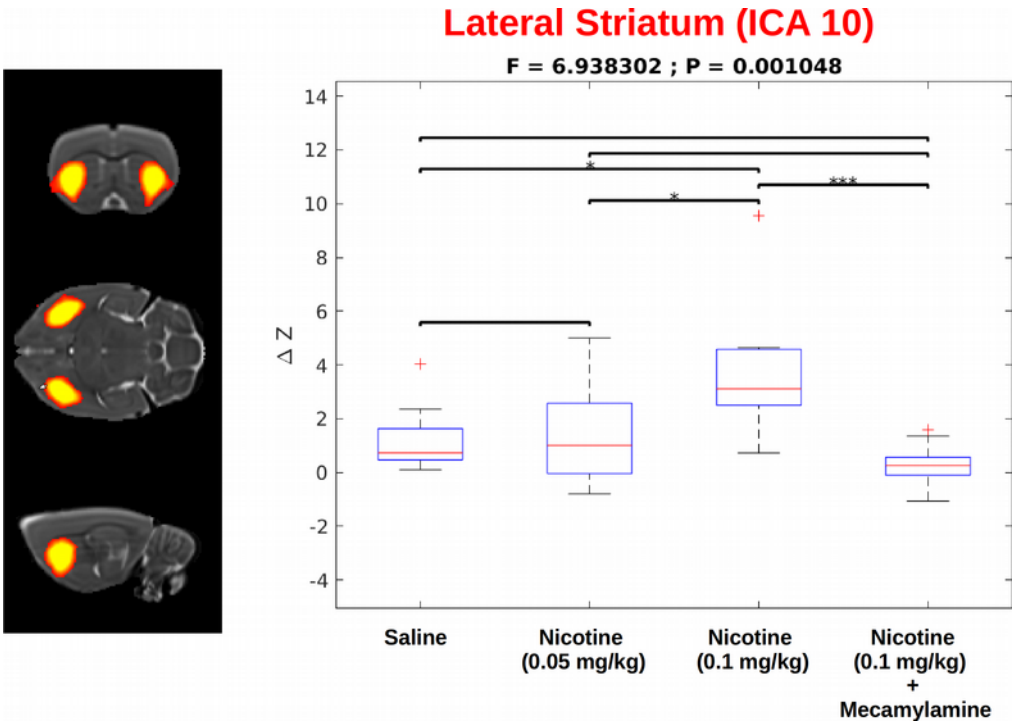

Figure 91: Nicotine effect on the ica component 10. Left panel shows its location and right chart show the difference of the correlation (ΔZ) due to the pharmacological challenge. F and P values are highlighted on top of the chart (***p <0.001,**p <0.01, *p <0.05) red crosses indicate the outliers excluded.

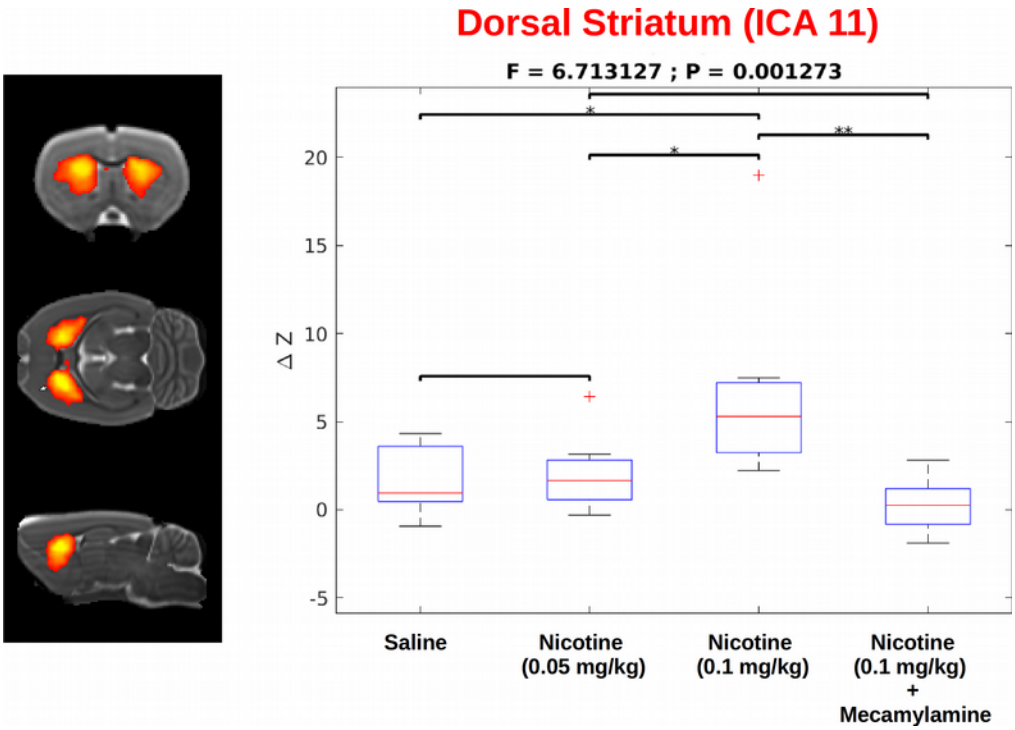

Figure 92: Nicotine effect on the ica component 11. Left panel shows its location and right chart show the difference of the correlation (ΔZ) due to the pharmacological challenge. F and P values are highlighted on top of the chart (***p <0.001,**p <0.01, *p <0.05) red crosses indicate the outliers excluded.

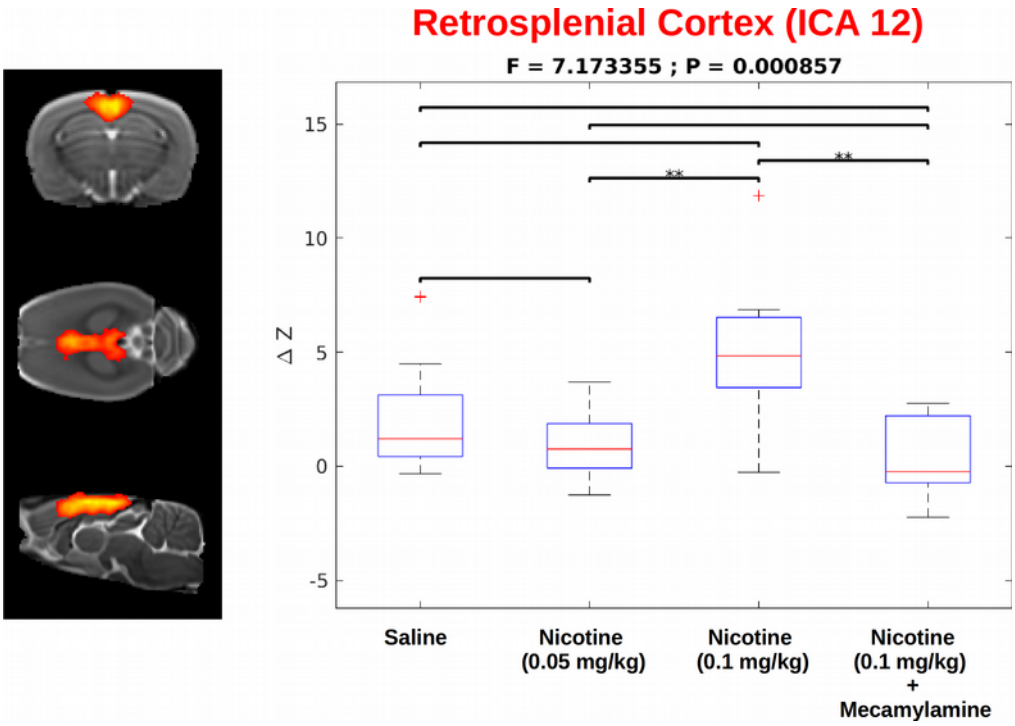

Figure 93: Nicotine effect on the ica component 12. Left panel shows its location and right chart show the difference of the correlation (ΔZ) due to the pharmacological challenge. F and P values are highlighted on top of the chart (***p <0.001,**p <0.01, *p <0.05) red crosses indicate the outliers excluded.

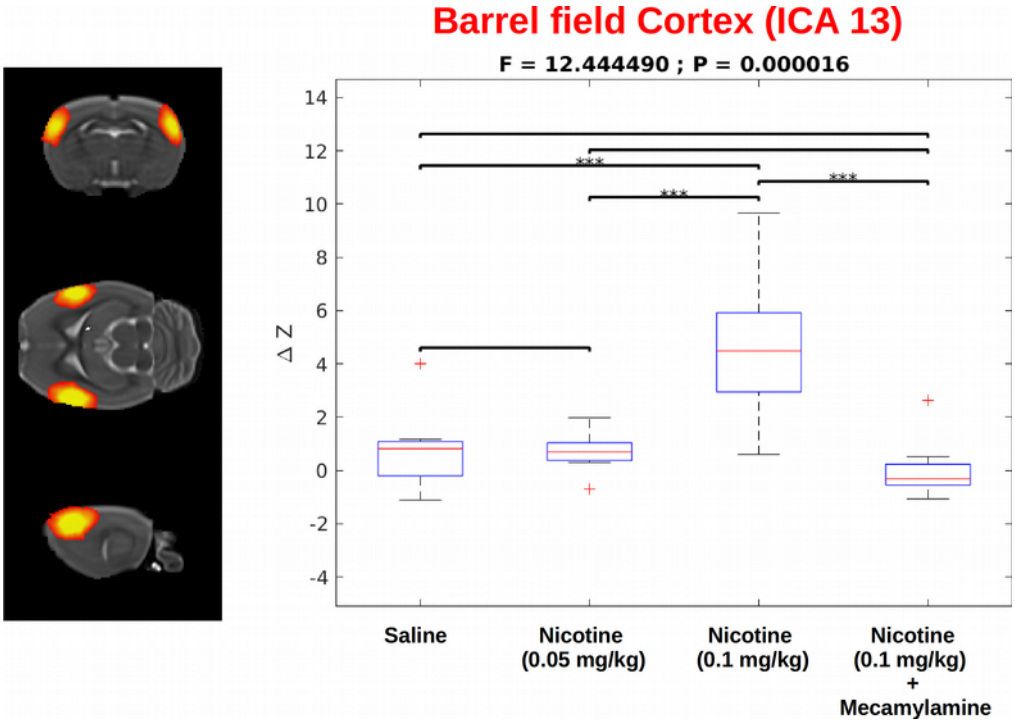

Figure 94: Nicotine effect on the ica component 13. Left panel shows its location and right chart show the difference of the correlation (ΔZ) due to the pharmacological challenge. F and P values are highlighted on top of the chart (***p <0.001,**p <0.01, *p <0.05) red crosses indicate the outliers excluded.

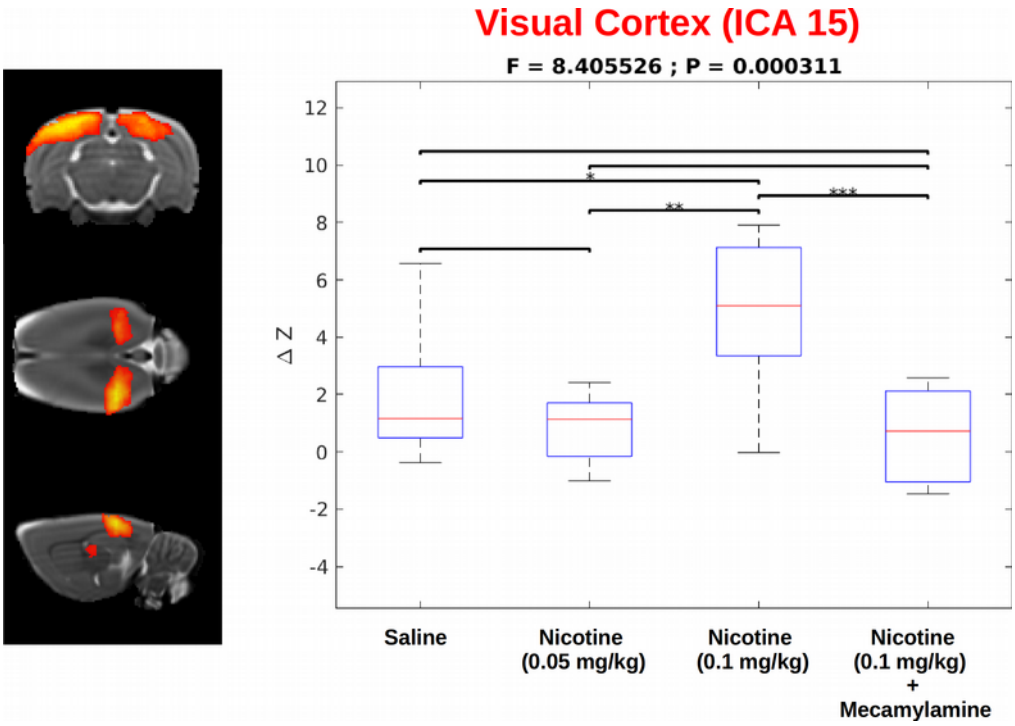

Figure 95: Nicotine effect on the ica component 15. Left panel shows its location and right chart show the difference of the correlation (ΔZ) due to the pharmacological challenge. F and P values are highlighted on top of the chart (***p <0.001,**p <0.01, *p <0.05) red crosses indicate the outliers excluded.

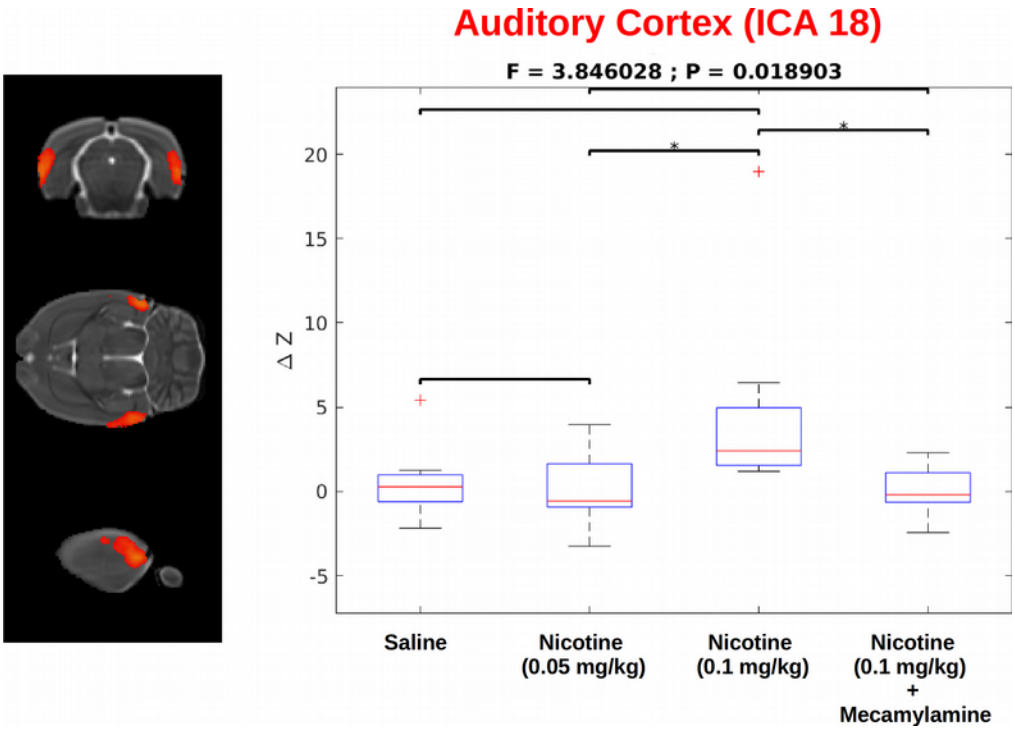

Figure 96: Nicotine effect on the ica component 18. Left panel shows its location and right chart show the difference of the correlation (ΔZ) due to the pharmacological challenge. F and P values are highlighted on top of the chart (***p <0.001,**p <0.01, *p <0.05) red crosses indicate the outliers excluded.

3.3.4 – Between component ICA analysis

Using the nets_hierarchy.m script embedded into FSLNets, it is possible to cluster the selected components to form larger resting-state networks basing on their timeseries. In Figure 97 the correlation between the time series of each component with the others 17 is denoted within each column. It can be seen that three networks were identified.

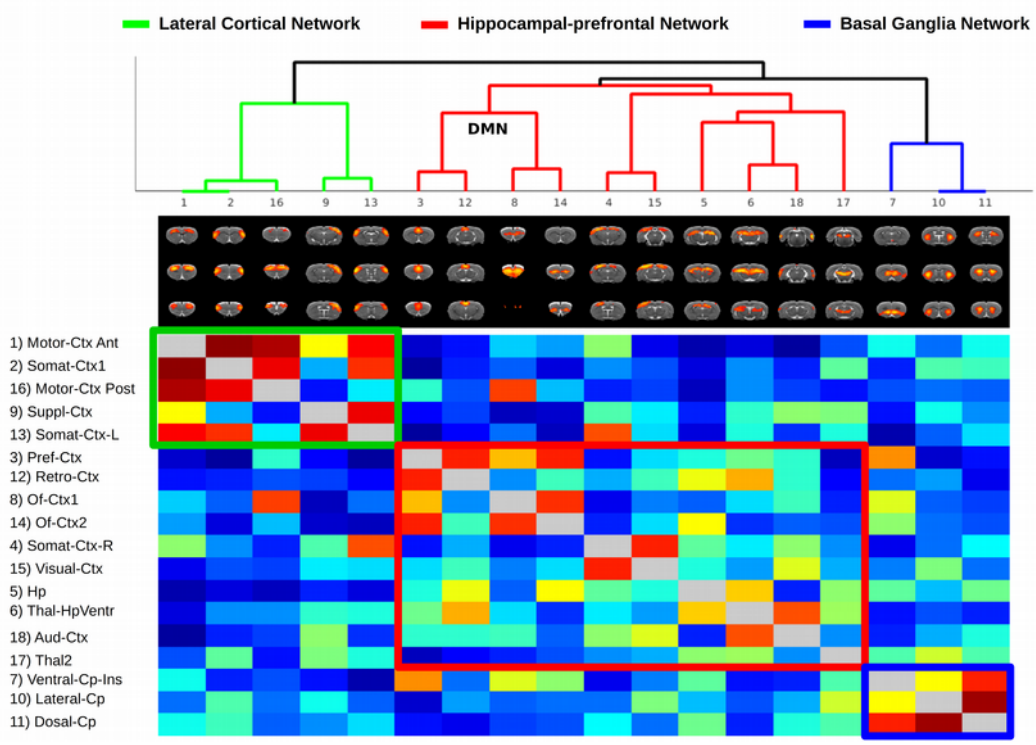

Figure 97: Hieratical network plot of the 18 selected components. Dark red indicates a highly positive correlation and dark blue represents highly negative correlation. Self-correlation is represented with gray values. On top of the matrix the tree plot represent the clustering of the networks that are also highlighted in the matrix with the same colors.

The difference of all the correlation values, shown in Figure 97, was computed between post and pre-injection (Δz) for each subject. The one-way ANOVA analysis was subsequently carried out to compare the four experimental groups. Results are shown in Figure 98 to 105. An increased synchronization between components belonging to the same network was detected. In particular, a significant increased correlation between two of the components belonging to the basal ganglia network (ICA 10 and 11) corresponding to the ventral and lateral striatum was seen after the injection of the higher dose of

nicotine (Figure 98). Similarly, a significant increased correlation between three of the components belonging to the DMN (composed by ICA 3, 12,14) was seen (Figure 99 to 101). Moreover, a significant decrease in the correlation between components belonging to different networks was seen after the injection of 0.1 g/kg of nicotine (Figure 102 to 105).

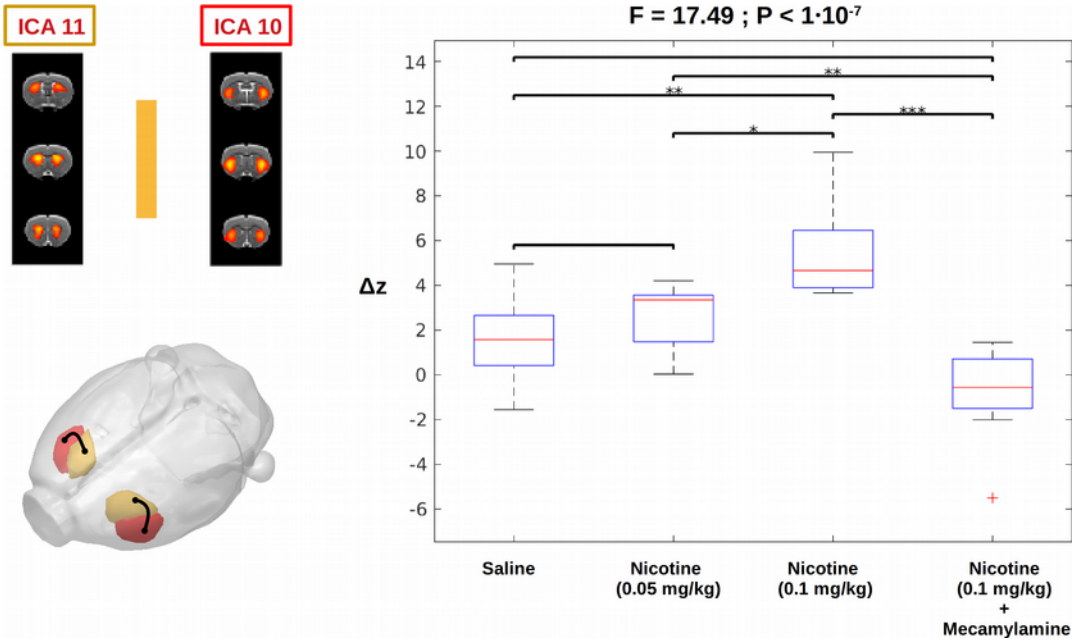

Figure 98: Effect of the nicotine administration on the correlation between component 10 and 11. Left panel represent the three-dimensional reconstructions of the two ICA considered. Results of the statistical analysis are represented in the right panel. ΔZ represents the difference in the correlation between the two components. Outliers are represented by red crosses and post-hoc tests results are indicated with ***p <0.001,**p <0.01, *p <0.05.

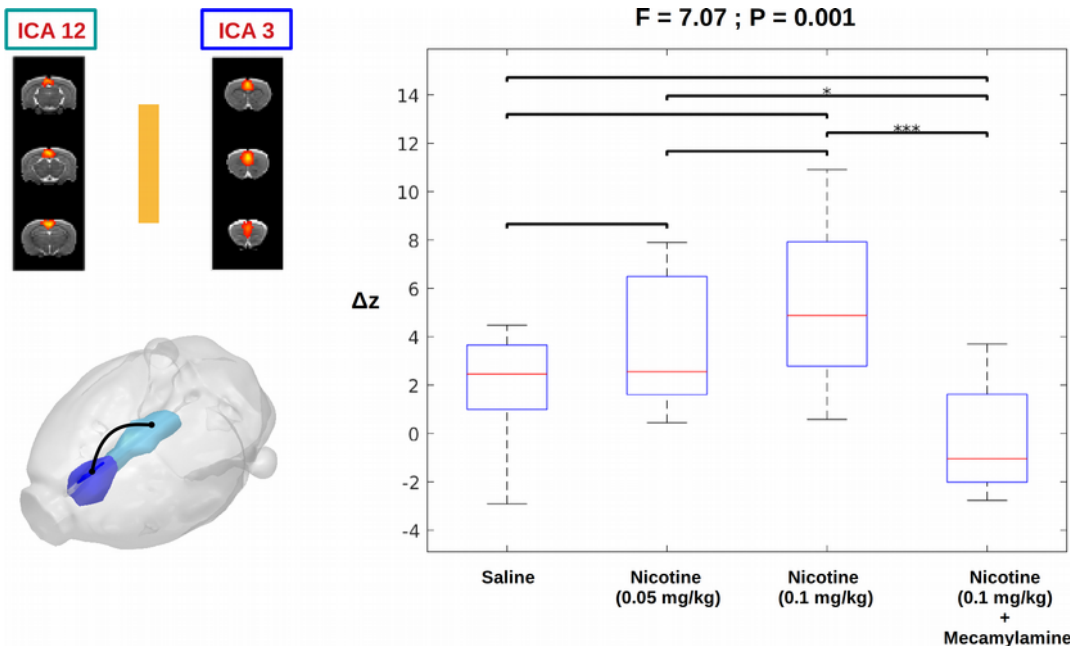

Figure 99: Effect of the nicotine administration on the correlation between component 12 and 3. Left panel represent the three-dimensional reconstructions of the two ICA considered. Results of the statistical analysis are represented in the right panel. ΔZ represents the difference in the correlation between the two components. Outliers are represented by red crosses and post-hoc tests results are indicated with ***p <0.001,**p <0.01, *p <0.05.

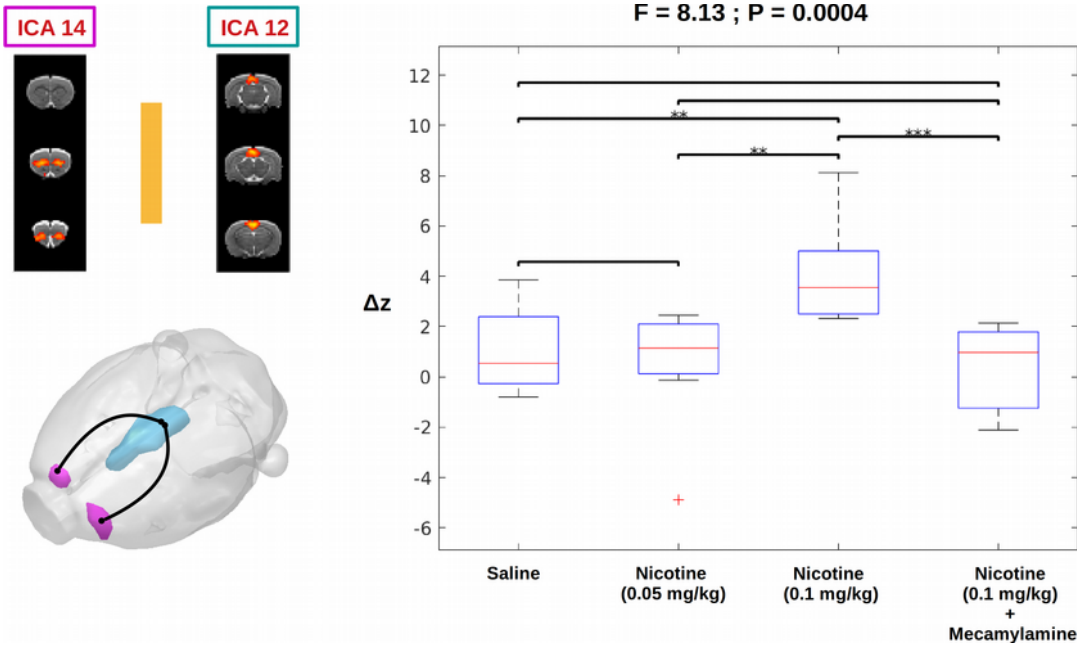

Figure 100: Effect of the nicotine administration on the correlation between component 14 and 12. Left panel represent the three-dimensional reconstructions of the two ICA considered. Results of the statistical analysis are represented in the right panel. ΔZ represents the difference in the correlation between the two components. Outliers are represented by red crosses and post-hoc tests results are indicated with ***p <0.001,**p <0.01, *p <0.05.

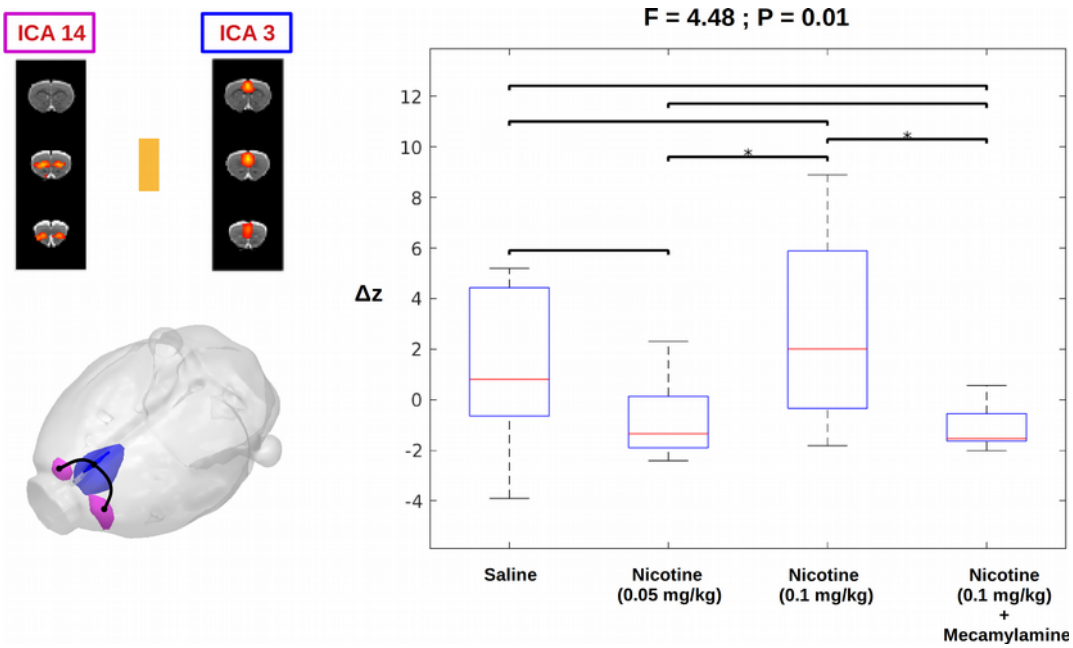

Figure 101: Effect of the nicotine administration on the correlation between component 14 and 3. Left panel represent the three-dimensional reconstructions of the two ICA considered. Results of the statistical analysis are represented in the right panel. ΔZ represents the difference in the correlation between the two components. Outliers are represented by red crosses and post-hoc tests results are indicated with ***p <0.001,**p <0.01, *p <0.05.

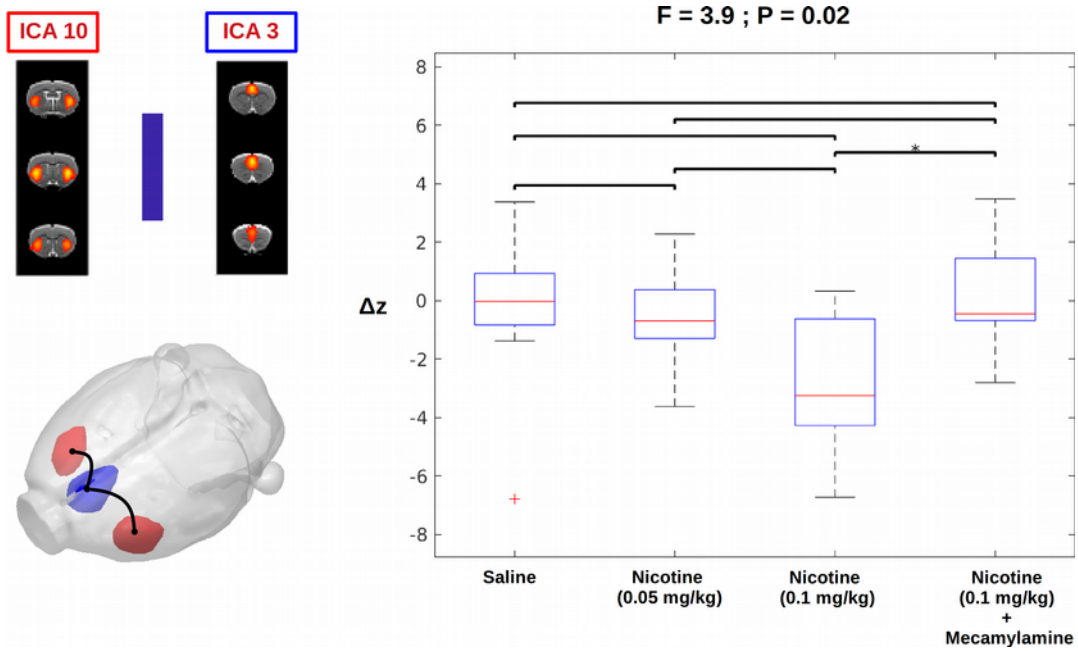

Figure 102: Effect of the nicotine administration on the correlation between component 10 and 3. Left panel represent the three-dimensional reconstructions of the two ICA considered. Results of the statistical analysis are represented in the right panel. ΔZ represents the difference in the correlation between the two components. Outliers are represented by red crosses and post-hoc tests results are indicated with ***p <0.001,**p <0.01, *p <0.05.

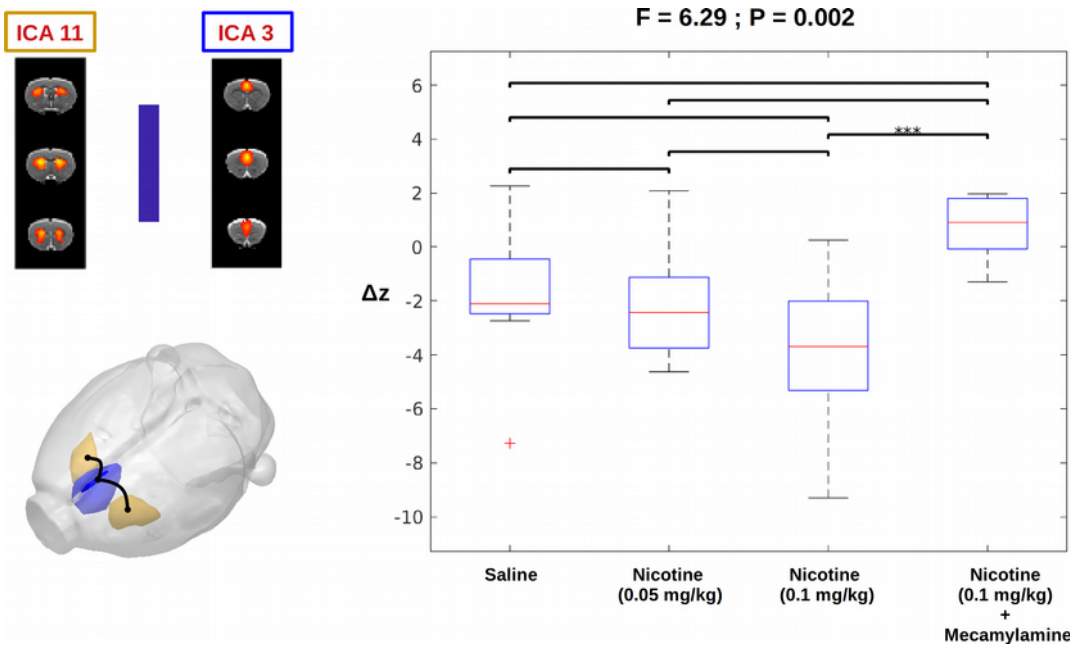

Figure 103: Effect of the nicotine administration on the correlation between component 11 and 3. Left panel represent the three-dimensional reconstructions of the two ICA considered. Results of the statistical analysis are represented in the right panel. ΔZ represents the difference in the correlation between the two components. Outliers are represented by red crosses and post-hoc tests results are indicated with ***p <0.001,**p <0.01, *p <0.05.

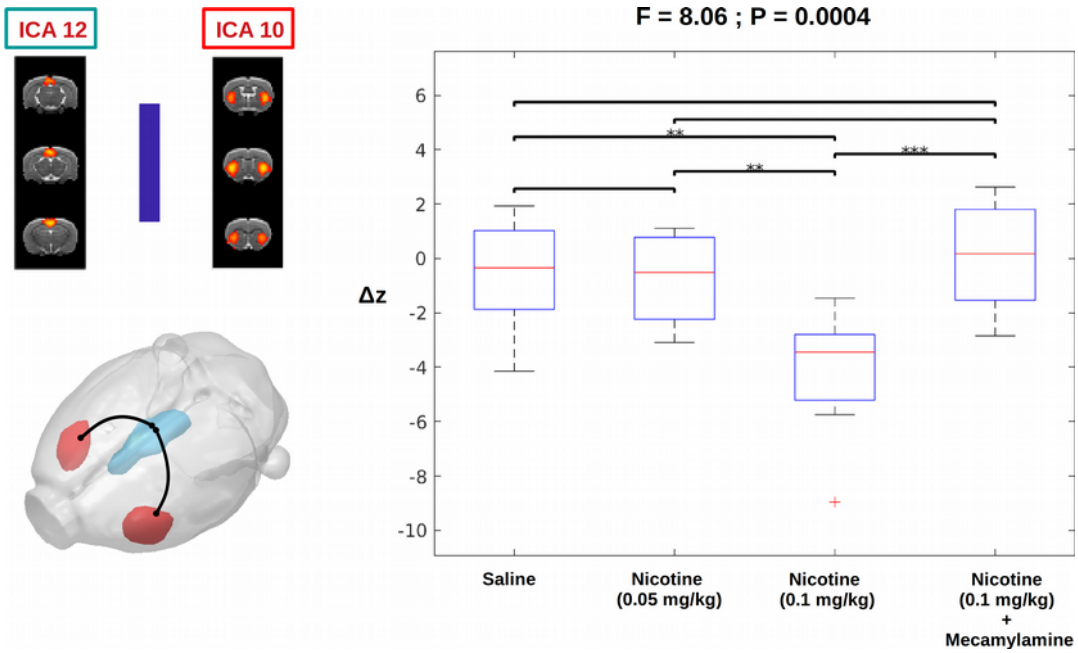

Figure 104: Effect of the nicotine administration on the correlation between component 12 and 10. Left panel represent the three-dimensional reconstructions of the two ICA considered. Results of the statistical analysis are represented in the right panel. ΔZ represents the difference in the correlation between the two components. Outliers are represented by red crosses and post-hoc tests results are indicated with ***p <0.001,**p <0.01, *p <0.05.

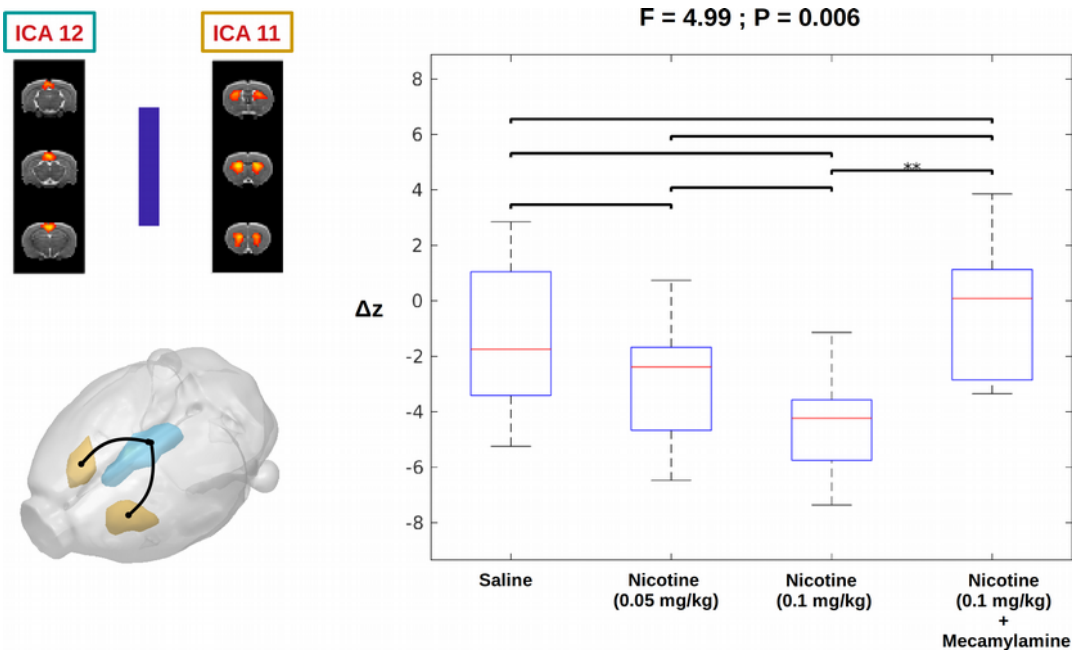

Figure 105: Effect of the nicotine administration on the correlation between component 12 and 11. Left panel represent the three-dimensional reconstructions of the two ICA considered. Results of the statistical analysis are represented in the right panel. ΔZ represents the difference in the correlation between the two components. Outliers are represented by red crosses and post-hoc tests results are indicated with ***p <0.001,**p <0.01, *p <0.05.

3.3.5 – Seed based analysis (SBA)

To assess the strength of the results obtained with the dual regression approach a SBA was carried out. This approach allow the assessment of the correlation between the time-course extracted in defined seed regions. Thus:

- A set of small seed regions of 3 × 3 × 3 voxels (corresponding to a 0,6 × 0,6 × 0,6 mm^3 volume) were selected (Figure 106) in the ventral and dorsal striatum, in the nucleus accumbens and in the region corresponding to the hippocampal-prefrontal network including the orbitofrontal, prefrontal, cingulate and retrosplenial cortices and the hippocampus (Adam J. Schwarz et al., 2013; A. J. Schwarz et al., 2013). Mean time-courses from each seed were extracted and inter-seed connectivity

matrices were obtained with FSL-Nets calculating the normalized covariance and transformed to Fisher-z scores.

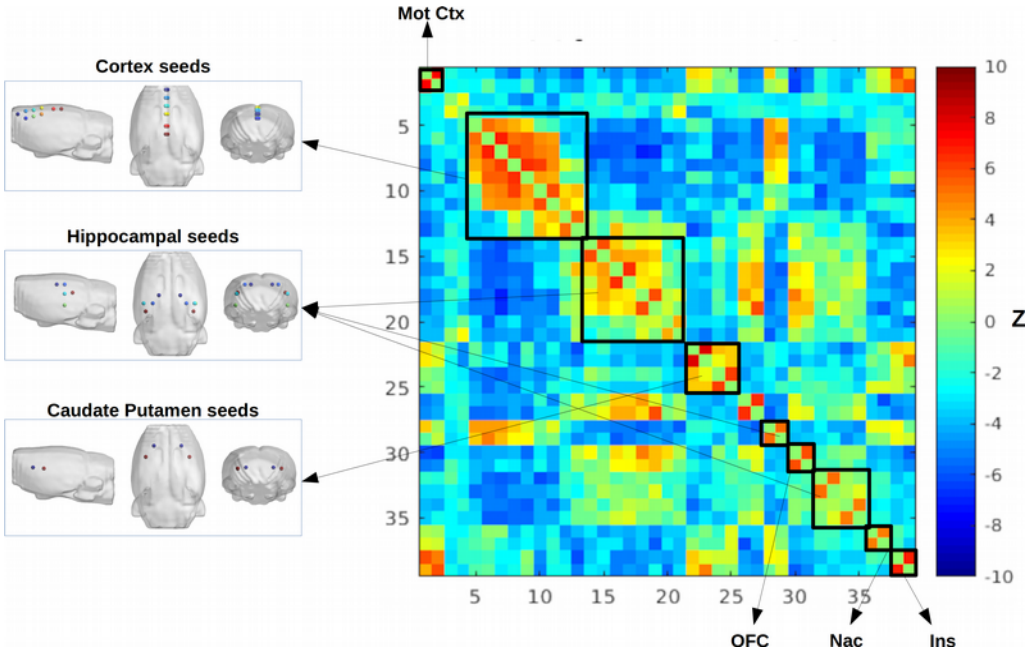

Figure 106: Seed positioning (Left) and matrix showing the mean correlation values (Z) between the timecourses extracted in the baseline acquisition. Abbreviations: Motor cortex (Mot ctx), Orbito Frontal Cortex (OFC), Nucleus accumbens (Nac) and Insula (Ins). The color-coded scale indicate positive correlations (Z > 0) with a red tonality, while negative correlation (Z < 0) are shown in a blue tonality indicating an anti-correlation between the two seed considered.

- The inter-seed connectivity matrices representing the pre-injection dataset were subtracted to the post-injection ones, obtaining a matrix of delta values for each subject.

- To evaluate the effect of the pharmacological challenge, a one-way anova was applied to compare the delta-connectivity matrices of the four groups (Figure 107).

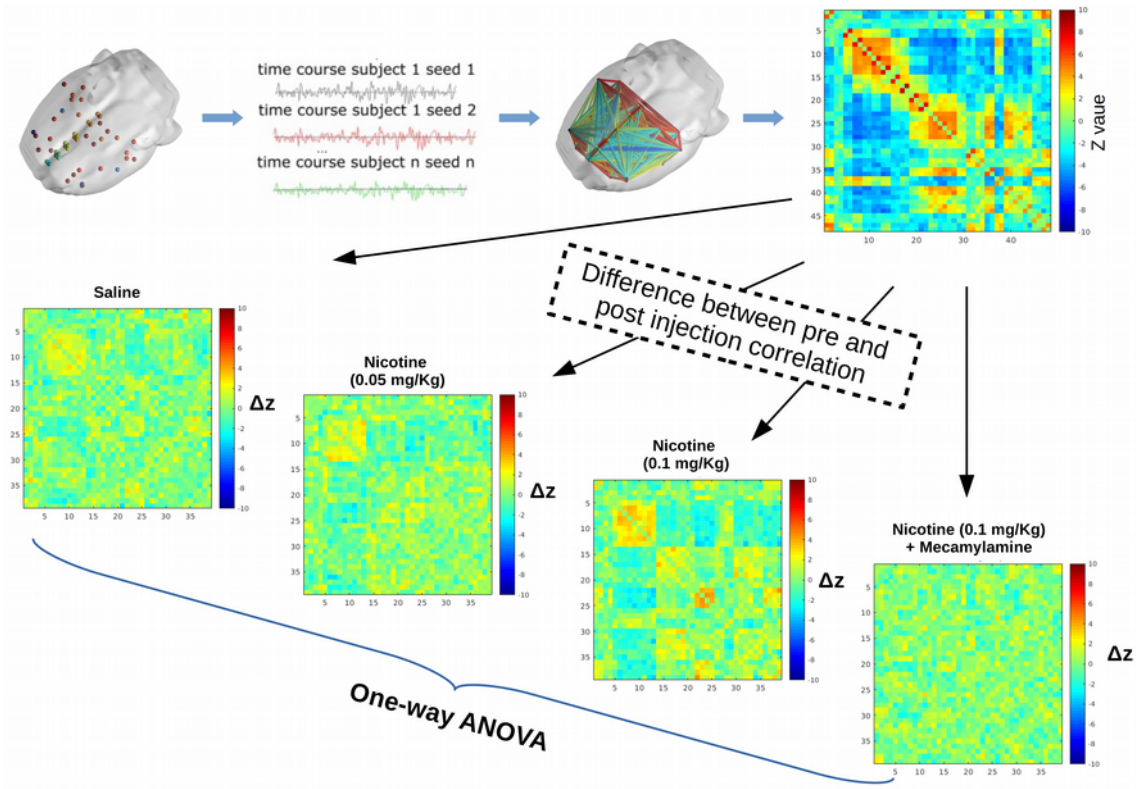

Figure 107: Seed analysis workflow. The time-course of each seed is extracted from each acquisition. The correlation between all seed is computed and the difference between pre and post injection correlation used to perform the statistical comparison.

Matrices of significance within this section are presented as (1 – P) rather than P values. Results of the SBA analysis are shown in Figure 108, it shows two matrices representing the F and P values obtained with the one way ANOVA. It can be seen that connections positioned into the cingulate and retrosplenial cortex (seeds 5 to 15), striatum (seeds 21 to 25) and hippocampal regions (seeds 16 to 20) present significantly different correlations between groups. A post-hoc tukey test was applied to connections significantly different between groups ($P < 0.95$) that are highlighted in the upper part of the matrix shown in Figure 108b.

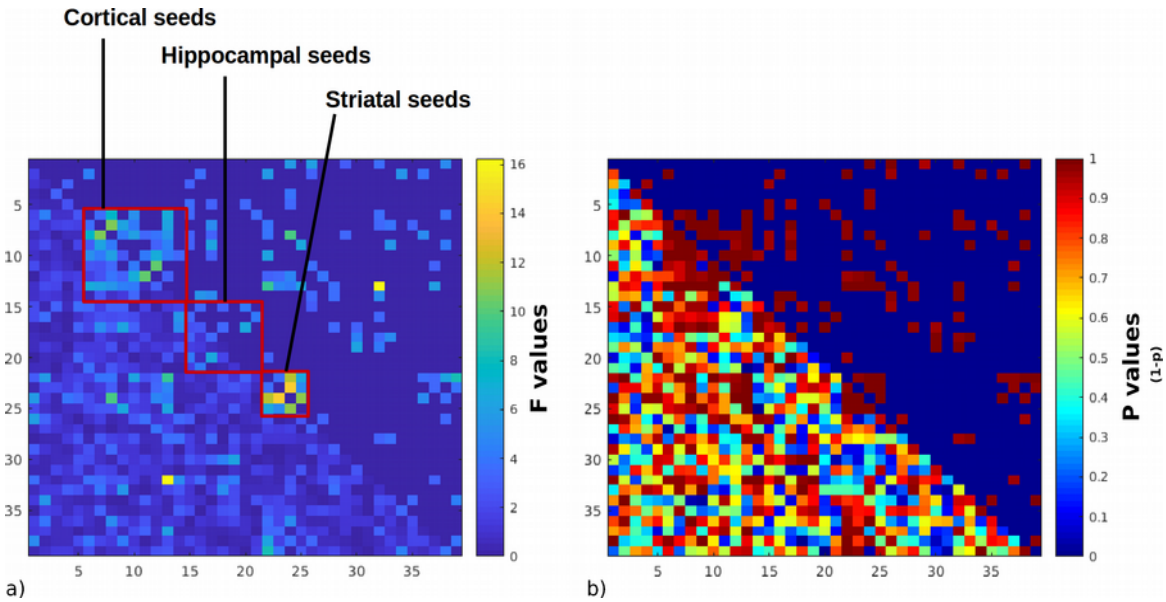

Figure 108: Matrices of the F-values (a) and P-values (b) obtained with the one way ANOVA analysis. Red squares, on the left panel, highlight the group of seeds positioned into the cortical, hippocampal and striatal regions. The upper part of these matrices contains only connections significantly different between groups [(1-P) > 0.95].

To ease the comprehension of results, the matrices representing the outcome of post-hoc tests (Figure 109 to 114) were separated into two different matrices presenting connections that increase or decrease its strength after the pharmacological challenge injection.

No significant differences are present when the group that received the saline solution was compared to the group that received 0.05g/kg of nicotine (Figure 109). Similarly, no difference were found when the group that received the saline solution was compared with the group injected with a dose of 0.1g/kg of nicotine followed by the mecamylamine dose (Figure 110). No differences was seen also when the group that received 0.05 g/kg of nicotine is compared to the group that received 0.1g/kg of nicotine followed by the mecamylamine dose. This suggests that the lower dose of nicotine does not influence the brain connectivity in rats. A statistically significant difference can be seen when rats received the 0.1 g/kg dose of nicotine (Figure 111, 113, 114). Similarly to what has been shown with the ICA analysis, seeds belonging to the same functional network show an

increased correlation after the injection of the higher dose. Thus seeds positioned within the cortical regions show increased connectivity and similarly seeds positioned within striatal regions. A decreased correlation was also seen between seeds belonging to different networks, such as seeds placed in the cingulate and retrosplenial cortex region with those placed in the striatal region.

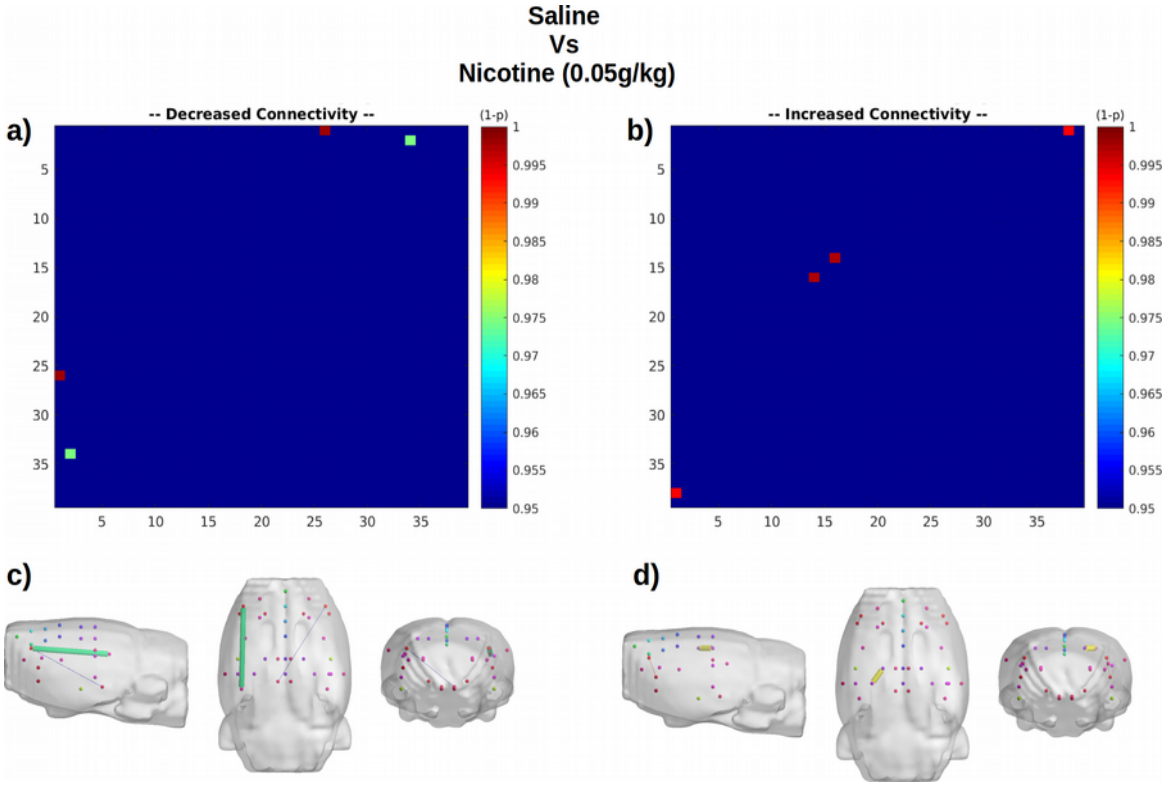

Figure 109: One way anova post-hoc analysis comparing the effect of the saline injection with the nicotine at a dose of 0.05 g/kg. (a) and (b) matrices contain connections that show significantly decreased and increased correlations. (c) and (d) show the three-dimensional representation of the above matrices.

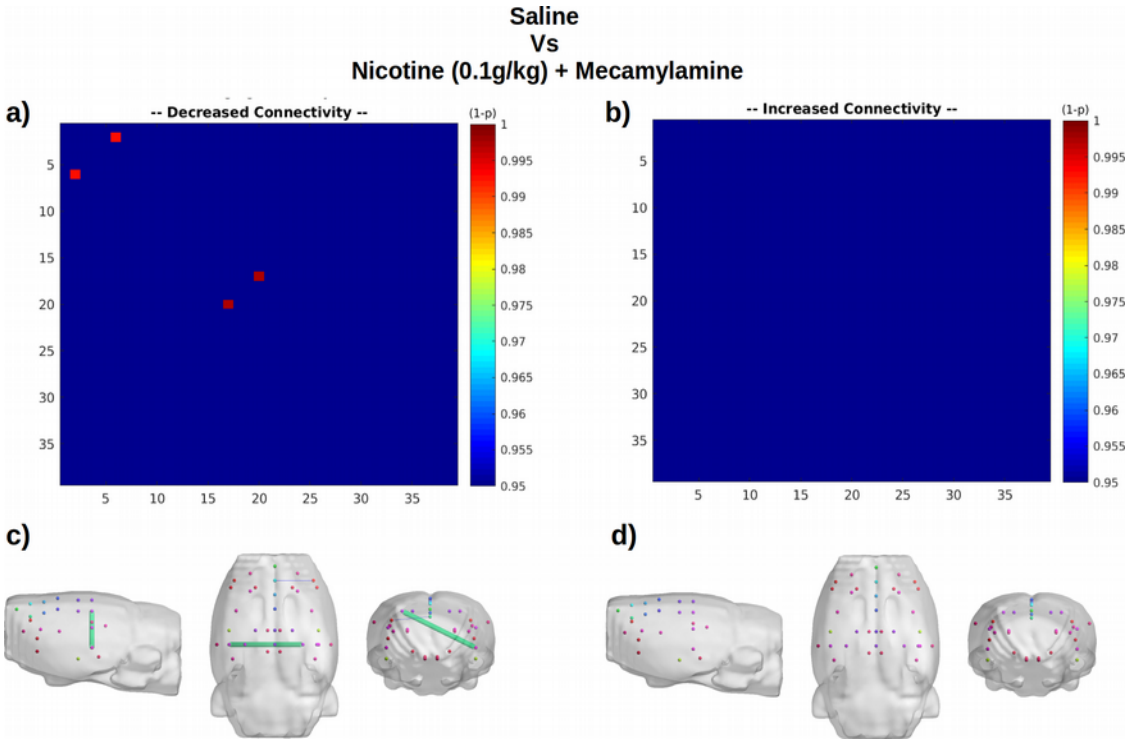

Figure 110: One way anova post-hoc analysis comparing the effect of the saline injection with the nicotine at a dose of 0.1 g/kg followed by the mecamylamine injection. (a) and (b) matrices contain connections that show significantly decreased and increased correlations. (c) and (d) show the three-dimensional representation of the above matrices.

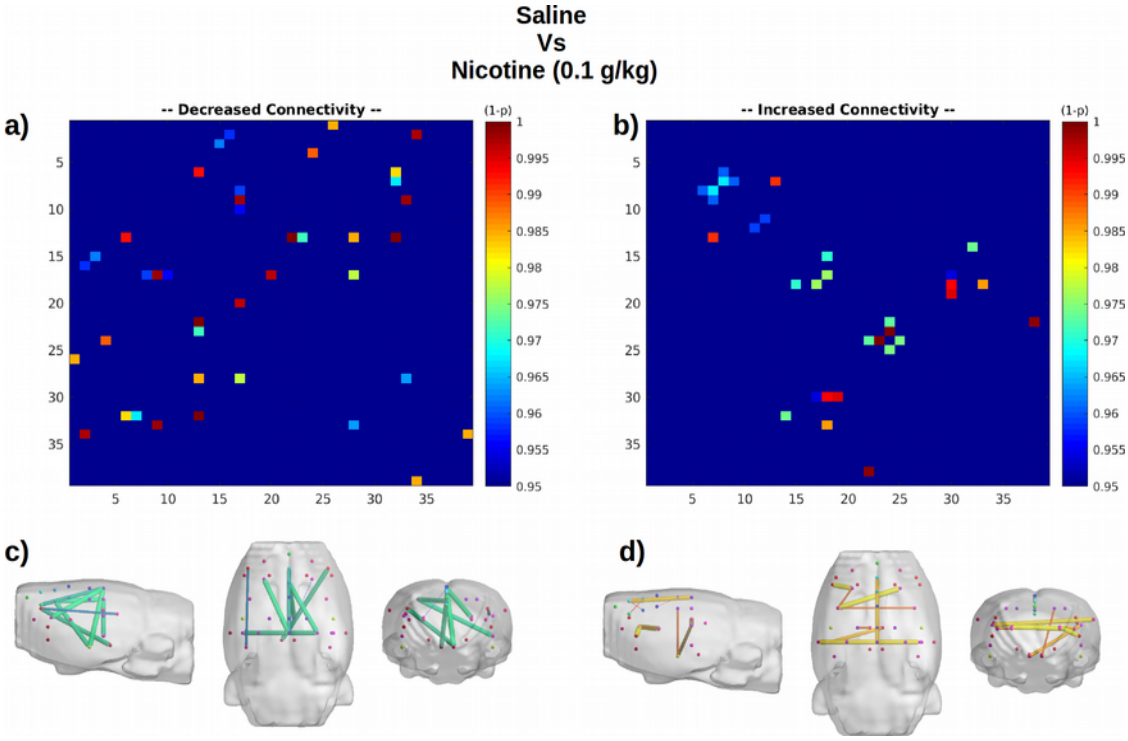

Figure 111: One way anova post-hoc analysis comparing the effect of the saline injection with the nicotine at a dose of 0.1 g/kg. (a) is the matrix and (c) the three-dimensional representation of the connections showing significantly decreased correlations between cortical and hippocampal seeds. Increased correlations within cortical and within striatal regions are shown in (c) and (d).

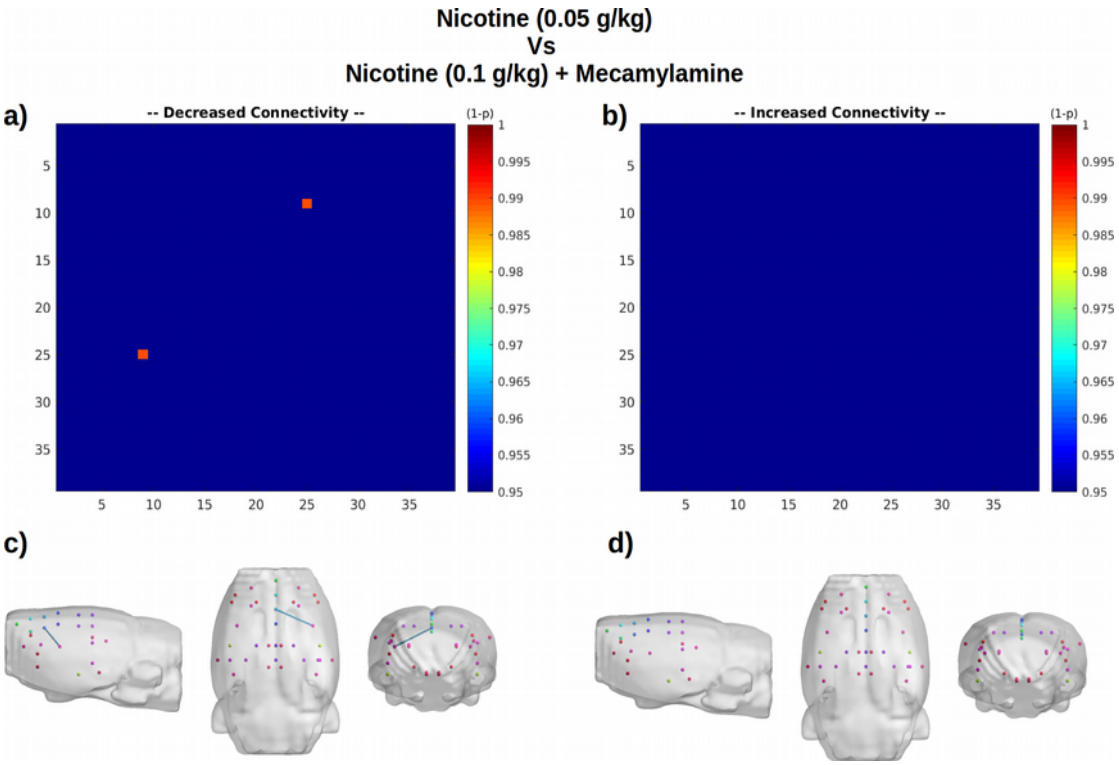

Figure 112: One way anova post-hoc analysis comparing the effect of the nicotine at a dose of 0.05 g/kg with the nicotine at a dose of 0.1 g/kg followed by the mecamylamine injection. (a) and (b) matrices contain connections that show significantly decreased and increased correlations. (c) and (d) show the three-dimensional representation of the above matrices.

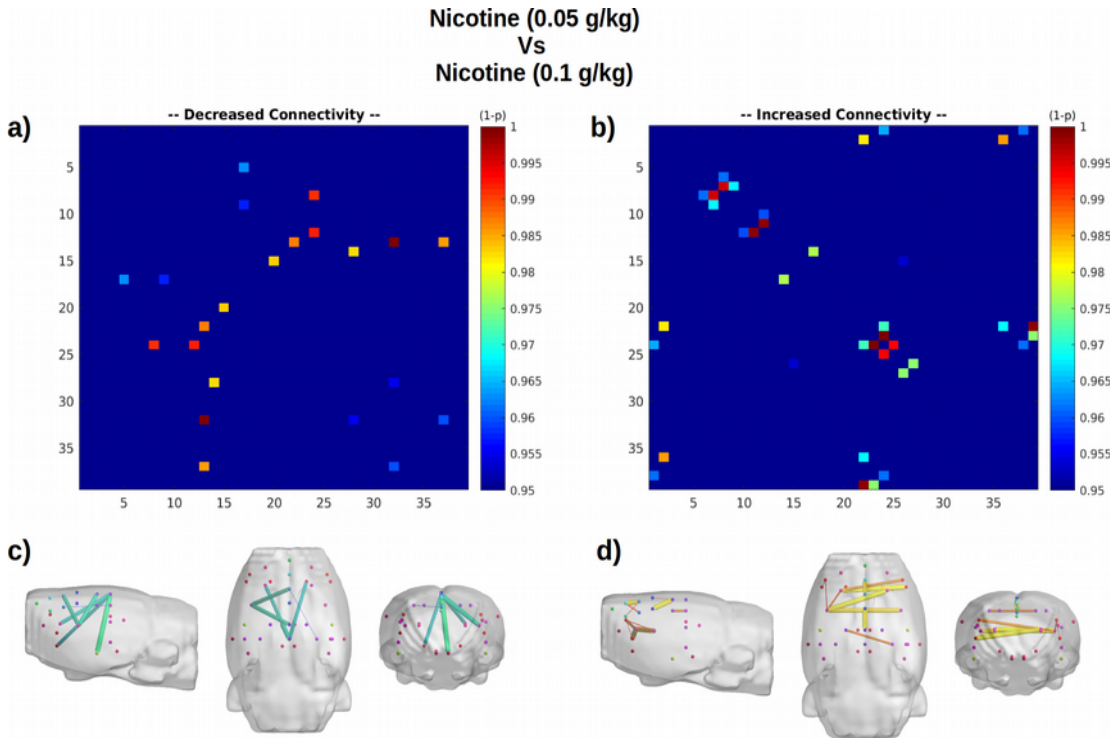

Figure 113: One way anova post-hoc analysis comparing the effect of the nicotine at a dose of 0.05 g/kg with the nicotine at a dose of 0.1 g/kg. (a) and (b) matrices contain connections that show significantly decreased and increased correlations. (c) and (d) show the three-dimensional representation of the above matrices.

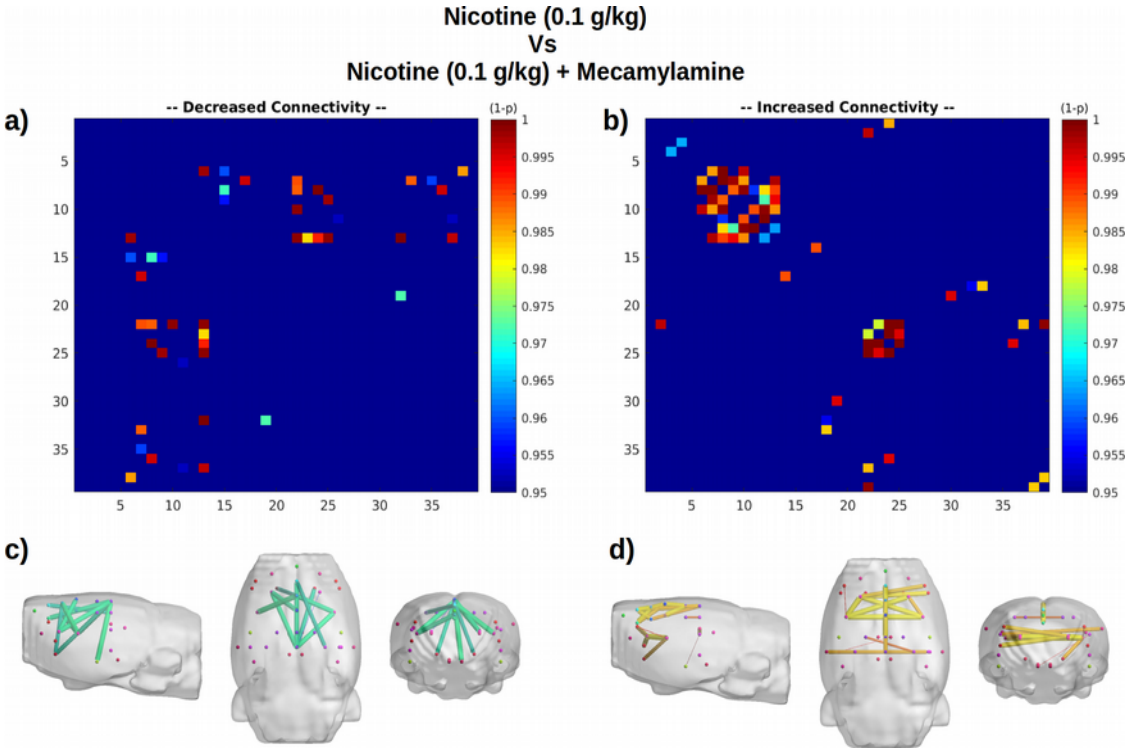

Figure 114: One way anova post-hoc analysis comparing the effect of the nicotine at a dose of 0.1 g/kg with the nicotine at a dose of 0.1 g/kg followed by the mecamylamine injection. (a) and (b) matrices contain connections that show significantly decreased and increased correlations. (c) and (d) show the three-dimensional representation of the above matrices.

3.3.7 – Summary (3)

The translation of an optimized rsfMRI analysis pipeline, that was recently introduced within the frame of the Human Connectome Project, was shown within this section. This pipeline include a preprocessing step, carried out with the FSL-FIX software aimed to clean the noise components induced by respiration and cardiac movement, and a post processing step, to assess the functional connectivity. The two widely adopted post-processing procedures (the dual-regression and the seed analysis) have been described and evidences that these are able to provide similar outcomes given. The reliability of the analysis pipeline adopted was assessed through a preliminary experiment that was carried out using rats instead of mice. This choice has been taken to ease the experimental conditions. The use of rats present different experimental advantages such as the size of

the brain and the better signal to noise ratio of the available surface coil. Moreover, to alter the functional connectivity of healthy rats a pharmacological challenge of nicotine has been injected and the effect of the doses investigated.

Results shown highlight that the application of the presented analysis pipeline have enabled the detection of an altered functional connectivity due to the acute nicotine administration with a dose of 0.1 mg/kg. We could infer that the observed variations are caused by the nicotine injection since no differences have been observed with the saline challenge or when a mecamylamine, a non-selective and non-competitive antagonist of the nicotinic acetylcholine receptors (nAChRs), was administered after nicotine. Since the described functional alterations were obtained with two different post-processiong procedures, the ICA and the SBA, we can confirm that the experimental set-up adopted was reliable.

The goodness of results obtained is supported also by the fact that the maps shown (Figure 115) present a robust anticorrelations between midline DMN-like regions and lateral cortical areas, which is a fundamental feature of the DMN previously described also in mice and humans (Adam J. Schwarz et al., 2013; Gozzi and Schwarz, 2016).

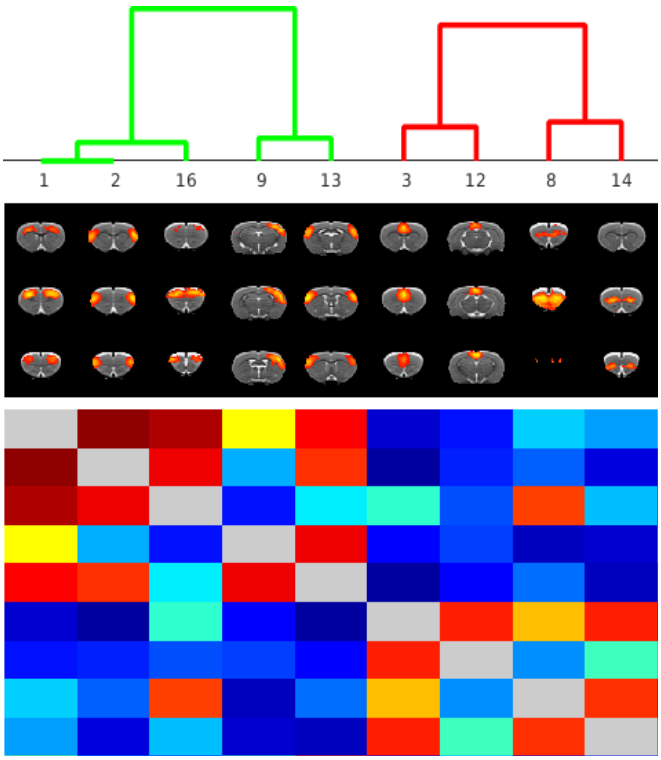

Figure 115: Cropped version of Figure 30 showing the measured anti-correlation between the cortical components (ICA3, 12) and the lateral network components (ICA 1,2,9,13,16)

Chapter 4 – Discussion and Conclusions

The objective of this thesis was to develop a multi-parametric framework of MRI techniques and operator independent analysis workflows able to describe most of the pathological alterations of the AD.

4.1 – Technical advancements

The major finding of the work was that the 2DG-CEST technique enabled, for the first time in a transgenic mouse model of AD, the detection of the impaired brain metabolism. Compared to the only previously published study on an AD mouse model (Wells et al., 2015), we focused on the region of the Z-spectrum affected by the presence of hydroxyl protons belonging to the 2DG. Since it is not metabolized, it remains internalized in the cells longer than glucose and it can be used to enhance the technique sensitivity. Our result indicates that the CEST technique is able to highlight a reduction of 2DG brain uptake at 20-month-old of age in the APP23 mice compared to WT mice. Differences in the brain metabolic activity can be detected within a few minutes after the injection of 2DG, and persisted for over an hour (Figure 47 and 52) in the cortex area. The blood 2DG contribution could be considered negligible and the increase in CEST asymmetry is mainly due to the extra-vascular concentration of 2DG and its metabolic product (2DG6P), which accumulates in cells. To our knowledge, only one study has been published in the APP23 mice with [^{18}F]FDG-PET, showing no changes in glucose metabolism at 13 months of age (Heneka et al., 2006). Moreover, even if hypometabolism is one of the earliest events in a subclinical stage of the pathology and progresses with age

(Mosconi et al., 2010, 2009), studies in AD mice models with [^{18}F]FDG-PET show a complex framework (see Table 2). The variability between these studies may be linked both to the intrinsic heterogeneity of transgenic mouse models and to issues related to differences in microPET acquisition parameters. Environmental factors (e.g. temperature, fasting time, stress level) could also affect mouse metabolism adding variability between different studies (Deleye et al., 2016; Goertzen et al., 2012; Kuntner et al., 2009).

The described analysis pipeline have further advantages such as the automatic and robust data analysis. The correction of B_0 and B_1 inhomogeneities (done here using a WASABI (Schuenke et al., 2016) sequence) is essential in order to translate the technique to humans, where static and excitation fields may present wide variability over the whole brain. The co-registration of GCE maps on a brain template enable to avoid mistakes due to manual tracing and permits a voxel-wise analysis.

Besides the steady-state acquisition, a dynamic acquisition covering the first 15 minutes after 2DG infusion was also acquired. We calculated the AUC_{Dyn} and no significant differences were detected in the dynamic acquisition during the infusion but there seemed to be a clear trend toward a more pronounced delivery of glucose in wild-type mice than transgenic mice at 20 months of age (Error: Reference source not found and 50). The interpretation of dynamic data is less straightforward than data obtained at longer times. To reduce the sampling time and to observe dynamic changes in the blood flow, it is not possible to acquire the whole Z-spectrum and integrate it. The acquisition of a single saturation frequency repeated every 9 seconds is hindered by the impossibility of B_0 and B_1 corrections, making this kind of measurement much more sensitive to fluctuations, leading to less robust results. Analyzing the Z-spectrum with a multi-pool fitting procedure permits the calculation of the asymmetry curve over a region of interest in the frequency offsets, reducing the noise contribution in the evaluation of the effects

observed. The signal change in the proximity of the injection may be the result of a mixed concentration of 2DG between extracellular glucose and the plasma fraction still present. Similarly the ventricles show an increased signal detected immediately after the injection through the dynamic acquisition. This effect disappears by the time of the first Z-spectrum acquisition (14 min after injection) which might be explained by a washout of 2DG from the ventricles where no accumulation is expected.

Few limitations in the reported study are present. Firstly, anesthesia is needed in preclinical studies, but it can inhibit glucose uptake in the brain (Lundgaard et al., 2015; Toyama et al., 2004); the use of a mechanical ventilator could help to control physiological parameters and reduce the variability. Secondly, adopting slightly different saturation procedures, like the spin-lock, it would be possible to use higher saturation power and shorter irradiation pulses enhancing the sensitivity of the technique and thus the use of lower 2DG doses (Jin and Kim, 2014; Jin et al., 2016). A similar approach has already been tested in oncology in humans (Paech et al., 2017; Schuenke et al., 2017a). Lastly, the detection of fast-exchanging OH-proton groups could become difficult at field strength lower than 7T making difficult the translation of this technique to clinical scanners which are commonly 1,5 or 3T (van Zijl et al., 2018).

Alongside with the longitudinal 2D-CEST study a multi-parametric MRI study has been carried out on the same cohort of mice to characterize their brain morphology, the brain structural connectivity and whether alterations in the T2 relaxation time are present. No differences in the brain morphology of APP23 mice were detected in our study or have been previously described in literature. Even if the APP23 is a transgenic model that has been widely adopted in research studies, this is not an unexpected result. As shown in Table 2, brain atrophy is often a minor component of the transgenic mice phenotype and sometimes it is not present when single transgenic models are studied (Borg and Chereul,

2008). Indeed, there are different methodological aspects that must be taken into account with such studies. The small size of mice brain and the low image contrast between GM and WM make the exact estimation of the volume shrinkage difficult. To overcome these limitation, the imaging of post-mortem brains have been adopted to increase the quality of results since it can boost the signal-to-noise ratio, as there is no motion, longer scan times can be acquired and the use of contrast agents in high concentrations is allowed (Holmes et al., 2017). However, the use of live animals do not suffer of distortions and dehydration from fixation, which may afflict the integrity of the tissues. More importantly, in-vivo imaging permits longitudinal studies and the reduction of animal needed in research. To increase the quality of in-vivo images, it become fundamental the use of cryogenic coils enabling the increase of the signal and contrast within acquisition times coherent with the length of the anesthesia (Baltes et al., 2009). Beside, the adoption of automated analysis procedures originally developed in human research can be a valuable tool since voxel based approaches able to determine atrophy more accurately by using stereotactic maps of the brain regions. Such analysis procedures have also the advantage to be operator independent and to ease the burden of time-consuming manual delineation of ROIs increasing the reproduciblity of results.

In addition to mouse studies, a preliminary rsfMRI experiment was performed in rats. The advantageous experimental condition enabled by the use of rats enabled the development of a reliable analysis pipeline that was translated directly from human studies. Results described highlight that the application of the presented analysis pipeline have enabled the detection of an altered functional connectivity due to the acute nicotine administration with a dose of 0.1 mg/kg. Previously published studies were not able to detect significant variations below a dose of 0.3 mg/kg (Bruijnzeel et al., 2014; Gozzi et al., 2006). For the first time in rats, a decreased functional connectivity between the

prefrontal cortex and the striatum after the injection of nicotine was shown. The same networks have been found to be involved in human studies of addiction (Janes et al., 2012).

4.2 – Relevance in AD research

The description of the AD pathology and the understanding of its causes is complicated by the concomitant presence of different events; such as the accumulation of the Aβ peptide as extracellular plaques and of the intracellullar NFT but also the presence of chronic neuroinflammation and astrogliosis. The failure of several trials (Mangialasche et al., 2010) have shown how it is difficult to treat symptoms after the disease onset and that cognitive skills are not easily recovered at later stages. Newly discovered treatments should be administered several years before the onset of the pathology to be effective, since Aβ deposition starts before the cortical tau pathology and the onset of clinical symptoms. Within this frame, the use of transgenic models could ease the development of new imaging biomarkers enabling the anticipation of the diagnosis and making new treatments more effective (Marizzoni et al., 2013).

Thus, in spite of the limitations characterizing the 2DG-CEST technique, it offers a promising alternative [^{18}F]FDG-PET for the study of neurodegenerative diseases avoiding the need of radioactive tracers.

Moreover, developing automatic analysis pipelines to study longitudinally the brain morphological alterations in transgenic mice it is possible to identify homologous imaging biomarkers in humans and mice, key elements to predict reliable results in drug testing.

In the end, the study of the brain functional connectivity by means of rsfMRI imaging is playing a fundamental role in the study of AD as functional alterations are the primary events occurring the pathological cascade. Resting state fMRI in AD patients has revealed decreased functional connectivity between numerous cortical brain regions and the hippocampus (Greicius et al., 2004; Sheline et al., 2010). Thus, the interest in fMRI studies of AD transgenic models has recently increased because such they were able to observe deficits in the hippocampus and/or in the cortex of transgenic mice, sometimes at early ages (Asaad and Lee, 2018)..

4.3 – Future perspectives

I hope that the presented work will be a useful starting point for future investigations. Different MRI acquisitions and analysis pipelines have been proposed. With these, the AD transgenic mouse models can be characterized obtaining data about the functional, metabolic and structural brain modifications.

The improvement of the 2DG-CEST sensitivity will be fundamental to enable the reduction of injected doses and thus a better physiology. It can become a powerful tool in drug discovery research and thus we must explore whether this method is able to detect changes in the brain glucose metabolism induced by pharmacological treatments.

A mild phenotype characterized by metabolic and structural deficit in a late stage of the pathology was described in the APP23 transgenic mouse. One of the issues characterizing these “first generation” models is that they present mutations that cause an over-production of total Aβ from APP that may lead to potential artifacts (Mucke et al., 2000). Future experiments will be carried out adopting the “second generation” $APP^{NL\text{-}G\text{-}F}$ and

APP^{NL-F} transgenic mice that were engineered to overproduce pathogenic Aβ without over-expressing APP (Saito et al., 2014; Sasaguri et al., 2017).

The advanced pipeline developed to investigate structural and functional alterations of the transgenic mouse brain will be soon adopted into a study involving different Italian research centers. As currently done in clinical studies, the standardization of acquisition parameters and of the analysis procedures between different research groups enables a further reduction of animals involved in research and the improvement of reproducible results.

Even if the described rsfMRI experiment was carried out in rats it was a necessary step to develop a reliable analysis procedure that will be translated to future studies in transgenic mouse models of AD.

The recent acquisition of a cryogenic coil for the mouse head and of a mechanical ventilation system will put us in condition to improve all the methods shown. A better signal-to-noise will enable to improve the resolution of the acquired images, with particular advantages for the 2DG-CEST and for the rsfMRI ones.

References

Acosta-Cabronero, J., Nestor, P.J., 2014. Diffusion tensor imaging in Alzheimer's disease: insights into the limbic-diencephalic network and methodological considerations. Front. Aging Neurosci. 6. https://doi.org/10.3389/fnagi.2014.00266

Alexopoulos, P., Sorg, C., Förschler, A., Grimmer, T., Skokou, M., Wohlschläger, A., Perneczky, R., Zimmer, C., Kurz, A., Preibisch, C., 2012. Perfusion abnormalities in mild cognitive impairment and mild dementia in Alzheimer's disease measured by pulsed arterial spin labeling MRI. Eur. Arch. Psychiatry Clin. Neurosci. 262, 69–77. https://doi.org/10.1007/s00406-011-0226-2

Alves, G.S., Oertel Knöchel, V., Knöchel, C., Carvalho, A.F., Pantel, J., Engelhardt, E., Laks, J., 2015. Integrating retrogenesis theory to Alzheimer's disease pathology: insight from DTI-TBSS investigation of the white matter microstructural integrity. BioMed Res. Int. 2015, 291658. https://doi.org/10.1155/2015/291658

Alves, S., Fol, R., Cartier, N., 2016. Gene Therapy Strategies for Alzheimer's Disease: An Overview. Hum. Gene Ther. 27, 100–107. https://doi.org/10.1089/hum.2016.017

Ameen-Ali, K.E., Wharton, S.B., Simpson, J.E., Heath, P.R., Sharp, P., Berwick, J., 2017. Review: Neuropathology and behavioural features of transgenic murine models of Alzheimer's disease. Neuropathol. Appl. Neurobiol. 43, 553–570. https://doi.org/10.1111/nan.12440

Ametamey, S.M., Treyer, V., Streffer, J., Wyss, M.T., Schmidt, M., Blagoev, M., Hintermann, S., Auberson, Y., Gasparini, F., Fischer, U.C., Buck, A., 2007. Human PET studies of metabotropic glutamate receptor subtype 5 with 11C-ABP688. J. Nucl. Med. Off. Publ. Soc. Nucl. Med. 48, 247–252.

Amlien, I.K., Fjell, A.M., 2014. Diffusion tensor imaging of white matter degeneration in Alzheimer's disease and mild cognitive impairment. Neuroscience 276, 206–215. https://doi.org/10.1016/j.neuroscience.2014.02.017

Andersson, J.L.R., Sotiropoulos, S.N., 2016. An integrated approach to correction for off-resonance effects and subject movement in diffusion MR imaging. NeuroImage 125, 1063–1078. https://doi.org/10.1016/j.neuroimage.2015.10.019

Asaad, M., Lee, J.H., 2018. A guide to using functional magnetic resonance imaging to study Alzheimer's disease in animal models. Dis. Model. Mech. 11, dmm031724. https://doi.org/10.1242/dmm.031724

Ashburner, J., Friston, K.J., 2000. Voxel-based morphometry--the methods. NeuroImage 11, 805–821. https://doi.org/10.1006/nimg.2000.0582

Avants, B.B., Tustison, N.J., Song, G., Cook, P.A., Klein, A., Gee, J.C., 2011a. A reproducible evaluation of ANTs similarity metric performance in brain image registration. NeuroImage 54, 2033–2044. https://doi.org/10.1016/j.neuroimage.2010.09.025

Avants, B.B., Tustison, N.J., Stauffer, M., Song, G., Wu, B., Gee, J.C., 2014. The Insight ToolKit image registration framework. Front. Neuroinformatics 8, 44. https://doi.org/10.3389/fninf.2014.00044

Avants, B.B., Tustison, N.J., Wu, J., Cook, P.A., Gee, J.C., 2011b. An open source multivariate framework for n-tissue segmentation with evaluation on public data. Neuroinformatics 9, 381–400. https://doi.org/10.1007/s12021-011-9109-y

Avants, B.B., Yushkevich, P., Pluta, J., Minkoff, D., Korczykowski, M., Detre, J., Gee, J.C., 2010. The optimal template effect in hippocampus studies of diseased populations. NeuroImage 49, 2457–2466. https://doi.org/10.1016/j.neuroimage.2009.09.062

Bagga, P., Crescenzi, R., Krishnamoorthy, G., Verma, G., Nanga, R.P.R., Reddy, D., Greenberg, J., Detre, J.A., Hariharan, H., Reddy, R., 2016. Mapping the alterations in glutamate with GluCEST MRI in a mouse model of dopamine deficiency. J. Neurochem. 139, 432–439. https://doi.org/10.1111/jnc.13771

Bai, J., Trinh, T.L.H., Chuang, K.-H., Qiu, A., 2012. Atlas-based automatic mouse brain image segmentation revisited: model complexity vs. image registration. Magn. Reson. Imaging 30, 789–798. https://doi.org/10.1016/j.mri.2012.02.010

Balducci, C., Forloni, G., 2011. APP transgenic mice: their use and limitations. Neuromolecular Med. 13, 117–137. https://doi.org/10.1007/s12017-010-8141-7

Balducci, C., Tonini, R., Zianni, E., Nazzaro, C., Fiordaliso, F., Salio, M., Vismara, L., Gardoni, F., Di Luca, M., Carli, M., Forloni, G., 2010. Cognitive deficits associated with alteration of synaptic metaplasticity precede plaque deposition in AβPP23 transgenic mice. J. Alzheimers Dis. JAD 21, 1367–1381.

Baltes, C., Radzwill, N., Bosshard, S., Marek, D., Rudin, M., 2009. Micro MRI of the mouse brain using a novel 400 MHz cryogenic quadrature RF probe. NMR Biomed. 22, 834–842. https://doi.org/10.1002/nbm.1396

Bartzokis, G., 2004. Age-related myelin breakdown: a developmental model of cognitive decline and Alzheimer's disease. Neurobiol. Aging 25, 5–18. https://doi.org/10.1016/j.neurobiolaging.2003.03.001

Basser, P.J., Mattiello, J., LeBihan, D., 1994a. Estimation of the effective self-diffusion tensor from the NMR spin echo. J. Magn. Reson. B 103, 247–254.

Basser, P.J., Mattiello, J., LeBihan, D., 1994b. MR diffusion tensor spectroscopy and imaging. Biophys. J. 66, 259–267. https://doi.org/10.1016/S0006-3495(94)80775-1

Beckmann, C., Mackay, C., Filippini, N., Smith, S., 2009. Group comparison of resting-state FMRI data using multi-subject ICA and dual regression. NeuroImage, Organization for Human Brain Mapping 2009 Annual Meeting 47, S148. https://doi.org/10.1016/S1053-8119(09)71511-3

Beckmann, C.F., DeLuca, M., Devlin, J.T., Smith, S.M., 2005. Investigations into resting-state connectivity using independent component analysis. Philos. Trans. R. Soc. Lond. B. Biol. Sci. 360, 1001–1013. https://doi.org/10.1098/rstb.2005.1634

Beckmann, C.F., Smith, S.M., 2004. Probabilistic independent component analysis for functional magnetic resonance imaging. IEEE Trans. Med. Imaging 23, 137–152. https://doi.org/10.1109/TMI.2003.822821

Beckmann, N., Gérard, C., Abramowski, D., Cannet, C., Staufenbiel, M., 2011. Noninvasive magnetic resonance imaging detection of cerebral amyloid angiopathy-related microvascular alterations using superparamagnetic iron oxide particles in APP transgenic mouse models of Alzheimer's disease: application to passive Abeta immunotherapy. J.

Neurosci. Off. J. Soc. Neurosci. 31, 1023–1031. https://doi.org/10.1523/JNEUROSCI.4936-10.2011

Benedikz, E., Kloskowska, E., Winblad, B., 2009. The rat as an animal model of Alzheimer's disease. J. Cell. Mol. Med. 13, 1034–1042. https://doi.org/10.1111/j.1582-4934.2009.00781.x

Bertero, A., Liska, A., Pagani, M., Parolisi, R., Masferrer, M.E., Gritti, M., Pedrazzoli, M., Galbusera, A., Sarica, A., Cerasa, A., Buffelli, M., Tonini, R., Buffo, A., Gross, C., Pasqualetti, M., Gozzi, A., 2018. Autism-associated 16p11.2 microdeletion impairs prefrontal functional connectivity in mouse and human. Brain J. Neurol. 141, 2055–2065. https://doi.org/10.1093/brain/awy111

Biswal, B., Yetkin, F.Z., Haughton, V.M., Hyde, J.S., 1995. Functional connectivity in the motor cortex of resting human brain using echo-planar MRI. Magn. Reson. Med. 34, 537–541.

Bondolfi, L., Calhoun, M., Ermini, F., Kuhn, H.G., Wiederhold, K.-H., Walker, L., Staufenbiel, M., Jucker, M., 2002. Amyloid-associated neuron loss and gliogenesis in the neocortex of amyloid precursor protein transgenic mice. J. Neurosci. Off. J. Soc. Neurosci. 22, 515–522.

Borg, J., Chereul, E., 2008. Differential MRI patterns of brain atrophy in double or single transgenic mice for APP and/or SOD. J. Neurosci. Res. 86, 3275–3284. https://doi.org/10.1002/jnr.21778

Braak, H., Braak, E., 1991. Neuropathological stageing of Alzheimer-related changes. Acta Neuropathol. (Berl.) 82, 239–259.

Braak, H., Del Tredici, K., 2014. Are cases with tau pathology occurring in the absence of Aβ deposits part of the AD-related pathological process? Acta Neuropathol. (Berl.) 128, 767–772. https://doi.org/10.1007/s00401-014-1356-1

Braakman, N., Matysik, J., van Duinen, S.G., Verbeek, F., Schliebs, R., de Groot, H.J.M., Alia, A., 2006. Longitudinal assessment of Alzheimer's beta-amyloid plaque development in transgenic mice monitored by in vivo magnetic resonance microimaging. J. Magn. Reson. Imaging JMRI 24, 530–536. https://doi.org/10.1002/jmri.20675

Brendel, M., Focke, C., Blume, T., Peters, F., Deussing, M., Probst, F., Jaworska, A., Overhoff, F., Albert, N., Lindner, S., von Ungern-Sternberg, B., Bartenstein, P., Haass, C., Kleinberger, G., Herms, J., Rominger, A., 2017. Time Courses of Cortical Glucose Metabolism and Microglial Activity Across the Life Span of Wild-Type Mice: A PET Study. J. Nucl. Med. Off. Publ. Soc. Nucl. Med. 58, 1984–1990. https://doi.org/10.2967/jnumed.117.195107

Brendel, M., Jaworska, A., Probst, F., Overhoff, F., Korzhova, V., Lindner, S., Carlsen, J., Bartenstein, P., Harada, R., Kudo, Y., Haass, C., Van Leuven, F., Okamura, N., Herms, J., Rominger, A., 2016. Small-Animal PET Imaging of Tau Pathology with 18F-THK5117 in 2 Transgenic Mouse Models. J. Nucl. Med. 57, 792–798. https://doi.org/10.2967/jnumed.115.163493

Brendel, Matthias, Probst, F., Jaworska, A., Overhoff, F., Korzhova, V., Albert, N.L., Beck, R., Lindner, S., Gildehaus, F.-J., Baumann, K., Bartenstein, P., Kleinberger, G., Haass, C., Herms, J., Rominger, A., 2016. Glial Activation and Glucose Metabolism in a Transgenic Amyloid Mouse Model: A Triple-Tracer PET Study. J. Nucl. Med. Off. Publ. Soc. Nucl. Med. 57, 954–960. https://doi.org/10.2967/jnumed.115.167858

Brown, R.W., Cheng, Y.C.N., Haacke, E.M., Thompson, M.R., Venkatesan, R., 2014. Magnetic Resonance Imaging. Wiley-Blackwell. https://doi.org/10.1002/9781118633953.fmatter

Bruijnzeel, A.W., Alexander, J.C., Perez, P.D., Bauzo-Rodriguez, R., Hall, G., Klausner, R., Guerra, V., Zeng, H., Igari, M., Febo, M., 2014. Acute Nicotine Administration Increases BOLD fMRI Signal in Brain Regions Involved in Reward Signaling and Compulsive Drug Intake in Rats. Int. J. Neuropsychopharmacol. 18. https://doi.org/10.1093/ijnp/pyu011

Buckner, R.L., Andrews-Hanna, J.R., Schacter, D.L., 2008. The brain's default network: anatomy, function, and relevance to disease. Ann. N. Y. Acad. Sci. 1124, 1–38. https://doi.org/10.1196/annals.1440.011

Buée, L., Bussière, T., Buée-Scherrer, V., Delacourte, A., Hof, P.R., 2000. Tau protein isoforms, phosphorylation and role in neurodegenerative disorders. Brain Res. Brain Res. Rev. 33, 95–130.

Buerger, K., Ewers, M., Pirttilä, T., Zinkowski, R., Alafuzoff, I., Teipel, S.J., DeBernardis, J., Kerkman, D., McCulloch, C., Soininen, H., Hampel, H., 2006. CSF phosphorylated tau protein correlates with neocortical neurofibrillary pathology in Alzheimer's disease. Brain J. Neurol. 129, 3035–3041. https://doi.org/10.1093/brain/awl269

Bukhari, Q., Schroeter, A., Cole, D.M., Rudin, M., 2017. Resting State fMRI in Mice Reveals Anesthesia Specific Signatures of Brain Functional Networks and Their Interactions. Front. Neural Circuits 11. https://doi.org/10.3389/fncir.2017.00005

Bush, A.I., 2003. The metallobiology of Alzheimer's disease. Trends Neurosci. 26, 207–214. https://doi.org/10.1016/S0166-2236(03)00067-5

Cai, K., Haris, M., Singh, A., Kogan, F., Greenberg, J.H., Hariharan, H., Detre, J.A., Reddy, R., 2012. Magnetic resonance imaging of glutamate. Nat. Med. 18, 302–306. https://doi.org/10.1038/nm.2615

Cai, K., Tain, R.-W., Zhou, X.J., Damen, F.C., Scotti, A.M., Hariharan, H., Poptani, H., Reddy, R., 2017. Creatine CEST MRI for Differentiating Gliomas with Different Degrees of Aggressiveness. Mol. Imaging Biol. MIB Off. Publ. Acad. Mol. Imaging 19, 225–232. https://doi.org/10.1007/s11307-016-0995-0

Candela, S., Giubilei, F., Orzi, F., 2013. Heterogeneous pathologies associated with dementia in Parkinsonism share a prion-like spreading mechanism. Arch. Ital. Biol. 151, 169–178.

Cardenas, V.A., Chao, L.L., Studholme, C., Yaffe, K., Miller, B.L., Madison, C., Buckley, S.T., Mungas, D., Schuff, N., Weiner, M.W., 2011. Brain atrophy associated with baseline and longitudinal measures of cognition. Neurobiol. Aging 32, 572–580. https://doi.org/10.1016/j.neurobiolaging.2009.04.011

Chishti, M.A., Yang, D.S., Janus, C., Phinney, A.L., Horne, P., Pearson, J., Strome, R., Zuker, N., Loukides, J., French, J., Turner, S., Lozza, G., Grilli, M., Kunicki, S., Morissette, C., Paquette, J., Gervais, F., Bergeron, C., Fraser, P.E., Carlson, G.A., George-Hyslop, P.S., Westaway, D., 2001. Early-onset amyloid deposition and cognitive deficits in transgenic mice expressing a double mutant form of amyloid precursor protein 695. J. Biol. Chem. 276, 21562–21570. https://doi.org/10.1074/jbc.M100710200

Chua, T.C., Wen, W., Slavin, M.J., Sachdev, P.S., 2008. Diffusion tensor imaging in mild cognitive impairment and Alzheimer's disease: a review. Curr. Opin. Neurol. 21, 83–92. https://doi.org/10.1097/WCO.0b013e3282f4594b

Clark, V.H., Resnick, S.M., Doshi, J., Beason-Held, L.L., Zhou, Y., Ferrucci, L., Wong, D.F., Kraut, M.A., Davatzikos, C., 2012. Longitudinal imaging pattern analysis (SPARE-CD index) detects early structural and functional changes before cognitive decline in healthy older adults. Neurobiol. Aging 33, 2733–2745. https://doi.org/10.1016/j.neurobiolaging.2012.01.010

Cohen, R.M., Rezai-Zadeh, K., Weitz, T.M., Rentsendorj, A., Gate, D., Spivak, I., Bholat, Y., Vasilevko, V., Glabe, C.G., Breunig, J.J., Rakic, P., Davtyan, H., Agadjanyan, M.G., Kepe, V., Barrio, J.R., Bannykh, S., Szekely, C.A., Pechnick, R.N., Town, T., 2013. A transgenic Alzheimer rat with plaques, tau pathology, behavioral impairment, oligomeric aβ, and frank neuronal loss. J. Neurosci. Off. J. Soc. Neurosci. 33, 6245–6256. https://doi.org/10.1523/JNEUROSCI.3672-12.2013

Cole, D.M., Beckmann, C.F., Long, C.J., Matthews, P.M., Durcan, M.J., Beaver, J.D., 2010. Nicotine replacement in abstinent smokers improves cognitive withdrawal symptoms with modulation of resting brain network dynamics. NeuroImage 52, 590–599. https://doi.org/10.1016/j.neuroimage.2010.04.251

Coleman, M., 2005. Axon degeneration mechanisms: commonality amid diversity. Nat. Rev. Neurosci. 6, 889–898. https://doi.org/10.1038/nrn1788

Collingwood, J.F., Chong, R.K.K., Kasama, T., Cervera-Gontard, L., Dunin-Borkowski, R.E., Perry, G., Pósfai, M., Siedlak, S.L., Simpson, E.T., Smith, M.A., Dobson, J., 2008. Three-dimensional tomographic imaging and characterization of iron compounds within Alzheimer's plaque core material. J. Alzheimers Dis. JAD 14, 235–245.

Connor, J.R., Menzies, S.L., Martin, S.M.S., Mufson, E.J., 1992. A histochemical study of iron, transferrin, and ferritin in Alzheimer's diseased brains. J. Neurosci. Res. 31, 75–83. https://doi.org/10.1002/jnr.490310111

Crescenzi, R., DeBrosse, C., Nanga, R.P.R., Byrne, M.D., Krishnamoorthy, G., D'Aquilla, K., Nath, H., Morales, K.H., Iba, M., Hariharan, H., Lee, V.M.Y.-, Detre, J.A., Reddy, R., 2016. Longitudinal imaging reveals sub-hippocampal dynamics in glutamate levels associated with histopathologic events in a mouse model of tauopathy and healthy mice. Hippocampus. https://doi.org/10.1002/hipo.22693

Crescenzi, R., DeBrosse, C., Nanga, R.P.R., Reddy, S., Haris, M., Hariharan, H., Iba, M., Lee, V.M.Y., Detre, J.A., Borthakur, A., Reddy, R., 2014. In vivo measurement of glutamate loss is associated with synapse loss in a mouse model of tauopathy. NeuroImage 101, 185–192. https://doi.org/10.1016/j.neuroimage.2014.06.067

Cunnane, S., Nugent, S., Roy, M., Courchesne-Loyer, A., Croteau, E., Tremblay, S., Castellano, A., Pifferi, F., Bocti, C., Paquet, N., Begdouri, H., Bentourkia, M., Turcotte, E., Allard, M., Barberger-Gateau, P., Fulop, T., Rapoport, S.I., 2011. Brain fuel metabolism, aging, and Alzheimer's disease. Nutr. Burbank Los Angel. Cty. Calif 27, 3–20. https://doi.org/10.1016/j.nut.2010.07.021

de Cristóbal, J., García-García, L., Delgado, M., Pérez, M., Pozo, M.A., Medina, M., 2014. Longitudinal assessment of a transgenic animal model of tauopathy by FDG-PET imaging. J. Alzheimers Dis. JAD 40 Suppl 1, S79-89. https://doi.org/10.3233/JAD-132276

Delatour, B., Guégan, M., Volk, A., Dhenain, M., 2006. In vivo MRI and histological evaluation of brain atrophy in APP/PS1 transgenic mice. Neurobiol. Aging 27, 835–847. https://doi.org/10.1016/j.neurobiolaging.2005.04.011

Deleye, S., Waldron, A.-M., Richardson, J.C., Schmidt, M., Langlois, X., Stroobants, S., Staelens, S., 2016. The Effects of Physiological and Methodological Determinants on 18F-FDG Mouse Brain Imaging Exemplified in a Double Transgenic Alzheimer Model. Mol. Imaging 15. https://doi.org/10.1177/1536012115624919

Dennis, E.L., Thompson, P.M., 2014. Functional brain connectivity using fMRI in aging and Alzheimer's disease. Neuropsychol. Rev. 24, 49–62. https://doi.org/10.1007/s11065-014-9249-6

Desmond, K.L., Moosvi, F., Stanisz, G.J., 2014. Mapping of amide, amine, and aliphatic peaks in the CEST spectra of murine xenografts at 7 T. Magn. Reson. Med. 71, 1841–1853. https://doi.org/10.1002/mrm.24822

Do Carmo, S., Cuello, A.C., 2013. Modeling Alzheimer's disease in transgenic rats. Mol. Neurodegener. 8, 37. https://doi.org/10.1186/1750-1326-8-37

Donat, C.K., Mirzaei, N., Tang, S.-P., Edison, P., Sastre, M., 2018. Imaging of Microglial Activation in Alzheimer's Disease by [11C]PBR28 PET. Methods Mol. Biol. Clifton NJ 1750, 323–339. https://doi.org/10.1007/978-1-4939-7704-8_22

Dorr, A.E., Lerch, J.P., Spring, S., Kabani, N., Henkelman, R.M., 2008. High resolution three-dimensional brain atlas using an average magnetic resonance image of 40 adult C57Bl/6J mice. NeuroImage 42, 60–69. https://doi.org/10.1016/j.neuroimage.2008.03.037

Dowsett, D., 2006. The Physics of Diagnostic Imaging, Second. ed. CRC Press.

Dudeffant, C., Vandesquille, M., Herbert, K., Garin, C.M., Alves, S., Blanchard, V., Comoy, E.E., Petit, F., Dhenain, M., 2017. Contrast-enhanced MR microscopy of amyloid plaques in five mouse models of amyloidosis and in human Alzheimer's disease brains. Sci. Rep. 7, 4955. https://doi.org/10.1038/s41598-017-05285-1

Dula, A.N., Smith, S.A., Gore, J.C., n.d. Application of Chemical Exchange Saturation Transfer (CEST) MRI for Endogenous Contrast at 7 Tesla. J. Neuroimaging 23, 526–532. https://doi.org/10.1111/j.1552-6569.2012.00751.x

Duyckaerts, C., Delatour, B., Potier, M.-C., 2009. Classification and basic pathology of Alzheimer disease. Acta Neuropathol. (Berl.) 118, 5–36. https://doi.org/10.1007/s00401-009-0532-1

Echeverria, V., Ducatenzeiler, A., Alhonen, L., Janne, J., Grant, S.M., Wandosell, F., Muro, A., Baralle, F., Li, H., Duff, K., Szyf, M., Cuello, A.C., 2004. Rat transgenic models with a phenotype of intracellular Abeta accumulation in hippocampus and cortex. J. Alzheimers Dis. JAD 6, 209–219.

Einstein, A., 1905. Über die von der molekularkinetischen Theorie der Wärme geforderte Bewegung von in ruhenden Flüssigkeiten suspendierten Teilchen. Ann. Phys.

Engelborghs, S., De Vreese, K., Van de Casteele, T., Vanderstichele, H., Van Everbroeck, B., Cras, P., Martin, J.-J., Vanmechelen, E., De Deyn, P.P., 2008. Diagnostic performance of a CSF-biomarker panel in autopsy-confirmed dementia. Neurobiol. Aging 29, 1143–1159. https://doi.org/10.1016/j.neurobiolaging.2007.02.016

Esquerda-Canals, G., Montoliu-Gaya, L., Güell-Bosch, J., Villegas, S., 2017. Mouse Models of Alzheimer's Disease. J. Alzheimers Dis. JAD 57, 1171–1183. https://doi.org/10.3233/JAD-170045

Fagan, A.M., Mintun, M.A., Mach, R.H., Lee, S.-Y., Dence, C.S., Shah, A.R., LaRossa, G.N., Spinner, M.L., Klunk, W.E., Mathis, C.A., DeKosky, S.T., Morris, J.C., Holtzman, D.M., 2006. Inverse relation between in vivo amyloid imaging load and cerebrospinal fluid Abeta42 in humans. Ann. Neurol. 59, 512–519. https://doi.org/10.1002/ana.20730

Ferreira, S.T., Klein, W.L., 2011. The Aβ oligomer hypothesis for synapse failure and memory loss in Alzheimer's diseas. Neurobiol. Learn. Mem. 96, 529–543. https://doi.org/10.1016/j.nlm.2011.08.003

Filippini, N., MacIntosh, B.J., Hough, M.G., Goodwin, G.M., Frisoni, G.B., Smith, S.M., Matthews, P.M., Beckmann, C.F., Mackay, C.E., 2009. Distinct patterns of brain activity in young carriers of the APOE-ε4 allele. Proc. Natl. Acad. Sci. U. S. A. 106, 7209–7214. https://doi.org/10.1073/pnas.0811879106

Flood, D.G., Lin, Y.-G., Lang, D.M., Trusko, S.P., Hirsch, J.D., Savage, M.J., Scott, R.W., Howland, D.S., 2009. A transgenic rat model of Alzheimer's disease with extracellular Abeta deposition. Neurobiol. Aging 30, 1078–1090. https://doi.org/10.1016/j.neurobiolaging.2007.10.006

Fodero-Tavoletti, M.T., Okamura, N., Furumoto, S., Mulligan, R.S., Connor, A.R., McLean, C.A., Cao, D., Rigopoulos, A., Cartwright, G.A., O'Keefe, G., Gong, S., Adlard, P.A., Barnham, K.J., Rowe, C.C., Masters, C.L., Kudo, Y., Cappai, R., Yanai, K., Villemagne, V.L., 2011. 18F-THK523: a novel in vivo tau imaging ligand for Alzheimer's disease. Brain 134, 1089–1100. https://doi.org/10.1093/brain/awr038

Foley, A.M., Ammar, Z.M., Lee, R.H., Mitchell, C.S., 2015. Systematic review of the relationship between amyloid-β levels and measures of transgenic mouse cognitive deficit in Alzheimer's disease. J. Alzheimers Dis. JAD 44, 787–795. https://doi.org/10.3233/JAD-142208

Folkesson, R., Malkiewicz, K., Kloskowska, E., Nilsson, T., Popova, E., Bogdanovic, N., Ganten, U., Ganten, D., Bader, M., Winblad, B., Benedikz, E., 2007. A transgenic rat expressing human APP with the Swedish Alzheimer's disease mutation. Biochem. Biophys. Res. Commun. 358, 777–782. https://doi.org/10.1016/j.bbrc.2007.04.195

Forster, D., Davies, K., Williams, S., 2013. Magnetic resonance spectroscopy in vivo of neurochemicals in a transgenic model of Alzheimer's disease: a longitudinal study of metabolites, relaxation time, and behavioral analysis in TASTPM and wild-type mice. Magn. Reson. Med. 69, 944–955. https://doi.org/10.1002/mrm.24349

Fox, M.D., Raichle, M.E., 2007. Spontaneous fluctuations in brain activity observed with functional magnetic resonance imaging. Nat. Rev. Neurosci. 8, 700–711. https://doi.org/10.1038/nrn2201

Franco, R., Cedazo-Minguez, A., 2014. Successful therapies for Alzheimer's disease: why so many in animal models and none in humans? Front. Pharmacol. 5. https://doi.org/10.3389/fphar.2014.00146

Frisoni, G.B., Fox, N.C., Jack, C.R., Scheltens, P., Thompson, P.M., 2010. The clinical use of structural MRI in Alzheimer disease. Nat. Rev. Neurol. 6, 67–77. https://doi.org/10.1038/nrneurol.2009.215

G, V., I, D., P, B., F, V.L., A, V. der L., n.d. Noninvasive in vivo MRI detection of neuritic plaques associated with iron in APP[V717I] transgenic mice, a model for Alzheimer's disease. Magn. Reson. Med. 53, 607–613. https://doi.org/10.1002/mrm.20385

Games, D., Adams, D., Alessandrini, R., Barbour, R., Berthelette, P., Blackwell, C., Carr, T., Clemens, J., Donaldson, T., Gillespie, F., 1995. Alzheimer-type neuropathology in transgenic mice overexpressing V717F beta-amyloid precursor protein. Nature 373, 523–527. https://doi.org/10.1038/373523a0

Gass, N., Schwarz, A.J., Sartorius, A., Schenker, E., Risterucci, C., Spedding, M., Zheng, L., Meyer-Lindenberg, A., Weber-Fahr, W., 2014. Sub-anesthetic ketamine modulates intrinsic BOLD connectivity within the hippocampal-prefrontal circuit in the rat. Neuropsychopharmacol. Off. Publ. Am. Coll. Neuropsychopharmacol. 39, 895–906. https://doi.org/10.1038/npp.2013.290

Goertzen, A.L., Bao, Q., Bergeron, M., Blankemeyer, E., Blinder, S., Cañadas, M., Chatziioannou, A.F., Dinelle, K., Elhami, E., Jans, H.-S., Lage, E., Lecomte, R., Sossi, V., Surti, S., Tai, Y.-C., Vaquero, J.J., Vicente, E., Williams, D.A., Laforest, R., 2012. NEMA NU 4-2008 comparison of preclinical PET imaging systems. J. Nucl. Med. Off. Publ. Soc. Nucl. Med. 53, 1300–1309. https://doi.org/10.2967/jnumed.111.099382

Gonzalez-Lima, F., Berndt, J.D., Valla, J.E., Games, D., Reiman, E.M., 2001. Reduced corpus callosum, fornix and hippocampus in PDAPP transgenic mouse model of Alzheimer's disease. Neuroreport 12, 2375–2379.

Gordon, B.A., Blazey, T.M., Su, Y., Hari-Raj, A., Dincer, A., Flores, S., Christensen, J., McDade, E., Wang, G., Xiong, C., Cairns, N.J., Hassenstab, J., Marcus, D.S., Fagan, A.M., Jack, C.R., Hornbeck, R.C., Paumier, K.L., Ances, B.M., Berman, S.B., Brickman, A.M., Cash, D.M., Chhatwal, J.P., Correia, S., Förster, S., Fox, N.C., Graff-Radford, N.R., la Fougère, C., Levin, J., Masters, C.L., Rossor, M.N., Salloway, S., Saykin, A.J., Schofield, P.R., Thompson, P.M., Weiner, M.M., Holtzman, D.M., Raichle, M.E., Morris, J.C., Bateman, R.J., Benzinger, T.L.S., 2018. Spatial patterns of neuroimaging biomarker change in individuals from families with autosomal dominant Alzheimer's disease: a longitudinal study. Lancet Neurol. 17, 241–250. https://doi.org/10.1016/S1474-4422(18)30028-0

Gore, J.C., 2003. Principles and practice of functional MRI of the human brain. J. Clin. Invest. 112, 4–9. https://doi.org/10.1172/JCI200319010

Gozzi, A., Schwarz, A., Reese, T., Bertani, S., Crestan, V., Bifone, A., 2006. Region-Specific Effects of Nicotine on Brain Activity: A Pharmacological MRI Study in the Drug-Naïve Rat. Neuropsychopharmacology 31, 1690–1703. https://doi.org/10.1038/sj.npp.1300955

Gozzi, A., Schwarz, A.J., 2016. Large-scale functional connectivity networks in the rodent brain. NeuroImage 127, 496–509. https://doi.org/10.1016/j.neuroimage.2015.12.017

Grandjean, J., Derungs, R., Kulic, L., Welt, T., Henkelman, M., Nitsch, R.M., Rudin, M., 2016. Complex interplay between brain function and structure during cerebral amyloidosis in APP transgenic mouse strains revealed by multi-parametric MRI comparison. NeuroImage 134, 1–11. https://doi.org/10.1016/j.neuroimage.2016.03.042

Grandjean, J., Schroeter, A., Batata, I., Rudin, M., 2014. Optimization of anesthesia protocol for resting-state fMRI in mice based on differential effects of anesthetics on functional connectivity patterns. NeuroImage 102 Pt 2, 838–847. https://doi.org/10.1016/j.neuroimage.2014.08.043

Grandjean, J., Zerbi, V., Balsters, J.H., Wenderoth, N., Rudin, M., 2017. Structural Basis of Large-Scale Functional Connectivity in the Mouse. J. Neurosci. 37, 8092–8101. https://doi.org/10.1523/JNEUROSCI.0438-17.2017

Grand'maison, M., Zehntner, S.P., Ho, M.-K., Hébert, F., Wood, A., Carbonell, F., Zijdenbos, A.P., Hamel, E., Bedell, B.J., 2013. Early cortical thickness changes predict β-amyloid deposition in a mouse model of Alzheimer's disease. Neurobiol. Dis. 54, 59–67. https://doi.org/10.1016/j.nbd.2013.02.005

Greicius, M.D., Srivastava, G., Reiss, A.L., Menon, V., 2004. Default-mode network activity distinguishes Alzheimer's disease from healthy aging: evidence from functional MRI. Proc. Natl. Acad. Sci. U. S. A. 101, 4637–4642. https://doi.org/10.1073/pnas.0308627101

Griffanti, L., Salimi-Khorshidi, G., Beckmann, C.F., Auerbach, E.J., Douaud, G., Sexton, C.E., Zsoldos, E., Ebmeier, K.P., Filippini, N., Mackay, C.E., Moeller, S., Xu, J., Yacoub, E., Baselli, G., Ugurbil, K., Miller, K.L., Smith, S.M., 2014. ICA-based artefact removal and accelerated fMRI acquisition for improved resting state network imaging. NeuroImage 95, 232–247. https://doi.org/10.1016/j.neuroimage.2014.03.034

Griffey, R.H., P. Flamig, D., 1990. VAPOR for solvent-suppressed, short-echo, volume-localized proton spectroscopy. J. Magn. Reson. 1969 88, 161–166. https://doi.org/10.1016/0022-2364(90)90120-X

Grimm, O., Gass, N., Weber-Fahr, W., Sartorius, A., Schenker, E., Spedding, M., Risterucci, C., Schweiger, J.I., Böhringer, A., Zang, Z., Tost, H., Schwarz, A.J., Meyer-Lindenberg, A., 2015. Acute ketamine challenge increases resting state prefrontal-hippocampal connectivity in both humans and rats. Psychopharmacology (Berl.) 232, 4231–4241. https://doi.org/10.1007/s00213-015-4022-y

Grundke-Iqbal, I., Iqbal, K., Tung, Y.C., Quinlan, M., Wisniewski, H.M., Binder, L.I., 1986. Abnormal phosphorylation of the microtubule-associated protein tau (tau) in Alzheimer cytoskeletal pathology. Proc. Natl. Acad. Sci. U. S. A. 83, 4913–4917.

Gunning-Dixon, F.M., Raz, N., 2000. The cognitive correlates of white matter abnormalities in normal aging: a quantitative review. Neuropsychology 14, 224–232.

Haacke, E.M., Cheng, N.Y.C., House, M.J., Liu, Q., Neelavalli, J., Ogg, R.J., Khan, A., Ayaz, M., Kirsch, W., Obenaus, A., 2005. Imaging iron stores in the brain using magnetic resonance imaging. Magn. Reson. Imaging 23, 1–25. https://doi.org/10.1016/j.mri.2004.10.001

Hall, A.M., Roberson, E.D., 2012. Mouse models of Alzheimer's disease. Brain Res. Bull. 88, 3–12. https://doi.org/10.1016/j.brainresbull.2011.11.017

Hardy, J., Allsop, D., 1991. Amyloid deposition as the central event in the aetiology of Alzheimer's disease. Trends Pharmacol. Sci. 12, 383–388.

Haris, M., Nath, K., Cai, K., Singh, A., Crescenzi, R., Kogan, F., Verma, G., Reddy, S., Hariharan, H., Melhem, E.R., Reddy, R., 2013a. Imaging of glutamate neurotransmitter alterations in Alzheimer's disease. NMR Biomed. 26, 386–391. https://doi.org/10.1002/nbm.2875

Haris, M., Singh, A., Cai, K., Nath, K., Crescenzi, R., Kogan, F., Hariharan, H., Reddy, R., 2013b. MICEST: a potential tool for non-invasive detection of molecular changes in Alzheimer's disease. J. Neurosci. Methods 212, 87–93. https://doi.org/10.1016/j.jneumeth.2012.09.025

Hébert, F., Grand'maison, M., Ho, M.-K., Lerch, J.P., Hamel, E., Bedell, B.J., 2013. Cortical atrophy and hypoperfusion in a transgenic mouse model of Alzheimer's disease. Neurobiol. Aging 34, 1644–1652. https://doi.org/10.1016/j.neurobiolaging.2012.11.022

Helpern, J.A., Lee, S.-P., Falangola, M.F., Dyakin, V.V., Bogart, A., Ardekani, B., Duff, K., Branch, C., Wisniewski, T., de Leon, M.J., Wolf, O., O'Shea, J., Nixon, R.A., 2004. MRI assessment of neuropathology in a transgenic mouse model of Alzheimer's disease. Magn. Reson. Med. 51, 794–798. https://doi.org/10.1002/mrm.20038

Heneka, M.T., Ramanathan, M., Jacobs, A.H., Dumitrescu-Ozimek, L., Bilkei-Gorzo, A., Debeir, T., Sastre, M., Galldiks, N., Zimmer, A., Hoehn, M., Heiss, W.-D., Klockgether, T., Staufenbiel, M., 2006. Locus ceruleus degeneration promotes Alzheimer pathogenesis in amyloid precursor protein 23 transgenic mice. J. Neurosci. Off. J. Soc. Neurosci. 26, 1343–1354. https://doi.org/10.1523/JNEUROSCI.4236-05.2006

Higuchi, M., Iwata, N., Matsuba, Y., Sato, K., Sasamoto, K., Saido, T.C., 2005. 19F and 1H MRI detection of amyloid beta plaques in vivo. Nat. Neurosci. 8, 527–533. https://doi.org/10.1038/nn1422

Hoenig, M.C., Bischof, G.N., Seemiller, J., Hammes, J., Kukolja, J., Onur, Ö.A., Jessen, F., Fliessbach, K., Neumaier, B., Fink, G.R., van Eimeren, T., Drzezga, A., 2018. Networks of tau distribution in Alzheimer's disease. Brain J. Neurol. 141, 568–581. https://doi.org/10.1093/brain/awx353

Holcomb, L., Gordon, M.N., McGowan, E., Yu, X., Benkovic, S., Jantzen, P., Wright, K., Saad, I., Mueller, R., Morgan, D., Sanders, S., Zehr, C., O'Campo, K., Hardy, J., Prada, C.M., Eckman, C., Younkin, S., Hsiao, K., Duff, K., 1998. Accelerated Alzheimer-type phenotype in transgenic mice carrying both mutant amyloid precursor protein and presenilin 1 transgenes. Nat. Med. 4, 97–100.

Holmes, C., Boche, D., Wilkinson, D., Yadegarfar, G., Hopkins, V., Bayer, A., Jones, R.W., Bullock, R., Love, S., Neal, J.W., Zotova, E., Nicoll, J.A.R., 2008. Long-term effects of Abeta42 immunisation in Alzheimer's disease: follow-up of a randomised, placebo-controlled phase I trial. Lancet Lond. Engl. 372, 216–223. https://doi.org/10.1016/S0140-6736(08)61075-2

Holmes, H.E., Powell, N.M., Ma, D., Ismail, O., Harrison, I.F., Wells, J.A., Colgan, N., O'Callaghan, J.M., Johnson, R.A., Murray, T.K., Ahmed, Z., Heggenes, M., Fisher, A., Cardoso, M.J., Modat, M., O'Neill, M.J., Collins, E.C., Fisher, E.M.C., Ourselin, S., Lythgoe, M.F., 2017. Comparison of In Vivo and Ex Vivo MRI for the Detection of Structural Abnormalities in a Mouse Model of Tauopathy. Front. Neuroinformatics 11. https://doi.org/10.3389/fninf.2017.00020

Hooper, C., Killick, R., Lovestone, S., 2008. The GSK3 hypothesis of Alzheimer's disease. J. Neurochem. 104, 1433–1439. https://doi.org/10.1111/j.1471-4159.2007.05194.x

Howlett, D.R., Richardson, J.C., Austin, A., Parsons, A.A., Bate, S.T., Davies, D.C., Gonzalez, M.I., 2004. Cognitive correlates of Abeta deposition in male and female mice bearing amyloid precursor protein and presenilin-1 mutant transgenes. Brain Res. 1017, 130–136. https://doi.org/10.1016/j.brainres.2004.05.029

Hsiao, K., Chapman, P., Nilsen, S., Eckman, C., Harigaya, Y., Younkin, S., Yang, F., Cole, G., 1996. Correlative memory deficits, Abeta elevation, and amyloid plaques in transgenic mice. Science 274, 99–102.

Iadecola, C., 2004. Neurovascular regulation in the normal brain and in Alzheimer's disease. Nat. Rev. Neurosci. 5, 347–360. https://doi.org/10.1038/nrn1387

Jack, C.R., Bennett, D.A., Blennow, K., Carrillo, M.C., Dunn, B., Haeberlein, S.B., Holtzman, D.M., Jagust, W., Jessen, F., Karlawish, J., Liu, E., Molinuevo, J.L., Montine, T., Phelps, C., Rankin, K.P., Rowe, C.C., Scheltens, P., Siemers, E., Snyder, H.M., Sperling, R., Contributors, 2018. NIA-AA Research Framework: Toward a biological definition of Alzheimer's disease. Alzheimers Dement. J. Alzheimers Assoc. 14, 535–562. https://doi.org/10.1016/j.jalz.2018.02.018

Jack, C.R., Bennett, D.A., Blennow, K., Carrillo, M.C., Feldman, H.H., Frisoni, G.B., Hampel, H., Jagust, W.J., Johnson, K.A., Knopman, D.S., Petersen, R.C., Scheltens, P., Sperling, R.A., Dubois, B., 2016. A/T/N: An unbiased descriptive classification scheme for Alzheimer disease biomarkers. Neurology 87, 539–547. https://doi.org/10.1212/WNL.0000000000002923

Jack, C.R., Garwood, M., Wengenack, T.M., Borowski, B., Curran, G.L., Lin, J., Adriany, G., Grohn, O.H.J., Grimm, R., Poduslo, J.F., 2004. In Vivo Visualization of Alzheimer's Amyloid Plaques by MRI in Transgenic Mice Without a Contrast Agent. Magn. Reson. Med. Off. J. Soc. Magn. Reson. Med. Soc. Magn. Reson. Med. 52, 1263–1271. https://doi.org/10.1002/mrm.20266

Jack, C.R., Knopman, D.S., Jagust, W.J., Shaw, L.M., Aisen, P.S., Weiner, M.W., Petersen, R.C., Trojanowski, J.Q., 2010. Hypothetical model of dynamic biomarkers of the Alzheimer's pathological cascade. Lancet Neurol. 9, 119–128. https://doi.org/10.1016/S1474-4422(09)70299-6

Jack, C.R., Wengenack, T.M., Reyes, D.A., Garwood, M., Curran, G.L., Borowski, B.J., Lin, J., Preboske, G.M., Holasek, S.S., Adriany, G., Poduslo, J.F., 2005. In Vivo Magnetic Resonance Microimaging of Individual Amyloid Plaques in Alzheimer's Transgenic Mice. J. Neurosci. Off. J. Soc. Neurosci. 25, 10041–10048. https://doi.org/10.1523/JNEUROSCI.2588-05.2005

Jagust, W., 2006. Positron emission tomography and magnetic resonance imaging in the diagnosis and prediction of dementia. Alzheimers Dement. J. Alzheimers Assoc. 2, 36–42. https://doi.org/10.1016/j.jalz.2005.11.002

Janel, N., Sarazin, M., Corlier, F., Corne, H., de Souza, L.C., Hamelin, L., Aka, A., Lagarde, J., Blehaut, H., Hindié, V., Rain, J.-C., Arbones, M.L., Dubois, B., Potier, M.C., Bottlaender, M., Delabar, J.M., 2014. Plasma DYRK1A as a novel risk factor for Alzheimer's disease. Transl. Psychiatry 4, e425. https://doi.org/10.1038/tp.2014.61

Janes, A.C., Nickerson, L.D., Frederick, B. deB., Kaufman, M.J., 2012. Prefrontal and limbic resting state brain network functional connectivity differs between nicotine-dependent smokers and non-smoking controls. Drug Alcohol Depend. 125, 252–259. https://doi.org/10.1016/j.drugalcdep.2012.02.020

Jara, H., Sakai, O., Mankal, P., Irving, R.P., Norbash, A.M., 2006. Multispectral quantitative magnetic resonance imaging of brain iron stores: a theoretical perspective. Top. Magn. Reson. Imaging TMRI 17, 19–30. https://doi.org/10.1097/01.rmr.0000245460.82782.69

Jellinger, K., Paulus, W., Grundke-Iqbal, I., Riederer, P., Youdim, M.B., 1990. Brain iron and ferritin in Parkinson's and Alzheimer's diseases. J. Neural Transm. Park. Dis. Dement. Sect. 2, 327–340.

Jenkinson, M., Beckmann, C.F., Behrens, T.E.J., Woolrich, M.W., Smith, S.M., 2012. FSL. NeuroImage 62, 782–790. https://doi.org/10.1016/j.neuroimage.2011.09.015

Jin, T., Kim, S.-G., 2014. Advantages of chemical exchange-sensitive spin-lock (CESL) over chemical exchange saturation transfer (CEST) for hydroxyl- and amine-water proton exchange studies. NMR Biomed. 27, 1313–1324. https://doi.org/10.1002/nbm.3191

Jin, T., Mehrens, H., Wang, P., Kim, S.-G., 2016. Glucose metabolism-weighted imaging with chemical exchange-sensitive MRI of 2-deoxyglucose (2DG) in brain: Sensitivity and biological sources. NeuroImage 143, 82–90. https://doi.org/10.1016/j.neuroimage.2016.08.040

Joel, S.E., Caffo, B.S., van Zijl, P.C., Pekar, J.J., 2011. On the relationship between seed-based and ICA-based measures of functional connectivity. Magn. Reson. Med. Off. J. Soc. Magn. Reson. Med. Soc. Magn. Reson. Med. 66, 644–657. https://doi.org/10.1002/mrm.22818

Johnson, K.A., Schultz, A., Betensky, R.A., Becker, J.A., Sepulcre, J., Rentz, D., Mormino, E., Chhatwal, J., Amariglio, R., Papp, K., Marshall, G., Albers, M., Mauro, S., Pepin, L., Alverio, J., Judge, K., Philiossaint, M., Shoup, T., Yokell, D., Dickerson, B., Gomez-Isla, T., Hyman, B., Vasdev, N., Sperling, R., 2016. Tau PET imaging in aging and early Alzheimer's disease. Ann. Neurol. 79, 110–119. https://doi.org/10.1002/ana.24546

Jonckers, E., Van Audekerke, J., De Visscher, G., Van der Linden, A., Verhoye, M., 2011. Functional connectivity fMRI of the rodent brain: comparison of functional connectivity networks in rat and mouse. PloS One 6, e18876. https://doi.org/10.1371/journal.pone.0018876

Jones, C.K., Huang, A., Xu, J., Edden, R.A.E., Schär, M., Hua, J., Oskolkov, N., Zacà, D., Zhou, J., McMahon, M.T., Pillai, J.J., van Zijl, P.C.M., 2013. Nuclear Overhauser enhancement (NOE) imaging in the human brain at 7T. NeuroImage 77, 114–124. https://doi.org/10.1016/j.neuroimage.2013.03.047

Khan, U.A., Liu, L., Provenzano, F.A., Berman, D.E., Profaci, C.P., Sloan, R., Mayeux, R., Duff, K.E., Small, S.A., 2014. Molecular drivers and cortical spread of lateral entorhinal cortex dysfunction in preclinical Alzheimer's disease. Nat. Neurosci. 17, 304–311. https://doi.org/10.1038/nn.3606

Kim, J., Basak, J.M., Holtzman, D.M., 2009. The Role of Apolipoprotein E in Alzheimer's Disease. Neuron 63, 287–303. https://doi.org/10.1016/j.neuron.2009.06.026

Kim, M., Gillen, J., Landman, B.A., Zhou, J., van Zijl, P.C.M., 2009. Water saturation shift referencing (WASSR) for chemical exchange saturation transfer (CEST) experiments. Magn. Reson. Med. 61, 1441–1450. https://doi.org/10.1002/mrm.21873

Klein, A., Andersson, J., Ardekani, B.A., Ashburner, J., Avants, B., Chiang, M.-C., Christensen, G.E., Collins, D.L., Gee, J., Hellier, P., Song, J.H., Jenkinson, M., Lepage, C., Rueckert, D., Thompson, P., Vercauteren, T., Woods, R.P., Mann, J.J., Parsey, R.V., 2009. Evaluation of 14 nonlinear deformation algorithms applied to human brain MRI registration. NeuroImage 46, 786–802. https://doi.org/10.1016/j.neuroimage.2008.12.037

Knobloch, M., Konietzko, U., Krebs, D.C., Nitsch, R.M., 2007. Intracellular Abeta and cognitive deficits precede beta-amyloid deposition in transgenic arcAbeta mice. Neurobiol. Aging 28, 1297–1306. https://doi.org/10.1016/j.neurobiolaging.2006.06.019

Kobayashi, D.T., Chen, K.S., 2005. Behavioral phenotypes of amyloid-based genetically modified mouse models of Alzheimer's disease. Genes Brain Behav. 4, 173–196. https://doi.org/10.1111/j.1601-183X.2005.00124.x

Kogan, F., Hariharan, H., Reddy, R., 2013. Chemical Exchange Saturation Transfer (CEST) Imaging: Description of Technique and Potential Clinical Applications. Curr. Radiol. Rep. 1, 102–114. https://doi.org/10.1007/s40134-013-0010-3

Kogan, F., Haris, M., Debrosse, C., Singh, A., Nanga, R.P., Cai, K., Hariharan, H., Reddy, R., 2014a. In vivo CEST Imaging of Creatine (CrCEST) in Skeletal Muscle at 3T. J. Magn. Reson. Imaging JMRI 40, 596–602. https://doi.org/10.1002/jmri.24412

Kogan, F., Haris, M., Singh, A., Cai, K., Debrosse, C., Nanga, R.P.R., Hariharan, H., Reddy, R., 2014b. Method for high-resolution imaging of creatine in vivo using chemical exchange saturation transfer. Magn. Reson. Med. 71, 164–172. https://doi.org/10.1002/mrm.24641

Kuntner, C., Kesner, A.L., Bauer, M., Kremslehner, R., Wanek, T., Mandler, M., Karch, R., Stanek, J., Wolf, T., Müller, M., Langer, O., 2009. Limitations of small animal PET imaging with [18F]FDDNP and FDG for quantitative studies in a transgenic mouse model of Alzheimer's disease. Mol. Imaging Biol. MIB Off. Publ. Acad. Mol. Imaging 11, 236–240. https://doi.org/10.1007/s11307-009-0198-z

Kuntner, C., Stout, D.B., 2014. Quantitative preclinical PET imaging: opportunities and challenges. Front. Phys. 2. https://doi.org/10.3389/fphy.2014.00012

Lane, C.A., Hardy, J., Schott, J.M., 2018. Alzheimer's disease. Eur. J. Neurol. 25, 59–70. https://doi.org/10.1111/ene.13439

Latif-Hernandez, A., Shah, D., Craessaerts, K., Saido, T., Saito, T., De Strooper, B., Van der Linden, A., D'Hooge, R., 2017. Subtle behavioral changes and increased prefrontal-hippocampal network synchronicity in APPNL-G-F mice before prominent plaque deposition. Behav. Brain Res. https://doi.org/10.1016/j.bbr.2017.11.017

Lau, J.C., Lerch, J.P., Sled, J.G., Henkelman, R.M., Evans, A.C., Bedell, B.J., 2008. Longitudinal neuroanatomical changes determined by deformation-based morphometry in a mouse model of Alzheimer's disease. NeuroImage 42, 19–27. https://doi.org/10.1016/j.neuroimage.2008.04.252

Le Bihan, D., 2014. Diffusion MRI: what water tells us about the brain. EMBO Mol. Med. 6, 569–573. https://doi.org/10.1002/emmm.201404055

Lee, D.-W., Chung, S., Yoo, H.J., Kim, S.J., Woo, C.-W., Kim, S.-T., Lee, D.-H., Kim, K.W., Kim, J.-K., Lee, J.S., Choi, C.G., Shim, W.H., Choi, Y., Woo, D.-C., 2016. Neurochemical Changes Associated with Stress-Induced Sleep Disturbance in Rats: In Vivo and In Vitro Measurements. PLOS ONE 11, e0153346. https://doi.org/10.1371/journal.pone.0153346

Leon, W.C., Canneva, F., Partridge, V., Allard, S., Ferretti, M.T., DeWilde, A., Vercauteren, F., Atifeh, R., Ducatenzeiler, A., Klein, W., Szyf, M., Alhonen, L., Cuello, A.C., 2010. A novel transgenic rat model with a full Alzheimer's-like amyloid pathology displays pre-plaque intracellular amyloid-beta-associated cognitive impairment. J. Alzheimers Dis. JAD 20, 113–126. https://doi.org/10.3233/JAD-2010-1349

Lewis, J., McGowan, E., Rockwood, J., Melrose, H., Nacharaju, P., Van Slegtenhorst, M., Gwinn-Hardy, K., Paul Murphy, M., Baker, M., Yu, X., Duff, K., Hardy, J., Corral, A., Lin, W.L., Yen, S.H., Dickson, D.W., Davies, P., Hutton, M., 2000. Neurofibrillary tangles,

amyotrophy and progressive motor disturbance in mice expressing mutant (P301L) tau protein. Nat. Genet. 25, 402–405. https://doi.org/10.1038/78078

Li, L., Wang, X.-Y., Gao, F.-B., Wang, L., Xia, R., Li, Z.-X., Xing, W., Tang, B.-S., Zeng, Y., Zhou, G.-F., Zhou, H.-Y., Liao, W.-H., 2016. Magnetic resonance T2 relaxation time at 7 Tesla associated with amyloid β pathology and age in a double-transgenic mouse model of Alzheimer's disease. Neurosci. Lett. 610, 92–97. https://doi.org/10.1016/j.neulet.2015.10.058

Li, Y., Rinne, J.O., Mosconi, L., Pirraglia, E., Rusinek, H., DeSanti, S., Kemppainen, N., Någren, K., Kim, B.-C., Tsui, W., de Leon, M.J., 2008. Regional analysis of FDG and PIB-PET images in normal aging, mild cognitive impairment, and Alzheimer's disease. Eur. J. Nucl. Med. Mol. Imaging 35, 2169–2181. https://doi.org/10.1007/s00259-008-0833-y

Li, Z., DiFranza, J.R., Wellman, R.J., Kulkarni, P., King, J.A., 2008. Imaging brain activation in nicotine-sensitized rats. Brain Res. 1199, 91–99. https://doi.org/10.1016/j.brainres.2008.01.016

Liang, Z., King, J., Zhang, N., 2012. Intrinsic organization of the anesthetized brain. J. Neurosci. Off. J. Soc. Neurosci. 32, 10183–10191. https://doi.org/10.1523/JNEUROSCI.1020-12.2012

Liang, Z., King, J., Zhang, N., 2011. Uncovering intrinsic connectional architecture of functional networks in awake rat brain. J. Neurosci. Off. J. Soc. Neurosci. 31, 3776–3783. https://doi.org/10.1523/JNEUROSCI.4557-10.2011

Liang, Z., Watson, G.D.R., Alloway, K.D., Lee, G., Neuberger, T., Zhang, N., 2015. Mapping the functional network of medial prefrontal cortex by combining optogenetics and fMRI in awake rats. NeuroImage 117, 114–123. https://doi.org/10.1016/j.neuroimage.2015.05.036

Liu, C.-C., Kanekiyo, T., Xu, H., Bu, G., 2013. Apolipoprotein E and Alzheimer disease: risk, mechanisms, and therapy. Nat. Rev. Neurol. 9, 106–118. https://doi.org/10.1038/nrneurol.2012.263

Liu, G., Song, X., Chan, K.W.Y., McMahon, M.T., 2013. Nuts and Bolts of CEST MR imaging. NMR Biomed. 26, 810–828. https://doi.org/10.1002/nbm.2899

Logothetis, N.K., 2008. What we can do and what we cannot do with fMRI. Nature 453, 869–878. https://doi.org/10.1038/nature06976

Lu, H., Zou, Q., Gu, H., Raichle, M.E., Stein, E.A., Yang, Y., 2012. Rat brains also have a default mode network. Proc. Natl. Acad. Sci. U. S. A. 109, 3979–3984. https://doi.org/10.1073/pnas.1200506109

Lundgaard, I., Li, B., Xie, L., Kang, H., Sanggaard, S., Haswell, J.D.R., Sun, W., Goldman, S., Blekot, S., Nielsen, M., Takano, T., Deane, R., Nedergaard, M., 2015. Direct neuronal glucose uptake heralds activity-dependent increases in cerebral metabolism. Nat. Commun. 6, 6807. https://doi.org/10.1038/ncomms7807

Luo, F., Rustay, N.R., Ebert, U., Hradil, V.P., Cole, T.B., Llano, D.A., Mudd, S.R., Zhang, Y., Fox, G.B., Day, M., 2012. Characterization of 7- and 19-month-old Tg2576 mice using multimodal in vivo imaging: limitations as a translatable model of Alzheimer's disease. Neurobiol. Aging 33, 933–944. https://doi.org/10.1016/j.neurobiolaging.2010.08.005

Ma, D., Cardoso, M.J., Modat, M., Powell, N., Wells, J., Holmes, H., Wiseman, F., Tybulewicz, V., Fisher, E., Lythgoe, M.F., Ourselin, S., 2014. Automatic Structural Parcellation of Mouse

Brain MRI Using Multi-Atlas Label Fusion. PLoS ONE 9. https://doi.org/10.1371/journal.pone.0086576

Ma, Y., Smith, D., Hof, P.R., Foerster, B., Hamilton, S., Blackband, S.J., Yu, M., Benveniste, H., 2008. In Vivo 3D Digital Atlas Database of the Adult C57BL/6J Mouse Brain by Magnetic Resonance Microscopy. Front. Neuroanat. 2, 1–1. https://doi.org/10.3389/neuro.05.001.2008

Mac Donald, C.L., Dikranian, K., Song, S.K., Bayly, P.V., Holtzman, D.M., Brody, D.L., 2007. Detection of traumatic axonal injury with diffusion tensor imaging in a mouse model of traumatic brain injury. Exp. Neurol. 205, 116–131. https://doi.org/10.1016/j.expneurol.2007.01.035

Macdonald, I.R., DeBay, D.R., Reid, G.A., O'Leary, T.P., Jollymore, C.T., Mawko, G., Burrell, S., Martin, E., Bowen, C.V., Brown, R.E., Darvesh, S., 2014. Early detection of cerebral glucose uptake changes in the 5XFAD mouse. Curr. Alzheimer Res. 11, 450–460.

Mahley, R.W., Rall, S.C., 2000. Apolipoprotein E: far more than a lipid transport protein. Annu. Rev. Genomics Hum. Genet. 1, 507–537. https://doi.org/10.1146/annurev.genom.1.1.507

Maier, F.C., Keller, M.D., Bukala, D., Bender, B., Mannheim, J.G., Brereton, I.M., Galloway, G.J., Pichler, B.J., 2015. Quantification of β-Amyloidosis and rCBF with Dedicated PET, 7 T MR Imaging, and High-Resolution Microscopic MR Imaging at 16.4 T in APP23 Mice. J. Nucl. Med. Off. Publ. Soc. Nucl. Med. 56, 1593–1599. https://doi.org/10.2967/jnumed.115.159350

Maier, F.C., Wehrl, H.F., Schmid, A.M., Mannheim, J.G., Wiehr, S., Lerdkrai, C., Calaminus, C., Stahlschmidt, A., Ye, L., Burnet, M., Stiller, D., Sabri, O., Reischl, G., Staufenbiel, M., Garaschuk, O., Jucker, M., Pichler, B.J., 2014. Longitudinal PET-MRI reveals β-amyloid deposition and rCBF dynamics and connects vascular amyloidosis to quantitative loss of perfusion. Nat. Med. 20, 1485–1492. https://doi.org/10.1038/nm.3734

Mangialasche, F., Solomon, A., Winblad, B., Mecocci, P., Kivipelto, M., 2010. Alzheimer's disease: clinical trials and drug development. Lancet Neurol. 9, 702–716. https://doi.org/10.1016/S1474-4422(10)70119-8

Mann, D.M.A., Pickering-Brown, S.M., Takeuchi, A., Iwatsubo, T., 2001. Amyloid Angiopathy and Variability in Amyloid β Deposition Is Determined by Mutation Position in Presenilin-1-Linked Alzheimer's Disease. Am. J. Pathol. 158, 2165–2175.

Marizzoni, M., Forloni, G., Frisoni, G.B., 2013. A new paradigm for testing AD drugs – neuroimaging biomarkers as surrogate outcomes homologous in animals and humans. Drug Discov. Today Ther. Strateg. 10, e63–e71. https://doi.org/10.1016/j.ddstr.2013.09.003

Maruyama, M., Shimada, H., Suhara, T., Shinotoh, H., Ji, B., Maeda, J., Zhang, M.-R., Trojanowski, J.Q., Lee, V.M.-Y., Ono, M., Masamoto, K., Takano, H., Sahara, N., Iwata, N., Okamura, N., Furumoto, S., Kudo, Y., Chang, Q., Saido, T.C., Takashima, A., Lewis, J., Jang, M.-K., Aoki, I., Ito, H., Higuchi, M., 2013. Imaging of Tau Pathology in a Tauopathy Mouse Model and in Alzheimer Patients Compared to Normal Controls. Neuron 79, 1094–1108. https://doi.org/10.1016/j.neuron.2013.07.037

Mathis, C.A., Bacskai, B.J., Kajdasz, S.T., McLellan, M.E., Frosch, M.P., Hyman, B.T., Holt, D.P., Wang, Y., Huang, G.-F., Debnath, M.L., Klunk, W.E., 2002. A lipophilic thioflavin-T

derivative for positron emission tomography (PET) imaging of amyloid in brain. Bioorg. Med. Chem. Lett. 12, 295–298.

Micotti, E., Paladini, A., Balducci, C., Tolomeo, D., Frasca, A., Marizzoni, M., Filibian, M., Caroli, A., Valbusa, G., Dix, S., O'Neill, M., Ozmen, L., Czech, C., Richardson, J.C., Frisoni, G.B., Forloni, G., 2015. Striatum and entorhinal cortex atrophy in AD mouse models: MRI comprehensive analysis. Neurobiol. Aging 36, 776–788. https://doi.org/10.1016/j.neurobiolaging.2014.10.027

Mielke, M.M., Hagen, C.E., Xu, J., Chai, X., Vemuri, P., Lowe, V.J., Airey, D.C., Knopman, D.S., Roberts, R.O., Machulda, M.M., Jack, C.R., Petersen, R.C., Dage, J.L., 2018. Plasma phospho-tau181 increases with Alzheimer's disease clinical severity and is associated with tau- and amyloid-positron emission tomography. Alzheimers Dement. J. Alzheimers Assoc. https://doi.org/10.1016/j.jalz.2018.02.013

Miller, C.O., Cao, J., Chekmenev, E.Y., Damon, B.M., Cherrington, A.D., Gore, J.C., 2015. Noninvasive measurements of glycogen in perfused mouse livers using chemical exchange saturation transfer NMR and comparison to (13)C NMR spectroscopy. Anal. Chem. 87, 5824–5830. https://doi.org/10.1021/acs.analchem.5b01296

Mlynárik, V., Cacquevel, M., Sun-Reimer, L., Janssens, S., Cudalbu, C., Lei, H., Schneider, B.L., Aebischer, P., Gruetter, R., 2012. Proton and phosphorus magnetic resonance spectroscopy of a mouse model of Alzheimer's disease. J. Alzheimers Dis. JAD 31 Suppl 3, S87-99. https://doi.org/10.3233/JAD-2012-112072

Mosconi, L., 2005. Brain glucose metabolism in the early and specific diagnosis of Alzheimer's disease. FDG-PET studies in MCI and AD. Eur. J. Nucl. Med. Mol. Imaging 32, 486–510. https://doi.org/10.1007/s00259-005-1762-7

Mosconi, L., Berti, V., Glodzik, L., Pupi, A., De Santi, S., de Leon, M.J., 2010. Pre-Clinical Detection of Alzheimer's Disease Using FDG-PET, with or without Amyloid Imaging. J. Alzheimers Dis. JAD 20, 843–854. https://doi.org/10.3233/JAD-2010-091504

Mosconi, L., Mistur, R., Switalski, R., Tsui, W.H., Glodzik, L., Li, Y., Pirraglia, E., De Santi, S., Reisberg, B., Wisniewski, T., de Leon, M.J., 2009. FDG-PET changes in brain glucose metabolism from normal cognition to pathologically verified Alzheimer's disease. Eur. J. Nucl. Med. Mol. Imaging 36, 811–822. https://doi.org/10.1007/s00259-008-1039-z

Mucke, L., 2009. Neuroscience: Alzheimer's disease. Nature 461, 895–897. https://doi.org/10.1038/461895a

Mucke, L., Masliah, E., Yu, G.Q., Mallory, M., Rockenstein, E.M., Tatsuno, G., Hu, K., Kholodenko, D., Johnson-Wood, K., McConlogue, L., 2000. High-level neuronal expression of abeta 1-42 in wild-type human amyloid protein precursor transgenic mice: synaptotoxicity without plaque formation. J. Neurosci. Off. J. Soc. Neurosci. 20, 4050–4058.

Mueggler, T., Meyer-Luehmann, M., Rausch, M., Staufenbiel, M., Jucker, M., Rudin, M., 2004. Restricted diffusion in the brain of transgenic mice with cerebral amyloidosis. Eur. J. Neurosci. 20, 811–817. https://doi.org/10.1111/j.1460-9568.2004.03534.x

Nanga, R.P.R., DeBrosse, C., Kumar, D., Roalf, D., McGeehan, B., D'Aquilla, K., Borthakur, A., Hariharan, H., Reddy, D., Elliott, M., Detre, J.A., Epperson, C.N., Reddy, R., n.d.

Reproducibility of 2D GluCEST in healthy human volunteers at 7 T. Magn. Reson. Med. 0. https://doi.org/10.1002/mrm.27362

Nasrallah, F.A., Pagès, G., Kuchel, P.W., Golay, X., Chuang, K.-H., 2013. Imaging brain deoxyglucose uptake and metabolism by glucoCEST MRI. J. Cereb. Blood Flow Metab. Off. J. Int. Soc. Cereb. Blood Flow Metab. 33, 1270–1278. https://doi.org/10.1038/jcbfm.2013.79

Nasrallah, F.A., Tay, H.-C., Chuang, K.-H., 2014. Detection of functional connectivity in the resting mouse brain. NeuroImage 86, 417–424. https://doi.org/10.1016/j.neuroimage.2013.10.025

Nelson, P.T., Head, E., Schmitt, F.A., Davis, P.R., Neltner, J.H., Jicha, G.A., Abner, E.L., Smith, C.D., Van Eldik, L.J., Kryscio, R.J., Scheff, S.W., 2011. Alzheimer's disease is not "brain aging": neuropathological, genetic, and epidemiological human studies. Acta Neuropathol. (Berl.) 121, 571–587. https://doi.org/10.1007/s00401-011-0826-y

Nelson, P.T., Jicha, G.A., Schmitt, F.A., Liu, H., Davis, D.G., Mendiondo, M.S., Abner, E.L., Markesbery, W.R., 2007. Clinicopathologic Correlations in a Large Alzheimer Disease Center Autopsy Cohort: Neuritic Plaques and Neurofibrillary Tangles "Do Count" When Staging Disease Severity. J. Neuropathol. Exp. Neurol. 66, 1136–1146. https://doi.org/10.1097/nen.0b013e31815c5efb

Ni, R., Rudin, M., Klohs, J., 2018. Cortical hypoperfusion and reduced cerebral metabolic rate of oxygen in the arcAβ mouse model of Alzheimer's disease. Photoacoustics 10, 38–47. https://doi.org/10.1016/j.pacs.2018.04.001

Nickerson, L.D., Smith, S.M., Öngür, D., Beckmann, C.F., 2017. Using Dual Regression to Investigate Network Shape and Amplitude in Functional Connectivity Analyses. Front. Neurosci. 11. https://doi.org/10.3389/fnins.2017.00115

Nie, J., Shen, D., 2013. Automated segmentation of mouse brain images using multi-atlas multi-ROI deformation and label fusion. Neuroinformatics 11, 35–45. https://doi.org/10.1007/s12021-012-9163-0

Nilsen, L.H., Melø, T.M., Saether, O., Witter, M.P., Sonnewald, U., 2012. Altered neurochemical profile in the McGill-R-Thy1-APP rat model of Alzheimer's disease: a longitudinal in vivo 1 H MRS study. J. Neurochem. 123, 532–541. https://doi.org/10.1111/jnc.12003

Nordberg, A., Rinne, J.O., Kadir, A., Långström, B., 2010. The use of PET in Alzheimer disease. Nat. Rev. Neurol. 6, 78–87. https://doi.org/10.1038/nrneurol.2009.217

Oakley, H., Cole, S.L., Logan, S., Maus, E., Shao, P., Craft, J., Guillozet-Bongaarts, A., Ohno, M., Disterhoft, J., Van Eldik, L., Berry, R., Vassar, R., 2006. Intraneuronal beta-amyloid aggregates, neurodegeneration, and neuron loss in transgenic mice with five familial Alzheimer's disease mutations: potential factors in amyloid plaque formation. J. Neurosci. Off. J. Soc. Neurosci. 26, 10129–10140. https://doi.org/10.1523/JNEUROSCI.1202-06.2006

Oddo, S., Caccamo, A., Shepherd, J.D., Murphy, M.P., Golde, T.E., Kayed, R., Metherate, R., Mattson, M.P., Akbari, Y., LaFerla, F.M., 2003. Triple-transgenic model of Alzheimer's disease with plaques and tangles: intracellular Abeta and synaptic dysfunction. Neuron 39, 409–421.

Ogawa, S., Lee, T.M., 1990. Magnetic resonance imaging of blood vessels at high fields: in vivo and in vitro measurements and image simulation. Magn. Reson. Med. 16, 9–18.

Ogawa, S., Lee, T.M., Kay, A.R., Tank, D.W., 1990. Brain magnetic resonance imaging with contrast dependent on blood oxygenation. Proc. Natl. Acad. Sci. U. S. A. 87, 9868–9872.

Oh, H., Madison, C., Baker, S., Rabinovici, G., Jagust, W., 2016. Dynamic relationships between age, amyloid-β deposition, and glucose metabolism link to the regional vulnerability to Alzheimer's disease. Brain J. Neurol. 139, 2275–2289. https://doi.org/10.1093/brain/aww108

Okamura, N., Suemoto, T., Shimadzu, H., Suzuki, M., Shiomitsu, T., Akatsu, H., Yamamoto, T., Staufenbiel, M., Yanai, K., Arai, H., Sasaki, H., Kudo, Y., Sawada, T., 2004. Styrylbenzoxazole derivatives for in vivo imaging of amyloid plaques in the brain. J. Neurosci. Off. J. Soc. Neurosci. 24, 2535–2541. https://doi.org/10.1523/JNEUROSCI.4456-03.2004

Olsen, M., Aguilar, X., Sehlin, D., Fang, X.T., Antoni, G., Erlandsson, A., Syvänen, S., 2018. Astroglial Responses to Amyloid-Beta Progression in a Mouse Model of Alzheimer's Disease. Mol. Imaging Biol. MIB Off. Publ. Acad. Mol. Imaging. https://doi.org/10.1007/s11307-017-1153-z

Paech, D., Schuenke, P., Koehler, C., Windschuh, J., Mundiyanapurath, S., Bickelhaupt, S., Bonekamp, D., Bäumer, P., Bachert, P., Ladd, M.E., Bendszus, M., Wick, W., Unterberg, A., Schlemmer, H.-P., Zaiss, M., Radbruch, A., 2017. T1ρ-weighted Dynamic Glucose-enhanced MR Imaging in the Human Brain. Radiology 285, 914–922. https://doi.org/10.1148/radiol.2017162351

Pagani, M., Damiano, M., Galbusera, A., Tsaftaris, S.A., Gozzi, A., 2016. Semi-automated registration-based anatomical labelling, voxel based morphometry and cortical thickness mapping of the mouse brain. J. Neurosci. Methods 267, 62–73. https://doi.org/10.1016/j.jneumeth.2016.04.007

Palmqvist, S., Mattsson, N., Hansson, O., 2016. Cerebrospinal fluid analysis detects cerebral amyloid-β accumulation earlier than positron emission tomography. Brain 139, 1226–1236. https://doi.org/10.1093/brain/aww015

Pan, W.-J., Billings, J.C.W., Grooms, J.K., Shakil, S., Keilholz, S.D., 2015. Considerations for resting state functional MRI and functional connectivity studies in rodents. Front. Neurosci. 9, 269. https://doi.org/10.3389/fnins.2015.00269

Pardo, J.V., Lee, J.T., Sheikh, S.A., Surerus-Johnson, C., Shah, H., Munch, K.R., Carlis, J.V., Lewis, S.M., Kuskowski, M.A., Dysken, M.W., 2007. Where the Brain Grows Old: Decline in Anterior Cingulate and Medial Prefrontal Function with Normal Aging. NeuroImage 35, 1231–1237. https://doi.org/10.1016/j.neuroimage.2006.12.044

Parent, M.J., Zimmer, E.R., Shin, M., Kang, M.S., Fonov, V.S., Mathieu, A., Aliaga, A., Kostikov, A., Do Carmo, S., Dea, D., Poirier, J., Soucy, J.-P., Gauthier, S., Cuello, A.C., Rosa-Neto, P., 2017. Multimodal Imaging in Rat Model Recapitulates Alzheimer's Disease Biomarkers Abnormalities. J. Neurosci. Off. J. Soc. Neurosci. 37, 12263–12271. https://doi.org/10.1523/JNEUROSCI.1346-17.2017

Pauling, L., Coryell, C.D., 1936. The Magnetic Properties and Structure of Hemoglobin, Oxyhemoglobin and Carbonmonoxyhemoglobin. Proc. Natl. Acad. Sci. U. S. A. 22, 210–216.

Paus, T., Collins, D.L., Evans, A.C., Leonard, G., Pike, B., Zijdenbos, A., 2001. Maturation of white matter in the human brain: a review of magnetic resonance studies. Brain Res. Bull. 54, 255–266. https://doi.org/10.1016/S0361-9230(00)00434-2

Pentkowski, N.S., Berkowitz, L.E., Thompson, S.M., Drake, E.N., Olguin, C.R., Clark, B.J., 2018. Anxiety-like behavior as an early endophenotype in the TgF344-AD rat model of Alzheimer's disease. Neurobiol. Aging 61, 169–176. https://doi.org/10.1016/j.neurobiolaging.2017.09.024

Pépin, J., Francelle, L., Carrillo-de Sauvage, M.-A., de Longprez, L., Gipchtein, P., Cambon, K., Valette, J., Brouillet, E., Flament, J., 2016. In vivo imaging of brain glutamate defects in a knock-in mouse model of Huntington's disease. NeuroImage 139, 53–64. https://doi.org/10.1016/j.neuroimage.2016.06.023

Petcharunpaisan, S., Ramalho, J., Castillo, M., 2010. Arterial spin labeling in neuroimaging. World J. Radiol. 2, 384–398. https://doi.org/10.4329/wjr.v2.i10.384

Poduslo, J.F., Wengenack, T.M., Curran, G.L., Wisniewski, T., Sigurdsson, E.M., Macura, S.I., Borowski, B.J., Jack, C.R., 2002. Molecular targeting of Alzheimer's amyloid plaques for contrast-enhanced magnetic resonance imaging. Neurobiol. Dis. 11, 315–329.

Poisnel, G., Hérard, A.-S., El Tannir El Tayara, N., Bourrin, E., Volk, A., Kober, F., Delatour, B., Delzescaux, T., Debeir, T., Rooney, T., Benavides, J., Hantraye, P., Dhenain, M., 2012. Increased regional cerebral glucose uptake in an APP/PS1 model of Alzheimer's disease. Neurobiol. Aging 33, 1995–2005. https://doi.org/10.1016/j.neurobiolaging.2011.09.026

Prince, M., Bryce, R., Albanese, E., Wimo, A., Ribeiro, W., Ferri, C.P., 2013. The global prevalence of dementia: a systematic review and metaanalysis. Alzheimers Dement. J. Alzheimers Assoc. 9, 63-75.e2. https://doi.org/10.1016/j.jalz.2012.11.007

Puntmann, V.O., Peker, E., Chandrashekhar, Y., Nagel, E., 2016. T1 Mapping in Characterizing Myocardial Disease: A Comprehensive Review. Circ. Res. 119, 277–299. https://doi.org/10.1161/CIRCRESAHA.116.307974

Radde, R., Bolmont, T., Kaeser, S.A., Coomaraswamy, J., Lindau, D., Stoltze, L., Calhoun, M.E., Jäggi, F., Wolburg, H., Gengler, S., Haass, C., Ghetti, B., Czech, C., Hölscher, C., Mathews, P.M., Jucker, M., 2006. Abeta42-driven cerebral amyloidosis in transgenic mice reveals early and robust pathology. EMBO Rep. 7, 940–946. https://doi.org/10.1038/sj.embor.7400784

Raichle, M.E., MacLeod, A.M., Snyder, A.Z., Powers, W.J., Gusnard, D.A., Shulman, G.L., 2001. A default mode of brain function. Proc. Natl. Acad. Sci. U. S. A. 98, 676–682. https://doi.org/10.1073/pnas.98.2.676

Redwine, J.M., Kosofsky, B., Jacobs, R.E., Games, D., Reilly, J.F., Morrison, J.H., Young, W.G., Bloom, F.E., 2003. Dentate gyrus volume is reduced before onset of plaque formation in PDAPP mice: a magnetic resonance microscopy and stereologic analysis. Proc. Natl. Acad. Sci. U. S. A. 100, 1381–1386. https://doi.org/10.1073/pnas.242746599

Rhein, V., Song, X., Wiesner, A., Ittner, L.M., Baysang, G., Meier, F., Ozmen, L., Bluethmann, H., Dröse, S., Brandt, U., Savaskan, E., Czech, C., Götz, J., Eckert, A., 2009. Amyloid-β and

tau synergistically impair the oxidative phosphorylation system in triple transgenic Alzheimer's disease mice. Proc. Natl. Acad. Sci. 106, 20057–20062. https://doi.org/10.1073/pnas.0905529106

Ridha, B.H., Anderson, V.M., Barnes, J., Boyes, R.G., Price, S.L., Rossor, M.N., Whitwell, J.L., Jenkins, L., Black, R.S., Grundman, M., Fox, N.C., 2008. Volumetric MRI and cognitive measures in Alzheimer disease : comparison of markers of progression. J. Neurol. 255, 567–574. https://doi.org/10.1007/s00415-008-0750-9

Rivlin, M., Horev, J., Tsarfaty, I., Navon, G., 2013. Molecular imaging of tumors and metastases using chemical exchange saturation transfer (CEST) MRI. Sci. Rep. 3, 3045. https://doi.org/10.1038/srep03045

Rivlin, M., Navon, G., 2016. Glucosamine and N-acetyl glucosamine as new CEST MRI agents for molecular imaging of tumors. Sci. Rep. 6. https://doi.org/10.1038/srep32648

Rivlin, M., Tsarfaty, I., Navon, G., 2014. Functional molecular imaging of tumors by chemical exchange saturation transfer MRI of 3-O-Methyl-D-glucose. Magn. Reson. Med. 72, 1375–1380. https://doi.org/10.1002/mrm.25467

Roalf, D.R., Nanga, R.P.R., Rupert, P.E., Hariharan, H., Quarmley, M., Calkins, M.E., Dress, E., Prabhakaran, K., Elliott, M.A., Moberg, P.J., Gur, R.C., Gur, R.E., Reddy, R., Turetsky, B.I., 2017. Glutamate imaging (GluCEST) reveals lower brain GluCEST contrast in patients on the psychosis spectrum. Mol. Psychiatry. https://doi.org/10.1038/mp.2016.258

Rocher, A.B., Chapon, F., Blaizot, X., Baron, J.-C., Chavoix, C., 2003. Resting-state brain glucose utilization as measured by PET is directly related to regional synaptophysin levels: a study in baboons. NeuroImage 20, 1894–1898.

Rodriguez-Vieitez, E., Ni, R., Gulyás, B., Tóth, M., Häggkvist, J., Halldin, C., Voytenko, L., Marutle, A., Nordberg, A., 2015. Astrocytosis precedes amyloid plaque deposition in Alzheimer APPswe transgenic mouse brain: a correlative positron emission tomography and in vitro imaging study. Eur. J. Nucl. Med. Mol. Imaging 42, 1119–1132. https://doi.org/10.1007/s00259-015-3047-0

Roher, A.E., Weiss, N., Kokjohn, T.A., Kuo, Y.-M., Kalback, W., Anthony, J., Watson, D., Luehrs, D.C., Sue, L., Walker, D., Emmerling, M., Goux, W., Beach, T., 2002. Increased A beta peptides and reduced cholesterol and myelin proteins characterize white matter degeneration in Alzheimer's disease. Biochemistry 41, 11080–11090.

Ruiz-Opazo, N., Kosik, K.S., Lopez, L.V., Bagamasbad, P., Ponce, L.R., Herrera, V.L., 2004. Attenuated hippocampus-dependent learning and memory decline in transgenic TgAPPswe Fischer-344 rats. Mol. Med. Camb. Mass 10, 36–44.

Saint-Aubert, L., Lemoine, L., Chiotis, K., Leuzy, A., Rodriguez-Vieitez, E., Nordberg, A., 2017. Tau PET imaging: present and future directions. Mol. Neurodegener. 12. https://doi.org/10.1186/s13024-017-0162-3

Saito, T., Matsuba, Y., Mihira, N., Takano, J., Nilsson, P., Itohara, S., Iwata, N., Saido, T.C., 2014. Single App knock-in mouse models of Alzheimer's disease. Nat. Neurosci. 17, 661–663. https://doi.org/10.1038/nn.3697

Salimi-Khorshidi, G., Douaud, G., Beckmann, C.F., Glasser, M.F., Griffanti, L., Smith, S.M., 2014. Automatic denoising of functional MRI data: combining independent component analysis

and hierarchical fusion of classifiers. NeuroImage 90, 449–468. https://doi.org/10.1016/j.neuroimage.2013.11.046

Sasaguri, H., Nilsson, P., Hashimoto, S., Nagata, K., Saito, T., De Strooper, B., Hardy, J., Vassar, R., Winblad, B., Saido, T.C., 2017. APP mouse models for Alzheimer's disease preclinical studies. EMBO J. 36, 2473–2487. https://doi.org/10.15252/embj.201797397

Scheltens, P., Blennow, K., Breteler, M.M.B., de Strooper, B., Frisoni, G.B., Salloway, S., Van der Flier, W.M., 2016. Alzheimer's disease. The Lancet 388, 505–517. https://doi.org/10.1016/S0140-6736(15)01124-1

Schuenke, P., Paech, D., Koehler, C., Windschuh, J., Bachert, P., Ladd, M.E., Schlemmer, H.-P., Radbruch, A., Zaiss, M., 2017a. Fast and Quantitative T1ρ-weighted Dynamic Glucose Enhanced MRI. Sci. Rep. 7, 42093. https://doi.org/10.1038/srep42093

Schuenke, P., Windschuh, J., Roeloffs, V., Ladd, M.E., Bachert, P., Zaiss, M., 2017b. Simultaneous mapping of water shift and B1(WASABI)-Application to field-Inhomogeneity correction of CEST MRI data. Magn. Reson. Med. 77, 571–580. https://doi.org/10.1002/mrm.26133

Schuenke, P., Windschuh, J., Roeloffs, V., Ladd, M.E., Bachert, P., Zaiss, M., 2016. Simultaneous mapping of water shift and B1 (WASABI)-Application to field-Inhomogeneity correction of CEST MRI data. Magn. Reson. Med. https://doi.org/10.1002/mrm.26133

Schwarz, A.J., Danckaert, A., Reese, T., Gozzi, A., Paxinos, G., Watson, C., Merlo-Pich, E.V., Bifone, A., 2006. A stereotaxic MRI template set for the rat brain with tissue class distribution maps and co-registered anatomical atlas: application to pharmacological MRI. NeuroImage 32, 538–550. https://doi.org/10.1016/j.neuroimage.2006.04.214

Schwarz, Adam J., Gass, N., Sartorius, A., Risterucci, C., Spedding, M., Schenker, E., Meyer-Lindenberg, A., Weber-Fahr, W., 2013. Anti-Correlated Cortical Networks of Intrinsic Connectivity in the Rat Brain. Brain Connect. 3, 503–511. https://doi.org/10.1089/brain.2013.0168

Schwarz, A. J., Gass, N., Sartorius, A., Zheng, L., Spedding, M., Schenker, E., Risterucci, C., Meyer-Lindenberg, A., Weber-Fahr, W., 2013. The low-frequency blood oxygenation level-dependent functional connectivity signature of the hippocampal-prefrontal network in the rat brain. Neuroscience 228, 243–258. https://doi.org/10.1016/j.neuroscience.2012.10.032

Serrano-Pozo, A., Qian, J., Monsell, S.E., Blacker, D., Gómez-Isla, T., Betensky, R.A., Growdon, J.H., Johnson, K.A., Frosch, M.P., Sperling, R.A., Hyman, B.T., 2014. Mild to moderate Alzheimer dementia with insufficient neuropathological changes. Ann. Neurol. 75, 597–601. https://doi.org/10.1002/ana.24125

Shah, D., Jonckers, E., Praet, J., Vanhoutte, G., Palacios, R.D. y, Bigot, C., D'Souza, D.V., Verhoye, M., Linden, A.V. der, 2013. Resting State fMRI Reveals Diminished Functional Connectivity in a Mouse Model of Amyloidosis. PLOS ONE 8, e84241. https://doi.org/10.1371/journal.pone.0084241

Shah, D., Praet, J., Latif Hernandez, A., Höfling, C., Anckaerts, C., Bard, F., Morawski, M., Detrez, J.R., Prinsen, E., Villa, A., De Vos, W.H., Maggi, A., D'Hooge, R., Balschun, D., Rossner, S., Verhoye, M., Van der Linden, A., 2016. Early pathologic amyloid induces hypersynchrony of BOLD resting-state networks in transgenic mice and provides an early therapeutic window before amyloid plaque deposition. Alzheimers Dement. J. Alzheimers Assoc. 12, 964–976. https://doi.org/10.1016/j.jalz.2016.03.010

Shah, M., Catafau, A.M., 2014. Molecular Imaging Insights into Neurodegeneration: Focus on Tau PET Radiotracers. J. Nucl. Med. Off. Publ. Soc. Nucl. Med. 55, 871–874. https://doi.org/10.2967/jnumed.113.136069

Sheline, Y.I., Raichle, M.E., 2013. Resting state functional connectivity in preclinical Alzheimer's disease. Biol. Psychiatry 74, 340–347. https://doi.org/10.1016/j.biopsych.2012.11.028

Sheline, Y.I., Raichle, M.E., Snyder, A.Z., Morris, J.C., Head, D., Wang, S., Mintun, M.A., 2010. Amyloid plaques disrupt resting state default mode network connectivity in cognitively normal elderly. Biol. Psychiatry 67, 584–587. https://doi.org/10.1016/j.biopsych.2009.08.024

Shu, X., Qin, Y.-Y., Zhang, S., Jiang, J.-J., Zhang, Y., Zhao, L.-Y., Shan, D., Zhu, W.-Z., 2013. Voxel-Based Diffusion Tensor Imaging of an APP/PS1 Mouse Model of Alzheimer's Disease. Mol. Neurobiol. 48, 78–83. https://doi.org/10.1007/s12035-013-8418-6

Sierra-Marcos, A., 2017. Regional Cerebral Blood Flow in Mild Cognitive Impairment and Alzheimer's Disease Measured with Arterial Spin Labeling Magnetic Resonance Imaging. Int. J. Alzheimers Dis. 2017. https://doi.org/10.1155/2017/5479597

Sigurdsson, E.M., Wadghiri, Y.Z., Mosconi, L., Blind, J.A., Knudsen, E., Asuni, A., Scholtzova, H., Tsui, W.H., Li, Y., Sadowski, M., Turnbull, D.H., de Leon, M.J., Wisniewski, T., 2008. A non-toxic ligand for voxel-based MRI analysis of plaques in AD transgenic mice. Neurobiol. Aging 29, 836–847. https://doi.org/10.1016/j.neurobiolaging.2006.12.018

Silver, I.A., Erecińska, M., 1994. Extracellular glucose concentration in mammalian brain: continuous monitoring of changes during increased neuronal activity and upon limitation in oxygen supply in normo-, hypo-, and hyperglycemic animals. J. Neurosci. Off. J. Soc. Neurosci. 14, 5068–5076.

Smith, A.D., 2002. Imaging the progression of Alzheimer pathology through the brain. Proc. Natl. Acad. Sci. 99, 4135–4137. https://doi.org/10.1073/pnas.082107399

Smith, S.M., Jenkinson, M., Johansen-Berg, H., Rueckert, D., Nichols, T.E., Mackay, C.E., Watkins, K.E., Ciccarelli, O., Cader, M.Z., Matthews, P.M., Behrens, T.E.J., 2006. Tract-based spatial statistics: voxelwise analysis of multi-subject diffusion data. NeuroImage 31, 1487–1505. https://doi.org/10.1016/j.neuroimage.2006.02.024

Smith, S.M., Vidaurre, D., Beckmann, C.F., Glasser, M.F., Jenkinson, M., Miller, K.L., Nichols, T.E., Robinson, E.C., Salimi-Khorshidi, G., Woolrich, M.W., Barch, D.M., Uğurbil, K., Van Essen, D.C., 2013. Functional connectomics from resting-state fMRI. Trends Cogn. Sci. 17, 666–682. https://doi.org/10.1016/j.tics.2013.09.016

Snellman, A., López-Picón, F.R., Rokka, J., Salmona, M., Forloni, G., Scheinin, M., Solin, O., Rinne, J.O., Haaparanta-Solin, M., 2013. Longitudinal amyloid imaging in mouse brain with 11C-PIB: comparison of APP23, Tg2576, and APPswe-PS1dE9 mouse models of Alzheimer disease. J. Nucl. Med. Off. Publ. Soc. Nucl. Med. 54, 1434–1441. https://doi.org/10.2967/jnumed.112.110163

Snellman, A., Rokka, J., López-Picón, F.R., Eskola, O., Salmona, M., Forloni, G., Scheinin, M., Solin, O., Rinne, J.O., Haaparanta-Solin, M., 2014. In vivo PET imaging of beta-amyloid deposition in mouse models of Alzheimer's disease with a high specific activity PET imaging agent [(18)F]flutemetamol. EJNMMI Res. 4, 37. https://doi.org/10.1186/s13550-014-0037-3

Snellman, A., Rokka, J., Lopez-Picon, F.R., Eskola, O., Wilson, I., Farrar, G., Scheinin, M., Solin, O., Rinne, J.O., Haaparanta-Solin, M., 2012. Pharmacokinetics of [^{18}F]flutemetamol in wild-type rodents and its binding to beta amyloid deposits in a mouse model of Alzheimer's disease. Eur. J. Nucl. Med. Mol. Imaging 39, 1784–1795. https://doi.org/10.1007/s00259-012-2178-9

Soesbe, T.C., Wu, Y., Dean Sherry, A., 2013. Advantages of paramagnetic chemical exchange saturation transfer (CEST) complexes having slow to intermediate water exchange properties as responsive MRI agents. NMR Biomed. 26, 829–838. https://doi.org/10.1002/nbm.2874

Sokoloff, L., 1981. Relationships among local functional activity, energy metabolism, and blood flow in the central nervous system. Fed. Proc. 40, 2311–2316.

Song, S.-K., Kim, J.H., Lin, S.-J., Brendza, R.P., Holtzman, D.M., 2004. Diffusion tensor imaging detects age-dependent white matter changes in a transgenic mouse model with amyloid deposition. Neurobiol. Dis. 15, 640–647. https://doi.org/10.1016/j.nbd.2003.12.003

Stebbins, G.T., Murphy, C.M., 2009. Diffusion tensor imaging in Alzheimer's disease and mild cognitive impairment. Behav. Neurol. 21, 39–49. https://doi.org/10.3233/BEN-2009-0234

Stewart, S., Cacucci, F., Lever, C., 2011. Which memory task for my mouse? A systematic review of spatial memory performance in the Tg2576 Alzheimer's mouse model. J. Alzheimers Dis. JAD 26, 105–126. https://doi.org/10.3233/JAD-2011-101827

Sturchler-Pierrat, C., Abramowski, D., Duke, M., Wiederhold, K.H., Mistl, C., Rothacher, S., Ledermann, B., Bürki, K., Frey, P., Paganetti, P.A., Waridel, C., Calhoun, M.E., Jucker, M., Probst, A., Staufenbiel, M., Sommer, B., 1997. Two amyloid precursor protein transgenic mouse models with Alzheimer disease-like pathology. Proc. Natl. Acad. Sci. U. S. A. 94, 13287–13292.

Sun, S.-W., Liang, H.-F., Cross, A.H., Song, S.-K., 2008. Evolving Wallerian degeneration after transient retinal ischemia in mice characterized by diffusion tensor imaging. NeuroImage 40, 1–10. https://doi.org/10.1016/j.neuroimage.2007.11.049

Sun, S.-W., Song, S.-K., Harms, M.P., Lin, S.-J., Holtzman, D.M., Merchant, K.M., Kotyk, J.J., 2005. Detection of age-dependent brain injury in a mouse model of brain amyloidosis associated with Alzheimer's disease using magnetic resonance diffusion tensor imaging. Exp. Neurol. 191, 77–85. https://doi.org/10.1016/j.expneurol.2004.09.006

Takkinen, J.S., López-Picón, F.R., Al Majidi, R., Eskola, O., Krzyczmonik, A., Keller, T., Löyttyniemi, E., Solin, O., Rinne, J.O., Haaparanta-Solin, M., 2016. Brain energy metabolism and neuroinflammation in ageing APP/PS1-21 mice using longitudinal (18)F-FDG and (18)F-DPA-714 PET imaging. J. Cereb. Blood Flow Metab. Off. J. Int. Soc. Cereb. Blood Flow Metab. 271678X16677990. https://doi.org/10.1177/0271678X16677990

Tang, X., Cai, F., Ding, D.-X., Zhang, L.-L., Cai, X.-Y., Fang, Q., 2018. Magnetic resonance imaging relaxation time in Alzheimer's disease. Brain Res. Bull. 140, 176–189. https://doi.org/10.1016/j.brainresbull.2018.05.004

Tapiola, T., Alafuzoff, I., Herukka, S.-K., Parkkinen, L., Hartikainen, P., Soininen, H., Pirttilä, T., 2009. Cerebrospinal fluid {beta}-amyloid 42 and tau proteins as biomarkers of Alzheimer-

type pathologic changes in the brain. Arch. Neurol. 66, 382–389. https://doi.org/10.1001/archneurol.2008.596

The amyloid hypothesis on trial. - PubMed - NCBI [WWW Document], n.d. URL https://www.ncbi.nlm.nih.gov/pubmed/30046080 (accessed 9.22.18).

Tolomeo, D., Micotti, E., Serra, S.C., Chappell, M., Snellman, A., Forloni, G., 2018. Chemical exchange saturation transfer MRI shows low cerebral 2-deoxy-D-glucose uptake in a model of Alzheimer's Disease. Sci. Rep. 8, 9576. https://doi.org/10.1038/s41598-018-27839-7

Tooyama, I., Yanagisawa, D., Taguchi, H., Kato, T., Hirao, K., Shirai, N., Sogabe, T., Ibrahim, N.F., Inubushi, T., Morikawa, S., 2016. Amyloid imaging using fluorine-19 magnetic resonance imaging ((19)F-MRI). Ageing Res. Rev. 30, 85–94. https://doi.org/10.1016/j.arr.2015.12.008

Toyama, H., Ichise, M., Liow, J.-S., Vines, D.C., Seneca, N.M., Modell, K.J., Seidel, J., Green, M.V., Innis, R.B., 2004. Evaluation of anesthesia effects on [18F]FDG uptake in mouse brain and heart using small animal PET. Nucl. Med. Biol. 31, 251–256. https://doi.org/10.1016/S0969-8051(03)00124-0

Tustison, N.J., Avants, B.B., Cook, P.A., Zheng, Y., Egan, A., Yushkevich, P.A., Gee, J.C., 2010. N4ITK: improved N3 bias correction. IEEE Trans. Med. Imaging 29, 1310–1320. https://doi.org/10.1109/TMI.2010.2046908

Valla, J., Schneider, L.E., Gonzalez-Lima, F., Reiman, E.M., 2006. Nonprogressive transgene-related callosal and hippocampal changes in PDAPP mice. Neuroreport 17, 829–832. https://doi.org/10.1097/01.wnr.0000220140.91294.15

van Zijl, P.C.M., Lam, W.W., Xu, J., Knutsson, L., Stanisz, G.J., 2018. Magnetization Transfer Contrast and Chemical Exchange Saturation Transfer MRI. Features and analysis of the field-dependent saturation spectrum. NeuroImage, Neuroimaging with Ultra-high Field MRI: Present and Future 168, 222–241. https://doi.org/10.1016/j.neuroimage.2017.04.045

van Zijl, P.C.M., Yadav, N.N., 2011. Chemical exchange saturation transfer (CEST): what is in a name and what isn't? Magn. Reson. Med. 65, 927–948. https://doi.org/10.1002/mrm.22761

von Bernhardi, R., 2007. Glial cell dysregulation: a new perspective on Alzheimer disease. Neurotox. Res. 12, 215–232.

von Kienlin, M., Künnecke, B., Metzger, F., Steiner, G., Richards, J.G., Ozmen, L., Jacobsen, H., Loetscher, H., 2005. Altered metabolic profile in the frontal cortex of PS2APP transgenic mice, monitored throughout their life span. Neurobiol. Dis. 18, 32–39. https://doi.org/10.1016/j.nbd.2004.09.005

Wadghiri, Y.Z., Li, J., Wang, J., Hoang, D.M., Sun, Y., Xu, H., Tsui, W., Li, Y., Boutajangout, A., Wang, A., de Leon, M., Wisniewski, T., 2013. Detection of amyloid plaques targeted by bifunctional USPIO in Alzheimer's disease transgenic mice using magnetic resonance microimaging. PloS One 8, e57097. https://doi.org/10.1371/journal.pone.0057097

Wadghiri, Y.Z., Sigurdsson, E.M., Sadowski, M., Elliott, J.I., Li, Y., Scholtzova, H., Tang, C.Y., Aguinaldo, G., Pappolla, M., Duff, K., Wisniewski, T., Turnbull, D.H., 2003. Detection of Alzheimer's amyloid in transgenic mice using magnetic resonance microimaging. Magn. Reson. Med. 50, 293–302. https://doi.org/10.1002/mrm.10529

Waldron, A.-M., Verhaeghe, J., wyffels, L., Schmidt, M., Langlois, X., Van Der Linden, A., Stroobants, S., Staelens, S., 2015a. Preclinical Comparison of the Amyloid-β Radioligands [(11)C]Pittsburgh compound B and [(18)F]florbetaben in Aged APPPS1-21 and BRI1-42 Mouse Models of Cerebral Amyloidosis. Mol. Imaging Biol. MIB Off. Publ. Acad. Mol. Imaging 17, 688–696. https://doi.org/10.1007/s11307-015-0833-9

Waldron, A.-M., Wintmolders, C., Bottelbergs, A., Kelley, J.B., Schmidt, M.E., Stroobants, S., Langlois, X., Staelens, S., 2015b. In vivo molecular neuroimaging of glucose utilization and its association with fibrillar amyloid-β load in aged APPPS1-21 mice. Alzheimers Res. Ther. 7, 76. https://doi.org/10.1186/s13195-015-0158-6

Waldron, A.-M., Wyffels, L., Verhaeghe, J., Bottelbergs, A., Richardson, J., Kelley, J., Schmidt, M., Stroobants, S., Langlois, X., Staelens, S., 2015c. Quantitative μPET Imaging of Cerebral Glucose Metabolism and Amyloidosis in the TASTPM Double Transgenic Mouse Model of Alzheimer's Disease. Curr. Alzheimer Res. 12, 694–703.

Waldron, A.-M., Wyffels, L., Verhaeghe, J., Richardson, J.C., Schmidt, M., Stroobants, S., Langlois, X., Staelens, S., 2017. Longitudinal Characterization of [18F]-FDG and [18F]-AV45 Uptake in the Double Transgenic TASTPM Mouse Model. J. Alzheimers Dis. JAD 55, 1537–1548. https://doi.org/10.3233/JAD-160760

Walker-Samuel, S., Ramasawmy, R., Torrealdea, F., Rega, M., Rajkumar, V., Johnson, S.P., Richardson, S., Gonçalves, M., Parkes, H.G., Arstad, E., Thomas, D.L., Pedley, R.B., Lythgoe, M.F., Golay, X., 2013. In vivo imaging of glucose uptake and metabolism in tumors. Nat. Med. 19, 1067–1072. https://doi.org/10.1038/nm.3252

Wang, F., Kopylov, D., Zu, Z., Takahashi, K., Wang, S., Quarles, C.C., Gore, J.C., Harris, R.C., Takahashi, T., 2016. Mapping murine diabetic kidney disease using chemical exchange saturation transfer MRI. Magn. Reson. Med. 76, 1531–1541. https://doi.org/10.1002/mrm.26045

Wang, H., Suh, J.W., Das, S.R., Pluta, J.B., Craige, C., Yushkevich, P.A., 2013. Multi-Atlas Segmentation with Joint Label Fusion. IEEE Trans. Pattern Anal. Mach. Intell. 35, 611–623. https://doi.org/10.1109/TPAMI.2012.143

Wang, H., Tan, L., Wang, H.-F., Liu, Y., Yin, R.-H., Wang, W.-Y., Chang, X.-L., Jiang, T., Yu, J.-T., 2015. Magnetic Resonance Spectroscopy in Alzheimer's Disease: Systematic Review and Meta-Analysis. J. Alzheimers Dis. JAD 46, 1049–1070. https://doi.org/10.3233/JAD-143225

Ward, K.M., Aletras, A.H., Balaban, R.S., 2000. A new class of contrast agents for MRI based on proton chemical exchange dependent saturation transfer (CEST). J. Magn. Reson. San Diego Calif 1997 143, 79–87. https://doi.org/10.1006/jmre.1999.1956

Webster, S.J., Bachstetter, A.D., Nelson, P.T., Schmitt, F.A., Van Eldik, L.J., 2014. Using mice to model Alzheimer's dementia: an overview of the clinical disease and the preclinical behavioral changes in 10 mouse models. Front. Genet. 5, 88. https://doi.org/10.3389/fgene.2014.00088

Weiss, C., Venkatasubramanian, P.N., Aguado, A.S., Power, J.M., Tom, B.C., Li, L., Chen, K.S., Disterhoft, J.F., Wyrwicz, A.M., 2002. Impaired eyeblink conditioning and decreased hippocampal volume in PDAPP V717F mice. Neurobiol. Dis. 11, 425–433.

Wells, J.A., O'Callaghan, J.M., Holmes, H.E., Powell, N.M., Johnson, R.A., Siow, B., Torrealdea, F., Ismail, O., Walker-Samuel, S., Golay, X., Rega, M., Richardson, S., Modat, M., Cardoso, M.J., Ourselin, S., Schwarz, A.J., Ahmed, Z., Murray, T.K., O'Neill, M.J., Collins, E.C., Colgan, N., Lythgoe, M.F., 2015. In vivo imaging of tau pathology using multi-parametric quantitative MRI. NeuroImage 111, 369–378. https://doi.org/10.1016/j.neuroimage.2015.02.023

Wiesmann, M., Capone, C., Zerbi, V., Mellendijk, L., Heerschap, A., Claassen, J.A.H.R., Kiliaan, A.J., 2015. Hypertension Impairs Cerebral Blood Flow in a Mouse Model for Alzheimer's Disease. Curr. Alzheimer Res. 12, 914–922.

Wiesmann, M., Zerbi, V., Jansen, D., Lütjohann, D., Veltien, A., Heerschap, A., Kiliaan, A.J., 2017. Hypertension, cerebrovascular impairment, and cognitive decline in aged AβPP/PS1 mice. Theranostics 7, 1277–1289. https://doi.org/10.7150/thno.18509

Windschuh, J., Zaiss, M., Meissner, J.-E., Paech, D., Radbruch, A., Ladd, M.E., Bachert, P., 2015. Correction of B1-inhomogeneities for relaxation-compensated CEST imaging at 7 T. NMR Biomed. 28, 529–537. https://doi.org/10.1002/nbm.3283

Winkler, A.M., Ridgway, G.R., Webster, M.A., Smith, S.M., Nichols, T.E., 2014. Permutation inference for the general linear model. NeuroImage 92, 381–397. https://doi.org/10.1016/j.neuroimage.2014.01.060

Wong, D.F., Rosenberg, P.B., Zhou, Y., Kumar, A., Raymont, V., Ravert, H.T., Dannals, R.F., Nandi, A., Brasić, J.R., Ye, W., Hilton, J., Lyketsos, C., Kung, H.F., Joshi, A.D., Skovronsky, D.M., Pontecorvo, M.J., 2010. In vivo imaging of amyloid deposition in Alzheimer disease using the radioligand 18F-AV-45 (florbetapir [corrected] F 18). J. Nucl. Med. Off. Publ. Soc. Nucl. Med. 51, 913–920. https://doi.org/10.2967/jnumed.109.069088

Xu, X., Chan, K.W.Y., Knutsson, L., Artemov, D., Xu, J., Liu, G., Kato, Y., Lal, B., Laterra, J., McMahon, M.T., van Zijl, P.C.M., 2015a. Dynamic glucose enhanced (DGE) MRI for combined imaging of blood-brain barrier break down and increased blood volume in brain cancer. Magn. Reson. Med. 74, 1556–1563. https://doi.org/10.1002/mrm.25995

Xu, X., Yadav, N.N., Knutsson, L., Hua, J., Kalyani, R., Hall, E., Laterra, J., Blakeley, J., Strowd, R., Pomper, M., Barker, P., Chan, K., Liu, G., McMahon, M.T., Stevens, R.D., van Zijl, P.C.M., 2015b. Dynamic Glucose-Enhanced (DGE) MRI: Translation to Human Scanning and First Results in Glioma Patients. Tomogr. J. Imaging Res. 1, 105–114. https://doi.org/10.18383/j.tom.2015.00175

Yamazaki, Y., Painter, M.M., Bu, G., Kanekiyo, T., 2016. Apolipoprotein E as a Therapeutic Target in Alzheimer's Disease: A Review of Basic Research and Clinical Evidence. CNS Drugs 30, 773–789. https://doi.org/10.1007/s40263-016-0361-4

Yanagisawa, D., Taguchi, H., Ibrahim, N.F., Morikawa, S., Shiino, A., Inubushi, T., Hirao, K., Shirai, N., Sogabe, T., Tooyama, I., 2014. Preferred features of a fluorine-19 MRI probe for amyloid detection in the brain. J. Alzheimers Dis. JAD 39, 617–631. https://doi.org/10.3233/JAD-131025

Yang, J., Wadghiri, Y.Z., Hoang, D.M., Tsui, W., Sun, Y., Chung, E., Li, Y., Wang, A., de Leon, M., Wisniewski, T., 2011. Detection of amyloid plaques targeted by USPIO-Aβ1-42 in Alzheimer's disease transgenic mice using magnetic resonance microimaging. NeuroImage 55, 1600–1609. https://doi.org/10.1016/j.neuroimage.2011.01.023

Yang, L., Rieves, D., Ganley, C., 2012. Brain amyloid imaging--FDA approval of florbetapir F18 injection. N. Engl. J. Med. 367, 885–887. https://doi.org/10.1056/NEJMp1208061

Yushkevich, P.A., Piven, J., Hazlett, H.C., Smith, R.G., Ho, S., Gee, J.C., Gerig, G., 2006. User-guided 3D active contour segmentation of anatomical structures: significantly improved efficiency and reliability. NeuroImage 31, 1116–1128. https://doi.org/10.1016/j.neuroimage.2006.01.015

Zaiss, M., Schmitt, B., Bachert, P., 2011. Quantitative separation of CEST effect from magnetization transfer and spillover effects by Lorentzian-line-fit analysis of z-spectra. J. Magn. Reson. San Diego Calif 1997 211, 149–155. https://doi.org/10.1016/j.jmr.2011.05.001

Zaiss, M., Xu, J., Goerke, S., Khan, I.S., Singer, R.J., Gore, J.C., Gochberg, D.F., Bachert, P., n.d. Inverse Z-spectrum analysis for spillover-, MT-, and T1-corrected steady-state pulsed CEST-MRI – application to pH-weighted MRI of acute stroke. NMR Biomed. 27, 240–252. https://doi.org/10.1002/nbm.3054

Zerbi, V., Grandjean, J., Rudin, M., Wenderoth, N., 2015. Mapping the mouse brain with rs-fMRI: An optimized pipeline for functional network identification. NeuroImage 123, 11–21. https://doi.org/10.1016/j.neuroimage.2015.07.090

Zerbi, V., Kleinnijenhuis, M., Fang, X., Jansen, D., Veltien, A., Van Asten, J., Timmer, N., Dederen, P.J., Kiliaan, A.J., Heerschap, A., 2013. Gray and white matter degeneration revealed by diffusion in an Alzheimer mouse model. Neurobiol. Aging 34, 1440–1450. https://doi.org/10.1016/j.neurobiolaging.2012.11.017

Zhang, H., Yushkevich, P.A., Rueckert, D., Gee, J.C., 2007. Unbiased White Matter Atlas Construction Using Diffusion Tensor Images, in: Medical Image Computing and Computer-Assisted Intervention – MICCAI 2007, Lecture Notes in Computer Science. Presented at the International Conference on Medical Image Computing and Computer-Assisted Intervention, Springer, Berlin, Heidelberg, pp. 211–218. https://doi.org/10.1007/978-3-540-75759-7_26

Zhang, J., Aggarwal, M., Mori, S., 2012. Structural insights into the rodent CNS via diffusion tensor imaging. Trends Neurosci. 35, 412–421. https://doi.org/10.1016/j.tins.2012.04.010

Zhang, S., Han, D., Tan, X., Feng, J., Guo, Y., Ding, Y., 2012. Diagnostic accuracy of 18 F-FDG and 11 C-PIB-PET for prediction of short-term conversion to Alzheimer's disease in subjects with mild cognitive impairment. Int. J. Clin. Pract. 66, 185–198. https://doi.org/10.1111/j.1742-1241.2011.02845.x

Zhou, I.Y., Wang, E., Cheung, J.S., Zhang, X., Fulci, G., Sun, P.Z., 2017. Quantitative chemical exchange saturation transfer (CEST) MRI of glioma using Image Downsampling Expedited Adaptive Least-squares (IDEAL) fitting. Sci. Rep. 7, 84. https://doi.org/10.1038/s41598-017-00167-y

Zhou, J., 2011. Amide proton transfer imaging of the human brain. Methods Mol. Biol. Clifton NJ 711, 227–237. https://doi.org/10.1007/978-1-61737-992-5_10

Zhou, J., Lal, B., Wilson, D.A., Laterra, J., van Zijl, P.C.M., 2003a. Amide proton transfer (APT) contrast for imaging of brain tumors. Magn. Reson. Med. 50, 1120–1126. https://doi.org/10.1002/mrm.10651

Zhou, J., Payen, J.-F., Wilson, D.A., Traystman, R.J., van Zijl, P.C.M., 2003b. Using the amide proton signals of intracellular proteins and peptides to detect pH effects in MRI. Nat. Med. 9, 1085–1090. https://doi.org/10.1038/nm907

Zimmer, E.R., Parent, M.J., Cuello, A.C., Gauthier, S., Rosa-Neto, P., 2014. MicroPET imaging and transgenic models: a blueprint for Alzheimer's disease clinical research. Trends Neurosci. 37, 629–641. https://doi.org/10.1016/j.tins.2014.07.002